Multiphysics Simulations of Ice Microstructure : Application to Europa Moon

Cyril Mergny

université PARIS-SACLAY

Multiphysics Simulations of Ice Microstructure: Application to Europa Moon

Simulations Multiphysiques de la Microstructure des Glaces: Application à Europe

Thèse de doctorat de l'université Paris-Saclay

École doctorale n° 579 : Sciences Mécaniques et Énergétiques, Matériaux et Géosciences (SMEMaG)
Spécialité de doctorat: Géosciences
Graduate School: Géosciences, climat, environnement et planètes
Référent : Faculté des Sciences d'Orsay

Thèse préparée dans l'unité de recherche GEOPS (Université Paris-Saclay, CNRS) sous la direction de **Frédéric Schmidt**, Professeur.

Thèse soutenue à Paris-Saclay, le 29 août 2024, par

Cyril MERGNY

Composition du jury

Membres du jury avec voix délibérative

François Costard Directeur de recherche - GEOPS, Orsay	Président
Bernard Schmitt Directeur de recherche - IPAG, Grenoble	Rapporteur & Examinateur
Gabriel Tobie Directeur de recherche - LPG, Nantes	Rapporteur & Examinateur
Bastian Gundlach Professor - Institut für Planetologie UM, Münster	Examinateur
Alice Le Gall Maîtresse de conférences HDR - UVSQ, Versailles	Examinatrice

THESE DE DOCTORAT

NNT : 2024UPASJ018

université PARIS-SACLAY

ÉCOLE DOCTORALE
Sciences mécaniques et énergétiques, matériaux et géosciences (SMEMAG)

Titre: Simulations Multiphysiques de la Microstructure des Glaces: Application à Europe
Mots clés: Surfaces Planétaires, Glace, Simulations Numériques

Résumé: La microstructure des surfaces planétaires glacées évolue sous l'influence d'une interaction complexe de processus physiques couplés. Cette thèse consiste en la construction d'un modèle de simulation multiphysique "Lunalcy", qui intègre une calcul précis du flux solaire, un solveur thermique stable et rapide, un modèle raffiné de métamorphisme de la glace, ainsi qu'un modèle de cristallisation par température et d'amorphisation par jardinage spatial. L'ensemble de ces processus sont interdépendants, et ce travail représente la première tentative en sciences planétaires d'étudier leur interaction couplée sur une échelle de temps du million d'années, avec une application spécifique à Europe, lune de Jupiter.

Tout comme les modèles de circulation générale (GCMs) sont devenus des outils essentiels pour étudier l'évolution des atmosphères planétaires, nous anticipons un développement de ces outils de simulation multiphysique pour l'étude des surfaces planétaires. Simuler ces processus hautement couplés contribue notamment à améliorer l'estimation des contraintes sur la taille des grains ou le taux de cristallisation de la glace. Ces avancées permettront d'affiner l'interprétation des mesures de surface telles que la spectroscopie et la spectro-photométrie, ce qui est essentiel pour l'analyse des observations passées et pour les futures missions telles que JUICE et Europa Clipper.

Title: Multiphysics Simulations of Ice Microstructure: Application to Europa Moon
Keywords: Planetary surfaces, Ice, Numerical simulations

Abstract: The microstructure of icy planetary surfaces evolves under the influence of a complex interplay of coupled physical processes. This thesis consists in the construction of a multiphysics simulation model "Lunalcy", which integrates an accurate solar flux calculation, a stable and fast thermal solver, a model of ice metamorphism/sintering, as well as a model of crystallization by temperature and amorphization by irradiation. These processes are interdependent, and this work represents the first attempt in planetary science to study their coupled interactions on a million-year timescale, with a specific application to Europa, a satellite of Jupiter.

Similar to how General Circulation Models (GCMs) have become essential tools for studying the evolution of planetary atmospheres, we anticipate further development of these multiphysics simulation tools for studying planetary surfaces. Simulating these highly coupled processes allows for better estimation of constraints on grain size or ice crystallization rates. These advancements will help refining the interpration of surface measurements such as spectroscopy and spectro-photometry, which is essential for analyzing past observations and for future missions such as JUICE and Europa Clipper.

Foreword

The work presented in this thesis is written in English to be accessible to the largest possible audience. Une synthèse de cette thèse est disponible en français pour les lecteurs francophones à la Section 6.4.3. The first time a technical word is encountered in the text, it is highlighted with a link to its definition that can be found in the Glossary.

This 3-year PhD program led to the redaction of 5 journal articles that will be presented in this dissertation:

1. **C. Mergny** and F. Schmidt, *MultIHeaTS: a Fast and Stable Thermal Solver for Multilayered Planetary Surfaces*, The Planetary Science Journal, DOI 10.3847/PSJ/ad6d6e, 2024
2. **C. Mergny** and F. Schmidt, *Gravity-Induced Ice Compaction and Subsurface Porosity on Icy Moons*, Icarus, DOI 10.1016/j.icarus.2024.116008, 2024
3. **C. Mergny** and F. Schmidt, *LunaIcy: Exploring Europa's Icy Surface Microstructure through Multiphysics Simulations*, The Planetary Science Journal, DOI 10.3847/PSJ/ad6d6d, 2024
4. **C. Mergny**, F. Schmidt and F. Keil, *Crystallinity of Europa's Surface*, *submitted to Icarus*, 2024
5. **C. Mergny**, F. Schmidt, F. Andrieu and I. Belgacem, *Photometric Map of Europa*, *in writing (not included in this thesis)*, 2024

The model developed in this PhD project is designed for use with any icy surface, but the focus here is on its application to the moon Europa. Discussions regarding applications on other surfaces can be found in Chapters 1 and 6.

Funding

The work presented in this dissertation was funded by the "specific doctoral contracts for normaliens" (CDSN) of the Ecole Normale Supérieure de Lyon, hosted at Université Paris-Saclay. We acknowledge support from the “Institut National des Sciences de l’Univers” (INSU), the “Centre National de la Recherche Scientifique” (CNRS) and “Centre National d’Etudes Spatiales” (CNES) through the “Programme National de Planétologie”.

Remerciements

Ces trois années de thèse ont été pour moi une expérience à la fois enrichissante et agréable. Cela n'a été possible que grâce au soutien de nombreuses personnes, que je vais essayer de remercier ici de la manière la plus exhaustive possible.

Premièrement, je tiens à exprimer toute ma gratitude à mon directeur de thèse, Frédéric. Dès le début, nous avons eu une excellente relation, et je te remercie pour la confiance que tu m'as rapidement accordée. Tu as su trouver l'équilibre parfait entre m'offrir l'autonomie nécessaire et me guider quand j'en avais besoin. J'ai particulièrement apprécié cette thèse parce que je n'ai jamais eu l'impression d'avoir un supérieur qui me donnait des ordres, mais plutôt un mentor qui m'accompagnait et me former à devenir un chercheur. Merci également pour toutes les opportunités que tu m'as offertes : les nombreuses conférences, workshops et séminaires en France et à l'international auxquels nous avons participé, et qui restent parmi mes meilleurs souvenirs. J'espère que nous continuerons à collaborer ensemble à l'avenir!

Je souhaite ensuite remercier les membres du jury qui ont tous contribué à améliorer mon manuscrit de thèse et m'ont guidé avec bienveillance. Un immense merci aux rapporteurs, à commencer par Bernard Schmitt, que j'ai rencontré à Grenoble lors de ma deuxième année de thèse et qui m'a immédiatement orienté vers des pistes pour perfectionner mon modèle. Merci également à Gabriel Tobie, qui a été mon directeur de stage de M2 et avec qui j'ai beaucoup apprécié travailler. Grâce à ses nombreux conseils et sa grande expertise, j'ai pu confronter mes travaux à davantage d'études issues de la littérature. Un grand merci à François Costard, qui a présidé ma soutenance avec brio, tout en apportant une touche de légèreté à l'atmosphère, ce qui m'a permis de me détendre en ce jour si important. Merci aussi pour ces bons moments (gastronomiques) passés en conférences ! Je tiens également à remercier les examinateurs, Alice Le Gall et Bastian Gundlach, pour leur intérêt marqué envers mes travaux tout au long de la thèse, ce qui m'a motivé à persévérer. Je les remercie aussi d'avoir accepté de faire partie de mon projet de post-doc. Un remerciement particulier une nouvelle fois à Alice Le Gall et Pascal Sailhac pour leur suivi constant dans le cadre de mon comité de thèse, veillant à ce que tout se déroule dans les meilleures conditions. Je souhaite aussi remercier plusieurs personnes sans qui ces années de thèse, et ma soutenance, ne se seraient aussi bien déroulées. Merci à Xavier Quidelleur, d'avoir fait en sorte que ma soutenance puisse se dérouler malgré la pause estivale, et aussi d'avoir été un très bon gardien de but lorsque l'on jouait au foot. Enfin, merci à toute l'équipe administrative, notamment Mylène et Georgette, qui ont géré avec efficacité l'administration de ma thèse et m'ont aidé

à organiser mes missions à l'étranger. Et bien sûr, merci au directeur de GEOPS, Christophe Colin.

Bien entendu, ce cadre de travail n'aurait pas été aussi agréable sans toutes les personnes avec qui j'ai partagé de bons moments. Merci à tous les doctorants, non-permanents et permanents de GEOPS. Un grand merci à Léo et Agathe, mes deux sparring partners, qui m'ont soutenu et régalé le jour de ma soutenance. Vous êtes les boss ! Merci à Guillaume, mon mentor, qui a toujours cru en moi et m'a constamment poussé à aller de l'avant. Merci aussi pour ces discussions autour de Fishou et ces moments inoubliables passés ensemble à l'étranger. Un merci aussi à François Andrieu, toujours là pour répondre à mes questions techniques et pour me poser des questions pointues lors de mes répétitions, me permettant de pousser ma réflexion. J'admire ton esprit critique et ta capacité d'analyse. Merci également aux doctorants du 504 de venir nous voir les midis, et bien sûr, un immense merci à la merveilleuse équipe du 509, que j'ai très vite décrite comme "une petite famille". Les pique-niques ensoleillés, les frites, les discussions, les frites, les rires, les activités sportives, les frites... m'ont permis de passer de si bons moments. Je tiens tout particulièrement à remercier les deux vielles branches Laure et Valérie, qui se bougent constamment pour essayer d'améliorer la vie au labo. Merci également à Claire, Julien, ainsi qu'à tous les étudiants qui sont passés par le 509 : Félix, Salman, Zongyu, Maxime, Killian, et tant d'autres. Bref, merci à vous tous du 509 : on n'a peut-être pas les locaux les plus modernes, mais l'ambiance y est incomparable.

En dehors du cadre du travail, il y a tout mon entourage qui a toujours été là pour moi et qui m'ont donné la force d'aller de l'avant.

Je commence par mes amis et mes proches, qui ont été d'un très grand soutien, que ce soit pour la thèse mais aussi tout au long de ma vie. Merci à tous mes Bordelais, et particulièrement à Axel, Cam, Gonzo et Tinou, vous êtes vraiment les boss des boss et je sais que je pourrai toujours compter sur vous. Merci à SC et merci à @fmdessine qui a illustré en partie cette thèse ! Merci à tous mes Lyonnais, notamment Louis, Raph et Seydou, soyez rassurés, la facture Engie fut dûment payée. Merci à tous mes Parisiens, aux anciens du LISN, comme aux anciens du KB. Merci à tous mes Muratais. Merci aussi à mes proches à l'étranger. Merci à Julia d'avoir été une grand source de soutien et de réconfort pendant ces années. Tu as su me montrer comment voir le verre à moitié plein et je t'en remercie. Merci à toute la famille Rodriguez, Sanchez et merci à Luna. Merci à The Institute, ses membres et son co-dirigeant N. Sangaré, qui m'ont poussé à accomplir ce rêve d'enfant. Merci Biggie, Makaveli, le Duc et merci la France.

Pour conclure, mes remerciements les plus profonds vont à ma famille. Merci Papa et Maman, vous êtes pour moi des modèles d'intégrité, que ce soit sur le plan professionnel ou humain. Vous avez toujours cru en moi, vous m'avez toujours encouragé et poussé à accomplir mes rêves. Merci pour tout. Vraiment. Merci énor-

mément à Pierrot, qui a su être le meilleur des grands frères. Je t'ai toujours admiré, que ce soit pour ta discipline et ton sérieux, mais aussi d'avoir toujours veillé sur moi. Tu m'as poussé à être meilleur dans toute situation et pour cela je te remercie. Merci aussi à mes grand parents de m'avoir aimé et encouragé dès le plus jeune âge. Merci mamie Régine, je t'admire pour ton calme et ta sagesse, et je suis content d'avoir pu autant échanger et apprendre à tes côtés. Merci mamie Iran, la personne avec le plus de bonté et de générosité que j'ai pu croiser de mon existence. Tu es depuis mon plus jeune âge, mon plus grand exemple. Je tiens également à remercier mes tontons et tatas. Merci à Kami, Michel et Nicole d'avoir été présents à ma soutenance, mais aussi merci Daniel, Minette, ainsi qu'à mes cousins et cousines, Franck, Emma, Melina. Merci aussi à Sofiane, avec qui je passe toujours de très bons moments en famille. Finalement, merci beaucoup à Didi, Hélène et Luc, qui ont fait partie intégrante de mon éducation, et dont j'applique encore aujourd'hui les précieux conseils. Et bien sûr, merci Icy :)

Enfin, merci à vous, lecteur, pour l'intérêt que vous portez à la lecture de ce travail.

Contents

CHAPTER 1

Introduction

Contents

1.1 Ices in the Solar System

1.1.1 Definitions

On Earth, "ice" commonly refers to water frozen into a solid state, typically at temperatures below 0 °C or 273.15 K at atmospheric pressure. Nearly all the ice on Earth is of a hexagonal crystalline structure, known as ice Ih. This structure consists of hexagonal rings formed by water molecules, with oxygen atoms at each vertex and hydrogen bonds along the edges of the rings.

In outer space and on extraterrestrial bodies, water forms various solid phases, more than any other element (Hobbs, 2010). This leads to a range of solid densities, from 920 kg m^{-3} for the common hexagonal ice, to as much as 1660 kg m^{-3} for the high-pressure phase, Ice VII (Prockter, 2005). In addition to various crystalline forms, water also exists in several amorphous phases. Amorphous solids have a long-range disordered arrangement of atoms or molecules in contrast to the long-range order characteristic of crystals. Figure 1.1 shows the phase diagram of the thermodynamically stable phases of ice and also includes the pressure-temperature regions where amorphous ices have been identified. Unlike other phases in the phase diagram, amorphous ices are metastable, meaning there is a crystalline phase of ice with lower energy. However, as we will see, ice can be locked into an amorphous state due to the slow kinetics of thermal crystallization at low temperatures. Due to the extreme conditions under which water condenses in molecular clouds, amorphous ice is likely the most common form of ice in the universe.

In astrophysics and planetary science, the term "ices" has a broader meaning: it refers to moderately-to-highly volatile chemical compounds in their frozen state (Schmitt, 1998). Volatiles are material with a low condensation temperature, like water, more likely to exist as a gas. While refractory materials, like metals, have a high condensation temperature, thus more likely to exist as a solid or liquid. In the solar system these ices mostly includes water (H_2O), ammonia (NH_3), sulfur dioxide (SO_2), carbon dioxide (CO_2), methane (CH_4), carbon monoxide (CO), and nitrogen (N_2) and constitute a significant portion of the mass of the outer solar system (Schmitt, 1998). As for water, these molecules can exist in crystalline or amorphous forms, with each molecule generally having a variety of phases for both their amorphous and crystalline cases. The specific phase depends largely on formation conditions, including temperature, initial state (gaseous or liquid), and subsequent thermal and irradiation history.

Ices found on and within solar system bodies are often not pure, either by being mixed to other ices or by containing impurities (minerals, metals, organics, ...). These mixed ices can take on different forms. Impurities or minor constituents may be randomly distributed as isolated molecules within the crystal lattice or amorphous matrix. Complexes such as hydrates can form, where a substance contains water or its constituent elements within its structure. To describe such compounds, we usually

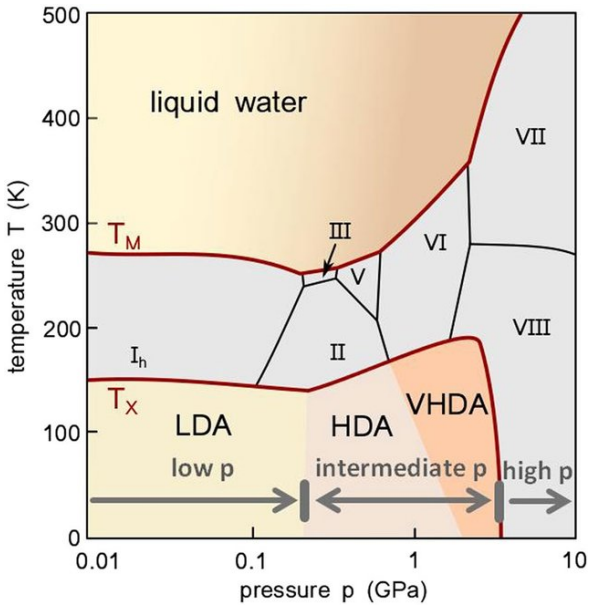

Figure 1.1: Phase diagram of water including the observation range for metastable amorphous ices. The stability regions for the crystalline phases are bounded by the melting line at higher temperatures and the crystallization line of the amorphous solid phases at lower temperatures (Stern et al., 2017)

use the notation "salt·$n$$H_2O$," where n represents the number of water molecules per formula unit of the salt, indicating that a salt is hydrated. Impurities can also form ice structures known as clathrates. A clathrate is a chemical compound in which a guest molecule is trapped within the crystal lattice of the host component. Although many molecules can form clathrates, those most relevant for planetary conditions are clathrate hydrates, which are clathrates formed by H_2O molecules, that could for instance trap CO_2 or N_2. While this thesis will primarily focus on pure ice, it is important to remember that the presence of impurities and mixed ices can influence the physical and chemical properties of ice, affecting how it interacts with its environment.

The Solar System

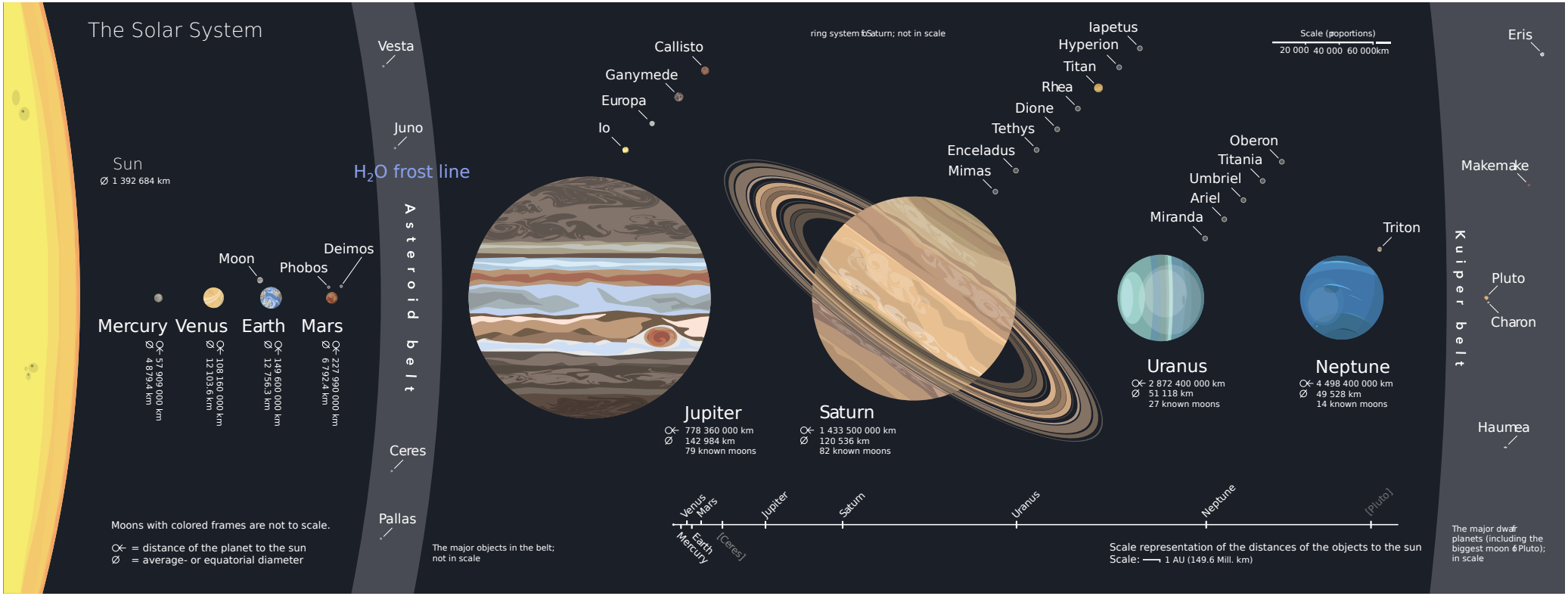

Figure 1.2: Comprehensive overview of the Solar System. The Sun, planets, dwarf planets and moons are at scale for their relative sizes, not for distances. A separate distance scale is at the bottom. Moons are listed near their planets by proximity of their orbits; only the largest moons are shown. Credit: Modified from Wikimedia Commons' solar system page to highlight the water frost line.

1.1.2 Origins and Distribution of Solar System Ices

1.1.2.1 Frost Lines

The distribution of ices throughout the solar system is closely related to how it was originally formed. Our Sun, like other stars, emerged from a cold interstellar cloud that collapsed under its own gravity, leading to the formation of a rotating proto-Sun surrounded by a rotating primordial solar nebula. The proto-Sun began to emit intense radiation and solar wind, which drove away much of the volatiles from the inner solar system. As the nebula started to cool, different elements condensed at varying distances from the Sun based on their condensation temperatures. Refractory materials, such as rocks and metals, solidified closer to the Sun, when temperatures dropped below 1300 K. Volatiles like water, carbon dioxide, nitrogen, and ammonia condensed at much lower temperatures, below 300 K, forming ice grains further from the Sun.

The frost line, also referred to as the *snow line* or *ice line*, is the minimum distance from the central protostar of a solar nebula where temperatures are low enough for volatile compounds to condense into solid grains. In the early solar system, this line marked the boundary where these materials could remain solid. Each volatile substance has its own frost line, determined by its condensation temperature in the pro-planetary disk (See Table 1.1).

Species	Condensation temperature (K)
H_2O	128-155
NH_3	74-86
CO_2	60-72
CH_4	26-32
N_2	12-15

Table 1.1: Condensation temperature ranges for ices corresponding to gas number densities of from 10^{10} to $10^{13}\,cm^{-3}$, suitable for disk mid-planes. Values from Zhang et al. (2015).

By estimating the pressure and temperature of the protoplanetary disk during the solar system's formation, we can determine the location of each frost line based on the sublimation curves of the volatiles. Among ices, water is the first to condense. Although the exact location is still debated, the water frost line is estimated to be within the asteroid belt between Mars and Jupiter (Prockter, 2005; Henin, 2018). In terms of astronomical units (AU), which is the average Earth-Sun distance ($1\,AU = 149 \times 10^6\,km$), this corresponds to a distance ranging from 3 to 5 AU (see Figure 1.2). At this distance, temperatures drop sufficiently to allow water to exist as ice.

As we move further outwards, temperatures decrease, causing more volatile com-

pounds to condense into icy particles. While it is less common to define frost lines for other volatile species, we can estimate their locations based on their condensation temperatures (see Table 1.1). The frost lines for ammonia and carbon dioxide are likely within Saturn's orbit (9.6 AU), while methane and nitrogen frost lines are roughly around Uranus's orbit (Henin, 2018).

1.1.2.2 The Role of Ices in Planet Formation

By knowing where each volatile condenses in our solar system, we can extrapolate the composition of the objects that formed in those regions These volatiles serve as the building blocks for planetesimals and other small solar system bodies.

In the inner solar system, which became depleted in volatiles, only heavier compounds can accumulate to form the typically small, rocky planets. The high temperatures prevent ices from remaining stable, and the solar wind further disperses light elements away from the Sun (Prockter, 2005). As a consequence, only terrestrial planets composed of refractory materials can form in the inner solar system.

The outer solar system lies beyond the water frost line, where ices constitute more than half of the mass of the material that condensed from the solar nebula (Prockter, 2005). This abundance of ices provided a lot more material for the formation of the outer planets, increasing the masses of planetesimals that collided to form large rock and ice cores. As a result, Jupiter and Saturn are believed to have rock/ice cores that are 10–15 times the mass of Earth, while Uranus and Neptune's cores are estimated to be 1–2 times Earth's mass (Prockter, 2005). Once these planets reached a certain size, they could attract and retain nearby gases, allowing them to accumulate thick atmospheres and become gas giants. Additionally, some of the gas surrounding the proto-gas giant planets formed rotating disks of material, which condensed to form small rock/ice moons. The composition of these moons varies with distance, similar to the planets formed around the Sun.

Separating the inner from the outer solar system, asteroids on the outer edges of the asteroid belt contain significant quantities of ices, whereas those on the inner part of the belt are generally devoid of ices. Due to minimal alteration, asteroid surfaces are very old and provide valuable insights into the conditions present during the solar system's formation.

Finally, one might wonder how terrestrial planets, like Earth, acquired substantial amounts of volatiles, such as water. The main theories suggest this was the result of the inward migration of Jupiter and Saturn towards the Sun, dragging many small objects along. These water-rich objects formed beyond the frost line, were thrown into the inner solar system, enriching it with volatiles. Lately, thanks to isotope studies, the Rosetta mission revealed that the water's isotopic ratio of Comet 67P/Churyumov-Gerasimenko differs from that of Earth's (Altwegg et al., 2015). These results indicate that most of Earth's water it did not originate from the Kuiper Belt but was likely delivered by asteroids.

As we have seen, ice represents a primordial material in the formation and evo-

lution of various planetary bodies. Although much of that icy material ended up in giant planets, ices are key to the formation and evolution of many smaller bodies.

1.1.3 Ices Across the Solar System

Ices are widespread throughout the solar system, spanning from the shaded regions of Mercury, the closest planet to the Sun, to the distant transneptunian objects. As our observational technology has improved, we have discovered more and more ices in diverse locations across the solar system. The majority of ices identified from telescopic observations and space missions are at the surface of planetary bodies. While water ice remains the most prevalent, a variety of other ices have also been observed throughout our solar system.

Mercury — Being the closest and hottest planet in our solar system, the presence of ice on Mercury's surface may seem unexpected. With daytime temperatures reaching up to 700 K, well above the condensation point of water, any ice would rapidly sublimate. However, both Earth-based observations (Slade et al., 1992) and data from NASA's MESSENGER spacecraft have uncovered ice deposits within craters near the planet's poles (Rubanenko et al., 2019). This discovery challenges conventional expectations, revealing that stable temperature and pressure conditions within permanently shadowed regions can allow ice to persist on Mercury's surface, despite its proximity to the Sun.

Venus — Among all the planets in our solar system, Venus stands out as the only one where any form of ice has ever been detected. The surface temperatures are simply too high to allow any form of ice to persist (Clark, Robert Carlson, et al., 2012).

Earth — Water covers 71% of the Earth's surface and can exist in three states: solid, liquid, and vapor. The United States Geological Survey (USGS) reports that approximately 96% of Earth's water exists in its oceans, seas, and bays, while the remaining 2% manifests in solid form, primarily as ice caps, glaciers, and permanent snow (See Figure 1.3a).

Moon — As with Mercury, it is likely that ice brought to the Moon by impacting bodies migrated towards the poles, where it became cold-trapped in shadowed regions. Neutron spectrometer data from the Lunar Prospector revealed the presence of hydrogen in the lunar polar areas (Murthy et al., 2013) and observations from the MESSENGER spacecraft confirmed the existence of ice in the permanently shadowed craters on the Moon (Rubanenko et al., 2019).

Mars — Both martian poles house ice caps made of water ice, covered by seasonal carbon dioxide ice, but the South pole has a permanent cover of CO_2 ice (see Figure 1.3b). The ices freezing points are within the range of seasonal, or even daily, temperature extremes, they can change phases over very short time periods. Additionally, the planet displays permafrost and geological features indicating glacial flow (Schmidt et al., 2022), along with the sublimation of water ice from beneath the surface.

The Asteroid Belt — It is hypothesized that some of the first water brought to Earth was delivered by asteroid impacts following the collision that produced the Moon. The presence of water ice was confirmed on the surface of asteroid 24 Themis using NASA's Infrared Telescope Facility on October 2009 (Rivkin et al., 2010; Campins et al., 2010). An absorption characteristic of water ice has been detected on 24 Themis, with its surface appearing to be completely covered in ice (Murthy et al., 2013).

Jupiter's system — As for the formation of the early solar system, the distribution of water ice within Galilean moons increases with the distance to Jupiter. Closest to Jupiter, Io is primarily rocky, while Europa, the next moon out, is mostly rock with a layer of water ice on its surface covering a liquid water ocean beneath. Ganymede, the third moon from Jupiter, has approximately equal proportions of ice and rock. In contrast, Callisto, the most distant Galilean moon, appears to be undifferentiated mixture of rock and ice. Europa surface (see Figure 1.3d) is the primary focus of application for the model developed in this thesis. For these reasons, the Jovian system has its own dedicated description at Section 1.2.

Saturn's system — Saturn has over 146 moons (at the date of 2023) (Sheppard et al., 2023), but here we focus on some of the larger regular satellites. Saturn's rings are composed of countless small particles, ranging in size from micrometers to meters, made almost entirely of water ice with minor amounts of rocky material and carbon dioxide. Spectroscopic studies by the Visual-Infrared Mapping Spectrometer (VIMS) on the Cassini spacecraft revealed that hexagonal water ice is a fundamental surface constituent on all these satellites (D. Cruikshank et al., 2005).

Among Saturn's inner moons, Mimas is the smallest, with a low density of $1150\,\mathrm{kg\,m^{-3}}$, indicating that it is primarily composed of water ice with only a small amount of rock. A recent analysis of Mimas's orbital motion based on Cassini data, revealed that its heavily cratered icy surface hides a global ocean (Lainey et al., 2024). Enceladus, though very small compared to other solar system satellites has an active geology due to tidal heating. The moon ejects icy water particles and gas creating a halo of ice dust that supplies Saturn's E-ring. Most of this material falls back onto Enceladus, keeping its surface bright white. The water jets originate from warm fractures known as "Tiger Stripes" (See Figure1.3d) and the plumes contain

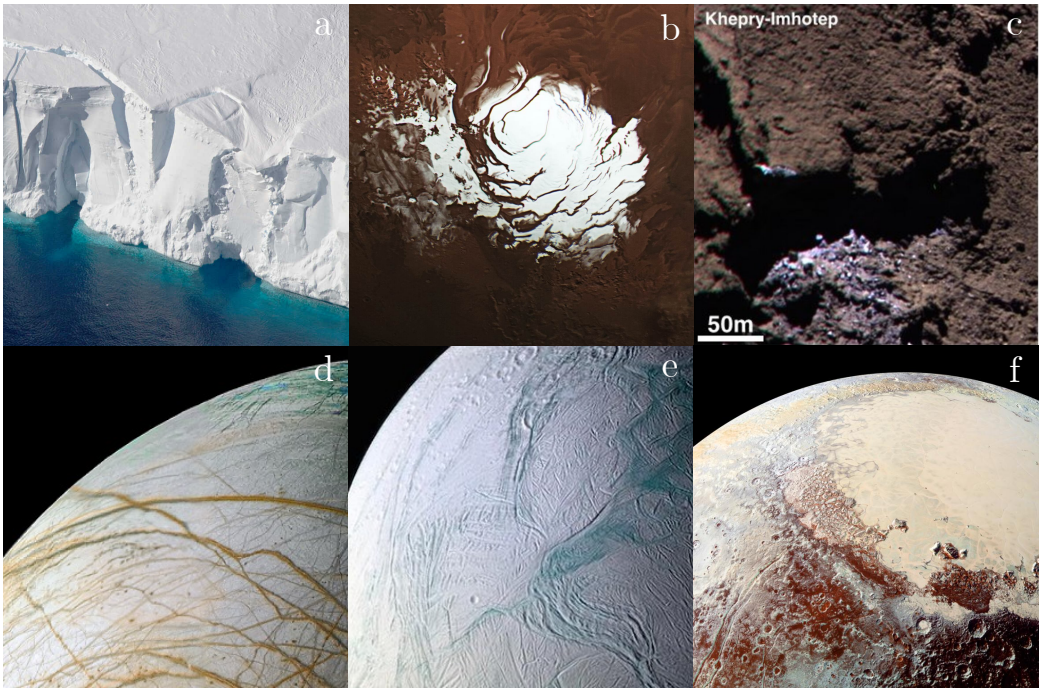

Figure 1.3: Variety of ices in the solar system. a) Earth, a growing cavity at the bottom of Thwaites Glacier (water ice) in West Antarctica, image $\sim$ 10 km wide, NASA/OIB. b) Mars, south polar ice cap composed of both carbon dioxide ice and water ice, image $\sim$ 500 km wide, ESA/DLR. c) Comet 67P/Churyumov-Gerasimenko, exposed water ice detected by Rosetta, ESA/DLR. d) Europa, water ice with reddish-brown ridges likely formed from a mix of water ice, salts, and sulfur, image $\sim$ 1200 km wide, NASA/JPL. e) Enceladus, water ice surface known for its plumes of material emanating from the Tiger Stripes, image $\sim$ 200 km wide, NASA/JPL. f) Pluto, surface crust of nitrogen ice, with mountains of water ice, and traces of methane and carbon monoxide ices, image $\sim$ 1500 km wide, NASA/JPL.

water vapor, carbon dioxide, methane, ammonia, and other gases, as well as salts and silica. Tethys has the lowest density of the major moons in the solar system, at $980\,\mathrm{kg\,m^{-3}}$, suggesting it is almost entirely made of water ice with just a small fraction of rock. Dione, on the other hand, consists of an icy mantle and crust over a silicate rocky core, with rock and water ice roughly equal in mass.

Among the outer moons, Rhea, is the second-largest of Saturn's moons, with a density of $1236\,\mathrm{kg\,m^{-3}}$, indicating that it is composed of approximately 25% rock and 75% ice. Titan, Saturn's largest moon and larger than Mercury, is made of icy materials and hydrocarbons. On January 15, 2005, the Huygens probe examined the clouds, atmosphere, and surface of Saturn's moon Titan during its descent. It is unique among the large moons, possessing a dense, cold atmosphere primarily of nitrogen with a small fraction of methane. Titan is also the only body in the Solar System besides Earth with liquid bodies on its surface, in the form of methane–ethane lakes. Iapetus, the third-largest of Saturn's moons, orbits at a distance of 3.5 million km, making it the most distant of Saturn's major moons and having the largest orbital inclination. It has a striking difference in coloration between its dark leading hemisphere and bright trailing hemisphere where CO_2 was detected trapped in H_2O ice (Buratti et al., 2005), along with a massive equatorial ridge running three-quarters of the way around the moon.

Uranus' system — The Uranian moons have only been imaged by a single spacecraft, Voyager 2, during its flyby in 1986 (Prockter, 2005). During this mission, broad water ice absorptions were observed on the surfaces of Uranus's five major satellites: Miranda, Ariel, Umbriel, Titania, and Oberon.

Neptune's system — Nearly all compositional information about ices in the Neptune system has been derived from Earth-based observations. Triton, Neptune's largest satellite, presents particularly intriguing and complex examples of outer solar system ice geology, leading to the identification of methane, nitrogen, and water ice absorptions. New spectrometers have significantly improved the quality of spectra, resulting in the discovery of CO, CO2, and C2H6 ices on Triton's surface (D. P. Cruikshank et al., 1993).

Pluto and Charon — Objects at Neptune's heliocentric distance and beyond, in the trans-Neptunian region, have surface temperatures low enough ($<$50 K) for multiple ices to condense. Both Pluto and its largest moon Charon, have densities about twice that of water, indicating a composition of rock and ice. The New Horizons mission, conducting a flyby on July 14, 2015, provided the first detailed measurements and observations of Pluto and its moons. The plains on Pluto's surface are primarily composed of nitrogen ice, with traces of methane and carbon monoxide, while the mountains consist mainly of water ice (See Figure 1.3e). Sputnik Planitia, a vast basin within Pluto's "Heart" region, comprises frozen nitrogen and carbon monox-

ide ices, arranged in polygonal cells, indicating convection activity. Following the New Horizons flyby, various surface features on Charon indicated that the moon is differentiated, and its surface appears to be dominated by the less volatile water ice.

Comets of the Kuiper Belt — Comets are composed of a primitive mixture of dust, gas, and ice, possibly unchanged from when they formed. As such, they serve as valuable laboratories for studying the primordial material of the early solar system. In 2014, the ESA mission Rosetta, with the objective of orbiting Comet 67P/Churyumov-Gerasimenko, deployed the Philae lander to its surface, conducting comprehensive scientific analyses. Using the high-resolution science camera aboard Rosetta, hundred patches of bright materials were detected on the comet's surface (see Figure 1.3c). Analysis of images captured by the OSIRIS NAC instrument suggests that these meter-sized bright spots correspond to exposed water ice at the comet's surface (Pommerol et al., 2015).

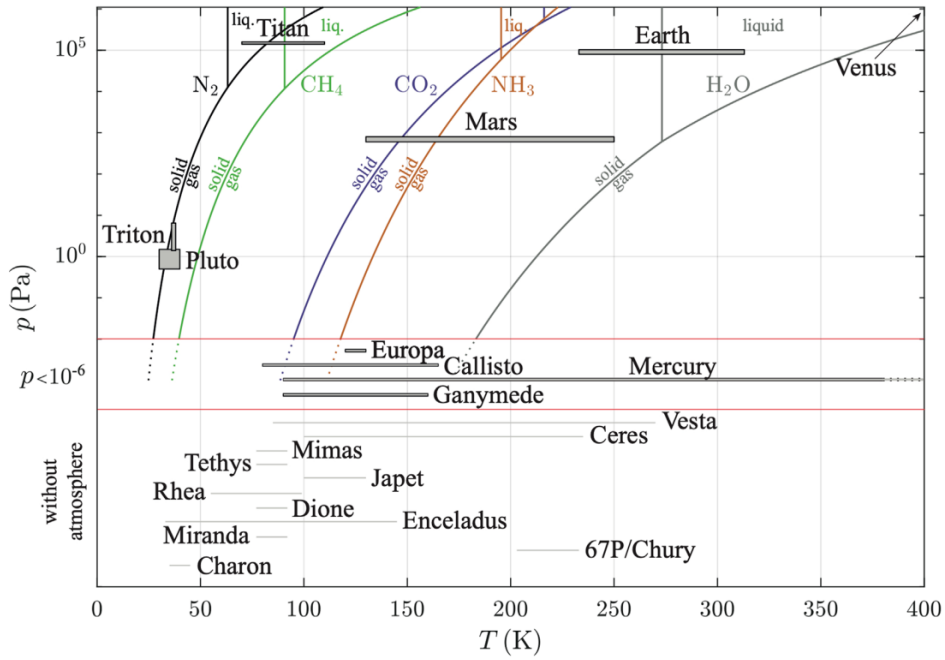

Figure 1.4: Superimposed phase diagrams of the mainly volatiles species (N_2, CH_4, CO_2, NH_3, H_2O) in the Solar System in the $P(T)$ space, based on Clausius-Clapeyron relation. The mean pressure and temperature conditions at the surface of planetary bodies likely to host ice are plotted (on average, shaded areas). The upper part of the figure corresponds to bodies with an atmosphere while the lower part contains bodies with little or no atmosphere. Figure from Carpy et al. (2023).

As we have seen, water ice is prevalent across the solar system, present in all planets and moons except Venus. Other ice species are also widespread beyond Earth

and a summary of their stability conditions has been represented on the superimposed phase diagrams of Figure 1.4. Studying and characterizing the properties of these ices is important as they help us understand the processes involved in the evolution of planetary surfaces. They influenced the composition in the early formation of planets and moons and continue to influence atmospheric and geological activities across various celestial bodies throughout the solar system.

1.2 The Jovian System

In the previous section, we have briefly reviewed the variety of ices found throughout our solar system. While all these icy surfaces are of great interest, in this PhD project we have chosen to concentrate our modeling efforts on Europa's surface, which still poses many unanswered questions. This section presents the current state of knowledge on Jupiter's system and its icy moon Europa, essential for understanding the work undertaken. While not exhaustive, we will highlight the key elements of the Jovian system, followed by a comprehensive description of Europa. This includes observed structures, compositions and morphologies, the processes that shape them, and insights into past and future explorations to the Jovian system.

1.2.1 Jupiter and the Galilean Moons

1.2.1.1 Jupiter

Jupiter, the fifth planet from the Sun, is the largest and most massive planet in the Solar System, orbiting at approximately 5.2 AU from the Sun. With a radius of $R_{\mathrm{J}} = 71,492$ km and mass of $m_{\mathrm{J}} = 1.9 \times 10^{27}$ kg, it is 11.2 times larger than Earth, and 317.8 heavier (Guillot et al., 2004). Jupiter has the shortest rotation period of any planet in our Solar System, completing a full rotation in just 10 hours. Its period of revolution around the Sun is $p_{\mathrm{J}} = 11.8$ years.

Jupiter's massive atmosphere consists of various latitudinal cloud bands, each rotating at different speeds, creating turbulence and storms. This differential rotation produces notable features such as the 'Great Red Spot,' a giant anticyclone twice the diameter of Earth. Figure 1.5 captured by the Junocam on the Juno spacecraft, show a view of the gas giant and its turbulent atmosphere. The atmosphere composition is primarily hydrogen and helium, similar to the Sun, with these elements making up over 87% of its mass (Guillot et al., 2004). The planet's interior is not well-constrained, but the warm conditions (around 20,000 K) suggest that the interior is mostly fluid with a dense rock and ice core. This core is surrounded by a helium-enriched metallic hydrogen envelope and an outer layer of molecular hydrogen.

Jupiter's strong gravitational field causes significant tidal forces on its orbiting bodies. These tidal forces induce stresses on the satellites, which vary depending on the materials involved. Stresses can be stored elastically, relieved through material

Figure 1.5: Jupiter as seen by the Juno spacecraft. Credits: NASA/JPL

failure, or relaxed viscously, with viscous effects being particularly important for icy satellites due to ice's low melting point (Wahr et al., 2009). As gravitational forces decrease inversely with the square root of the distance, tidal heating becomes less important the further away from Jupiter. This leads to variations on the heat budget and internal structure of each satellite.

1.2.1.2 The Jovian Magnetosphere

Convection in Jupiter's deep layer of liquid metallic hydrogen generates a massive magnetic field, creating a magnetosphere that significantly influences any object orbiting the planet, especially the closest ones. The magnetosphere is divided into three parts: inner, middle, and outer. The middle magnetosphere includes the Galilean moons, with Io playing a major role through its interaction with the magnetosphere. Io continuously emits large amounts of sulfur dioxide via volcanic activity. These eruption products are dissociated and ionized by electron impacts from Jupiter's magnetosphere, producing ions of sulfur and oxygen, forming a 'plasma torus' of charged particles along Io's orbit (Cooper, 2001) (see Figure 1.6). This plasma torus, though less influential in the outer magnetosphere, is responsible for Jupiter's Auroras and strongly affects the surfaces of the moons orbiting close to Io in the middle magnetosphere. The charged particles significantly impact the surface composition and surface properties of the icy Galilean satellites.

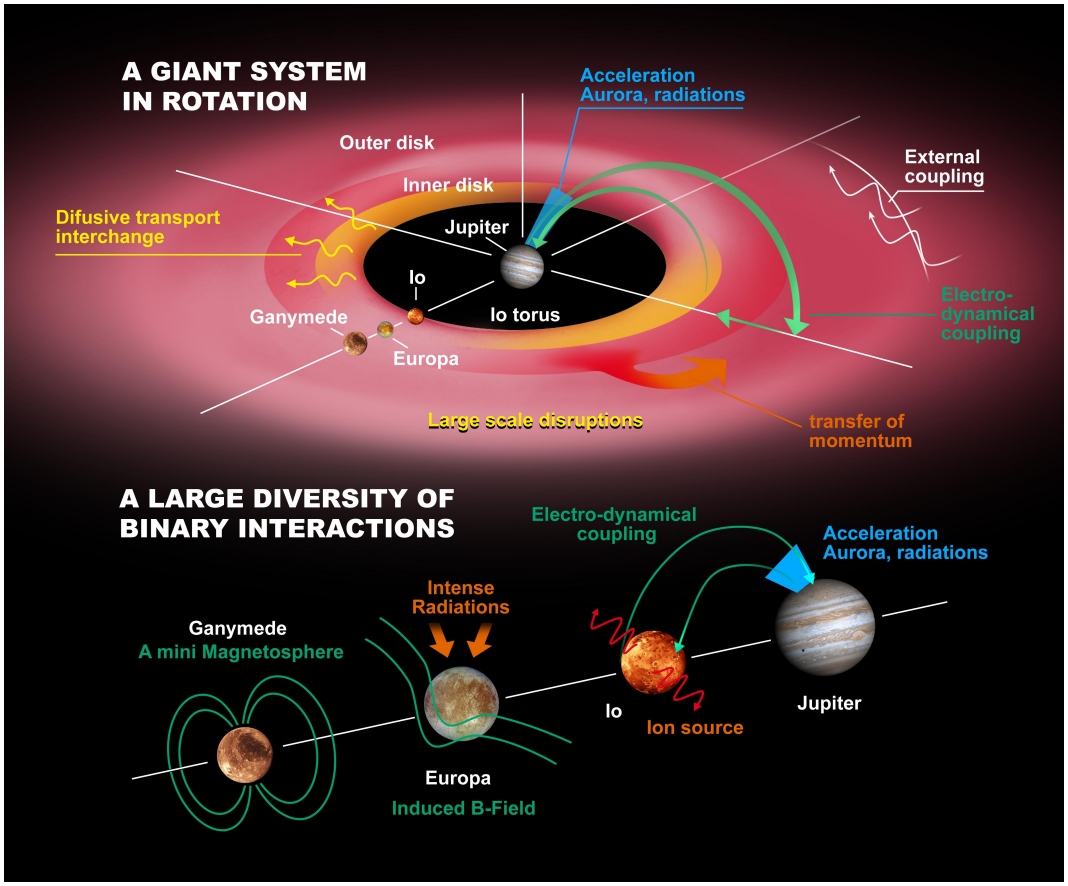

Figure 1.6: Electrodynamic interactions play a variety of roles in the Jovian system: generation of plasma at the Io torus, magnetosphere / satellite interactions, dynamics of a giant plasma disc coupled to Jupiter's rotation by the auroral current system, generation of Jupiter's intense radiation belts. Credit: MPS/ESA/NASA.

1.2.1.3 The Galilean Moons

The Jovian system is made of 79 known natural satellites, with the four Galilean moons accounting for 99.997% of the total satellite mass. The majority of these moons (62) have retrograde orbits, which is explained by the Galilean moons' efficiency in ejecting prograde orbit satellites (Astakhov et al., 2003). Ganymede, Europa, and Io have a 1:2:4 resonance, known as Laplace resonance, where Ganymede completes one orbit, Europa completes two, and Io completes four. This resonance prevents the three Galilean moons from having a completely circular orbit, leading to strong tidal forces from Jupiter. The four Galilean moons are tidally locked to Jupiter, meaning that one hemisphere always faces the planet. This hemisphere is referred to as the sub-Jovian hemisphere, while the opposite hemisphere is known as the anti-Jovian hemisphere. Similarly, we differentiate between the leading hemisphere, which faces the direction of the moon's orbit, and the trailing hemisphere, which faces the opposite direction.

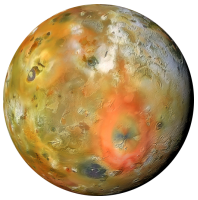

Io — Io, the closest Galilean moon to Jupiter and the second smallest, has a radius of 1820 km. With the highest density of $3528\,\mathrm{kg\,m^{-3}}$, it is primarily composed of rock. Due to its proximity to Jupiter, Io experiences strong tidal forces, resulting in significant internal heating. This important internal heating leads to the ongoing volcanic activity (Hussmann et al., 2004; Tyler et al., 2015), and can also cause surface displacements of up to 100 m.
The yellowish color of Io's surface is due to sulfur compounds produced by its volcanic activity (McEwen et al., 2004), resulting a in high bond albedo of 0.63. The dominant species is SO_2 ice (McEwen, 1988), which sublimates during the day due to relatively high surface temperatures. Although most of it recondenses locally during the nighttime, SO_2 molecules slowly migrate toward higher latitudes and colder regions (Nash, 1983). The continuous volcanic eruptions constantly renew Io's surface, making it the youngest in the Solar System, with an age of approximately 1.9-3.6 kyr (McEwen et al., 2004). As discussed in Section 1.2.1.2, this volcanic activity is also responsible for providing the magnetosphere of the Galilean moons with sulfur and oxygen ions.

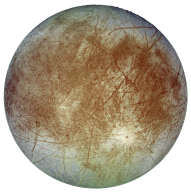

Europa — Europa is the second Galilean moon and the smallest, with a radius of 1560 km. With a density of $3014\,\mathrm{kg\,m^{-3}}$, the moon is completely differentiated with a solid iron core, a rocky mantle and a water layer of about 100 km thick (Vance et al., 2018). Galileo's magnetometer has detected an induced magnetic field, which suggests the presence of a conductive layer beneath the surface, likely due to the presence of a subsurface ocean of salted liquid water (Khurana et al., 1998).

Europa is the brightest Galilean moon with a global bond albedo of 0.68. Its surface, predominantly water ice mixed with non-ice materials, is marked with long lineaments, some stretching thousands of kilometers. The scarcity of craters suggests a young surface, estimated to be approximately 30 Myr old (Pappalardo et al., 1998). Being the primary focus of this thesis, Europa has it own dedicated description at Section 1.2.2.

Ganymede — The third Galilean moon, is the largest satellite of the entire solar system, with a radius of 2630 km. With a density of 1942 $\mathrm{kg\,m^{-3}}$, Ganymede is entirely differentiated with an iron core, a rocky mantle and an ice shell of about 800 km (J. D. Anderson, Lau, et al., 1996). Ganymede contains more ice than Europa, but has a dark surface with an average bond albedo of 0.44 (Pater et al., 2014). The major source of this dark material is probably meteoritic infall, which should also occur on Europa, but Europa's active resurfacing likely buried the meteoritic material within the ice shell. In contrast, the surface of Ganymede is heavily cratered, with an estimate age of approximately 2 Gyr (Zahnle et al., 2003).

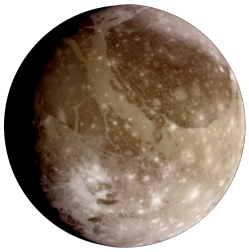

Ganymede is the only natural satellite to generate its own magnetic field (See Figure 1.6). The iron core of Ganymede, believed to exceed 1300 K in temperature (J. D. Anderson, Lau, et al., 1996), is thought to be in a liquid state, driving convection and producing the moon's magnetic field. This magnetic shield protects the equatorial regions from most energetic particle radiation, redirecting it towards the polar regions. As a consequence, the interaction between Jupiter's magnetosphere and Ganymede influences surface features and generate Auroras.
Under its ice surface, Ganymede host a global liquid ocean, inferred by measurements of an the induced magnetic field (Kivelson et al., 2002). The ocean is not in direct contact with the rocky mantle but separated by hundred of kilometers of high-pressure ice which imply that a strong thermal gradient must exist inside Ganymede's ice shell to allow the presence of a liquid layer.

Callisto — Callisto is the furthest Galilean satellite, with a radius of 2410 km, it is about the size of Mercury. Being far away from Jupiter, it does not participate in the resonance in which the three inner Galilean satellite. With a density of 1834 $\mathrm{kg\,m^{-3}}$, Callisto is only partly differentiated, with a composition that is a mixed of approximately equal parts water ice and rocky silicates. As for Europa and Ganymede, the detection of an induced magnetic field by Galileo's magnetometer, suggest the presence of a global water ocean.

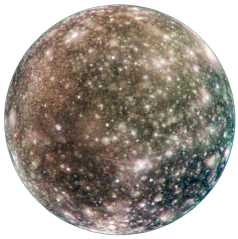

Callisto has the darkest surface among the Galilean satellites, with a global bond albedo of 0.22. Interestingly, its leading side appears darker than the trailing one, contrary to the pattern observed on its counterparts (Moore et al., 2004). The surface is heavily cratered with an age estimated between 3.9 and 4.3 Gyr making it the oldest of the Solar System.

Property	Io	Europa	Ganymede	Callisto
Semi-major axis (10^6 km)	421	671	1070	1882
Radius (km)	1820	1560	2630	2410
Orbital period (days)	1.77	3.55	7.155	16.689
Density (kg m^{-3})	3528	3014	1942	1834
Estimated surface age	~ 3 kyr	~ 30 Myr	~ 2 Gyr	> 4 Gyr
Bond albedo	0.63	0.68	0.44	0.19
Surface temperatures, min-mean-max (K)	90-110-130	50-102-125	70-110-152	80-134-165

Table 1.2: Principal characteristics of the Galilean moons based on Pater et al. (2014).

The icy Galilean moons are of significant scientific interest due to their potential habitability, characterized by the presence of stable liquid water, essential organic building blocks, and an energy source (Priscu et al., 2012). Their subsurface oceans, surface chemistry, and signs of activity make them intriguing candidates for harboring life. A summary of their principal characteristics is provided in Table 1.2.

1.2.2 Focus on Europa

Europa holds the minimum requirements for the emergence of life: stable liquid water, building blocks of organic material (C, H, N, O, P, S) and a source of energy. For these reasons, Europa was quickly a priority candidate for space exploration, from Earth-based telescopic observation to dedicated space missions, bringing more and more information on the moon's habitability potential.

Although a few flybys of the Jovian system by space probes (Pioneer, Voyager 1 and 2, New Horizons) provided initial insights into Europa's surface, most of the current data comes from the Galileo spacecraft. Galileo orbited Jupiter from 1995 to 2003, performing numerous close flybys of Europa. The Juno spacecraft made a few flybys of Europa in September 2022, but as of the writing of this thesis, the data has not yet been made publicly available.

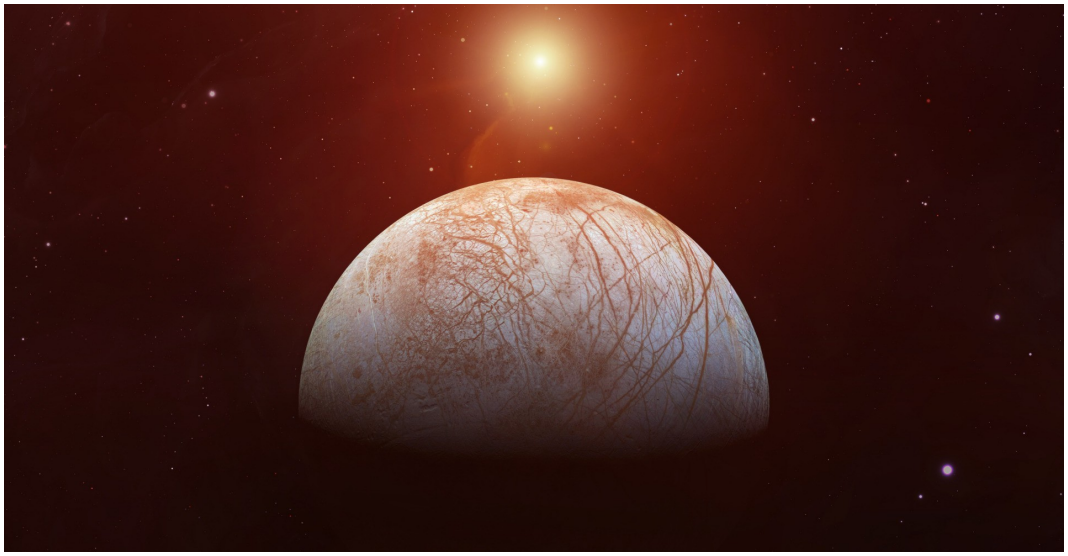

Figure 1.7: Artist view of Europa. Credits: wallpaper from Kipish_fon.

1.2.2.1 Internal Structure

The Galileo spacecraft measured the gravity field around Europa during its flybys, indirectly providing information about the moon's interior. The moment of inertia of Europa of about 0.346 (J. D. Anderson, Schubert, et al., 1998), suggests that Europa is differentiated, with denser materials at its core and a low-density layer at the surface. The moon likely possesses a metallic core (J. D. Anderson, Schubert, et al., 1998). If it did not, its interior would need to be a mix of rock and metal with a much higher density than Io's. Such a metal enrichment within Europa is unlikely. Therefore, it is more plausible that Europa has a silicate mantle and a metallic core. To match the measured moment of inertia, the core's thickness can vary from 13% to 45% of Europa's diameter, depending on the material's density and the thickness of other layers (Sohl et al., 2002).

Additionally, Europa's moment of inertia indicates that the outer water layer is at least 80 km thick (J. D. Anderson, Schubert, et al., 1998). A thinner water layer would only be possible if the mantle had a lower density, which is not plausible given the pressures within Europa's mantle (J. D. Anderson, Schubert, et al., 1998). The maximum thickness of the outer water layer is estimated to be about 170 km (J. D. Anderson, Schubert, et al., 1998). As previously discussed, the induced magnetic field measured by the Galileo magnetometer near Europa suggests the presence of a global liquid ocean beneath the ice shell. This implies that a silicate mantle is in direct contact with a subsurface ocean, shielded by a thick ice shell, with internal heating provided by strong tidal forces from Jupiter. These conditions are of high interest for the search for life, as they resemble those found at hydrothermal vents in Earth's deep ocean, where life may have originated. A detailed modeling of Europa's internal structure has been conducted by Vance et al. (2018), based on the physical

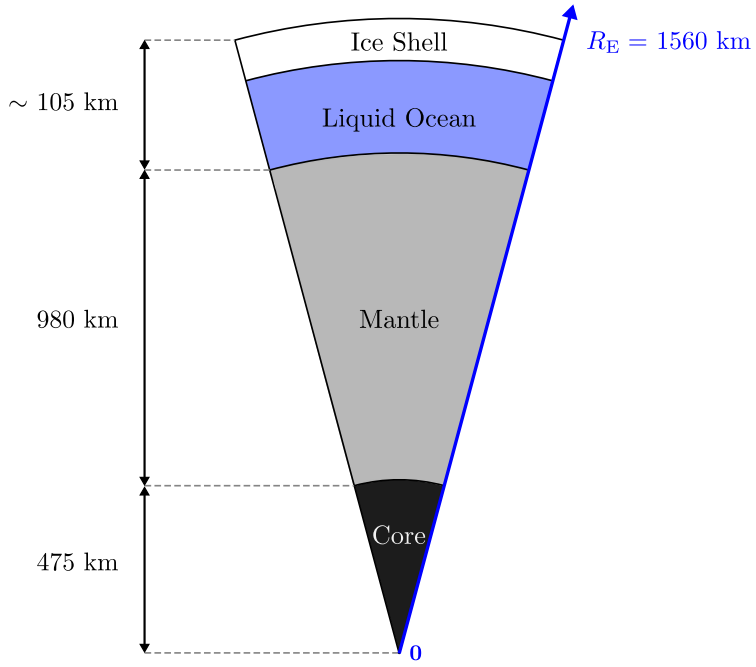

Figure 1.8: Schematic representation of Europa's interior using Vance et al. (2018) thicknesses. Thickness and materials are deduced from measurement of Europa's moment of inertia and density constraints. Spectroscopy shows that the surface is made of water ice and measurements of an induce magnetic field give evidence for a inner liquid water ocean.

parameters of the supposed materials composing it, leading the proposed internal structure in Figure 1.8.

1.2.2.2 Surface Geology

Europa is characterized by an heterogeneous surface showing various geological features which can be classified into multiple categories:

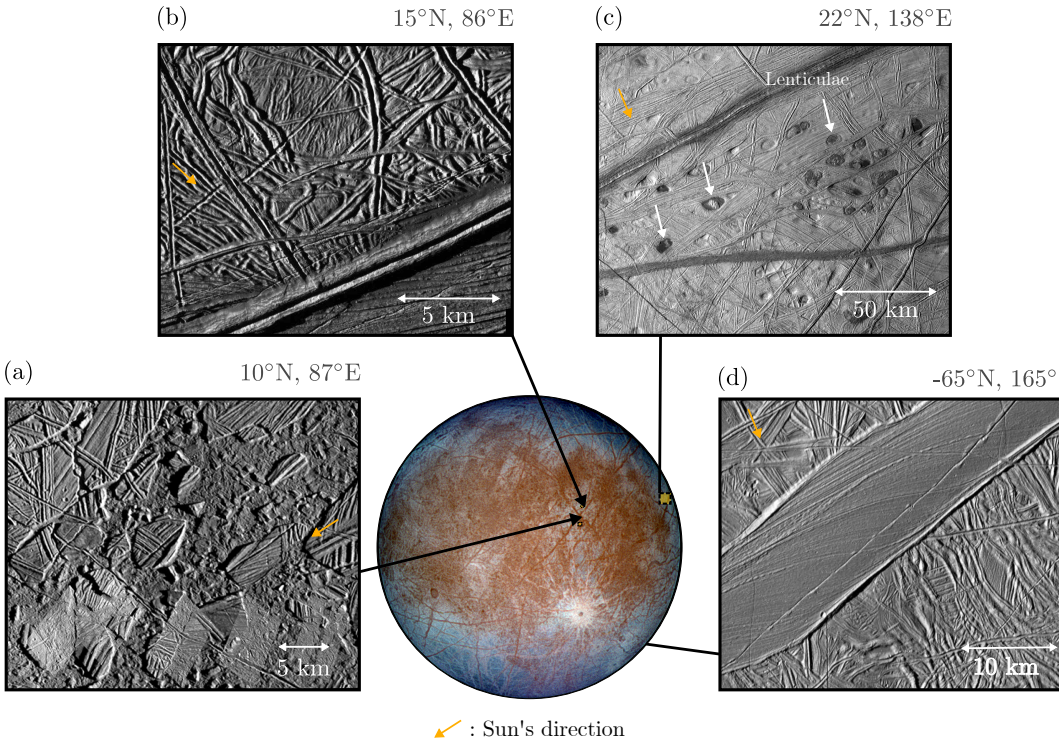

Figure 1.9: Satellite images of different surfaces features mapped to a composite representation of Europa: *(a)* Ice raft in the Conamara Chaos region (10° N, 87° E); *(b)* Double ridges separating a ridge plain and a smooth terrain, north from the Conamara Chaos region (15° N, 86° E); *(c)* Low albedo features: spots, pits and ridges, north-west of Rhadamanthys Linea (22° N, 138° E); *(d)* A smooth band opened a ridge plain, showing evidence of extension at −65° N, 165° E.

Chaos : chaotic terrains on Europa consist of ice rafts that have been moved around, rotated, and partially submerged by a mobile material (see Figure 1.9 (a), in Conamara Chaos region). The lower matrix of ice surrounding these ice blocks may have been formed as water or warm ice rose up from below the surface.

These ice rafts look a lot like the large chunks of ice at Earth's poles which break away and move to new positions. Chaos are evidences for the resurfacing of warm material like potentially, liquid water.

Ridges: roughly linear structures covering most of Europa's surface. The prominent ridge seen in Figure (1.9 (b)) is 2.6 km wide and 300 meters high but ridges can range from a hundred meter to few kilometers high. Although most of Europa's ridges are double ridges, they can take other shapes like isolated trough, raised flank trough, triple ridges, medial trough and complex ridges. It is thought (Greenberg et al., 1998) that these different types of morphologies are evolution stages of the same object. However, the processes of formation of Europa's ridges, and notably double ridges, is still highly debated today in the scientific community. Part of our experimental investigation is to provide more knowledge on the formation of these surface features.

Lenticulae: these low-albedo (reddish) spots are quasi-elliptical features (pits, domes, small chaos) each about 10 km across interpreted to be the result of the upwelling of warm material near the surface (see Figure 1.9 (c)). Manga et al. (2017) proposed that lenticulae are the surface expression of saucer shaped sills of liquid water in Europa's ice crust. These sub-surface water reservoirs could be formed by the rise of the liquid water from the subsurface ocean or partial melting of the surrounding ice by a hot rising plume. This general phenomenon, called cryovolcanism by analogy to silicate volcanism on Earth, has been modeled in several ways, including reservoir freezing (Lesage et al., 2020). Manga et al. (2017) proposed that pits are the early stage evolution of domes (or small chaos). Hence, pits would be relevant regions to look for pockets of liquid water in future space missions.

Smooth bands: Usually wider than ridges (see in Figure 1.9 (d) a smooth band about 15 km wide), these bands present a smooth and regular topography in contrast to the surrounding terrain. Studies like Schenk et al. (1989) have shown that by removing the band material, preexisting lineaments on either side of the bands could be reconstructed. This indicates that a complete opening of the lithosphere has occurred, with new material filling in the newly created gap. Also, some of these pull apart bands appear to be composed of a low-albedo material likely containing water ice mixed with hydrated salts (McCord et al., 1999). These salts are possible evidence of a water resurfacing from the subsurface ocean.

A global geologic map of Europa made by Leonard et al. (2024) highlighting the main geomorphological features, is shown in Figure 1.10, *Top*. The map displays the

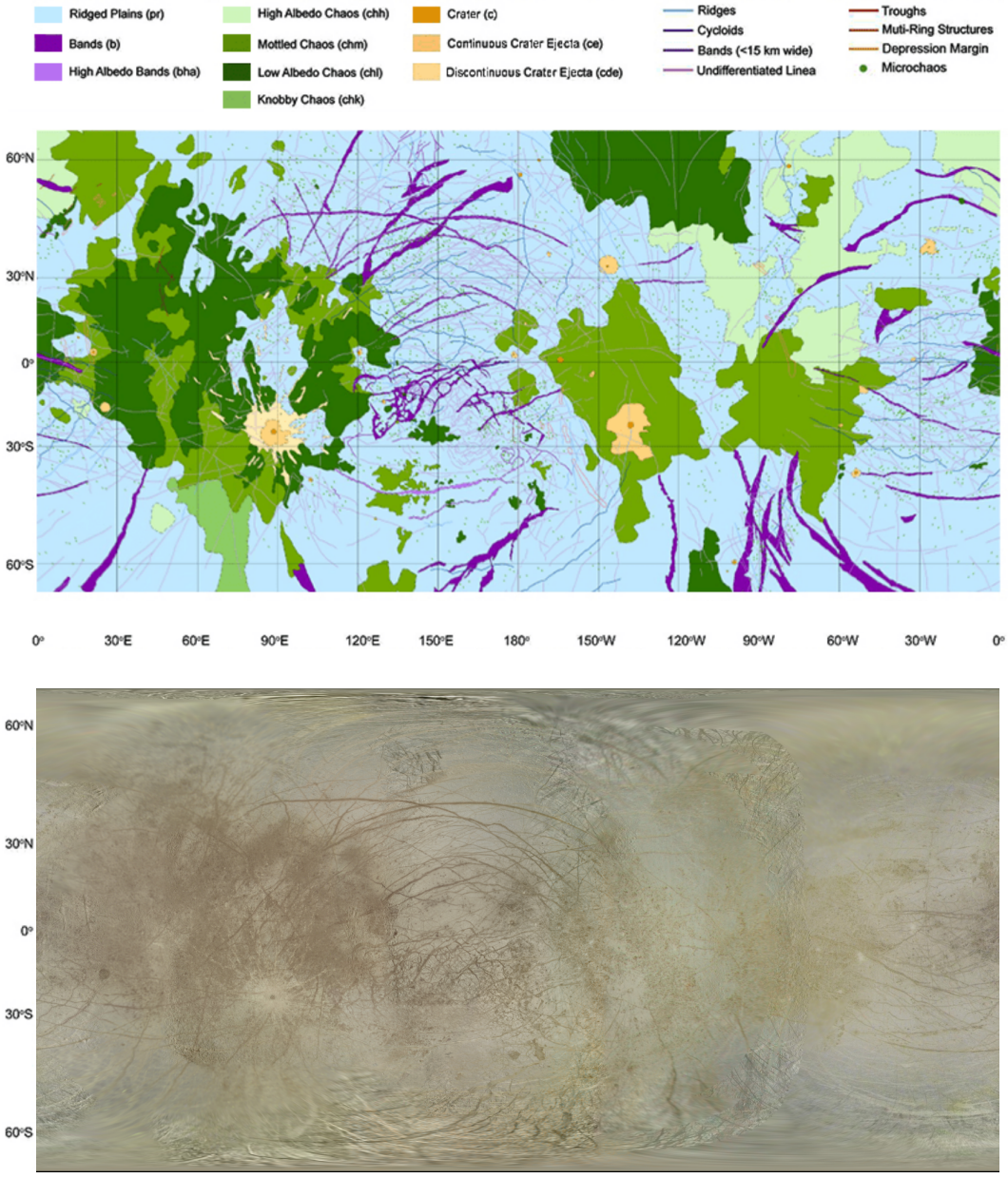

Figure 1.10: (*Top*): Global geologic map of Europa (Leonard et al., 2024). Credit:NASA/Erin Leonard. (*Bottom*) Global color mosaic of Europa's surface, color map by Jónsson (2015).

dominant features on Europa's surface, including ridged plains, chaos and lineaments.

1.2.2.3 Europa Surface Composition

The surface composition of Europa has been a subject of extensive investigation, particularly through spectrometer measurements. The first spectroscopic studies Kuiper (1957) and Harris (1961), consistently revealed the predominant presence of H2O molecules, with spectra showing remarkable similarities to those of pure water ice in terms of characteristic absorption bands' positions and shapes.

Spectroscopy additionally revealed traces of hydrated minerals, with various surface features showing a reddish color, potentially indicative of organics (see Figure 1.10, *Bottom*). The main salts identified are $MgSO_4$, Na_2SO_4, NaCl, and MgCl (Ligier et al., 2016; Trumbo, Brown, and Hand, 2019) . The abundance of these hydrated compounds changes across different locations. Composition likely follows the various endogenous and exogenous processes but their effects on surface chemistry remains unclear (R.W. Carlson, M. Anderson, R. Johnson, et al., 2002; R.W. Carlson, M. Anderson, Mehlman, et al., 2005). A clear dichotomy appears between hemispheres. On the trailing hemisphere, observations of small distortion of the spectral bands suggest the presence of non-ice components (Clark and Mc Cord, 1980). This surface darkening is likely due to the influence of the Jovian magnetosphere, favouring the establishment of a radiolytic sulfur cycle which in turns leads to the presence of sulfuric acid (R.W. Carlson, M. Anderson, R. Johnson, et al., 2002; R.W. Carlson, M. Anderson, Mehlman, et al., 2005). In contrast, the leading hemisphere shows an enrichment in water ice content, but the impact of space gardening on its surface composition remains poorly understood.

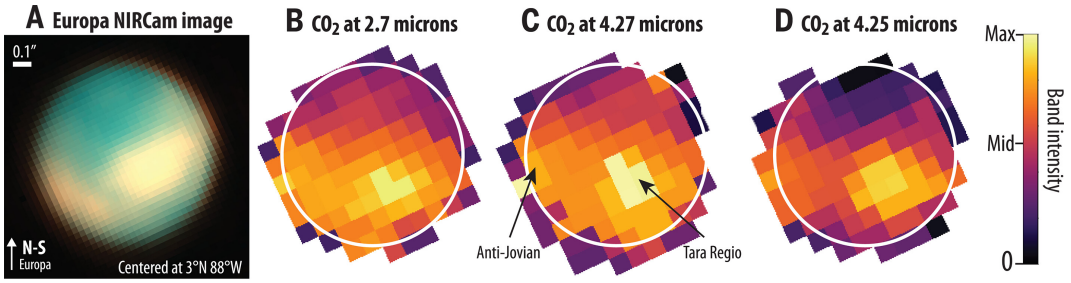

Figure 1.11: Distribution of CO_2 on Europa. (A) False-color image of Europa during JWST observations. (B) Band intensity of the CO_2 2.7 µm feature, modeled as CO_2 crystalline ice. The white circle indicates Europa's size in (A). (C) Band intensity of the 4.25 µm peak, modeled as CO_2 crystalline ice. (D) Band intensity of the 4.27 µm peak, modeled as CO_2 noncrystalline ice.

Recently, (Villanueva et al., 2023) have observed Europa with the James Webb Space Telescope (JWST) to search for active release of material by probing its surface and atmosphere. While no plume was observed, four spectral features of carbon

dioxide (CO2) ice were detected (see Figure 1.11). Their spectral shapes and distribution across Europa's surface indicate that the CO_2 is mixed with other compounds and concentrated in Tara Regio (-10°N, 75°W). The authors concluded that the most likely origin of the observed CO2 is endogenous, suggesting that Europa's interior ocean is the source of carbon.

Although we have outlined the primary results regarding surface composition, there remains a considerable amount yet to be understood about Europa's surface composition. For example, Cruz-Mermy et al. (2023) showed that only water ice (amorphous or crystalline) and sulfuric acid octahydrate are formally required. Hydrated sulfates and chlorinated salts are more difficult to distinguish. So, determining the composition of Europa's surface presents a significant challenge, as it results from a complex interaction of various processes, each having considerable variability across different locations.

1.2.2.4 Exosphere

Observations with the Goddard High Resolution Spectrograph on the Hubble Space Telescope detected a tenuous atmosphere primarily composed of O_2 at approximately 10^{-6} Pa (D. T. Hall et al., 1995). The O_2 presence on icy satellites originates from interaction with the Jovian magnetosphere. Charged particles accelerated by magnetic fields bombard the surface, ejecting O_2, H_2, H_2O, and other trace species (Leblanc, A. Oza, et al., 2017). This phenomenon, known as magnetospheric ion sputtering, leads to the production of O_2 and H_2 through radiolysis (R. Johnson et al., 1982; R. E. Johnson, 1990; Teolis et al., 2017). The spatial distribution of O_2 may be significantly influenced by the local surface temperature. As a result, the near-surface O_2 atmosphere can directly react to variations in solar flux (A. V. Oza et al., 2018). A recent analysis using JUNO JADE data, showed that O_2 produced within Europa's surface is less than previously thought (Szalay et al., 2024). In 2012, the HST detected increased hydrogen and oxygen emissions in the ultraviolet region over Europa's southern hemisphere, persisting for hours, indicating atmospheric variability (Roth et al., 2014). These emissions, absent in earlier HST images, were likely due the result of plume activity, possibly linked to internal processes and surface features.

Smaller amounts of sodium (Na) and potassium (K) were also detected (Brown et al., 1996; Leblanc, R. Johnson, et al., 2002). These elements may originate from external sources such as Io's atmosphere or from the sputtering of salts on the surface. Also, more recent far-ultraviolet observations by HST also revealed a stable water vapor atmosphere, confined to Europa's trailing hemisphere, likely due to sublimation and particle sputtering of surface ices (Roth, 2021).

1.2.3 Exploration of the Jovian System

The exploration of the Jovian system is challenging due to its distance to Earth as well as its intense radiation environment, yet it remains a fascinating space destination in our search for habitability. Through a series of missions, generations of scientists have gathered crucial data about the interior, the surface, the environment and the potential habitability of the Galilean moons.

1.2.3.1 Earth-Based

The observation of the Galilean moons started from Earth on January 8, 1610, when Galileo Galilei discovered Europa along with Jupiter, Io, Ganymede and Callisto using a refracting telescope with 20x magnification. Since then observations of the Jovian system, have significantly advanced through the utilization of various powerful telescopes.

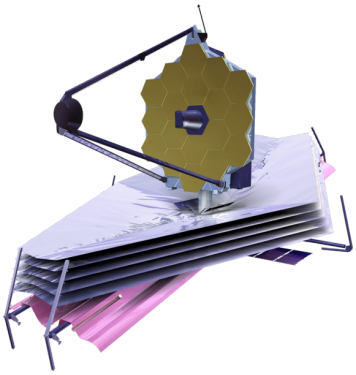

Figure 1.12: The James Webb Space Telescope.

In the 1970s and 1980s, observations with the Hale telescopes (O. Hansen, 1973) and the Very Large Array telescopes (VLA) (Pater et al., 2014) in the radio frequencies allowed to estimate the near-surface thermal properties and brightness temperature of the Galilean moons. Then, the Hubble Space Telescope (HST) was launched in 1990, and notably provided evidence of water vapor plumes from Europa's surface, notably thank to its ultraviolet capabilities which have help studying its thin atmosphere (Roth et al., 2014). The Very Large Telescope (VLT), operational since 1998, has offered high-resolution imaging and spectroscopy, enabling, for example, global-scale analysis of Europa's surface composition (Ligier et al., 2016). The Atacama Large Millimeter/submillimeter Array (ALMA), in use since 2011, has enhanced knowledge of Europa's surface and subsurface properties by observing its thermal characteristics (Trumbo, Brown, and Butler, 2018). The James Webb Space Telescope (JWST), launched in 2021, with its advanced infrared capabilities, allowed for the discovery of CO_2 ices at the surface of Europa (Villanueva et al., 2023). Finally, the Extremely Large Telescope (ELT), anticipated to be operational in the late 2020s,

will offer unprecedented resolution thanks to a 39 meters main mirror and will be the largest visible and infrared light telescope in the world (Gilmozzi et al., 2007).

1.2.3.2 Past Missions

The Jovian system was first explored by The Pioneer missions, launched by NASA in 1972, aimed primarily to explore the environment of Jupiter (Hall, 1974). Pioneer 10 and 11 were the first spacecraft to photograph Europa, with a resolution of approximately 200 km per pixel, and gathered data on Jupiter's and its magnetosphere.

Then, in 1979, Voyager 1 and 2 traversed the Jovian system during their journey to the outer solar system, capturing additional images of Europa's icy surface with resolutions of up to 2 km per pixel. These images revealed a remarkably smooth surface with few craters, marked by various-sized lineaments. Over time, as space exploration advanced, the Jovian system has been the target of seven missions from the 1970s to the present day. Many of these missions were flybys en route to their primary destinations, such as New Horizons, which passed Jupiter in 2007 on its way to Pluto, and Cassini, which encountered Jupiter in 2000 en route to Saturn.

Figure 1.13: The Galileo spacecraft.

Galileo — The Galileo spacecraft, was the first mission entirely dedicated to explore the Jovian system. Built by the NASA's Jet Propulsion Laboratory and launched on October 18, 1989, it reached Jupiter in 1995 and operated until 2003, making history as the first spacecraft to orbit an outer planet. Galileo was intentionally sent into Jupiter's atmosphere on September 21, 2003, ending its mission. Powered by Radioisotope Thermoelectric Generators (RTG) generators, it had a large high-gain antenna that failed to deploy in space, so it used a slower low-gain antenna for data transfer. The Galileo spacecraft was made of various scientific instruments:

- SSI - Solid-state imager: Provided images with spatial resolution up to 6 m/pixel

on localized regions and $\sim 2\,\mathrm{km}$/pixel for global coverage (Bland et al., 2021), capturing a wide variety of surface morphologies.

- NIMS - Near-infrared mapping spectrometer: Covered wavelengths from 0.7 to 5.2 µm, mapping light intensity across different wavelengths for spectral analysis.
- UVS/EUV - Ultraviolet spectrometer: Analyzed ultraviolet emissions for atmospheric and surface composition studies.
- PPR - Photopolarimeter-radiometer: Measured temperatures of Jupiter's atmosphere and satellites, and analyzed reflected and emitted light properties.
- DDS - Dust-detector subsystem: Determined mass, electric charge, and velocity of incoming particles for understanding the dust environment.
- EPD - Energetic-particles detector: Detected ions and electrons with energies exceeding about 20 keV for studying particle radiation.
- HIC - Heavy-ion counter: Detected heavy ions using stacked silicon wafers for understanding ion composition.
- MAG - Magnetometer: Measured three orthogonal components of the magnetic field for magnetic field mapping.
- PLS - Plasma subsystem: Collected charged particles from seven fields of view for energy and mass analysis.
- PWS - Plasma-wave subsystem: Studied plasma electric and magnetic fields using an electric dipole antenna and two magnetic antennas.

1.2.3.3 Current and Upcoming Missions

In this section is presented the three ongoing/future missions targeting the Galilean moons: JUNO, Europa Clipper, and JUICE. Special emphasis is placed on the Europa Clipper mission, as it is directly relevant to my PhD focused on Europa. For each instrument aboard Europa Clipper, I describe how it will improve our understanding of Europa's ice microstructure. Definitions and details of relevant microstructure terms are provided in Section1.3.

Juno — Developed by NASA's Jet Propulsion Laboratory, the Juno spacecraft was launched on August 5, 2011, and reached Jupiter in 2016. Its mission is to answer questions surrounding the origin and evolution of Jupiter, as well as to provide insights into the formation of our solar system and other giant planets throughout the universe. Since 2021, Juno initiated the exploration of Jupiter's Galilean moons. In June 2021, Juno completed a flyby of Ganymede, the closest approach by any

Figure 1.14: The Juno spacecraft.

spacecraft since Galileo. Then, in September 2022, Juno conducted a flyby of Europa. Two flybys of Io occurred in December 2023 and February 2024, during which Juno collected observational data on volcanic activity. Starting since April 2024, Juno is doing a series of experiments aimed at further understanding Jupiter's interior shape and structure.

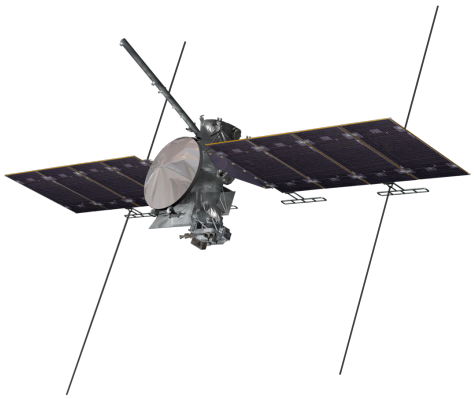

Figure 1.15: The Europa Clipper spacecraft.

Europa Clipper — Developed jointly by the Jet Propulsion Laboratory and the Applied Physics Laboratory, the Europa Clipper mission is scheduled for launch in October 2024. The spacecraft will use gravity assists from Mars in February 2025 and Earth in December 2026, and expected to reach Europa in April 2030. The mission aims to thoroughly explore Europa, assess its potential habitability, and assist in choosing a suitable landing site for the future Europa Lander. Powered by a combination of Radioisotope Thermoelectric Generators (RTGs) and photovoltaic systems, Europa Clipper is equipped with a scientific payload comprising nine instruments:

- E-THEMIS - The Europa Thermal Emission Imaging System: Provides high-

resolution, multispectral imaging in the mid to far infrared bands, for the detection of geologically active sites such as potential water plumes. The high-resolution thermal mapping from E-THEMIS will help us derive the thermal properties of Europa's near-surface down to a scale of a few meters per pixel. Combined with advanced modeling, this will improve constraints on grain sizes, porosity, and cementation of the ice grains, providing a more detailed understanding of Europa's regolith. More details can be found Appendix 2.7.3.

- MISE - The Mapping Imaging Spectrometer for Europa: An imaging near-infrared spectrometer for probing surface composition, identifying organics, salts, water ice phases, and other materials. The various geometries and illuminations during Europa Clipper flybys will produce detailed solar phase curves across UV, visible, and near-IR wavelengths, which can be used to derive grain size and scattering parameters of the ice (Becker et al., 2024) using Hapke's theory (Hapke, 1986). By modeling the solar phase curve reflectances measured by EIS, MISE, and Europa-UVS, it will also be possible to constrain porosity. Different wavelengths, each with distinct absorption characteristics, will probe varying depths, enabling us to assess how grain size changes with depth. MISE, EIS and Europa-UVS data will be used to constrain the distribution of grain sizes, crystallinity, and of water ice globally on Europa's surface (Becker et al., 2024).

- EIS - The Europa Imaging System: Comprising a wide-angle camera (WAC) and a narrow-angle camera (NAC), EIS will produce stereoscopic and color images. The system will map about 90 percent of Europa at 100 m/pixel, providing much higher resolution coverage compared to the Galileo mission. The narrow-angle camera will capture certain areas at half a meter per pixel resolution. This high-resolution stereo topography will allow us to determine the nature of the surface at the meter scale, to assess potential hazards for Europa lander mission concepts. Additionally, the improved visible map of Europa's surface will help refine our estimation of the bond albedo, as detailed in Section 5.5.2. See MISE for additional microstructure-related applications.

- Europa-UVS - The Europa Ultraviolet Spectrograph: Detects small plumes and provides data on the moon's exosphere composition and dynamics. By analyzing the exosphere and plumes, Europa-UVS could infer composition and properties of the surface and subsurface materials being ejected (Becker et al., 2024). See MISE for microstructure-related applications.

- REASON - The Radar for Europa Assessment and Sounding: Ocean to Near-surface: A dual-frequency ice-penetrating radar for characterizing Europa's ice shell and potential subsurface water pockets. As the first ice-penetrating radar deployed in the outer solar system, REASON will search for the moon's hypothesized ocean, measure ice thickness, and examine the internal structure of

the ice, including surface topography, composition, and roughness (Blankenship et al., 2024). The reflectometry sensitivity to near-surface properties makes REASON highly effective for studying ice characteristics. The radar's reflectometry measurements will provide insights into the bulk density of surface ice and materials within the upper few hundred meters below the surface. These near-surface density estimates will complement the thermal anomaly investigations conducted by E-THEMIS by helping to constrain porosity variations (Grima et al., 2014; Blankenship et al., 2024). Additionally, REASON will help determining regolith cohesiveness, thickness, and surface roughness (Blankenship et al., 2024).

- ECM - Europa Clipper Magnetometer: Characterizes magnetic fields around Europa. In conjunction with PIMS, ECM could be used to determine the spatial distribution of charged particle radiations impacting the surface. This will improve our modeling of near-surface processes, indirectly helping us better constrain parameters influenced by radiation, such as crystallinity.

- PIMS - The Plasma Instrument for Magnetic Sounding: Measures plasma to characterize magnetic fields generated by plasma currents. The goal of the instrument is to reveal Europa's ocean depth and conductivity, and ice shell thickness. For microstructure-related benefits, see ECM.

- MASPEX - The Mass Spectrometer for Planetary Exploration: Determines surface and subsurface ocean composition by analyzing Europa's atmosphere and ejected surface materials. MASPEX collects gases and determines the molecules composing it by measuring their mass. As the gas composition directly reflects the surface material, this provides new constraints on the surface composition. Also, MASPEX will study how Jupiter's radiation alters Europa's surface compounds. By mapping the spatial distribution of radiation effects, MASPEX will help us better understand and constrain the crystallinity of the ice.

- SUDA - The SUrface Dust Analyzer: A mass spectrometer analyzing solid particles ejected from Europa, offering insight into surface and potential plumes composition. Micrometeorites and charged particles constantly eject fragments of Europa's surface into space through a process called sputtering. Since these grains are direct samples from the moon's icy surface, determining their composition will help define and constrain geological activities of the near-surface. SUDA's primary goal is to produce a spatially resolved compositional map of Europa. By measuring the dust's spatial distribution, we can also infer the spatial distribution of sputtering rates. This information will indicate where the surface is most heavily bombarded, providing insights for better modeling of the microstructure, such as crystallinity, as discussed in Chapter 5.

One key takeaway here is that microstructure parameters are never directly measured. Instead, they are inferred from measurements of physical properties, such as brightness temperature or reflectance, through the use of models. The accuracy of these inferred parameters, depends on both the quality of the dataset and the robustness of the modeling and assumptions used. Therefore, only by combining data from multiple instruments and improving modeling techniques can we effectively reduce the uncertainties surrounding the ice microstructure.

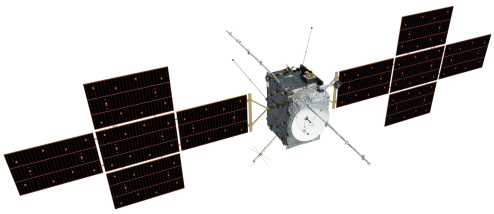

Figure 1.16: The Jupiter Icy Moons Explorer spacecraft.

JUICE — ESA's Jupiter Icy Moons Explorer, JUICE, was launched on April 14, 2023, and will make detailed observations of the giant gas planet and its three large icy moons. It will be the first spacecraft ever to orbit a moon other than Earth's, focusing primarily on Jupiter's largest moon, Ganymede, once it enters orbit around it in 2034. JUICE's mission objectives encompass two main themes. Firstly, it will explore the habitable zone of the Jovian system, characterize the oceans, icy shells, compositions, surfaces, environments, and activity of Ganymede, Europa, and Callisto. Secondly, it will extend its exploration to the broader Jupiter system, investigating Jupiter's atmosphere, magnetic environment, ring system, and other satellites, including Io (Grasset et al., 2013). The JUICE spacecraft is equipped with a diverse array of scientific instruments designed to maximize the scientific yield of the mission:

- JANUS - Jovis, Amorum ac Natorum Undique Scrutator: A camera system providing images of Ganymede and selected regions of Callisto at resolutions better than 400 m/pixel.
- MAJIS - Moons and Jupiter Imaging Spectrometer: A visible and infrared imaging spectrometer covering wavelengths from 400 nm to 570 µm, studying cloud features on Jupiter and surface composition on the icy moons.
- UVS - UV Imaging Spectrograph: Captures images in the $55 - 210$ nm wavelength range, characterizing exospheres and aurorae on the icy moons and studying Jupiter's upper atmosphere.

- SWI - Sub-millimeter Wave Instrument: Studies Jupiter's atmosphere and the exospheres and surfaces of the icy moons using a spectrometer operating in the 1080–1275 GHz and 530–601 GHz frequency ranges.
- GALA - Ganymede Laser Altimeter: Measures topography and tidal deformations on Ganymede using laser altimetry with high precision.
- RIME - Radar for Icy Moons Exploration: Penetrates the subsurface of Jovian moons to depths of up to 9 km, providing insights into their internal structures.
- J-MAG - JUICE-Magnetometer: Investigates subsurface oceans and magnetic field interactions between Jupiter and Ganymede.
- PEP - Particle Environment Package: Measures various particles in the Jupiter system, from ions to energetic neutral atoms, to study the magnetosphere and interactions with the moons.
- RPWI - Radio and Plasma Wave Investigation: Characterizes plasma environments and radio emissions surrounding the spacecraft.
- 3GM - Gravity and Geophysics of Jupiter and Galilean Moons: Studies the gravity field and internal oceans of the icy moons.
- PRIDE - Planetary Radio Interferometer and Doppler Experiment: Utilizes interferometry to precisely measure the gravity fields of Jupiter and its moons.

1.3 Ice Microstructure on Europa: Outstanding Questions

Ice microstructure refers to the microscopic arrangement and characteristics of ice on planetary bodies, such as icy moons. This includes the size, shape, orientation, and distribution of ice grains, the crystallinity of the ice phase, as well as the presence of pores, impurities, roughness, and other small-scale features that influence the ice's physical properties. Given this, a question arises: What is the current state of Europa's ice microstructure?

Understanding the microstructure of a material is crucial, as it significantly impacts its physical properties, including light absorption, heat conductivity, strength, hardness, resistance, as well as other optical, thermal and mechanical properties. This knowledge improves our understanding of Europa's surface, refines spectroscopic, spectrophotometric, thermophysical models, and the choice of potential landing sites, among other applications.

Currently, our knowledge of Europa's microstructure is limited, with the best satellite imagery resolution of the surface being ~ 10 meters per pixel. Therefore, we lack detailed information about the surface properties—is it fluffy or consolidated,

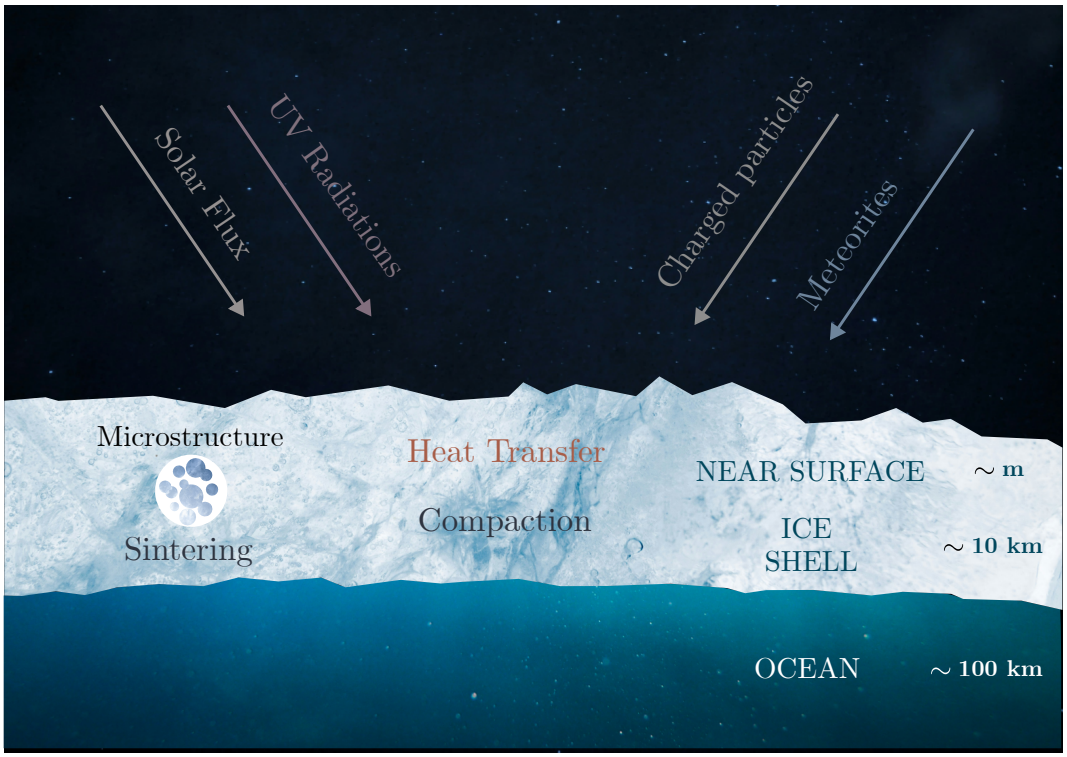

Figure 1.17: Europa's icy surface and subsurface are shaped by various coupled physical processes: solar flux, heat conduction, gravity-induced compaction, ice sintering, thermal crystallization, radiation-induced amorphization, meteorites bombardment (not modeled yet). This thesis focuses on the modeling and coupling of these physics to better understand the evolution of the ice microstructure.

crystalline or amorphous, rough or smooth? Should we even call it ice or snow? Various physical processes can alter the icy surface's microstructure, as shown by Figure 1.17. Among them: heat transfer, gravity-induced compaction, ice sintering, thermal crystallization and radiation-induced amorphization will be developed in this thesis. These processes only have a noticeable effect on the near surface of Europa, hence we will focus on the first few meters near the surface. Here, we introduce the key questions raised by each of these physical processes affecting the surface.

1.3.1 Ice Temperature

The ice temperature is the main parameter that dictate the kinetics of the physical processes interacting with the ice microstructure. For this reason, the first goal of this PhD was to accurately estimate the temperature evolution with depth and time of an icy surface. The surface of Europa is heated by the solar flux and potential internal heat source, and this heat is conducted toward lower depths or remitted as long-wave radiations at the surface (see Figure 1.18).

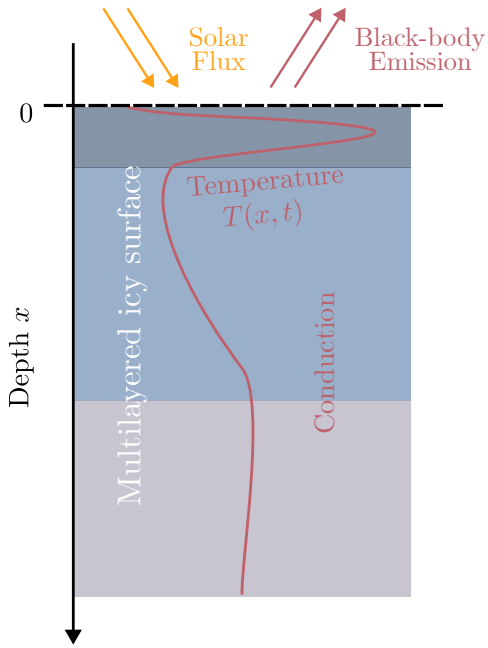

Figure 1.18: Heat conduction through a multilayered icy surface. Icy moons, like Europa, likely have varying thermal properties with depth. These gradients may arise from compositional differences, such as a thin dust layer covering the surface, or from surface processes like sintering that alter the ice microstructure.

In the near-surface, heat transfer occurs through conduction and is influenced by the thermal properties: the thermal conductivity, the specific heat capacity, the density, thermal emissivity and bond albedo. Measurements of brightness temperature from the Galileo Photopolarimeter-Radiometer (PPR) and Earth-based ob-

servations have been used to determine the thermal inertia of Europa's subsurface (Spencer et al., 1989; Rathbun et al., 2010; Trumbo, Brown, and Butler, 2018). These studies used thermophysical models with the assumption of an homogeneous icy surface. However, telescopic measurements (O. Hansen, 1973) during solar eclipses by Jupiter have shown that the regolith on Europa appears to be strongly layered: the top few millimeters have a low thermal inertia, while the underlying layer has a much higher thermal inertia. These results raise important questions: How is surface temperature affected when accounting for multilayered surfaces? What is the effect of Jupiter's solar eclipses on the sub-Jovian hemisphere?

In our effort to model the evolution of ice under processes that may span over large timescales, significant technical challenges arise. Although thermal solvers exist in various fields, the nonlinear boundary conditions specific to planetary surfaces necessitate additional modeling for the numerical development. Are the thermal solvers developed in the literature efficient enough to simulate daily heat variations over such long timescales? Additionally, modeling over large timescales requires considering variations in solar flux over such extended periods: What is the effect of long-term variations in Europa's orbit on temperature profiles?

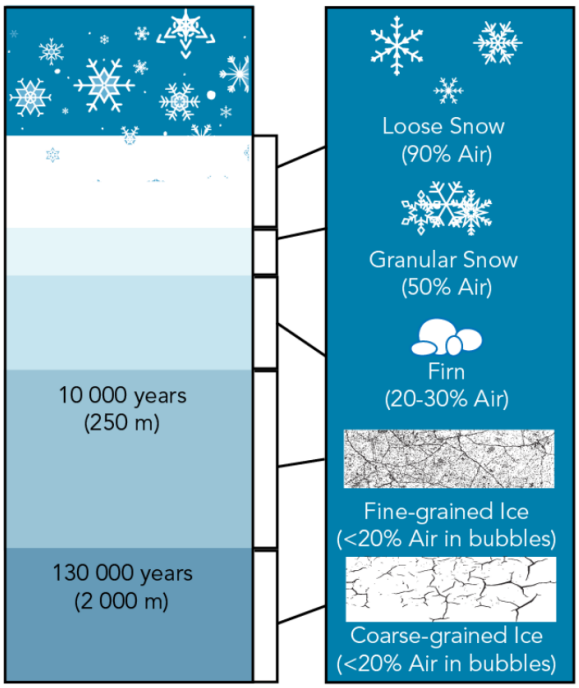

Figure 1.19: Compaction of snow with depth on Earth. Here, "air" can also refer to porosity. Figure from Let's Talk Science 2021, inspired by an image by Marshak (2012).

1.3.2 Ice Porosity and Gravity-induced Compaction

Various studies provide compelling evidence that the surface of icy satellites is made of a porous material (Spencer et al., 1989; Rathbun et al., 2010; Ferrari et al., 2016; Cruz-Mermy et al., 2023; A. V. Oza et al., 2018). On Earth, notable changes in porosity from ice core measurements have been observed at depths on Antarctica and North Greenland ice, with a variation lengthscale of approximately 20 meters (Alley et al., 1982; Hörhold et al., 2011; Gerland et al., 1999). This compaction leads to variations of density, from fresh snow to firn, and from firn to bubbled ice (see Figure 1.19). The conditions at the surface of icy moons, such as Europa's surface gravity and temperature, are vastly different from those on Earth. This raises the question: How does compaction on icy moons differ from that on Earth?

The Cryobot mission concept (Vale Pereira et al., 2023) aims to dig through Europa's ice shell to reach its subsurface oceans. Understanding the evolution of ice properties at different scales is crucial for this mission. This leads to the question: What is the typical compaction scale of porous ice on Europa? Additionally, when modeling the thermal properties of the near-surface, we may wonder: Does gravity induce noticeable changes in the density of Europa's near-surface?

1.3.3 Ice Sintering

Ice sintering, also referred to as *annealing* or *metamorphism*, involves transport of matter from ice grains to their bond region, resulting in changes in the thermal, optical, and mechanical characteristics of the ice. This process is primarily driven by the reduction in surface energy of the system. The kinetics of sintering are highly sensitive to temperature and grain size, with faster rates observed at warmer temperatures and with smaller grains. In Figure 1.20 is shown the sintering of two grains at 253 K, where the formation of a bond in about ~ 1 h is noticeable (Molaro et al., 2019).

On Earth, the process of sintering, a form of snow metamorphism, has been extensively studied. There is generally a distinction between dry and wet snow metamorphism and metamorphism under isothermal/equilibrium or temperature gradient conditions, each leading to notably different snowpack structures. Earth-based studies on metamorphism are primarily focused on snowpack modeling for avalanche forecasting, using models such as SNOWPACK (Lehning et al., 2002), CROCUS (Vionnet et al., 2012), and COSIPY (Sauter et al., 2020). These multiphysics models inspired my PhD research. However, because field studies can be conducted on Earth, the sintering rates used in their models are either fully or partially based on empirical data relevant only to Earth's snow. Advanced numerical models also exist, such as the model developed by Miller (2002), which combines heat conduction, mass conservation, and phase change equations, and the three-dimensional modeling of curvature-dependent snow metamorphism by Flin et al. (2003). For icy moons, due to the much larger timescales involved, simpler models need to be used for com-

putational efficiency.

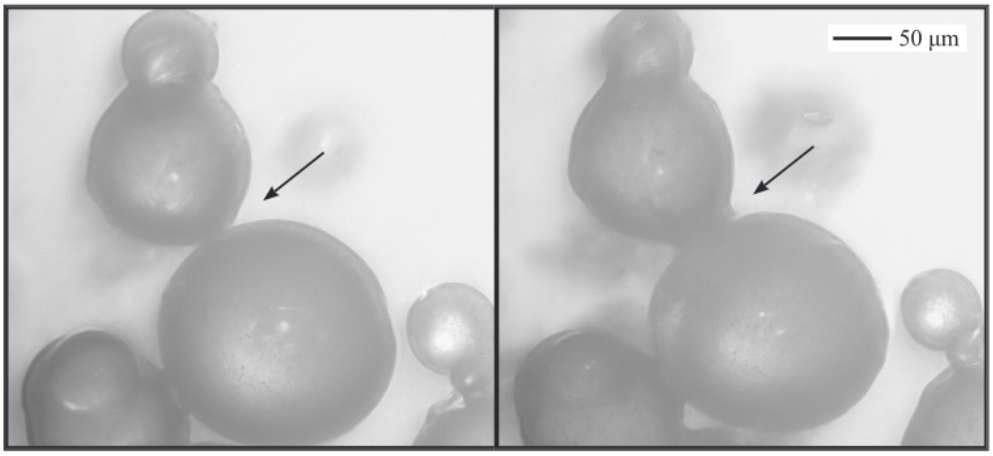

Figure 1.20: Water ice grains sintering at 253 K at the first observation (*Left*) and after 57 min (*Right*), showing growth of the neck (*arrow*) from 33 to 65 µm. The grains have starting radii of 101 and 73 µm, shrinking by 3% and 4%, respectively, after 57 min. Figure from Molaro et al. (2019).

Sintering is expected to take place on the surfaces of icy moons, but due to the much lower temperatures involved, its efficiency is not clear. The basis of the sintering theory used in the planetary science community comes from metallurgy studies (Swinkels et al., 1981). Estimations of the sintering timescale on Europa, based on surface temperatures and grain sizes, were provided by Molaro et al. (2019), ranging from a lower limit of 10^4 years to an upper limit of 10^9 years (Molaro et al., 2019). The difference between these two timescales is considerable. Whether the sintering timescale leans towards the lower or upper limit can significantly impact our understanding of surface properties, which raises the questions: Are the conditions on Europa favorable for sintering to occur ? How do grain sizes and thermal properties quantitatively influence the sintering rates?

Sintering is particularly important because it changes the optical, thermal, and mechanical properties of ice. The formation of bonds increases the contact area between grains, increasing heat conduction within the ice (Piqueux et al., 2009) (see Figure 1.21). This raises the question: How does heat conduction change with the microstructural variations induced by sintering?

Finally, in anticipation of a Europa Lander mission, determining sintering rates becomes essential as it affects surface strength. To broadly characterize safety potential of potential landing sites, sintering informs us on the surface cohesiveness. So we may wonder: Which regions of Europa currently consist of isolated or interconnected ice grains?

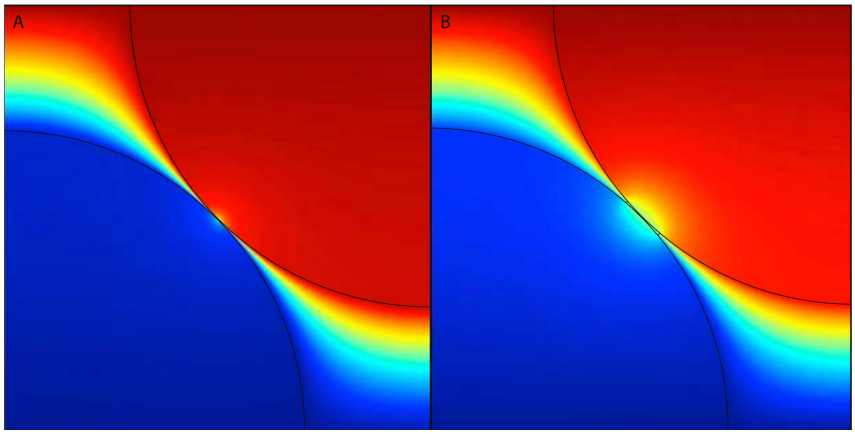

Figure 1.21: Relative temperatures from numerical simulations of a cubic centered cell without bond (a) and with a pendular ring of cement (b). The color scale is linear and relative, going from coldest temperatures, in blue, to hottest temperature, in red. Figure from Piqueux et al. (2009)

1.3.4 Ice Crystalline Fraction

Below approximately 135 K, amorphous ice (see Figure 1.22) is expected to condense from the vapor phase. Despite the thermodynamic stability of the crystalline structure at these temperatures, the kinetics of crystallization can be slow enough to allow metastable amorphous ice to persist on the moons' surfaces. Spectroscopic studies of Europa (G. B. Hansen, 2004; Ligier et al., 2016; Cruz-Mermy et al., 2023) indicate that the surface contains a mixture of crystalline and amorphous ice. Results from G. B. Hansen (2004) also suggests a potential gradient of crystallinity with depth, with the surface layer being predominantly amorphous and deeper layers made of crystalline ice.

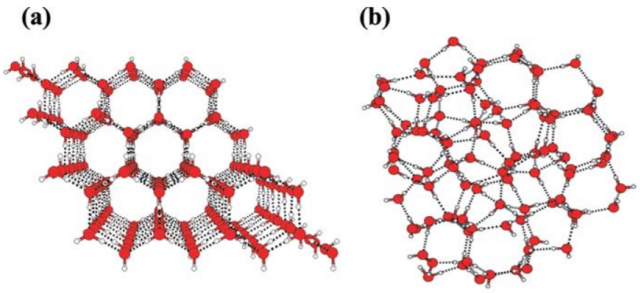

Figure 1.22: Molecular arrangement of (a) Ice Ih, (b) Low Density Amorphous ice (LDA). Almost all molecules join in the network of hydrogen bonds (black dashes). Figure from Belosludov et al. (2008)

The surface of Europa experiences a balance between thermally-induced crystallization and radiation-induced amorphization processes, resulting in alterations to its

crystalline structure. How does the timescale of thermal crystallization vary with the range of thermal parameters found on Europa? What is the efficiency of radiation in amorphizing Europa's surface? How do these two competing processes relate to the observed crystallinity of Europa?

Furthermore, the bombardment by high-energy electrons, protons, and heavy ions from Jupiter's magnetosphere is expected to be strongest on the trailing hemisphere (Paranicas et al., 2001). Simultaneously, different latitudes and longitudes have varying albedo, and the sub-Jovian hemisphere experiences eclipses that could impact thermal crystallization. How does the crystallinity of Europa's icy surfaces change with location and depth? UV radiation can also induce amorphization, and the solar flux heating the surface varies on daily, seasonal, and geological timescales, potentially influencing the intensity of these processes. Could there be observable periodic changes in the surface crystallinity of Europa?

1.3.5 Motivations for Multiphysics Simulations

On Earth, our understanding of the surface is significantly helped by the ability to conduct field studies. The samples collected are analyzed in laboratories and provide robust constraints for geological models. However, when it comes to other planetary bodies, such analyses are not yet possible. So, how can we study these icy surfaces?

One option is to build and send spacecrafts. These missions have yielded a wealth of invaluable information, significantly contributing to our understanding of icy moons. However, such projects are limited by their high costs, the technological challenges involved, and their considerable environmental impact also need to be taken into account. As result, most of the current space-based observations are from the Galileo mission, which provided data over 20 years ago. While the ongoing Juno mission will soon offers some new insights on Europa, the upcoming missions JUICE and Europa Clipper will not reach the Jovian system for at least another six years.

As discussed in Section 1.2.3.1, one possibility is also to use Earth-based observations which provide valuable insights into the surfaces of icy moons, particularly on a global scale. However, due to the large distances involved, it is challenging to accurately constrain the microstructural parameters of these surfaces from Earth.

Another approach is to conduct laboratory experiments. By running such experiments in environments analogous to the surface conditions of icy moons, we can gain insights into how these bodies' surfaces would behave. These experiments are valuable for improving our understanding of these moons and often serve as references for models. However, conducting experiments requires time and resources, and simulating certain environments can be challenging. Some processes involve multiple physics occurring on different timescales, including some timescales and conditions that are not accessible in the laboratory. For example, here is an analogy: if one would want to predict the weather on Earth, it would be very challenging to do so

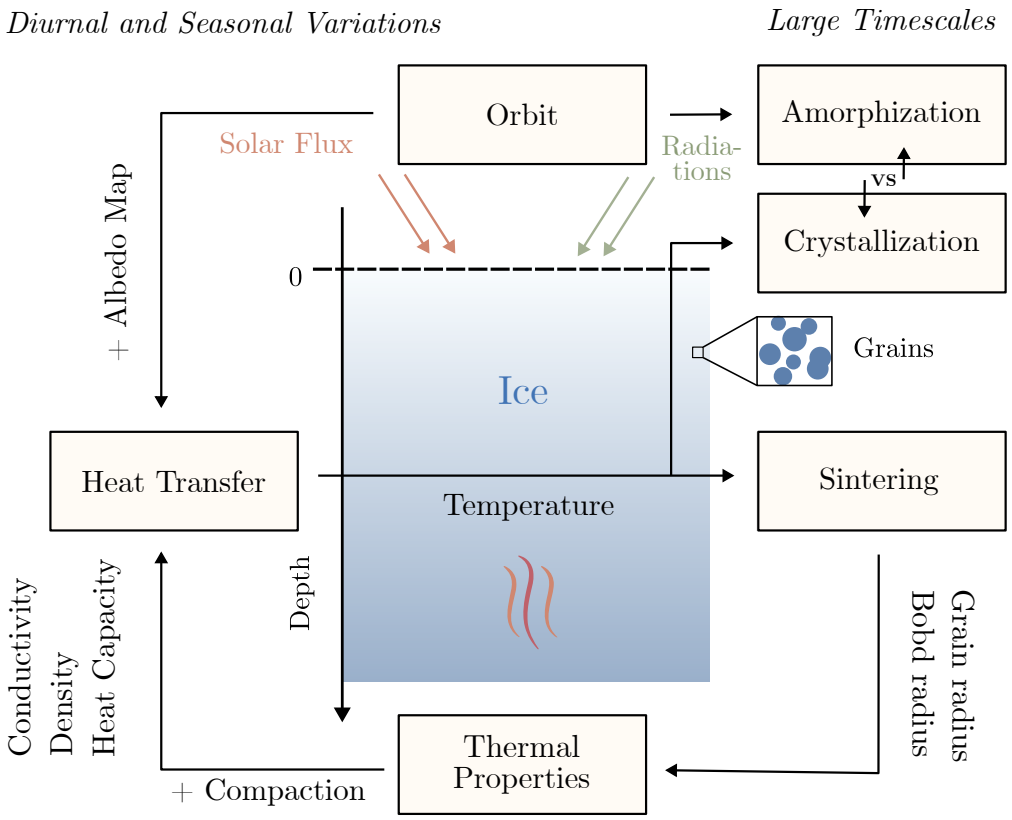

Figure 1.23: Block diagram of the proposed simulation model LunaIcy showing the multiphysics coupling between each modules.

in a experimental setting.

So what can we do while we wait for Europa Clipper and JUICE to reach the Jovian system ?

A possibility is to build analytical/numerical models, validate them by confronting them to space or experimental data, and then used them to study the evolution of these surfaces. Existing models have traditionally approached the description of these physical processes independently, such as heat transfer modeling (Spencer et al., 1989), ice sintering (Molaro et al., 2019) and crystallinity (Berdis et al., 2020), among others. While valuable for providing first order estimations of the effects of each process, in reality, there is a strong coupling between these physics (see Figure 1.23):

The temperature of Europa's near-surface is calculated based on heat transfer, relying on our knowledge of the thermal properties and input solar flux. The thermal properties, like density, are affected by compaction processes and obtaining the solar flux requires a detailed computation of Europa's orbit. On one hand, sintering is extremely temperature-sensitive, so it requires a precise knowledge of the temperature evolution. On the other hand, sintering forms bonds that changes the thermal properties of ice, thereby affecting the temperature in return. Last but not least, ice crystallization and amorphization are both heavily reliant on temperature, and may also induce fluctuations in ice thermal properties.

Given the coupled nature of these physics, can we truly estimate their effects independently? Following the previous analogy, would it be possible to predict the weather without considering the influence of oceans or lands?

The core concept of this PhD project is to integrate the various physical phenomena that affect Europa's ice microstructure and couple them within a 1D multiphysics simulation model named "LunaIcy" (see Figure 1.23). Just as scientists have developed General Circulation Models (GCMs) for climate studies, the study of planetary icy surfaces would benefit from the creation of multiphysics numerical models. This kind of simulation would be an analogous to snowpack models used for avalanche prediction, but here for solar system ices. Initially, the plan for this PhD was not to develop the analytic of each physic from scratch, but rather to integrate existing models from the literature. However, as will be seen in the following chapters, some existing models required refinement and further analytical development to be effectively incorporated into our numerical model.

Author's Note

From this point, the reader may have the following questions:

Q: *Why were not all physical processes affecting the surface included? (For instance : meteorite bombardment, sublimation, radiation-induced densification, etc...)*
A: To our knowledge, this is the first attempt to built a multiphysics model of icy surfaces and the three-year period of a PhD program only allows for limited modeling. We have focused on the selected mechanisms because we believe they have the most significant first-order effects on the surface microstructure. There are plans to include many more modules to the model which are discussed in more detail in Chapter 6. Estimates of surface sublimation rates are discussed in Section 4.8.2.

Q: *Why was Europa chosen over other planetary bodies?*
A: Europa is one of the prime candidates for the search for potential habitability and is the among the focal point of upcoming flagship missions from both ESA and NASA. A better understanding of Europa's surface microstructure will greatly help the analysis of data from these missions and the selection of potential landing sites for the Europa lander. I will be very happy to apply the model to other icy surfaces but I also need to leave some material for postdoctoral research :)

1.3.6 PhD Plan

To address these open questions, this thesis is divided into chapters, each focusing on one (or more) physic implemented in LunaIcy. These chapters are based on articles redacted during this PhD, some of which are published, other under revisions, and some have been submitted. However, these thesis chapters offer additional figures and discussion that could not find place within the length constraints of journal articles. Chapter 2 details the development of our thermal solver MultIHeaTS to compute heat transfer and the description of the thermal properties. This model is the core of the multiphysics simulations. Chapter 3 will introduce our estimation of gravity-driven compaction in the near surface. Chapter 4 is dedicated to the development of a new ice sintering model based on existing equations, alongside the description and first version of our multiphysics model LunaIcy. Chapter 5 outlines the development of thermal crystallization and radiation-induced amorphization, and presents the derived crystallinity map of Europa. Finally, Chapter 6 concludes the thesis by outlining future developments and applications of LunaIcy, along with their implications.

Bibliography for Chapter 1

Alley, Richard B., John F. Bolzan, and Ian M. Whillans (1982). "Polar Firn Densification and Grain Growth". In: *Annals of Glaciology* 3, pp. 7–11. DOI: 10.3189/s0260305500002433.

Altwegg, K. et al. (Jan. 2015). "67P/Churyumov-Gerasimenko, a Jupiter family comet with a high D/H ratio". In: *Science* 347.6220. ISSN: 1095-9203. DOI: 10.1126/science.1261952.

Anderson, J. D., E. L. Lau, et al. (Dec. 1996). "Gravitational constraints on the internal structure of Ganymede". In: *Nature* 384.6609, pp. 541–543. ISSN: 1476-4687. DOI: 10.1038/384541a0.

Anderson, J. D., G. Schubert, et al. (Sept. 1998). "Europa's Differentiated Internal Structure: Inferences from Four Galileo Encounters". In: *Science* 281.5385, pp. 2019–2022. DOI: 10.1126/science.281.5385.2019.

Astakhov, Sergey A. et al. (May 2003). "Chaos-assisted capture of irregular moons". In: *Nature* 423.6937, pp. 264–267. ISSN: 1476-4687. DOI: 10.1038/nature01622.

Becker, T. M. et al. (June 2024). "Exploring the Composition of Europa with the Upcoming Europa Clipper Mission". In: *Space Science Reviews* 220.5. ISSN: 1572-9672. DOI: 10.1007/s11214-024-01069-y.

Belosludov, R. V. et al. (Sept. 2008). "Crystal-like low frequency phonons in the low-density amorphous and high-density amorphous ices". In: *The Journal of Chemical Physics* 129.11. ISSN: 1089-7690. DOI: 10.1063/1.2977975.

Berdis, Jodi R. et al. (May 2020). "Europa's surface water ice crystallinity: Discrepancy between observations and thermophysical and particle flux modeling". In: *Icarus* 341, p. 113660. ISSN: 0019-1035. DOI: 10.1016/j.icarus.2020.113660.

Bland, Michael T. et al. (Dec. 2021). "Improving the Usability of Galileo and Voyager Images of Jupiter's Moon Europa". In: *Earth and Space Science* 8.12. ISSN: 2333-5084. DOI: 10.1029/2021ea001935.

Blankenship, Donald D. et al. (June 2024). "Radar for Europa Assessment and Sounding: Ocean to Near-Surface (REASON)". In: *Space Science Reviews* 220.5. ISSN: 1572-9672. DOI: 10.1007/s11214-024-01072-3.

Brown, Michael E. and Richard E. Hill (Mar. 1996). "Discovery of an extended sodium atmosphere around Europa". In: *Nature* 380.6571, pp. 229–231. ISSN: 1476-4687. DOI: 10.1038/380229a0.

Buratti, B. J. et al. (Mar. 2005). "Cassini Visual and Infrared Mapping Spectrometer Observations of Iapetus: Detection of CO 2". In: *The Astrophysical Journal* 622.2, pp. L149–L152. ISSN: 1538-4357. DOI: 10.1086/429800.

Campins, Humberto et al. (Apr. 2010). "Water ice and organics on the surface of the asteroid 24 Themis". In: *Nature* 464.7293, pp. 1320–1321. ISSN: 1476-4687. DOI: 10.1038/nature09029.

Carlson, R.W., M.S. Anderson, R.E. Johnson, et al. (June 2002). "Sulfuric Acid Production on Europa: The Radiolysis of Sulfur in Water Ice". In: *Icarus* 157.2, pp. 456–463. ISSN: 0019-1035. DOI: 10.1006/icar.2002.6858.

Carlson, R.W., M.S. Anderson, R. Mehlman, et al. (Oct. 2005). "Distribution of hydrate on Europa: Further evidence for sulfuric acid hydrate". In: *Icarus* 177.2, pp. 461–471. ISSN: 0019-1035. DOI: 10.1016/j.icarus.2005.03.026.

Carpy, Sabrina, Maï Bordiec, and Olivier Bourgeois (May 2023). "Scaling laws for ablation waves formed by ice sublimation and rock dissolution: applications to the Earth, Mars and Pluto". In: *Frontiers in Astronomy and Space Sciences* 10. ISSN: 2296-987X. DOI: 10.3389/fspas.2023.1176158.

Clark, Roger N., Robert Carlson, et al. (Apr. 2012). "Observed Ices in the Solar System". In: *Astrophysics and Space Science Library*. Springer New York, pp. 3–46. ISBN: 9781461430766. DOI: 10.1007/978-1-4614-3076-6_1.

Clark, Roger N. and Thomas B. Mc Cord (Mar. 1980). "The Galilean satellites: New near-infrared spectral reflectance measurements (0.65–2.5 um) and a 0.325–5 um summary". In: *Icarus* 41.3, pp. 323–339. ISSN: 0019-1035. DOI: 10.1016/0019-1035(80)90217-1.

Cooper, J (Jan. 2001). "Energetic Ion and Electron Irradiation of the Icy Galilean Satellites". In: *Icarus* 149.1, pp. 133–159. DOI: 10.1006/icar.2000.6498.

Cruikshank, D et al. (May 2005). "A spectroscopic study of the surfaces of Saturn's large satellites: HO ice, tholins, and minor constituents". In: *Icarus* 175.1, pp. 268–283. ISSN: 0019-1035. DOI: 10.1016/j.icarus.2004.09.003.

Cruikshank, Dale P. et al. (Aug. 1993). "Ices on the Surface of Triton". In: *Science* 261.5122, pp. 742–745. ISSN: 1095-9203. DOI: 10.1126/science.261.5122.742.

Cruz-Mermy et al. (Apr. 2023). "Selection of chemical species for Europa's surface using Galileo/NIMS". In: *Icarus* 394, p. 115379. ISSN: 0019-1035. DOI: 10.1016/j.icarus.2022.115379.

Ferrari, C. and A. Lucas (Mar. 2016). "Low thermal inertias of icy planetary surfaces". In: *Astronomy and Astrophysics* 588, A133. DOI: 10.1051/0004-6361/201527625.

Flin, Frédéric et al. (Apr. 2003). "Full three-dimensional modelling of curvature-dependent snow metamorphism: first results and comparison with experimental tomographic data". In: *Journal of Physics D: Applied Physics* 36.10A, A49–A54. DOI: 10.1088/0022-3727/36/10a/310.

Gerland, S. et al. (1999). "Density log of a 181 m long ice core from Berkner Island, Antarctica". In: *Annals of Glaciology* 29, pp. 215–219. DOI: 10.3189/172756499781821427.

Gilmozzi, Roberto and Jason Spyromilio (2007). "The European extremely large telescope (E-ELT)". In: *The Messenger* 127.11, p. 3.

Grasset, O. et al. (Apr. 2013). "JUpiter ICy moons Explorer (JUICE): An ESA mission to orbit Ganymede and to characterise the Jupiter system". In: *Planetary and Space Science* 78, pp. 1–21. DOI: 10.1016/j.pss.2012.12.002.

Greenberg, Richard et al. (Sept. 1998). "Tectonic Processes on Europa: Tidal Stresses, Mechanical Response, and Visible Features". In: *Icarus* 135.1, pp. 64–78. DOI: 10.1006/icar.1998.5986.

Grima, Cyril et al. (Oct. 2014). "Surface slope control on firn density at Thwaites Glacier, West Antarctica: Results from airborne radar sounding". In: *Geophysical Research Letters* 41.19, pp. 6787–6794. ISSN: 1944-8007. DOI: 10.1002/2014gl061635.

Guillot, Bertrand and Yves Guissani (Mar. 2004). "Investigation of vapor-deposited amorphous ice and irradiated ice by molecular dynamics simulation". In: *The Journal of Chemical Physics* 120.9, pp. 4366–4382. ISSN: 1089-7690. DOI: 10.1063/1.1644095.

Pioneer 10/11 spacecraft and missions to Jupiter (Sept. 1974). URL: https://ui.adsabs.harvard.edu/abs/1974amst.iafcR....H.

Hall, D. T. et al. (Feb. 1995). "Detection of an oxygen atmosphere on Jupiter's moon Europa". In: *Nature* 373.6516, pp. 677–679. ISSN: 1476-4687. DOI: 10.1038/373677a0.

Hansen, Gary B. (2004). "Amorphous and crystalline ice on the Galilean satellites: A balance between thermal and radiolytic processes". In: *Journal of Geophysical Research* 109.E1. DOI: 10.1029/2003je002149.

Hansen, O.L. (Feb. 1973). "Ten-micron eclipse observations of Io, Europa, and Ganymede". In: *Icarus* 18.2, pp. 237–246. ISSN: 0019-1035. DOI: 10.1016/0019-1035(73)90208-x.

Hapke, Bruce (Aug. 1986). "Bidirectional reflectance spectroscopy". In: *Icarus* 67.2, pp. 264–280. ISSN: 0019-1035. DOI: 10.1016/0019-1035(86)90108-9.

Harris, Daniel L. (1961). "Photometry and Colorimetry of Planets and Satellites". In: *Planets and Satellites*. Ed. by Gerard P. Kuiper and Barbara M. Middlehurst, p. 272. URL: https://ui.adsabs.harvard.edu/abs/1961plsa.book..272H.

Henin, Bernard (2018). *Exploring the Ocean Worlds of Our Solar System*. Springer International Publishing. ISBN: 9783319934761. DOI: 10.1007/978-3-319-93476-1.

Hobbs, Peter Victor (2010). *Ice physics*. Oxford University Press, p. 837. ISBN: 9780199587711.

Hörhold, M. W. et al. (Jan. 2011). "The densification of layered polar firn". In: *Journal of Geophysical Research: Earth Surface* 116.F1, n/a–n/a. DOI: 10.1029/2009jf001630.

Hussmann, Hauke and Tilman Spohn (Oct. 2004). "Thermal-orbital evolution of Io and Europa". In: *Icarus* 171.2, pp. 391–410. ISSN: 0019-1035. DOI: 10.1016/j.icarus.2004.05.020.

Johnson, R.E., L.J. Lanzerotti, and W.L. Brown (July 1982). "Planetary applications of ion induced erosion of condensed-gas frosts". In: *Nuclear Instruments and Methods in Physics Research* 198.1, pp. 147–157. ISSN: 0167-5087. DOI: 10.1016/0167-5087(82)90066-7.

Johnson, Robert E. (1990). *Energetic Charged-Particle Interactions with Atmospheres and Surfaces*. DOI: 10.1007/978-3-642-48375-2. URL: https://ui.adsabs.harvard.edu/abs/1990ecpi.book.....J.

Jónsson, B. (2015). "Mapping europa". In: *http://www.planetary.org/blogs/guest-blogs/2015/0218-mapping-europa.html*.

Khurana, K. K. et al. (Oct. 1998). "Induced magnetic fields as evidence for subsurface oceans in Europa and Callisto". In: *Nature* 395.6704, pp. 777–780. ISSN: 1476-4687. DOI: 10.1038/27394.

Kivelson, M.G., K.K. Khurana, and M. Volwerk (June 2002). "The Permanent and Inductive Magnetic Moments of Ganymede". In: *Icarus* 157.2, pp. 507–522. ISSN: 0019-1035. DOI: 10.1006/icar.2002.6834.

Kuiper, G. P. (Nov. 1957). "Infrared observations of planets and satellites". In: 62, pp. 245–245. URL: https://ui.adsabs.harvard.edu/abs/1957AJ....62..245K.

Lainey, V. et al. (Feb. 2024). "A recently formed ocean inside Saturn's moon Mimas". In: *Nature* 626.7998, pp. 280–282. ISSN: 1476-4687. DOI: 10.1038/s41586-023-06975-9.

Leblanc, F., R.E. Johnson, and M.E. Brown (Sept. 2002). "Europa's Sodium Atmosphere: An Ocean Source?" In: *Icarus* 159.1, pp. 132–144. ISSN: 0019-1035. DOI: 10.1006/icar.2002.6934.

Leblanc, F., A.V. Oza, et al. (Sept. 2017). "On the orbital variability of Ganymede's atmosphere". In: *Icarus* 293, pp. 185–198. ISSN: 0019-1035. DOI: 10.1016/j.icarus.2017.04.025.

Lehning, Michael et al. (Nov. 2002). "A physical SNOWPACK model for the Swiss avalanche warning". In: *Cold Regions Science and Technology* 35.3, pp. 147–167. DOI: 10.1016/s0165-232x(02)00073-3.

Leonard, Erin J., D. Alex Patthoff, and David A. Senske (2024). *Global geologic map of Europa*. DOI: 10.3133/sim3513.

Lesage, Elodie, Hélène Massol, and Frédéric Schmidt (Jan. 2020). "Cryomagma ascent on Europa". In: *Icarus* 335, p. 113369. ISSN: 0019-1035. DOI: 10.1016/j.icarus.2019.07.003.

Ligier, N. et al. (May 2016). "VLT/SINFONI observations of Europa: new insights into the surface composition". In: *The Astronomical Journal* 151.6, p. 163. ISSN: 1538-3881. DOI: 10.3847/0004-6256/151/6/163.

Manga, Michael and Chloé Michaut (Apr. 2017). "Formation of lenticulae on Europa by saucer-shaped sills". In: *Icarus* 286, pp. 261–269. ISSN: 0019-1035. DOI: 10.1016/j.icarus.2016.10.009.

Marshak, Stephen (2012). *Earth. Portrait of a planet*. 4. ed., internat. stud. ed. New York [u.a.]: Norton. ISBN: 9780393935189.

McCord, Thomas B. et al. (May 1999). "Hydrated salt minerals on Europa's surface from the Galileo near-infrared mapping spectrometer (NIMS) investigation". In: *Journal of Geophysical Research: Planets* 104.E5, pp. 11827–11851. ISSN: 0148-0227. DOI: 10.1029/1999je900005.

McEwen, Alfred S. (Mar. 1988). "Global color and albedo variations on Io". In: *Icarus* 73.3, pp. 385–426. ISSN: 0019-1035. DOI: 10.1016/0019-1035(88)90053-x.

McEwen, Alfred S. et al. (2004). "The lithosphere and surface of Io". In: *Jupiter. The Planet, Satellites and Magnetosphere*. Ed. by Fran Bagenal, Timothy E. Dowling, and William B. McKinnon. Vol. 1, pp. 307–328. URL: https://ui.adsabs.harvard.edu/abs/2004jpsm.book..307M.

Miller, Daniel August (2002). "An integrated microstructural study of dry snowmetamorphism under generalized thermal conditions". PhD thesis. MONTANA STATE UNIVERSITY.

Molaro, J. L. et al. (Feb. 2019). "The Microstructural Evolution of Water Ice in the Solar System Through Sintering". In: *Journal of Geophysical Research: Planets* 124.2, pp. 243–277. DOI: 10.1029/2018je005773.

Moore, Jeffrey M. et al. (2004). "Callisto". In: *Jupiter. The Planet, Satellites and Magnetosphere*. Ed. by Fran Bagenal, Timothy E. Dowling, and William B. McKinnon. Vol. 1, pp. 397–426. URL: https://ui.adsabs.harvard.edu/abs/2004jpsm.book..397M.

Murthy, S. Gudipati and Castillo-Rogez Julie (2013). *The Science of Solar System Ices*. Springer New York. ISBN: 9781461430766. DOI: 10.1007/978-1-4614-3076-6.

Nash, Douglas B. (June 1983). "Io's 4-um band and the role of adsorbed SO2". In: *Icarus* 54.3, pp. 511–523. ISSN: 0019-1035. DOI: 10.1016/0019-1035(83)90243-9.

Oza, Apurva V., Robert E. Johnson, and François Leblanc (May 2018). "Dusk/-dawn atmospheric asymmetries on tidally-locked satellites: O2 at Europa". In: *Icarus* 305, pp. 50–55. ISSN: 0019-1035. DOI: 10.1016/j.icarus.2017.12.032.

Pappalardo, R. T. et al. (Jan. 1998). "Geological evidence for solid-state convection in Europa's ice shell". In: *Nature* 391.6665, pp. 365–368. DOI: 10.1038/34862.

Paranicas, C., R. W. Carlson, and R. E. Johnson (Feb. 2001). "Electron bombardment of Europa". In: *Geophysical Research Letters* 28.4, pp. 673–676. ISSN: 1944-8007. DOI: 10.1029/2000gl012320.

Pater, Imke de and Jack J. Lissauer (Dec. 2014). *Planetary Sciences*. Cambridge University Press. ISBN: 9781316165270. DOI: 10.1017/cbo9781316165270.

Piqueux, S. and P. R. Christensen (Sept. 2009). "A model of thermal conductivity for planetary soils: 2. Theory for cemented soils". In: *Journal of Geophysical Research* 114.E9. DOI: 10.1029/2008je003309.

Pommerol, A. et al. (Oct. 2015). "OSIRIS observations of meter-sized exposures of H2O ice at the surface of 67P/Churyumov-Gerasimenko and interpretation using laboratory experiments". In: *Astronomy and Astrophysics* 583, A25. ISSN: 1432-0746. DOI: 10.1051/0004-6361/201525977.

Priscu, John C. and Kevin P. Hand (Jan. 2012). "Microbial Habitability of Icy Worlds: As our exploration of space begins its sixth decade, we have new tools and techniques to probe questions of planetary habitability". In: *Microbe Magazine* 7.4, pp. 167–172. ISSN: 1558-7460. DOI: 10.1128/microbe.7.167.1.

Prockter, Louise (Jan. 2005). "Ice in the solar system". In: *Johns hopkins ApL TechnicAL DigesT* 26.

Rathbun, Julie A., Nathaniel J. Rodriguez, and John R. Spencer (Dec. 2010). "Galileo PPR observations of Europa: Hotspot detection limits and surface thermal properties". In: *Icarus* 210.2, pp. 763–769. DOI: 10.1016/j.icarus.2010.07.017.

Rivkin, Andrew S. and Joshua P. Emery (Apr. 2010). "Detection of ice and organics on an asteroidal surface". In: *Nature* 464.7293, pp. 1322–1323. ISSN: 1476-4687. DOI: 10.1038/nature09028.

Roth, Lorenz (Oct. 2021). "A Stable H2O Atmosphere on Europa's Trailing Hemisphere From HST Images". In: *Geophysical Research Letters* 48.20. ISSN: 1944-8007. DOI: 10.1029/2021gl094289.

Roth, Lorenz et al. (Jan. 2014). "Transient Water Vapor at Europa's South Pole". In: *Science* 343.6167, pp. 171–174. ISSN: 1095-9203. DOI: 10.1126/science.1247051.

Rubanenko, Lior, Jaahnavee Venkatraman, and David A. Paige (July 2019). "Thick ice deposits in shallow simple craters on the Moon and Mercury". In: *Nature Geoscience* 12.8, pp. 597–601. ISSN: 1752-0908. DOI: 10.1038/s41561-019-0405-8.

Sauter, Tobias, Anselm Arndt, and Christoph Schneider (Nov. 2020). "COSIPY v1.3 – an open-source coupled snowpack and ice surface energy and mass balance model". In: *Geoscientific Model Development* 13.11, pp. 5645–5662. DOI: 10.5194/gmd-13-5645-2020.

Schenk, Paul M. and William B. McKinnon (May 1989). "Fault offsets and lateral crustal movement on Europa: Evidence for a mobile ice shell". In: *Icarus* 79.1, pp. 75–100. ISSN: 0019-1035. DOI: 10.1016/0019-1035(89)90109-7.

Schmidt, Frédéric et al. (Jan. 2022). "Circumpolar ocean stability on Mars 3 Gy ago". In: *Proceedings of the National Academy of Sciences* 119.4. ISSN: 1091-6490. DOI: 10.1073/pnas.2112930118.

Schmitt, B. (1998). *Solar System Ices. Based on Reviews Presented at the International Symposium "Solar System Ices" held in Toulouse, France, on March 27-30, 1995*. Ed. by C. Bergh and M. Festou. Astrophysics and Space Science Library 227. Dordrecht: Springer. 810 pp. ISBN: 9789401152525.

Sheppard, Scott S. et al. (May 2023). "New Jupiter and Saturn Satellites Reveal New Moon Dynamical Families". In: *Research Notes of the AAS* 7.5, p. 100. ISSN: 2515-5172. DOI: 10.3847/2515-5172/acd766.

Slade, Martin A., Bryan J. Butler, and Duane O. Muhleman (Oct. 1992). "Mercury Radar Imaging: Evidence for Polar Ice". In: *Science* 258.5082, pp. 635–640. ISSN: 1095-9203. DOI: 10.1126/science.258.5082.635.

Sohl, F. et al. (May 2002). "Implications from Galileo Observations on the Interior Structure and Chemistry of the Galilean Satellites". In: *Icarus* 157.1, pp. 104–119. ISSN: 0019-1035. DOI: 10.1006/icar.2002.6828.

Spencer, John, Larry Lebofsky, and Mark Sykes (Apr. 1989). "Systematic biases in radiometric diameter determinations". In: *Icarus* 78.2, pp. 337–354. DOI: 10.1016/0019-1035(89)90182-6.

Stern, J. and T. Loerting (June 2017). "Crystallisation of the amorphous ices in the intermediate pressure regime". In: *Scientific Reports* 7.1. ISSN: 2045-2322. DOI: 10.1038/s41598-017-03583-2.

Swinkels, F.B. and M.F. Ashby (Feb. 1981). "A second report on sintering diagrams". In: *Acta Metallurgica* 29.2, pp. 259–281. DOI: 10.1016/0001-6160(81)90154-1.

Szalay, J. R. et al. (Mar. 2024). "Oxygen production from dissociation of Europa's water-ice surface". In: *Nature Astronomy* 8.5, pp. 567–576. ISSN: 2397-3366. DOI: 10.1038/s41550-024-02206-x.

Teolis, B. D. et al. (Oct. 2017). "Water Ice Radiolytic O2, H2, and H2O2 Yields for Any Projectile Species, Energy, or Temperature: A Model for Icy Astrophysical Bodies". In: *Journal of Geophysical Research: Planets* 122.10, pp. 1996–2012. ISSN: 2169-9100. DOI: 10.1002/2017je005285.

Trumbo, Samantha K., Michael E. Brown, and Bryan J. Butler (Sept. 2018). "ALMA Thermal Observations of Europa". In: *The Astronomical Journal* 156.4, p. 161. ISSN: 1538-3881. DOI: 10.3847/1538-3881/aada87.

Trumbo, Samantha K., Michael E. Brown, and Kevin P. Hand (June 2019). "Sodium chloride on the surface of Europa". In: *Science Advances* 5.6. ISSN: 2375-2548. DOI: 10.1126/sciadv.aaw7123.

Tyler, Robert H., Wade G. Henning, and Christopher W. Hamilton (June 2015). "TIDAL HEATING IN A MAGMA OCEAN WITHIN JUPITER'S MOON Io". In: *The Astrophysical Journal Supplement Series* 218.2, p. 22. ISSN: 1538-4365. DOI: 10.1088/0067-0049/218/2/22.

Vale Pereira, Paula do et al. (May 2023). "Experimental Validation of Cryobot Thermal Models for the Exploration of Ocean Worlds". In: *The Planetary Science Journal* 4.5, p. 81. DOI: 10.3847/psj/acc2b7.

Vance, Steven D. et al. (Jan. 2018). "Geophysical Investigations of Habitability in Ice-Covered Ocean Worlds". In: *Journal of Geophysical Research: Planets* 123.1, pp. 180–205. ISSN: 2169-9100. DOI: 10.1002/2017je005341.

Villanueva, G. L. et al. (Sept. 2023). "Endogenous CO 2 ice mixture on the surface of Europa and no detection of plume activity". In: *Science* 381.6664, pp. 1305–1308. ISSN: 1095-9203. DOI: 10.1126/science.adg4270.

Vionnet, V. et al. (May 2012). "The detailed snowpack scheme Crocus and its implementation in SURFEX v7.2". In: *Geoscientific Model Development* 5.3, pp. 773–791. DOI: 10.5194/gmd-5-773-2012.

Wahr, John et al. (Mar. 2009). "Modeling stresses on satellites due to non-synchronous rotation and orbital eccentricity using gravitational potential theory". In: *Icarus* 200.1, pp. 188–206. ISSN: 0019-1035. DOI: 10.1016/j.icarus.2008.11.002.

Zahnle, Kevin et al. (June 2003). "Cratering rates in the outer Solar System". In: *Icarus* 163.2, pp. 263–289. ISSN: 0019-1035. DOI: 10.1016/s0019-1035(03)00048-4.

Zhang, Ke, Geoffrey A. Blake, and Edwin A. Bergin (June 2015). "vEvidence of fast pebble growth near condensation fronts in the HL tau protoplanetary disk". In: *The Astrophysical Journal* 806.1, p. L7. ISSN: 2041-8213. DOI: 10.1088/2041-8205/806/1/l7.

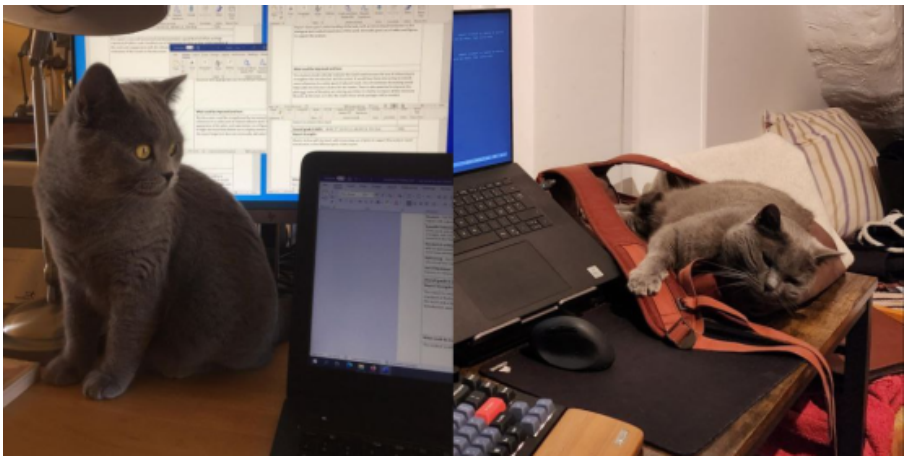

Figure 1.24: While it may seem like the name LunaIcy cleverly refers to "icy moons", with "luna" being the Spanish word for "moon", the reality is quite different. Luna (left) and Icy (right) are the names of the two cats who run the business in my family.

CHAPTER 2

Heat Transfer

The work presented in this chapter comes from the article titled *"MultIHeaTS: a Fast and Stable Thermal Solver for Multilayered Planetary Surfaces" by C. Mergny and F.Schmidt, 2024* The Planetary Science Journal, DOI 10.3847/PSJ/ad6d6e

Contents

Foreword

Temperature Evolution — Temperature drives the kinetics of various physical processes, such as sintering (Chapter 4) and crystallization/amorphization (Chapter 5). Therefore, it is important to accurately estimate the temperature evolution with depth of the near surface ice. Achieving this requires three components: 1) Obtaining the input solar flux from the current orbit, latitude, longitude and albedo 2) Determining the current thermal properties of the ice with depth: the conductivity, the heat capacity and the density and 3) Solving the heat equation with these conditions (see Figure 2.1).

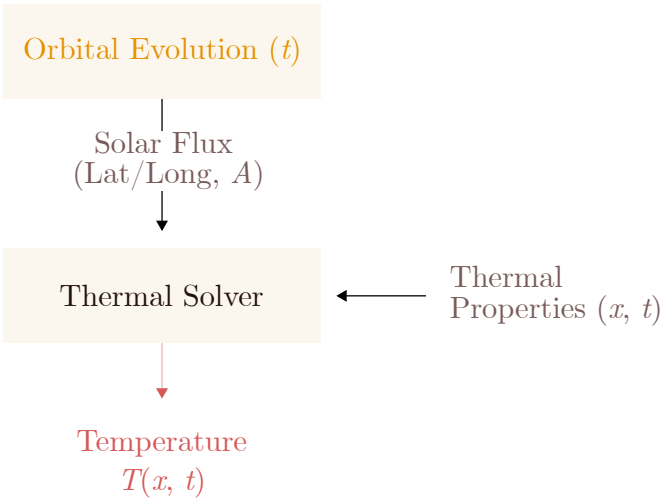

Figure 2.1: Simplified block diagram of a thermal solver in planetary science.

This chapter presents the development of these three aspects, apart from the specific focus on the density profile with depth that is described in Chapter 3.

Yet another thermal solver ? — There are plenty of thermal solvers available in the literature, spanning across various field. They are not only found in planetary sciences (J. Spencer et al., 1989), but also widely used in geophysics (Bonneville et al., 1999), material science (Rojek et al., 2022), mechanical and electrical engineering (Anderson et al., 2020), and computational fluid dynamics (Janna, 2018), among others.

So, why develop another one ? The reason is that the unique conditions necessary to model the complex planetary surfaces require some special treatments that are not properly addressed in the existing literature. These requirements are as follows:

1. **Stability:** To be more precise, unconditional stability under classical conditions (see Section 2.6.2). Fully implicit and semi-implicit solvers are far more efficient than the explicit time step schemes that still dominate planetary thermal models today. This paper is the only study that takes the approach of a

fully implicit scheme, providing a novel numerical derivation and analysis not previously explored in this field.

2. **Compatibility with Heterogeneous Media:** This is crucial as many solvers in planetary science rely on the simplifying assumption of homogeneous materials. However, this assumption does not hold true in numerous scenarios, such as dust over ice on Iapetus, CO2 ice over regolith on Mars, or snow covers with depth-dependent porosity on Earth. While some models may use workarounds for handling two-layered materials, our approach offers the flexibility to handle any number of layers, making it applicable to a broader range of realistic planetary scenarios.

3. **Inclusion of a Thermal Emission Equilibrium:** This has important implications in planetary science. While solvers fulfilling conditions 1) and 2) have probably been developed in other research domains, to the best of our knowledge, their application to planetary surfaces remains unexplored. The development or adaptation of thermal solvers specifically designed for planetary surfaces are necessary due to the non-linear nature of the thermal emission equilibrium at the surface due to the Stefan-Boltzmann law.

In addition to verifying the three conditions mentioned above, because our thermal solver is at the core of the multiphysics model it must satisfy two additional technical requirements:

4. **Modularity:** Each module developed in this thesis needs to be coupled with others and communicate easily, requiring special treatment on the numerical aspect. Python was chosen as the primary language due to its ease of use, numerous libraries, extensive online resources, and strengths when used properly. Therefore all physics modules will be written in Python. The open-source nature of Python and its widespread use in the scientific community facilitate dissemination of the code and collaboration through open-source repositories.

5. **Speed:** The solver must be highly computationally efficient. The coupled surface physics involved, such as sintering, are very sensitive to daily variations, but their effects become noticeable only after accumulating over geological timescales ($\sim 1\,\mathrm{Myr}$). This creates a numerical challenge, as a high number of calls to the thermal solver will need to happen over such large timescales. Therefore, the solver speed need to be optimized while satisfying the Python requirement 4). This can be achieved through proper coding practices and the use of optimized python functions that call C libraries.

Collaborations — However, the need for such thermal solver, does not only come from our own goals but has also be expressed by others in the community. The solver, named MultIHeaTS, was presented at the TherMoPS IV workshop at ESA/ESTEC in April 2023 and was very well-received by the planetary science community. Additionally, the thermal solver was showcased at multiple international and national conferences and seminars, leading to a collaboration with Dr. Alice Le Gall and PhD student Raza Salman. The project of this LATMOS/IPSL team is to study Iapetus' hemispheric dichotomy by modeling microwave observations obtained from the Very Large Array (VLA) radio telescope. The goal of their study is to discern the composition and thickness of the exogenous deposit layer on Iapetus' dark hemisphere. To achieve this, they developed a comprehensive model (see Figure 2.2) to reproduce the VLA observations of Iapetus, which includes our thermal solver MultIHeaTS, combined with a multilayer radiative transfer model and a model to account for the beam convolution of the VLA telescope.

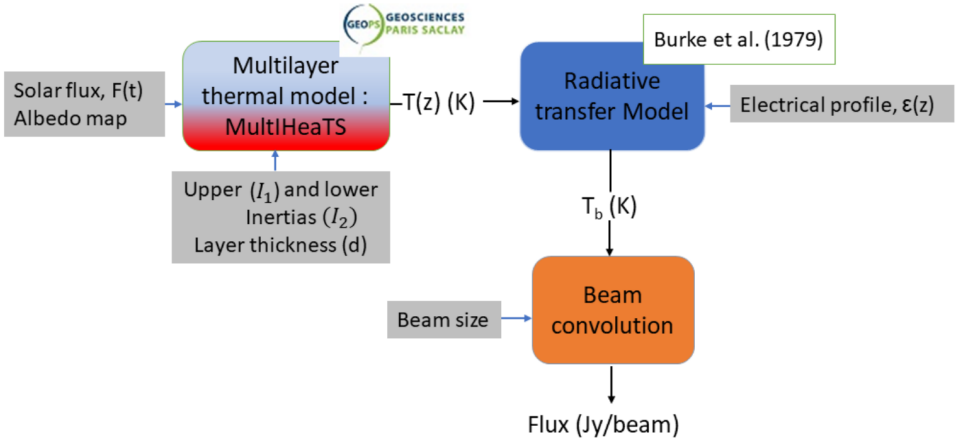

Figure 2.2: Block diagram of the thermal emission model used by Raza and Le Gall. Figure from Md Salman Raza's internship report.

Through the comparison of their model with the VLA observations, they explored the influence of key parameters on the thermal emission of Iapetus: the thermal inertia of the leading and trailing faces, the thickness of the dark deposit, and the complex permittivity of the different compositions. Moreoever, the team is also working to use the thermal solver to study the scattering and thermal anomalies at Enceladus using Cassini radar observations. Both projects have been the subject of two abstracts that will be presented at the Europlanet Science Congress (EPSC) 2024 conference in Berlin.

The work presented in this Chapter is our attempt to develop a thermal solver that satisfies all of these requirements.

Abstract

A fully implicit scheme is proposed for solving the heat equation in 1D heterogeneous media, available as a computationally efficient open-source Python code. The algorithm uses finite differences on an irregular grid and is unconditionally stable due to the implicit formulation. The thermal solver is validated against a stiff analytical solution, demonstrating its robustness in handling stiff initial conditions. Its general applicability for heterogeneous cases is demonstrated through its use in a planetary surface scenario with non-linear boundary conditions induced by black body thermal emission. MultIHeaTS advantageous stability allows for computation times up to 100 times faster than Spencer's explicit solver, making it ideal for simulating processes on large timescales. This solver is used to compare the thermal signatures of homogeneous and bilayer profiles on Europa. Results show that homogeneous materials cannot reproduce the thermal signature observed in bilayer profiles, emphasizing the need for multilayer solvers. In order to optimize the scientific return of space mission, we propose a strategy made of three local time observations that is enough to identify a bilayer media, for instance for the next missions to the Jovian system. A second application of the solver is the estimation of the temperature profile of Europa's near surface (first 10 meters) throughout a one-million-year simulation with varying orbital parameters. The probability distribution of temperature through depth is obtained. Among its various applications, MultIHeaTS serves as the core thermal solver in a multiphysics simulation model detailed in Chapter 4.

2.1 Introduction

The heat equation is a fundamental partial differential equation that governs the behavior of heat transfer in various physical systems. However, when dealing with heterogeneous media, where the thermal properties of the material vary spatially, this equation becomes too complex to solve analytically (Jaeger, 1950; Loeb et al., 2019). In one dimension, the heat equation for conduction transfer can be expressed as:

$$\rho(x,t)c_{\mathrm{p}}(x,t)\frac{\partial T(x,t)}{\partial t} = \frac{\partial}{\partial x}\left(k(x,t)\frac{\partial}{\partial x}T(x,t)\right) + Q(x,t) \tag{2.1}$$

where x denotes space and t denotes time, T is the temperature, ρ is the density, c_{p} is heat capacity, k is thermal conductivity, and Q denotes an additional and optional source or sink term. We propose to solve numerically Equation 4.25 where all thermal properties can vary continuously over space and time, and with non-constant time and space increments. For the near surface, the vertical temperature gradients induced by the input solar flux is often much larger than any lateral heat variations, justifying the use of a 1D model for many planetary science applications. At greater depths (hundreds of meters), a 3D model would be beneficial due to reduced solar flux influence, but given the lack of knowledge on lateral heat transfer of icy moons, the 1D model will suffice.

Numerous numerical methods have been developed in various fields to solve the 1D heat equation for heterogeneous media. These methods include finite element and finite difference approaches (Roubíček, 1990; Lage, 1996; Nissen et al., 2017; Loeb et al., 2019; Masson et al., 2020). However, in planetary sciences, widely used solvers such as Thermprojrs (J. Spencer et al., 1989), MARSTHERM (N Putzig, 2007), KRC (Kieffer, 2013), and Heat1D (Hayne et al., 2015), rely on explicit finite difference schemes which are known to have instability issues (Press et al., 1992). While there are semi-implicit solvers, most notably Schorghofer's Planetary Code Collection (Schorghofer, 2022) [1] and later Young, 2017, none have pursued a fully implicit derivation, despite its known numerical stability. Our study stands out as the first to take the approach of a fully implicit scheme in the context of planetary thermal modeling.

The target science case is in Earth and Planetary science with surface conditions subject to solar illumination. In this scenario, the upper boundary condition (i.e., the flux leaving the surface) is determined by the energy equilibrium between the input solar flux and the gray body emission from the surface (J. Spencer et al., 1989).

$$\forall t, k(0,t)\left.\frac{\partial T(x,t)}{\partial x}\right|_{x=0} = -F_{\mathrm{solar}}(t) + \epsilon \cdot \sigma_{\mathrm{SB}} \cdot T(0,t)^4 \tag{2.2}$$

where ϵ is the thermal emissivity and σ_{SB} the Stefan-Boltzmann constant. A simplified model for solar illumination at the equator with zero obliquity throughout a

[1] Schorghofer's Planetary Code Collection was developed between 2001 and 2003.

sidereal day can be expressed as a truncated sinusoidal function (J. Spencer et al., 1989) :

$$F_{\text{solar}}(t) = \begin{cases} (1-A)\,\dfrac{G_{\text{SC}}}{d^2}\cos\left(\dfrac{2\pi t}{P}\right) & \text{if } 2\pi t/P \text{ in } \left[-\frac{\pi}{2}, \frac{\pi}{2}\right] \\ \text{or} & \\ 0 & \text{if } 2\pi t/P \text{ in } \left]\frac{\pi}{2}, \frac{3\pi}{2}\right[\end{cases} \tag{2.3}$$

where A is the surface albedo, G_{SC} the solar constant in W.m^{-2} and d the distance between the Sun and the planet in AU. While this simplified model captures the essential features of solar illumination, more realistic estimations, for instance from NASA's SPICE toolkit (C. H. Acton, 1996; C. Acton et al., 2018) can be easily integrated to account for different inclinations, eccentricities and more, as shown in Section 2.4.1.

In the planetary science context, various numerical models have been developed to study the behavior of both homogeneous surfaces (Wesselink, 1948; Rozitis et al., 2011; Kieffer, 2013), and heterogeneous media, as shown in Spencer's implementation of the explicit Euler scheme (J. Spencer et al., 1989). Although the explicit method is easier to numerically implement and could have a faster computational time per iteration, its main drawback is its conditional stability (Press et al., 1992). A Crank-Nicolson scheme (Crank et al., 1947) has been implemented for planetary science cases by Schorghofer (2022). This scheme is more complex to implement and requires the inversion of tridiagonal matrix. In return, it offers the advantage of being unconditionally stable and more precise than first-order explicit and fully implicit schemes for homogeneous media, owing to its second-order truncation error in time (Mazumder, 2016). However, the development of a fully implicit algorithm is also advantageous, as it can easily account for spatial heterogeneities by staying stable (Press et al., 1992; Østerby, 2003; Langtangen et al., 2017).

Although the implicit Euler scheme is also unconditionally stable, to our knowledge, there are no codes available online that use it to solve the heat equation in a heterogeneous medium for planetary surfaces. Therefore, our goal is to provide the scientific community with an open-source, easy-to-use, and versatile fully implicit solver called MultIHeaTS (Multi-layered Implicit Heat Transfer Solver) for solving the heat equation in such conditions. The source code is available online[2]. Even though our target science is planetary science with surface conditions subject to solar illumination (Wesselink, 1948; J. Spencer et al., 1989; Schorghofer, 2022; Rozitis et al., 2011; Kieffer, 2013), this approach is applicable in a wide range of boundary conditions for a large set of scientific and technical cases.

When thermal properties depend on temperature, they introduce non-linearity into the heat equation, making it challenging to solve, regardless of the numerical scheme. For instance, both thermal conductivity $k(T)$ and heat capacity $c_p(T)$ exhibit strong temperature dependence when considering conditions on silicate bodies

[2]MultIHeaTS open-source code is available at the IPSL Data Catalog:DOI: 10.14768/9763d466-db02-4f29-8ad5-16e6e0187bd4

within a distance of less than 3 AU from the Sun (Watson, 1964; Woods-Robinson et al., 2019). Nevertheless, by linearizing the temperature-dependent thermal properties, we can effectively solve the modified heat equation. This approach, used for example in Heat1D (Hayne et al., 2015) and Schorghofer, 2022 expresses the thermal properties as functions of the previous temperature, allowing iterative updates at each time step using time-dependent variables $k(t), c_p(t)$, and $\rho(t)$. It is important to note that the linearization process may impact numerical stability, particularly in situations involving significant temperature variations. While further stability analysis would be advised for future studies, using smaller time steps and finer linearization (like discussed in Section 2.2.3) will solve the stability issues.

In the first section of this article, we begin by presenting the mathematical derivation of the heat equation in heterogeneous media using the implicit Euler method. We then proceed to validate the MultIHeaTS algorithm by comparing its results to analytical solutions and other existing algorithms. Then, our thermal model is used to investigate the thermal signatures of bilayer profiles on Europa, providing valuable insights that can guide the timing of measurements for upcoming missions. Finally, the thermal model is applied to a one million year simulation of Europa's temperature profile, using a precise orbital description.

2.2 Methods

To discretize the heat equation, we used finite differences on an irregular spatial grid consisting of n_x points, which we iterated for a total of n_t iterations. The spatial and temporal parameters were discretized as follows:

$$\begin{cases} x \to x_n & = x_{n-1} + \Delta x_n \\ t \to t^i & = t^{i-1} + \Delta t^i. \end{cases} \tag{2.4}$$

Here, n is an integer such that $n \in \{0, \dots, n_x - 1\}$, representing the nth element in the spatial dimension, and i is an integer such that $i \in \{0, \dots, n_t - 1\}$, representing the ith element in the time dimension. It is worth noting that both the spatial Δx_n and temporal Δt^i increments may not be constant respectively over the spatial and temporal grid.

2.2.1 Backward Euler Finite Differences on an Irregular Grid

Following the method described in (Sundqvist et al., 1970), the first order derivative of function f using the central difference approximation can be written as :

$$\frac{\partial f}{\partial x}(x_n) = \frac{f_{n+1} - f_n}{2\Delta x_n} + \frac{f_n - f_{n-1}}{2\Delta x_{n-1}} + \mathcal{O}(\Delta x_n^2) \tag{2.5}$$

and the second order derivative as :

$$\frac{\partial f^2}{\partial x^2} = \frac{2\left(f_{n+1}\Delta x_{n-1} + f_{n-1}\Delta x_n - f_n\left(\Delta x_n + \Delta x_{n-1}\right)\right)}{\Delta x_n \Delta x_{n-1}\left(\Delta x_n + \Delta x_{n-1}\right)} + \mathcal{O}(\Delta x_n^3) \tag{2.6}$$

By using Equations 2.5 and 2.6, the heat equation can be discretized with second order accuracy in space and first order in time. After factorizing each temperature term, the resulting equation is given by:

$$\begin{aligned} T_n^i + r_n^i Q_n^i =& T_{n-1}^{i+1}\left[\frac{-r_n}{\Delta x_{n-1}}\left(-\frac{1}{2}\frac{\partial k}{\partial x} + \frac{2k_n}{\Delta x_n + \Delta x_{n-1}}\right)\right] \\ &+ T_n^{i+1}\left[1 - \frac{r_n}{\Delta x_n \Delta x_{n-1}}\left(\frac{(\Delta x_n - \Delta x_{n-1})}{2}\frac{\partial k}{\partial x} - 2k_n\right)\right] \\ &+ T_{n+1}^{i+1}\left[\frac{-r_n}{\Delta x_n}\left(\frac{1}{2}\frac{\partial k}{\partial x} + \frac{2k_n}{\Delta x_n + \Delta x_{n-1}}\right)\right] \end{aligned} \tag{2.7}$$

with T_n^i the temperature of the nth cell at time t^i, and r_n a coefficient expressed as $r_n^i = \Delta t^i/(\rho_n^i c_{\mathrm{p},n}^i)$. With matrix notation this is equivalent to the system :

$$\begin{pmatrix} b_0 & c_0 & & & \dots & & 0 \\ a_1 & b_1 & c_1 & & & & \\ & \ddots & \ddots & \ddots & & & \\ \vdots & & a_n & b_n & c_n & & \vdots \\ & & & \ddots & \ddots & \ddots & \\ & & & & a_{n_x-2} & b_{n_x-2} & c_{n_x-2} \\ 0 & & \dots & & & a_{n_x-1} & b_{n_x-1} \end{pmatrix} \cdot \begin{pmatrix} T_0 \\ \vdots \\ T_{n-1} \\ T_n \\ T_{n+1} \\ \vdots \\ T_{n_x-1} \end{pmatrix}^{i+1} = \begin{pmatrix} s_0 \\ \vdots \\ s_{n-1} \\ s_n \\ s_{n+1} \\ \vdots \\ s_{n_x-1} \end{pmatrix}^{i} \tag{2.8}$$

where the coefficients a_n, b_n, c_n and s_n are given by

$$\forall n \in \{1, \dots, n_x - 2\} \begin{cases} a_n = \dfrac{-r_n}{\Delta x_{n-1}}\left(-\dfrac{1}{2}\dfrac{\partial k}{\partial x} + \dfrac{2k_n}{\Delta x_n + \Delta x_{n-1}}\right) \\ b_n = 1 - \dfrac{r_n}{\Delta x_n \Delta x_{n-1}}\left(\dfrac{(\Delta x_n - \Delta x_{n-1})}{2}\dfrac{\partial k}{\partial x} - 2k_n\right) \\ c_n = \dfrac{-r_n}{\Delta x_n}\left(\frac{1}{2}\dfrac{\partial k}{\partial x} + \dfrac{2k_n}{\Delta x_n + \Delta x_{n-1}}\right) \\ s_n = T_n^i + r_n^i Q_n^i \end{cases} \tag{2.9}$$

and by the boundary conditions for $n = 0$ and $n = n_x - 1$.

2.2.2 Linear Boundary Conditions

MultIHeaTS accepts any type of boundary conditions, including imposed flux or imposed temperatures at the boundaries. A detailed derivation of the Dirichlet boundary conditions can be found in Supplementary Materials Section 1. In the case of planetary surface evolution, we are specifically interested in Neumann boundary

conditions, which involve imposed flux. In this scenario, the heat flux Φ is prescribed at the upper boundary ($n = 0$) by

$$\forall t, k_0 \left.\frac{\partial T(x,t)}{\partial x}\right|_{x_0} = \Phi_0(t). \tag{2.10}$$

By injecting Equation 2.10 into the discretized heat Equation 2.7, the upper boundary condition becomes:

$$T_0^{i+1} = T_0^i + r_0^i \left[\frac{\Phi_0^i}{\Delta x_0 k_0^i}\left(k_1^i - 3k_0^i\right) + Q_0^i\right] + 2\frac{r_0^i k_0^i}{\Delta x_0^2} T_1^{i+1} - 2\frac{r_0^i k_0^i}{\Delta x_0^2} T_0^{i+1} \tag{2.11}$$

which gives the expression of the first coefficients of the tri-diagonal matrix

$$\begin{cases} b_0 = 1 + 2r_0 k_0/\Delta x_0^2 \\ c_0 = -2r_0 k_0/\Delta x_0^2 \\ s_0 = T_0 + r_0\left(\Phi_0/k_0\left(k_1 - 3k_0\right)/\Delta x_0 + Q_0\right). \end{cases} \tag{2.12}$$

The same reasoning can be applied to the bottom boundary condition :

$$\forall t, k_{n_x-1} \left.\frac{\partial T(x,t)}{\partial x}\right|_{x_{n_x-1}} = \Phi_{n_x-1}(t) \tag{2.13}$$

which gives the expression of the last tri-diagonal coefficients :

$$\begin{cases} a_{n_x-1} = -2r_{n_x-1}k_{n_x-1}/\Delta x_{n_x-1}^2 \\ b_{n_x-1} = 1 + 2r_{n_x-1}k_{n_x-1}/\Delta x_{n_x-1}^2 \\ s_{n_x-1} = T_{n_x-1} + r_{n_x-1}\left[\Phi_{n_x-1}/k_{n_x-1}\left(k_{n_x-2} - 3k_{n_x-1}\right)/\Delta x_{n_x-1} + Q_{n_x-1}\right] \end{cases} \tag{2.14}$$

2.2.3 Non-Linear Boundary Conditions

When dealing with planetary-like surfaces, a non-linearity problem arises from the energy equilibrium described in Equation 4.26. This non-linearity comes from the Stefan-Boltzmann law, which states that the emitted surface flux Φ is proportional to T_0^4, making it a non-linear function of temperature:

$$\Phi(t, T_0) \propto T_0^4 \tag{2.15}$$

For the explicit scheme, the non-linearity in the surface flux does not pose any issue as the surface flux can be pre-calculated using the previous surface temperature. However, for Crank-Nicolson and Backward Euler schemes, the non-linearity of the Stefan-Boltzmann law makes it impossible to solve the implicit formulation of the upper boundary conditions as given in Equation 2.12. To circumvent this issue, a workaround exist by linearizing the black body emission around a reference temperature T_r (Williams et al., 1977; Schorghofer, 2022):

$$T_0^{i+1^4} = \left(T_\mathrm{r} + \delta T\right)^4 \approx T_\mathrm{r}^4 + 4T_\mathrm{r}^3 \delta T \tag{2.16}$$

where T_r is chosen to be equal to the previous surface temperature T_0^i and $\delta T = T_0^{i+1} - T_0^i$.

For the MultIHeaTS solver, the boundary surface flux can be calculated either using Equation 2.16 or the previous surface temperature. Our validation tests, discussed in Section 2.3, demonstrate that following the same approach as for the explicit scheme does not introduce large errors and the algorithm remains stable. One advantage of the implicit scheme is that such formulation of the surface flux can be used, while maintaining stability and adding little to no errors (Beam et al., 1982). Unless stated otherwise, this is the method chosen for computing the upper boundary conditions in the rest of this article. We propose that this robustness may be due to the strong damping of oscillations discussed in Section 2.6.2. Similar to the Crank-Nicolson solver, the fully implicit scheme looses its unconditional stability when there are abrupt changes in surface temperatures with such non linear conditions. Nonetheless, the scheme is capable of accurately estimating the upper boundary condition and its domain of stability remains much larger than the explicit solvers as shown in Section 2.3.2.2.

2.3 Results

2.3.1 Validation with an Analytical Solution

Since analytical solutions of the heat equation do not exist in the general case, analytical validation of our model can only be achieved for homogeneous profiles. If we consider a stiff initial condition given by a step function defined on $[0, L]$ by the expression :

$$\forall x \in [0, L],\, T(x, 0) = \begin{cases} 0, & \text{if } x < L/2 \\ 1, & \text{if } x \geq L/2. \end{cases} \tag{2.17}$$

then the analytical solution with zero-flux boundary conditions can be obtained through Fourier series decomposition

$$T_\mathrm{R}(x, t) = \frac{1}{2} - \sum_{j=1}^{+\infty} \frac{2}{\pi j} \sin\left(\frac{\pi j}{2}\right) \cos\left(\frac{\pi j x}{L}\right) e^{-\alpha\left(\frac{\pi j}{L}\right)^2 t}. \tag{2.18}$$

To validate our model, we need to compare the computed temperatures with the analytical solutions for the same set of thermal parameters. This is done by computing the error, defined as the absolute value of difference between the temperature produced by the numerical model T and the reference temperature T_R. The maximum error e_+ is expressed as :

$$e_+ = \max_{n,i} \left| \frac{T_n^i - T_{\mathrm{R},n}^i}{\langle T \rangle} \right| \tag{2.19}$$

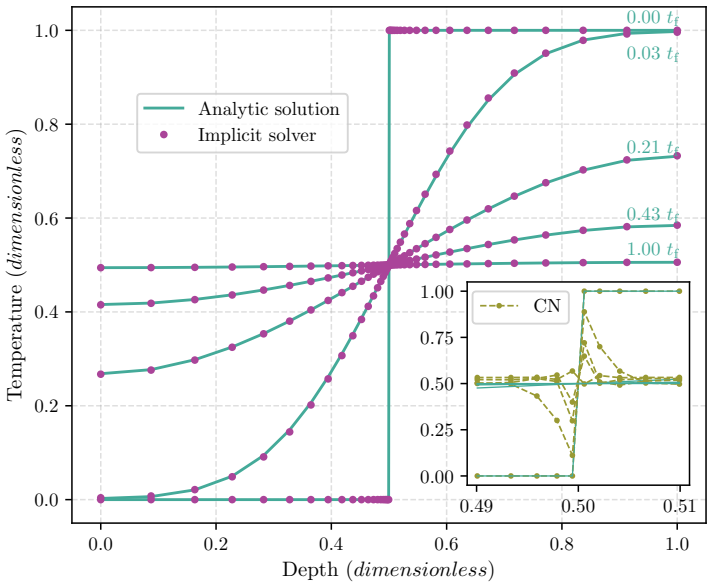

Figure 2.3: Analytical validation for a stiff initial condition and homogeneous thermal properties on an irregular grid for different timesteps. Here $t_\mathrm{f} = n_t \Delta t$. Despite the discontinuity at $x = 0.5$, the fully implicit solver MultIHeaTS can compute the evolution of temperature with a very close match (maximum error $e_+ < 0.5\%$) to the analytic solution. (*Bottom Right*) Zoom on the spurious oscillations of the Crank-Nicolson solver at the location of the initial discontinuity.

where $\langle T \rangle$ is the mean temperature and the average error $\overline{e}$ as

$$\overline{e} = \frac{1}{n_x n_t} \sum_{n,i} \left| \frac{T_n^i - T_{\mathrm{R},n}^i}{\langle T \rangle} \right| \tag{2.20}$$

with $T_{\mathrm{R},n}^i$ the reference temperature obtained from the analytical Equation (2.18) at location x_n and time t^i. For proper validation, both the numerical solver and the reference solution need to be calculated with exactly the same thermal properties and conditions (see Figure 2.3). To showcase the advantages of using a solver capable of handling irregular grids, we specifically compute the temperature on an uneven spatial grid, strategically denser near the temperature discontinuity $\mu = L/2$. The grid spacing is determined by the following expression:

$$\begin{cases} x_0 = 0 \\ x_n = x_{n-1} + \dfrac{g(x'_n)}{\sum_1^{n_x-1} g(x'_k)} L, \; \forall n \in \{1, \; \dots \; , n_x - 1\} \end{cases} \tag{2.21}$$

where g is normalized sigmoid function defined by

$$g \colon x' \longmapsto 2 \left(1 + e^{\left(1 - \frac{|x' - \mu|}{\mu}\right)/d} \right)^{-1}, \tag{2.22}$$

where d is a parameter controlling the streepness of the sigmoid and $x'_n = n/(n_x - 1) \times L$. For a set of $n_x = 40$ grid points defining the box of length $L = 1\,\mathrm{m}$ of constant diffusivity $\alpha = k/(\rho c_\mathrm{p}) \approx 0.55\,\mathrm{m^2\,s^{-1}}$ and $n_t = 700$ iterations of timestep $\Delta t = 2.3\,\mathrm{ms}$, the maximum error e_+ between the analytical solution and the fully implicit solver is less than 0.5% and the mean error $\overline{e}$ is under 0.02%. Results show a very close fit between the numerical and analytic solutions which proves that the MultIHeaTS model works well for homogeneous media.

The same test was performed using the Crank-Nicolson solver (Schorghofer, 2022) to evaluate its ability to handle stiff initial conditions. Using the same parameters as previously, the Crank-Nicolson solver produced spurious oscillations that were located around the initial discontinuity position (Figure 2.3, *Bottom Right*). The maximum error e_+ between the analytical solution and the Crank-Nicolson solver reaches up to 38% and the mean error $\overline{e}$ averages 3%. Although these oscillations eventually slowly disappear with time (Østerby, 2003), it demonstrates that despite being the most accurate finite difference scheme, the Crank-Nicolson solver is less reliable in handling stiff initial conditions (Press et al., 1992; Østerby, 2003; Langtangen et al., 2017), such as when two materials with different temperatures come into contact. Such scenarios could arise in planetary science, such as when hot lava interacts with the Earth's surface, cryolava deposits on the icy surface of Europa, or CO_2 precipitates on the regolith of Mars.

2.3.2 Comparison with Spencer's explicit Thermal Model

2.3.2.1 Validation by Numerical Comparison

In more complex cases, in particular when the thermal conductivity vary with depth, the heat equation becomes too complex to solve analytically (Jaeger, 1950). In these cases, validation of the model is typically performed through comparison with experimental data and/or other well-established numerical algorithms. Since our target application is the study of realistic planetary surface conditions, we decided to compare our method with Spencer's explicit scheme (J. Spencer et al., 1989), which is a commonly used algorithm in planetary science. Spencer's algorithm was implemented in IDL and can be obtained from the author's personal website[3].

Parameters	Value
Distance to Sun d	9.51 AU
Emissivity ϵ	1
Albedo A	0.015
Grid points n_x	100
Max Depth L	2 m
Initial Temperature T	90 K
Solar Period P	79.3 days
Number of Periods	5
Number of iterations n_t	50000
Time Step Δt	685 s

Table 2.1: Physical and numerical parameters used for comparing Spencer algorithm with MultIHeaTS. While closely related to the Iapetus case, this dataset serves more as a reference scenario.

Thermal Properties	Unit	Top value	Bottom value	Interface
Density ρ	$\mathrm{kg.m^{-3}}$	800	2000	25 cm
Heat Capacity c_p	$\mathrm{J.kg^{-1}.K^{-1}}$	600	1800	50 cm
Inertia Γ_th	$\mathrm{J.m^{-2}.K^{-1}.s^{-1/2}}$	200	20	100 cm

Table 2.2: Thermal properties of a bilayered surfaced used for comparison of Spencer's explicit algorithm with MultIHeaTS. Although some of these values are close to what could be found on realistic icy surfaces, they were varied smoothly over large scales for validation purposes.

Both algorithms were run with meticulous attention with the exact same thermal properties and numerical parameters that can be found in Table 2.1, along with

[3] https://www.boulder.swri.edu/~spencer/thermprojrs/

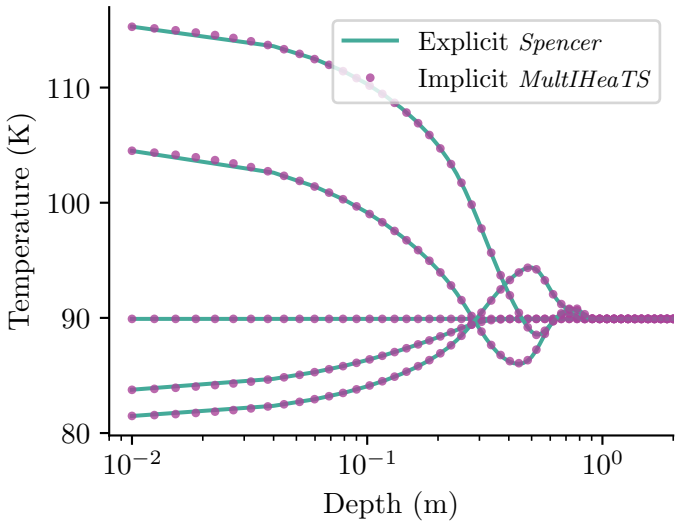

Figure 2.4: Validation of MultIHeaTS against Spencer's explicit algorithm. Temperature profiles for different times are plotted simultaneously $i = 0$, 200, 14050, 34959, 49000. MultIHeaTS is as accurate as Spencer's explicit solver with the advantage of stability. Note the uneven grid spacing of MultiHeaTS, denser at the surface, shown by the logarithmic horizontal axis.

identical solar flux at the surface given by Equation 2.3, and a zero bottom heat flux.

The computation presented here were computed on an irregular grid given by the relation of recurrence:

$$\forall n \in \{0, \ldots, n_x - 1\},\ x_n = \left(\frac{n}{n_x - 1}\right)^{p_{\text{ow}}} L \tag{2.23}$$

where the exponent $p_{\text{ow}} = 4$ and L is the bottom layer's depth. The characteristic depth of penetration of oscillating temperature wave with period p, is given by the thermal skin depth $\delta = \sqrt{\alpha p/\pi}$ (see demonstration in Section 2.7.1). Such grid was chosen to increase spatial step with depth according to a power law, reflecting the exponential decrease in temperature variations and reduced spatial precision needed after the diurnal skin depth δ_{d}. For the sake of validation, values of density, heat capacity and conductivity are varied through the depth by the largest scales allowed by Spencer's explicit scheme stability criteria (see Table 2.2).

Overall, the results, presented in Figure 2.4, show a very good similarity between the temperature profiles produced by the explicit and fully implicit schemes, with negligible differences between the two methods. The maximum error between MultIHeaTS and the Spencer's solver is $e_+ = 0.68\%$ and the mean error is $\overline{e} = 0.052\%$. This comparison demonstrates that the MultIHeaTS solver can accurately compute temperature profiles for planetary surfaces, without the limitations of conditional

stability that can be encountered with explicit methods.

2.3.2.2 Computational Efficiency of Implicit Solvers

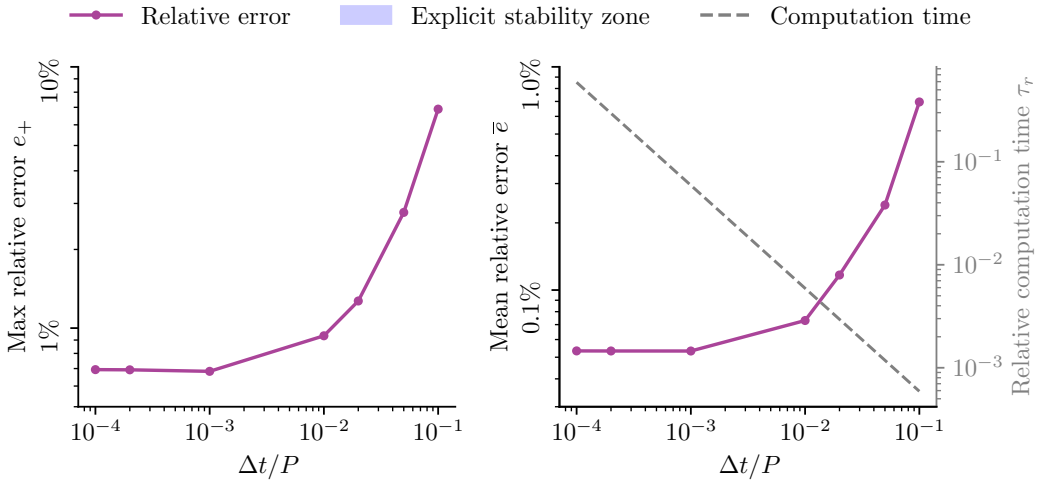

Figure 2.5: Relative errors produced by the fully implicit scheme when increasing the timestep Δt (log-scales). The reference is Spencer's explicit thermal model computed with 10^4 points per day. Timestep Δt is represented as a fraction of the surface flux' period P. The stability zone of the explicit scheme $F < 1/2$ is represented in light blue. (*Left*) Maximum error e_+. (*Right*) Average error $\overline{e}$ and relative computation time τ_r. The computational advantage of the fully implicit solver enables much faster temperature calculations.

While both the explicit and fully implicit schemes can compute the same temperature, in this section we focus on comparing the computational speed of these solvers. On a 6 cores Intel i7-10750H CPU at 3.6 GHz, using the parameters shown in Tables 2.1 and 2.2, Spencer's thermal model is capable of performing 27,000 iterations per second. In contrast, MultIHeaTS on the same hardware can achieve up to 47,000 iterations in the same time, resulting already in a 60% faster computation. However, the primary advantage of using an unconditionally stable solver lies in its ability to remove restrictions on the parameter space. Unlike the Spencer's explicit model, which is limited by the stability criteria defined in Equation 2.46, MultIHeaTS can handle arbitrarily large timesteps.

To demonstrate this, Figure 2.5 depicts the temperature difference between our fully implicit scheme and the Spencer scheme as a function of the timestep. We observe that as the timestep increases, the differences gradually increase as well. Nonetheless, even with a timestep 100 times larger than the reference ($\Delta t/P \sim 10^{-2}$), the maximum relative error e_+ remains below 1% and the mean relative error $\overline{e}$ remains below 0.1%. This indicates that we can compute the same temperature with

significantly larger timesteps while maintaining a reasonably low error. It is important to note that comparing the Crank-Nicolson scheme, a second-order method in time, to the first-order Spencer scheme would not yield meaningful results. However, due to its second-order precision, the semi-implicit scheme will show higher accuracy in terms of mean error compared to the other two schemes when compared to the ground truth temperature.

We conducted a comparison of the computational speed required by both solvers to calculate the final temperature after a given time $t_\mathrm{f} = 5P$. To quantify this, we introduced the relative computational time τ_r, defined as:

$$\tau_r = \frac{\tau_\mathrm{implicit}}{\tau_\mathrm{spencer}} \tag{2.24}$$

where τ_spencer represents the computational time required for the reference Spencer model to compute the final temperature, while τ_implicit represents the time taken by MultIHeaTS to compute the same final temperature.

Figure 2.5 (Right) illustrates the computational advantage of the implicit schemes. By requiring fewer iterations, the total computational time of the fully implicit solver τ_implicit is significantly smaller than that of the explicit scheme τ_spencer. Consequently, our MultIHeaTS solver can compute the same temperature for a given time up to 100 times faster than the explicit method while staying accurate. This is particularly advantageous for simulating processes on large timescales. For instance, if we aim to determine the temperature after one million years to study the thermal evolution of the icy crust of a Galilean moon, a computation that would take a year on the explicit solver could be reduced to less than 4 days using MultIHeaTS.

2.4 Applications

2.4.1 Bilayer Thermal Signature for Remote Sensing

Surface temperature variations are crucial measurements obtained by space probes for inferring the thermal properties of planetary surfaces, using measurement of brightness temperature in infrared wavelength such as THEMIS on Mars (Christensen, Jakosky, et al., 2004) or CIRS for the Saturn system (Jennings et al., 2017). The same principle also applies on radar frequencies, such as Cassini RADAR passive-mode for the Saturn System (Elachi et al., 2004). Therefore, accurately simulating the temperature evolution of complex profiles becomes essential for comparing with measurements and extracting valuable properties through inverse problems. Here, we applied our thermal model to Europa's surface at latitude and longitude (0°, 180°) to investigate the differences in surface temperatures without eclipses and explore the thermal signatures associated with four distinct profiles of thermal properties.

First, we assume two types of homogeneous icy surfaces. The first one, called material "H" (for high thermal inertia), is a porous but bulkier water ice a heat

capacity of $c_\mathrm{p} = 839\,\mathrm{J\,kg^{-1}\,K^{-1}}$ (Klinger, 1981), and a thermal inertia of $\Gamma_\mathrm{H} = 196\,\mathrm{SI}$. This "H" material has significantly lower thermal inertia than bulk ice at these temperatures (Klinger, 1981), yet it is termed "high" because its values exceed those derived from brightness temperature measurements on Europa (Rathbun et al., 2010; Trumbo et al., 2018). The second one, called material "L" (for low thermal inertia), is a icy regolith similar to the highly porous lunar type regolith. This leads to modified values for density $\rho = \rho_0(1-\phi)$ and heat conductivity $k = k_0(1-\phi)$. In the case of the small grain deposit, the material L can have very high porosity. We chose a porosity of $\phi \sim 85\,\%$, resulting in low thermal inertia of $\Gamma_\mathrm{L} = 28\,\mathrm{SI}$.

The third test case is a bilayered profile made of material L over H, called $\mathrm{bilayer_{LH}}$ which can represent a layer of small grains deposited from a plume on top of a bulk icy surface. The fourth case is a bilayered profile of material H over L, called $\mathrm{bilayer_{HL}}$ which can represent cryolava deposited over a highly porous icy regolith-type, it leads to a situation where a material of high thermal inertia H can overlay a material of low thermal inertia L.

The main question is whether it is possible to distinguish these four situations from spaceborne measurement that can only access surface temperature. If such a distinction is achievable, what recommendations should be considered for mission planning to effectively distinguish these situations?

Parameters	Value
Interface HL d_HL	5.00 cm
Interface LH d_LH	1.00 cm
Diurnal skin depth of H δ_dH	7.97 cm
Diurnal skin depth of L δ_dL	1.13 cm
Low thermal inertia Γ_L	27.8 SI
High thermal inertia Γ_H	196 SI
Emissivity ϵ	0.94
Bond albedo A	0.6
Grid points n_x	100
Max depth L	6 m
Initial temperature T	105 K
Number of Europa days	5
Number of iterations n_t	300
Time step Δt	5000 s

Table 2.3: Physics and numerical parameters used for the thermal signature application, based on the Europa case. The diurnal period is $p_\mathrm{E} = 3.55\,\mathrm{days}$ and the SI unit of thermal inertia is $\mathrm{J\,m^{-2}\,K^{-1}\,s^{-1/2}}$

To answer this question, we compare different types of profiles made of the aforementioned materials. Importantly, the interface depth of both bilayer profiles was

deliberately selected to be thinner than the thermal diurnal skin depth δ_d (see Table 2.3). This choice is crucial because when the interface is significantly deeper than the skin depth, then the surface temperatures are predominantly influenced by the upper layer and indistinguishable from the case of constant properties. Depending on the interface depth, between 20 to 30 grid points are used to describe the top layer.

To obtain accurate simulations, we incorporate solar flux data from NASA's SPICE Toolkit (C. H. Acton, 1996; C. Acton et al., 2018) arbitrarily chosen at UTC 23 August 1997, which provides precise information on the distance to the sun and solar incidence at the specific point on Europa's surface. These parameters are integrated instead of the simplified solar flux from Equation 2.3, allowing us to run realistic simulations over a span of 5 Europa days.

A similar study conducted by N Putzig, 2007 on Mars using THEMIS presented results in terms of apparent thermal inertia instead of surface temperature. They varied the upper layer thickness within the range of $\delta_d/512$ to δ_d, where δ_d represents the skin depth for Mars' dust (approximately 21 cm).

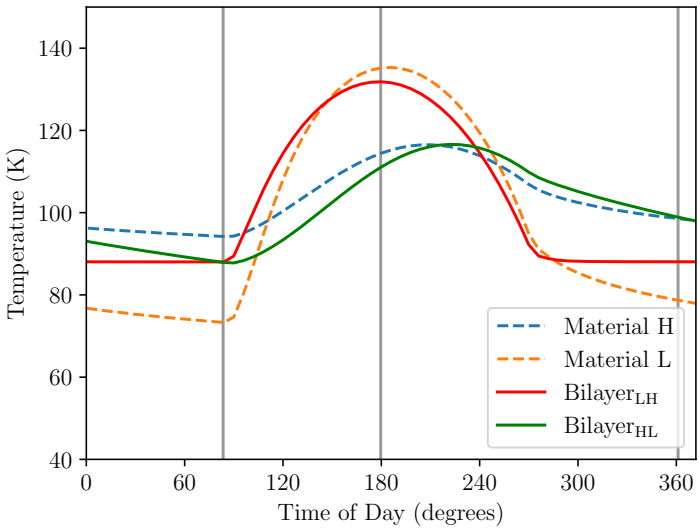

Figure 2.6: Daily surface temperatures on Europa for four different ground profiles at Lat/Long (0, 180). Dashed lines show monolayered profiles and solid lines show bilayered profiles. No homogeneous ground profile could match the thermal signature of bilayered ones. The grey vertical lines indicate the recommended measurement time for a space probe to discern between a homogeneous surface and a bilayered one.

The results in Figure 2.6 show the expected behavior in the case of homogeneous thermal inertia. In the case of low thermal inertia (L), the peak with highest temperature is close to local noon (Time of Day 180°), the maximum surface temperature is close to the equilibrium temperature and night time temperature are relatively

cold and cooling significantly during the night. On the contrary, for high thermal inertia (H), the peak with highest temperature is shifted toward the afternoon, the maximum surface temperature is lower and night time temperatures are warmer (N Putzig, 2007). The results shown in Figure 2.6 also reveal the particular trends of bilayered profiles. In the particular case of an interface close to the thermal diurnal skin depth, the expected trends are mixed. The bilayer$_{\mathrm{LH}}$ has a high centered day-side temperature bell shape and almost constant night temperatures, consistent with the observations from bilayer thermal models by Squyres (1980). In contrast, the bilayer$_{\mathrm{HL}}$ has a shifted day-side temperature peak and strong cooling at the end of the night. Over the range of inertia bounded by Γ_{L} and Γ_{H}, no homogeneous ground profile could match the thermal signature of bilayered ones. We thus recommend to observe the same surface at three strategic local times as shown by the grey vertical lines in Figure 2.6. Measuring the surface at the morning sunrise, at noon and at midnight, would help a distinguish a bilayered surface with an interface close to the diurnal skin depth to a homogeneous surface.

This strategy would be interesting for the preparation of the upcoming missions, such as JUICE (Grasset et al., 2013) and Europa Clipper (Phillips et al., 2014). Solvers like MultIHeaTS, that can accommodate any observations set (whatever their observation time) with depth-dependant properties, will be highly valuable in enhancing our understanding of Europa's surface profiles. Whether the surface exhibits, for example, homogeneous porosity of ice grains or a depth-dependent variation, distinct brightness temperature patterns would be observed and measured. In addition to the surface temperature profiles, radiometer or sub-millimeter instruments can probe brightness temperature at different wavelengths to distinguish materials at various depths. By comparing the solver's output with actual measurements, valuable information regarding the surface properties can be retrieved.

2.4.2 Million Year Simulation of Europa

2.4.2.1 Orbit and Solar flux

To apply the model to Europa over a million-year timescale, we must account for variations in solar flux during this period. During periods of day, for a given time, latitude λ and longitude ψ, the solar flux is given by J. Spencer et al. (1989):

$$F_{\mathrm{solar}}(t,\lambda,\psi) = (1 - A(\lambda,\psi))\,\frac{G_{\mathrm{SC}}}{d(t)^2}\cos(\theta_i(t,\lambda,\psi)) \tag{2.25}$$

where A is the surface bond albedo, G_{SC} the solar constant, θ_i the solar incidence angle and d the distance to the Sun in AU (see Figure 2.7).

Distance to the Sun and orbital parameters — To determine the distance to the Sun, we initially need to obtain Europa's position in its orbit around Jupiter, which gradually varies over a million year. Given the negligible difference in distance

between Europa and its planet, compared to Jupiter's distance from the Sun, we can directly calculate the flux received by Jupiter, which deviates by less than 0.02% from that received by Europa.

Describing a body's motion around the Sun can be done using its orbital elements, such as the semi-major axis a, eccentricity e, perihelion longitude ω, inclination I, ascending node longitude Ω, and mean longitude Ψ. For a period of million years, some orbital elements remain relatively constant. For instance, the semi-major axis remains stable at $a = 5.204\,\text{AU}$ in the secular regime (Laskar, 2008). Similarly, due to the near-flat inclination of Europa's orbit to Jupiter's equator plane and low Europa's obliquity (Bills et al., 2009), we fix theses values to 0. In reality, the sub-solar latitude on Europa varies by $\pm 3.7°$ (Ashkenazy, 2019), which would need to be considered for high-latitude computations but is beyond the scope of this paper. Moreover, as the perihelion longitude ω and ascending node longitude Ω do not influence solar flux, we assigned them arbitrarily, to their values at J2000, using VSOP2013 (Simon et al., 2013).

However, the eccentricity parameter can fluctuate over a million-year timescale, leading to changes in solar flux which necessitates consideration (Laskar, 2008). For short simulations, precise estimates of the eccentricity could be obtained using SPICE kernels, but these are only available for Europa for up to a thousand years, not a million. In order to obtain the periodicity of eccentricity, we used the studies from Jacques Laskar, 2003; Laskar, 2008, which conducted frequency analysis of Jupiter's motion over 50 My. Their results show that the quasiperiodic approximation of eccentricity can be expressed as the sum of five harmonics:

$$e = e_0 + \sum_{i=1}^{5} e_i \cos\left(\nu_i t + \vartheta_i\right) \tag{2.26}$$

where the values of e_i, ν_i an ϑ_i are found in Table 7 of Laskar, 2008. These five harmonics have periods spanning from 27,000 years to 1.1 million years, with eccentricity values fluctuating over the course of our simulation from $e = 0.027$ to $e = 0.061$. At maximum eccentricity ($e = 0.061$), Jupiter's heliocentric distance ranges from 4.88 to 5.52 AU within an orbit, while at minimum eccentricity ($e = 0.027$), it varies between 5.04 to 5.35 AU. Based on Equation 4.27, this leads, for example, to a variation of the maximum solar flux at the equator of up to $\sim 7\%$ at the same solar longitude.

Finally, the mean longitude changes periodically over one orbit, and is updated over time using the equation:

$$\Psi(t) \equiv \Psi(t_J) + \frac{2\pi}{p_\text{J}}(t - t_J) \pmod{2\pi} \tag{2.27}$$

where p_J is the orbital period of Jupiter and t_J is the reference time at J2000.

At each iteration, the six orbital elements are computed and passed to the ELLXYZ subroutine from VSOP2013 (Simon et al., 2013), which calculates the

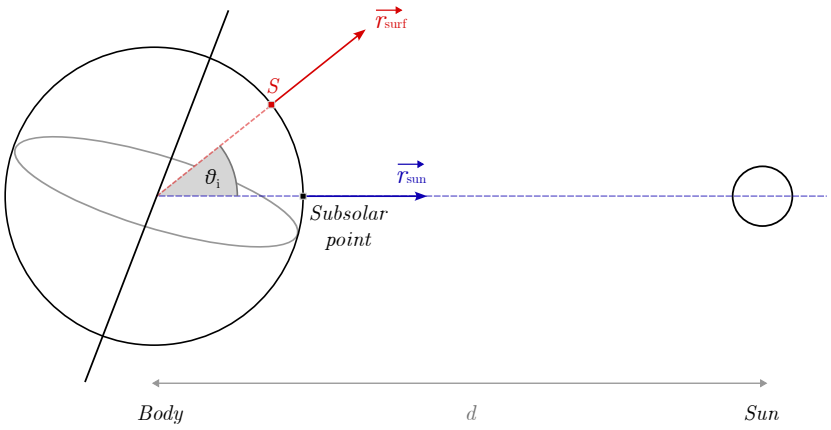

Figure 2.7: Schematic representation of the target body and Sun system. The solar incidence angle θ_i is defined as the angle between the normal vector at the target surface of the body r_{surf} and the normal vector at the sub-solar point r_{sun}.

planetary rectangular coordinates. Then, these coordinates are used to determine the distance from Europa to the Sun for each iteration, which is essential for computing the solar flux.

Solar Incidence — Now to compute the solar incidence of a particular point on Europa's surface at a given latitude λ and longitude ψ, we express the surface normal and the sub-solar point surface normal unit vector as:

$$\vec{r}_{\text{surf}} = \begin{pmatrix} \cos(\lambda)\cos(\psi) \\ \cos(\lambda)\sin(\psi) \\ \sin(\lambda) \end{pmatrix}, \quad \vec{r}_{\text{sun}} = \begin{pmatrix} \cos(\psi_{\text{sub}}) \\ \sin(\psi_{\text{sub}}) \\ 0 \end{pmatrix} \tag{2.28}$$

with the sub-solar point longitude being updated as

$$\psi_{\text{sub}}(t) \equiv \psi_{\text{sub}}(0) + \frac{2\pi}{p_{\text{E}}} t \pmod{2\pi} \tag{2.29}$$

where p_{E} is the orbital period of Europa and we arbitrarily take $\psi_{\text{sub}}(0) = 0$. In absence of other information, we assumed that the rotation period of Europa remains constant. The solar incidence angle θ_i is then given by the scalar product between the surface's normal and the sub-solar point normal:

$$\theta_i = \arccos\left(\vec{r}_{\text{sun}} \cdot \vec{r}_{\text{surf}}\right) \tag{2.30}$$

Then for periods of day, when θ_i in $\left[-\frac{\pi}{2}, \frac{\pi}{2}\right]$, the solar flux is computed using Equation 4.27 and for periods of night, when θ_i in $\left]\frac{\pi}{2}, \frac{3\pi}{2}\right[$, the solar flux is zero $F_{\text{solar}} = 0$. At each iteration of the model, the solar flux is computed for current time and injected at the top boundary condition of the thermal solver to compute the heat transfer.

2.4.2.2 Thermal Properties

Europa surface and subsurface is made mainly of water ice (Cruz-Mermy et al., 2023). There are number of evidence showing that its icy surface is porous. For instance using spaceborne thermal infrared instrument, the thermal inertia is in the range $\Gamma = 40 - 150\,\mathrm{W\,m^{-2}\,K^{-1}\,s^{-1/2}}$ (J. R. Spencer et al., 1999; Rathbun et al., 2010). Using Earth-based observations, another team obtained a thermal inertia of $\Gamma = 95\,\mathrm{W\,m^{-2}\,K^{-1}\,s^{-1/2}}$ (Trumbo et al., 2018). Theses values are order of magnitude inferior to the thermal inertia of solid ice at these range of temperature $\Gamma_{\mathrm{ice}} \approx 2600\,\mathrm{W\,m^{-2}\,K^{-1}\,s^{-1/2}}$ (Klinger, 1981). Such difference can be explained by adding porosity into the ice, significantly lowering its thermal inertia (J. R. Spencer et al., 1999). The thermal inertia depends on thermal parameters according to the expression $\Gamma = \sqrt{k\rho c_p}$. Although porosity doesn't directly influence the specific heat capacity, it does alter ice density and conductivity.

Ice Density and Porosity — To obtain the porous ice density, we must evaluate if the porosity can vary due to compaction at the depths affected by temperature variations caused by the periodic oscillations of solar flux input at the surface. Various compaction mechanisms can intervene (e.g., sputtering or sintering induced); however, we focus solely on gravity-induced compaction for this analysis. Following, Mergny et al., 2024a (see Chapter 3), the expression for density as a function of depth is

$$\rho(x) = \rho_0 \left(1 + \frac{\phi(0)}{1-\phi(0)} \exp\left(-\frac{x}{H}\right)\right)^{-1} \tag{2.31}$$

where ρ_0 is the bulk ice density, $\phi(0)$ the surface porosity and H the characteristic lengthscale of compaction.

The diurnal and seasonal thermal skin depths on Europa are much shallower than the gravity-driven compaction length scale H, which is on the order of hundreds of meters (Mergny et al., 2024a). However eccentricity variations happen on large timescales (Equation 2.26) and are highly dominated by a $\sim 54\,\mathrm{kyrs}$ period harmonic, which lead to a "geological" thermal skin depth of up to 130 m. Our simulations are computed up to depth $L = 50\,\mathrm{m}$, which results in small variations, up to 1 K, of the bottom temperature within geological timescales. Extending to depths of hundreds of meters would 1) increase the computation cost 2) increase complexity due to density being affected by gravity at these depths. While feasible, these computations are beyond our focus ; MultiHeaTS is part of a multiphysics model, LunaIcy, simulating near-surface interactions on the ice microstructure (Mergny et al., 2024b), with processes like ice grain sintering only having noticeable effect within the first few meters. Other compaction processes, such as those induced by micrometeorite impacts will influence the density of the near surface, but these are not considered in this study and remain to be explored in future work. Therefore, at the depths relevant to our thermal analysis, $x \ll H$, the porosity is assumed to remain constant,

resulting in the simplified expression for the density of porous ice

$$\rho(\phi) = \rho_0(1 - \phi). \tag{2.32}$$

Porous Ice Conductivity — Number of studies have work on formulating the conductivity of compacted spheres. One common approach describes thermal conductivity as a function of the porosity ϕ as $k(\phi) = k_b(1 - \phi)$ (Ferrari, Galdemard, et al., 2005). However, to reach the low thermal inertia of Europa reported in the literature (J. R. Spencer et al., 1999), such approach would require a porosity of $\phi = 0.99$, which seems unlikely. One important aspect that this first formulation does not take into account is the quality of contact between grains. Considering that ice conducts heat much better than radiation in the pores, accounting for the contact area between grains becomes crucial in porous materials. The pores are at near-vacuum so heat transfer across pores is likely predominantly by radiation. This concept was explored in an early study by Adams et al., 1993, where they developed a physical model for snow conductivity of packed spheres, distinguishing between ice conduction, conduction in the pore space, and vapor transport. Subsequent papers, such as the SNOWPACK model for avalanche warning (Lehning et al., 2002), adopted the same formulation with refinements. Models like Gusarov et al. (2003) have also addressed the conductivity of packed spheres, particularly in cases where there is a limited contact region between grains. Some difficulties arise from these formulations as they rely on the coordination number, which is often calculated through empirical means based on snow data on Earth. For these reasons, these models are appropriate for highly porous material with small regions of contact, but for low porosity, they lead to porous conductivity higher than the bulk ice conductivity which is not realistic.

Another method, is to use the Hertzian theory to determine the efficiency of heat exchanged between grains (Gundlach et al., 2012). This effect is taken into account by the introduction of the so-called Hertz factor, which accounts for the reduction in effective cross-section area of the porous material due to its porosity. While numerous studies have explore in details how to express the Hertz factor as a function of the temperature and grain size, here we adopt the definition of the Hertz factor as the ratio between the radius of contact r_b and the grain radius r_g. When two grains come into contact, they deform elastically and the initial radius of contact depends on the forces applied on the grains. For ice grains, the adhesion stage occurs due to the Van der Waals interaction between particles, leading to the expression of the bond radius (Molaro et al., 2019):

$$r_\mathrm{b} \approx \left(\frac{\gamma r_\mathrm{g}^2}{10\mu}\right)^{1/3} \tag{2.33}$$

where γ is surface tension of water ice and μ its shear modulus.

Following Ferrari and Lucas, 2016, the expression of the porous conductivity can then be generalized to

$$k(\phi, r_\mathrm{b}, r_\mathrm{g}, T) = k_0(T) S(\phi) \mathcal{H}(r_\mathrm{b}, r_\mathrm{g}) \tag{2.34}$$

where k_0 is the conductivity of bulk ice for a given temperature, $\mathcal{H}$ is the Hertz factor and $S(\phi)$ is a factor accounting for the reduction of conductivity due to porosity with multiple formulations existing in the literature (Shoshany et al., 2002; Gusarov et al., 2003; Gundlach et al., 2012; Ferrari and Lucas, 2016). In this study, to avoid empirical expressions, we favor a straightforward analytical form $S(\phi) = 1 - \phi$ which lead to the expression of the porous conductivity

$$k(\phi, r_\mathrm{b}, r_\mathrm{g}) = k_0(T) \, (1 - \phi) \, \frac{r_\mathrm{b}}{r_\mathrm{g}}. \tag{2.35}$$

where the bulk ice conductivity for a given temperature is computed using the expression $k_0 = 567/T$ (Klinger, 1981). Updating the temperature-dependent conductivity requires to recalculate the tridiagonal matrix terms of Equation 2.9, which is computationally expensive. A performance test conducted for a grid of 100 points, reveals that this results in a slowdown of computation by a factor 2. Therefore, for the current study we maintain a constant bulk ice conductivity based on the surface equilibrium temperature. While temperature variations on Europa do not have a significant impact on conductivity compared to porosity and grain contact changes, it can be valuable to include it in future work when the temperature is highly varying. Also, while the radius of contact r_b and porosity ϕ are treated as free parameters, they inherently influence each other. As the radius of contact approaches the grain radius, the pore space decreases, leading to a reduction in porosity towards zero.

For this simulation, we used the following parameters: porosity of $\phi = 0.4$, grain size of $r_\mathrm{g} = 100\,\mu\mathrm{m}$, and a temperature of $100\,\mathrm{K}$. Equation (4.1) yields a contact area of $r_\mathrm{b} = 0.39\,\mu\mathrm{m}$ and Equation (4.29) results in a conductivity of $k = 0.013\,\mathrm{W\,m^{-1}\,K^{-1}}$ for the porous medium.

2.4.2.3 Anti-Jovian Hemisphere

Using the MultIHeaTS thermal solver combined with our solar flux model and thermal properties, we can simulate heat transfer on Europa's icy surface for a million year in about four days of computation time. With this numerical approach, we have flexibility with the parameters used in the simulation, such as albedo, surface porosity, latitude, and longitude.

In this section we present the result of a simulation on the anti-Jovian hemisphere with latitude 0°, longitude 180° and a porosity of $\phi = 0.4$. This leads to a thermal inertia of $\Gamma = 83\,\mathrm{W\,m^{-2}\,K^{-1}\,s^{-1/2}}$, coherent with the observations (J. Spencer et al., 1989; Trumbo et al., 2018), without needing excessive value of the porosity. Here, the grid spacing is given by Equation 2.23 with the exponent $p_\mathrm{ow} = 5$ and maximum depth $L = 50\,\mathrm{m}$. This simulation was specifically computed for high albedo, here

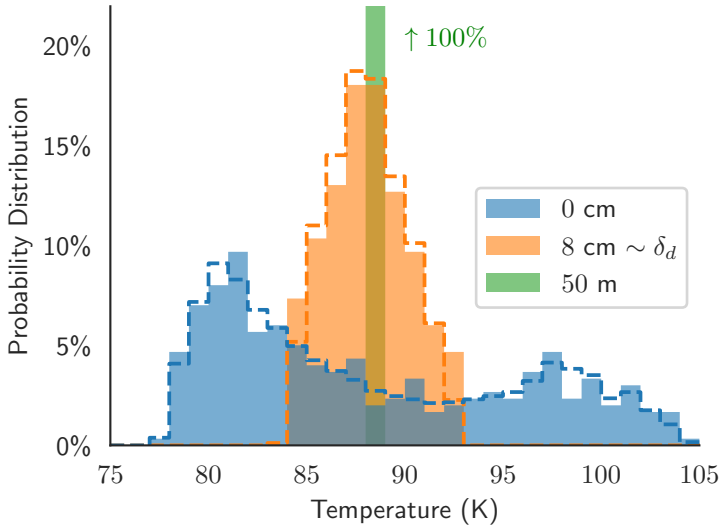

Figure 2.8: Temperature distribution on Europa at Lat/Long $(0°, 180°)$ with albedo $A = 0.8$ for three strategic depths: at the top layer, close to the diurnal thermal skin depth, and at the bottom layer. The histogram shows the frequency of each temperature at each depth. Filled bars represent the one million year simulation, and dotted lines represent a single Jupiter year.

$A = 0.8$ and $\epsilon = 0.9$, so that temperatures remain low enough (less than 105 K) such that ice sintering is negligible during the million year timeframe. The goal here is first to look at the temperature distribution without eclipses (see Fig. 2.8), in a condition where the ice microstructure remains constant. The joint paper (Mergny et al., 2024b) expand upon this with low albedo simulations, by coupling the MultIHeaTS thermal solver to an ice sintering model that also changes the thermal properties.

The temperature distribution after one million year are plotted in Figure (2.8, *filled bars*) for three strategic depths: at the top layer, close to the diurnal thermal skin depth and at the bottom layer. Long integration time is require to converge towards a stable regime at depth. We have found that, after 20 orbits, the temperature at depth remains constant to seasonal variations, thus we exclude the initial $\sim$ 250 years from the temperature distribution. Given the extensive computational load of simulating one million years, storing each of the three billion iterations is impractical due to size constraints. To address this, we opted for periodic saving of the temperature profile at asynchronous intervals, specifically at $p_{\mathrm{save}} = 10.1 \times p_{\mathrm{J}}$, ensuring that we capture all diurnal and orbital variations. Figure 2.8 illustrates the attenuation of the heat wave, noticeable around depths corresponding to the diurnal thermal skin depth, $\delta_{\mathrm{d}} = 5.6\,\mathrm{cm}$. While the bottom layer has a constant temperature, temperature variations are significantly higher near the surface. We observe an asymmetric temperature distribution for the top surface, with night-time temperatures predominantly colder than the equilibrium temperature (89 K). Some

of the surface temperatures exceed the equilibrium by more than 15 K, which are crucial for temperature-dependent processes such as sintering, as investigated in the joint paper (Mergny et al., 2024b).

Such distribution differs from one that would be acquired through a single orbit of Jupiter (Figure 2.8, *dotted lines*), due to the periodic changes of the orbital elements throughout a million year. While the temperature histograms have similar trends, some noticeable differences emerge, especially at high temperature ($\sim 100\,\mathrm{K}$) which is relevant for precise estimation of temperature dependent processes. The one million year temperature distribution can also be beneficial for one-way coupling models. For instance, if a certain temperature is reached with a probability $p(T)$ during a simulation lasting t_f, it could be analog to a model maintaining a constant temperature T during a time $t = p(T) \times t_\mathrm{f}$.

2.4.2.4 Sub-Jovian Hemisphere

In contrast to the anti-Jovian hemisphere, the sub-jovian hemisphere has multiple interactions with Jupiter that affects the diurnal flux reaching the surface.

Jupiter's Emitted and Reflected Flux — Jupiter emits longwave radiation that can affect Europa's surface temperature. Since Europa is tidally locked to Jupiter, the sub-Jovian hemisphere always absorbs this radiation. Based on the emission temperature and distance to Europa, Ashkenazy (2019) computed the radiation flux with a maximum at the equator of $0.056\,\mathrm{W\,m^{-2}}$, very close to Europa's estimated internal heating. This value is orders of magnitude smaller than the solar flux at Europa's heliocentric distance $\sim 50\,\mathrm{W\,m^{-2}}$, and thus, like internal heating, it will be neglected in this study.

In addition to emitting radiation, Jupiter also reflects some of the solar flux it receives back to Europa. The reflected flux from the sun by Jupiter, F_R, can be modeled as

$$F_\mathrm{R} = A_\mathrm{J} \left(\frac{R_\mathrm{J}}{d_\mathrm{E}} \right)^2 \frac{G_\mathrm{SC}}{d^2} \tag{2.36}$$

where $R_\mathrm{J} = 70\,000\,\mathrm{km}$ is Jupiter's radius, $A_\mathrm{J} = 0.34$ is Jupiter's Bond albedo, and $d_\mathrm{E} = 671\,000\,\mathrm{km}$ is the distance between Europa and Jupiter. This computation leads to a reflected flux value of $F_\mathrm{R} \approx 0.18\,\mathrm{W\,m^{-2}}$, which is still two orders of magnitude lower than the solar flux at Europa's heliocentric distance. However, since this flux can reach the surface during nighttime and is about three times higher than the longwave radiation, it is not clear if it leads to significant temperature variations during the night. Using Equation 4.26 at equilibrium and substituting the solar flux with F_R, we find an equilibrium temperature of 36 K, which is still much colder than Europa's nighttime temperatures (see Figure 2.8 for reference). For context, in terms of the time of day, this flux is equivalent to the solar flux at the equator 0.23° before sunset and near the poles ($\lambda = 80°$), 1.40° before sunset. While the reflected flux is higher than the emitted longwave radiation, its influence is still much lower than

flux directly coming from the sun. Incorporating it into the model adds complexity without significantly improving the accuracy of the temperature estimates, hence it will be ignored in this study.

Eclipses — While Ashkenazy (2019) estimated that eclipses on Europa result in a general temperature decrease of only 0.3 K, we believe that some simplifications used there lead to an underestimation of the eclipse effects. Specifically, the model smooths the impact of eclipses over the entire diurnal period, resulting only in a slightly lower average solar flux (see Equation 30 of his article). In addition, this previous approach does not account for the fact that in some regions, eclipses occur during peak solar flux periods, causing brief but significant temperature drops. In this study, we investigate the effects of these eclipses through numerical simulations to more accurately consider their potential impact.

We have explored the effect of eclipses on Europa by integrating them into the input flux as a step function for a duration of about 2.8 hours (see Ashkenazy (2019), parameter "p"). The timing of the eclipse is determined by the current longitude, for instance the middle of the eclipse is occurring at noon for longitude 0°. Here, we only account for the umbra effect and consider that the flux is zero during the eclipse, ignoring the penumbra, due to the considerable distance between Jupiter and the Sun, and Europa's proximity to Jupiter (Ashkenazy, 2019). To estimate the maximum effect of eclipses we have chosen the potential warmest scenario on Europa, where we have the same thermal properties as previously but the albedo is now $A = 0.4$ and we look at the equator where the solar flux is at his highest.

Taking into account Europa's eclipses, that are short phenomena, requires a very precise timestep. Discontinuity in the input solar flux can lead to brief errors in the surface temperature, that will be dissipated better with a higher number of timesteps and improved boundary condition using Equation 2.16. While more advanced formulations of the upper boundary condition can be more robust to discontinuity (Schorghofer, 2022), for reasons of simplicity here, we choose a high number of $n_t = 200$ timesteps per day to prevent appearance of errors. Due to this higher resolution, we computed the eclipse histograms over a period of only 1000 years to keep computation time reasonable.

In Figure (2.9 *Left*, *green histogram*), we have plotted the distribution of the surface temperatures for a surface at latitude 0° and longitude 0°, over 1000 years (excluding the initial convergence). Naturally, with reduced solar flux, there is a noticeable temperature decrease, up to 5 K, compared to the anti-Jovian hemisphere unaffected by eclipses (see Figure 2.9 *Left*, *purple histogram*). On the leading sub-jovian hemisphere, eclipses occur during the morning, stopping the surface heating and thereby reducing the maximum daily temperature. The general shape of the distribution (not represented here) is similar to the non-eclipse histogram (Figure 2.9 *Left*, *purple histogram*), but shifted towards lower temperatures. On the trailing sub-jovian hemisphere, eclipses occur during the afternoon, after the peak daily solar

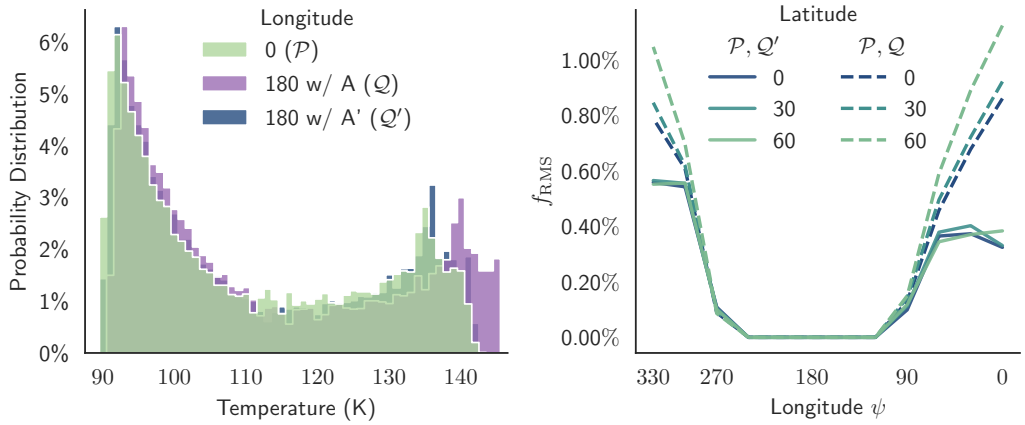

Figure 2.9: (*Left*) Surface temperature distributions at Europa's equator for three different scenarios: $\mathcal{P}$ at longitude 0° (sub-Jovian, with eclipse) and $\mathcal{Q}$ at longitude 180° (anti-Jovian without eclipse) both with albedo $A = 0.4$, and $\mathcal{Q}'$ at longitude 180° with equivalent albedo $A' = 0.453$. (*Right*) RMS distance between eclipse temperature distributions $\mathcal{P}$ and non-eclipse distributions with unchanged albedo $\mathcal{Q}$ or with equivalent albedo $\mathcal{Q}'$ as a function of longitude and latitude. Using an equivalent albedo allows to approximate, at first order, the surface temperature distribution of the sub-Jovian hemisphere without having to compute eclipses.

flux. The surface has been heated enough to reach the anti-Jovian maximum temperature but only for a short duration. These histograms (not represented here) are characterized by a smaller second peak at mid temperatures, that is the temperature at which the surface drops during the eclipse.

Equivalent Albedo — To run simulations on the million year timescale within a reasonable computation time, we propose to introduce an equivalent albedo that approximates the effect of eclipses on surface temperature distributions. First, we consider a surface at longitude 180° with albedo A and temperature at depth $T_\infty = T_{n_x-1}$, that is on the anti-Jovian hemisphere, not experiencing any eclipses. Following J. Spencer et al. (1989), the temperature at depth is proportional to the sub-solar temperature T_{SS}:

$$T_\infty = g(\Theta) T_{\mathrm{SS}}(A) \tag{2.37}$$

where g is the function given by the "T_{DEEP}" curve on Figure 2 of J. Spencer et al. (1989) and Θ is the thermal parameter defined by:

$$\Theta = \frac{\Gamma\sqrt{2\pi/p_{\mathrm{E}}}}{(\epsilon\sigma)^{1/4}} \left(\frac{d^2}{(1-A)G_{\mathrm{SC}}}\right)^{3/4} \tag{2.38}$$

where for Europa's thermal inertia and albedo range, $\Theta > 1$, classifying it as a fast rotator. In contrast, a surface on the sub-Jovian hemisphere is subject to eclipses, so

it receives less solar energy, resulting in a colder temperature at depth $T'_\infty < T_\infty$. To address this, we propose approximating such surface by an equivalent surface that does not experience eclipses ($\psi = 180°$) but has a modified albedo $A' > A$ such that the temperature at depth matches T'_∞. Using Equation 2.37 and developing the expression of the sub-solar temperature (J. Spencer et al., 1989), this leads to the expression of the temperature at depth:

$$T'_\infty = g(\Theta') \left((1 - A') \frac{G_{\mathrm{SC}}}{\epsilon \sigma d^2} \right)^{1/4}. \tag{2.39}$$

Although Θ is a function of A, in the case $\Theta > 1$, the variations of $g(\Theta(A))$ with A are small enough to be considered constant at first order, so $g(\Theta') = g(\Theta)$. Using the ratio of Equation 2.39 for the two presented cases, leads to an expression of the equivalent albedo:

$$A' = 1 - (1 - A) \left(\frac{T'_\infty}{T_\infty} \right)^4 \tag{2.40}$$

which can be computed knowing the original albedo A, the reference ($\psi = 180°$) temperature at depth T_∞ and the temperature at depth T'_∞ of the surface subjected to an eclipse

Using our numerical model, a parameter exploration was run on the longitudes ranging from 0° to 360° with a step of 30°, and latitudes 0°, 30°, 60° (due to symmetry), for an albedo of $A = 0.4$. This allows us to obtain the temperatures at depth $T'_\infty(\lambda, \psi)$, notably for each of the sub-Jovian longitudes. Using Equation 2.40, we obtain an equivalent albedo, $A' = 0.433$ for longitudes 60° and 300°, $A' = 0.449$ for longitudes 30° and 330° and $A' = 0.453$ at longitude 0°. No noticeable changes is observed with latitude. The borders of the sub-Jovian hemisphere (longitudes 90° and 270°) only experience half the duration of an eclipse respectively at the very beginning and end of the day, leading to an almost identical temperature distribution than on the anti-Jovian hemisphere.

As shown by Figure 2.9, at first order, the temperature distribution $\mathcal{P}$ in the sub-Jovian hemisphere (*green histogram*) can be approached using an equivalent albedo A' at longitude 180° (*blue histogram*). The temperature distribution $\mathcal{Q}'$ using the equivalent albedo is considerably closer to reality than the distribution $\mathcal{Q}$ where albedo remains unchanged (*purple histogram*) . To quantify the approximation error, we introduce the root mean square (RMS) distance between the two distributions:

$$f_{\mathrm{RMS}}(\mathcal{P}, \mathcal{Q}) = \sqrt{\frac{1}{n_{\mathrm{B}}} \sum_{b \in \mathrm{B}} \left(\mathcal{P}(T_b) - \mathcal{Q}(T_b) \right)^2} \tag{2.41}$$

where B is the set of bins, n_{B} is the number of bins and T_b the temperature of bin b.

First, the RMS distance is computed between eclipse-inclusive simulations distributions $\mathcal{P}$ and non-eclipse simulations distributions $\mathcal{Q}$ with the same albedo A (2.9 *Right*, *dotted*). The mean RMS for the sub-Jovian leading hemisphere is 0.57%, for the sub-Jovian trailing hemisphere is 0.70%, and at longitude 0° is 0.86%. Then, the

RMS distance is computed between eclipse-inclusive simulations distributions $\mathcal{P}$ and the non-eclipse distributions using equivalent albedos $\mathcal{Q}'$ (2.9 *Right*, *lines*). In this case, the mean RMS for the sub-Jovian leading hemisphere is 0.37%, for the sub-Jovian trailing hemisphere is 0.51%, and at longitude 0° is 0.32%. Errors are higher on the sub-Jovian trailing hemisphere due to the second peak at mid-latitudes.

Overall, the results show that the RMS distance is consistently smaller for the equivalence approximation, particularly effective at approximating the eclipse scenario at longitude 0° where eclipses significantly reduce the solar flux. In this case, the errors are divided by a factor of more than 3. With this approximation, the errors are limited to 0.5% in the RMS distribution with 1K-wide bins, meaning that on average only 0.5% of the time spent on a particular temperature set (bounded by $\pm 0.5\,\mathrm{K}$) is incorrect. Such simplification allows to extrapolate the results of our simulations to the sub-Jovian hemisphere, with limited errors and without requiring the high resource costs associated with eclipse modeling. While this equivalence is not perfect, it allows to run longitude-independent simulations, which are highly useful for multiphysics coupling, as discussed in the joint publication (Mergny et al., 2024b).

2.5 Conclusion and Perspective

We have developed an efficient open-source fully implicit algorithm called MultIHeaTS, which uses finite differences to solve the heat equation on 1D heterogeneous media with an irregular grid. While our primary focus is planetary science, our algorithm is adaptable and can accommodate different types of boundary conditions and surfaces.

For homogeneous cases, the algorithm was validated using a known analytical solution. This validation which used a discontinuous initial condition showed the robustness of MultIHeaTS to stiff conditions, in contrary to the Crank-Nicolson method. For heterogeneous cases, MultIHeaTS was validated by comparison to a well established explicit algorithm in planetary science (J. Spencer et al., 1989). Our fully implicit scheme remained accurate and stable, producing results that closely matched Spencer's explicit model. Thanks to its advantageous stability, MultIHeaTS can compute the same temperature for a given time up to 100 times faster than Spencer's explicit method. This is particularly advantageous for simulating processes that occur on large timescales. Future research should conduct a detailed stability analysis to accurately quantify the limitations of the linearization of temperature-dependent properties and the Stefan-Boltzmann equation.

The capability of MultIHeaTS to simulate complex media were illustrated by computation of a bilayer surface. Based on our findings, we recommend an observation strategy: measuring the surface temperature at the morning sunrise, at noon and at midnight to characterize between bilayer and homogeneous surface profiles. A second application took advantage of the fast computation capability of MultI-

HeaTS by estimating the temperature profile of an anti-Jovian surface on Europa during one million year, which includes the diurnal variations and the variation of the orbital element of the Galilean moon. This enabled us to draw for the first time the temperature distribution with depth on such a large timescale. Finally, the effect of Jupiter's eclipses on the sub-Jovian hemisphere was explored, enabling us to propose an equivalence using a modified albedo with limited errors. MultIHeaTS has a wide range of potential applications and is notably at the core of our multi-physics simulations to study ice microstructure presented in the joint article (Mergny et al., 2024b). Thanks to its finite-difference formulation, the solver can be easily coupled with other processes, such as sintering, or phase change.

2.6 Article's Appendices

2.6.1 Dirichlet Boundary Conditions

The temperature is fixed at the boundaries which gives us at the top boundary $x = 0$:

$$\forall t, T(0,t) = T_0(t) \implies \begin{cases} b_0^i = 1 \\ c_0^i = 0 \\ s_0^i = T_0^i, \end{cases} \tag{2.42}$$

at at the bottom boundary $x = L$,

$$\forall t, T(L,t) = T_{nx-1}(t) \implies \begin{cases} a_{n_x-1}^i = 0 \\ b_{n_x-1}^i = 1 \\ s_{n_x-1}^i = T_{n_x-1}^i. \end{cases} \tag{2.43}$$

2.6.2 Stability and Accuracy of the Finite Difference Schemes in Standard Conditions

Before analyzing the behavior of finite difference schemes in heterogeneous media and non-linear boundary conditions, it is instructive to perform a stability analysis in simpler homogeneous media and classical linear conditions. We follow the Fourier transform approach as described in (Pearson, 1965; Giles, 1995; Thomas, 1995; Østerby, 2003; Langtangen et al., 2017): by injecting wave components of different frequencies $\nu \in [-\pi, \pi]$ into the heat Equation 4.25, we can look at the response and behavior of the different schemes.

The propagation of the finite difference solution from one time step to the next is governed by the growth factor which for the explicit method (Press et al., 1992) is

$$g(\nu) = 1 - 4F \sin^2 \frac{\nu}{2} \tag{2.44}$$

where values of ν close to 0 indicate low frequency components and values close to π indicate high oscillatory wave components and F is the Fourier number defined as

$$F = \frac{\alpha \Delta t}{\Delta x^2} \tag{2.45}$$

The growth of numerical wave components occurs when the absolute value of $g(\nu)$ exceeds 1, which for explicit scheme happens if $F > \frac{1}{2}$. This leads to the magnification of the corresponding wave component, indicating instability. Consequently, the explicit scheme is numerically unstable, and its domain of stability is given by

$$F < 1/2 \tag{2.46}$$

The same analysis (Press et al., 1992) for the Backward Euler scheme leads to a growth factor of

$$g(\nu) = \left(1 + 4F \sin^2 \frac{\nu}{2}\right)^{-1} \tag{2.47}$$

In this case, the growth factor is constrained by $|g(\nu)| \leq 1$ for all F and ν, meaning that the fully implicit scheme is unconditionally stable.

Finally the growth factor of the Crank-Nicolson method (Press et al., 1992) is given by

$$g(\nu) = \frac{1 - 2F \sin^2 \frac{\nu}{2}}{1 + 2F \sin^2 \frac{\nu}{2}}. \tag{2.48}$$

It is clear that the Crank-Nicolson method is also unconditionally stable as $|g(\nu)| \leq 1$ for all values of F and ν. However we note that for high frequency components $\nu \to \pm\pi$ then $g(\nu) \to -1$, especially for large F, meaning that these components are propagated as weakly damped oscillations.

Notably, the growth factor of the fully implicit scheme is relatively small for high Fourier Numbers, which means that the components that exhibit the most problematic behavior in the Crank-Nicolson method are the same components that are most effectively damped by the fully implicit method (Østerby, 2003). Thus, the fully implicit scheme has an advantage of stability when handling stiff initial conditions, which is illustrated in the results section.

2.7 Thesis' Supplementary Material

2.7.1 Thermal Skin Depth and Pseudo Thermal Wave

To understand the origin of the thermal depth expression, let's consider a semi-infinite solid with a surface temperature that varies periodically with time. The surface layer is subject to a periodic thermal forcing given by

$$T(0, t) = T_0 \cos(\omega t - \psi). \tag{2.49}$$

We seek a periodic solution to the 1D heat equation of the form

$$T(x,t) = f(x)e^{j(\omega t - \psi)} \tag{2.50}$$

where f is a function of x only and $j^2 = -1$. By substituting this expression into the heat equation we obtain

$$\frac{\partial^2 f(x)}{\partial x^2} - \frac{j\omega}{\alpha} f(x) = 0 \tag{2.51}$$

The solution of the second order differential equation of f can be expressed as

$$f(x) = A_* e^{-\sqrt{\frac{j\omega}{\alpha}}x} + B_* e^{\sqrt{\frac{j\omega}{\alpha}}x} \tag{2.52}$$

The solution must be finite as $x \to \infty$ which implies $B_* = 0$. The boundary condition equation gives

$$T(0,0) = T_0 = f(0) = A_* \tag{2.53}$$

Thus the solution can be written as

$$T(x,t) = T_0 e^{j(\omega t - \psi) - \sqrt{\frac{j\omega}{\alpha}}x} \tag{2.54}$$

which is equivalent to:

$$T(x,t) = T_0 \cos\left(\omega t - \psi - \frac{x}{\delta}\right) e^{-x/\delta} \tag{2.55}$$

where we retrieve the expression of δ, the thermal skin depth

$$\delta = \sqrt{\frac{2\alpha}{\omega}}. \tag{2.56}$$

Note, that while this is referred to as a damped thermal "wave", it is not truly a wave because it does not satisfy d'Alembert's wave equation.

2.7.2 Improving Past Thermal Analysis of Europa

Current coverage of Europa's surface temperature is based on Galileo PPR brightness temperature measurements, which have a resolution of $\sim 100\,\mathrm{km/pixel}$ (Rathbun et al., 2010). The regolith was modeled under the assumption of vertical homogeneity, allowing for the fitting of a unique thermal inertia and albedo pair for each location to reproduce the PPR dataset.

However, Hansen (1973), based on thermal analysis from Earth-based telescope measurements during eclipses, showed that homogeneous models cannot accurately reproduce Europa's thermal profile. Additionally, ice sintering, detailed in Chapter 4, is thought to occur on Europa and would lead to a vertical gradient in thermal properties. Lastly, the varying penetration depths of energetic particles, as described

in Chapter 5, may also induce changes in thermal properties within the diurnal thermal skin depth.

For these reasons, it would be more realistic to model the near-surface of Europa as a material with vertically varying thermal properties. However, this is not trivial because even fitting the simplest heterogeneous case, such as a bilayer profile, introduces many more unknowns. Using a bilayer model to fit the brightness temperatures requires fitting not only the albedo but also the thermal inertia of the top layer, the bottom layer, and the depth of the interface. Some of these unknowns could be reduced using other instruments. For example, the albedo could be retrieved from UV-visible data, as done by Trumbo et al. (2018) in their Earth-based thermal study of Europa. The albedo map produced in Section 5.5.2 could, for example, be used to avoid fitting the albedo from the thermal analysis. Still, deriving multilayered thermal properties from brightness measurements is not straightforward and will require further modeling work and improved datasets from Europa Clipper and JUICE. This is actually what PhD student Salman Raza is currently working on for the surface of Iapetus and Enceladus in his PhD project with Alice Le Gall, as part of our collaboration.

2.7.3 E-THEMIS Future Thermal Analysis of Europa

The current thermal data of Europa has low spatial resolution, resulting in the derived thermal property that are only indicative of the surface at scales $> 100\,\mathrm{km}$ and with limited spatial coverage. Improving upon this, the Europa Clipper spacecraft will provide advanced measurements of Europa's temperature and derive physical properties using the Europa Thermal Emission Imaging System (E-THEMIS). This instrument will measure Europa's emitted infrared radiation using three wavelength bands from 7 to 80 µm (Christensen, J. R. Spencer, et al., 2024). The main scientific goals of the instrument are to 1) Detect and monitor recent activity. 2) Identify safe landing sites for future lander concepts.

In terms of resolution, E-THEMIS will provide a global thermal map of $\sim 80\%$ of Europa's surface at a resolution of $< 8\,\mathrm{km/pixel}$ to identify thermal anomalies. The instrument will also produce a regional thermal imaging dataset of $\sim 30\%$ of the surface at a resolution $< 250\,\mathrm{m/pixel}$ to better characterize the regolith's physical properties (Christensen, Jakosky, et al., 2004). This is already a significant improvement over the Galileo PPR thermal imaging resolution of over $100\,\mathrm{km/pixel}$. The high spatial resolution is necessary to identify small regions of recent geologic activity. At the closest approach, the resolution of $4\,\mathrm{m/pixel}$ will help us derive Europa's thermal properties close to the meter scale, greatly improving our understanding of the near-surface.

In addition to the improved resolution, E-THEMIS will capture both daytime and nighttime temperatures, allowing us to determine the bilayer nature of the surface based on our proposed observations from Section 2.4.1. The instrument will

measure not only the diurnal variations of surface temperature but also the variations caused by eclipses on very short timescales and due to seasonal variations in Jupiter's insolation (Christensen, J. R. Spencer, et al., 2024). The expected lifespan of the spacecraft ~ 4 years , and its numerous flybys will allow coverage of the same location throughout a Europan season ~ 12 years. The variations in brightness temperature over these timescales (eclipses, diurnal, and seasonal) will provide information on the thermal properties at varying depths due to the changing thermal skin depths, (respectively from millimeters to centimeters to meters). As a result, this will also help confirm whether the near surface is vertically heterogeneous or not, and determine the thermal properties gradient.

The science team claims that using surface thermal inertia, they will be able to determine surface particle sizes to within 10% (Piqueux et al., 2009a; Piqueux et al., 2009b; Christensen, J. R. Spencer, et al., 2024). However, the near-surface regolith is likely composed of varying thermal properties with depth, including distributions of grain sizes, of degrees of sintering, of porosities, impurities, and more. The relationship between these microphysical parameters and thermal properties needs to be integrated into a multi-layered thermal model to accurately interpret the E-THEMIS data. Again, this modeling introduces numerous parameters to invert, all of which are currently unconstrained. While E-THEMIS will help better constrain these parameters, achieving a 10% accuracy on grain size seems unlikely without making strong assumptions about the regolith properties, such as assuming it is completely homogeneous and unconsolidated.

In conclusion, accurate inversion of microphysical parameters from brightness temperature measurements requires further modeling due to our current lack of knowledge about several factors. However, by combining E-THEMIS data with measurements made from other instruments onboard Europa Clipper and from JUICE, such as spectroscopy for grain sizes and UV-visible observations for albedo, we will achieve a more comprehensive understanding and better constrain of Europa's near-surface microstructure.

Bibliography for Chapter 2

Acton, Charles et al. (Jan. 2018). "A look towards the future in the handling of space science mission geometry". In: *Planetary and Space Science* 150, pp. 9–12. DOI: 10.1016/j.pss.2017.02.013.

Acton, Charles H. (Jan. 1996). "Ancillary data services of NASA's Navigation and Ancillary Information Facility". In: *Planetary and Space Science* 44.1, pp. 65–70. DOI: 10.1016/0032-0633(95)00107-7.

Adams, Edward E. and Atsushi Sato (1993). "Model for effective thermal conductivity of a dry snow cover composed of uniform ice spheres". In: *Annals of Glaciology* 18, pp. 300–304. DOI: 10.3189/s026030550001168x.

Anderson, Dale A. et al. (Dec. 2020). *Computational Fluid Mechanics and Heat Transfer*. CRC Press. ISBN: 9781351124027. DOI: 10.1201/9781351124027.

Ashkenazy, Yosef (June 2019). "The surface temperature of Europa". In: *Heliyon* 5.6, e01908. ISSN: 2405-8440. DOI: 10.1016/j.heliyon.2019.e01908.

Beam, R.M, R.F Warming, and H.C Yee (Nov. 1982). "Stability analysis of numerical boundary conditions and implicit difference approximations for hyperbolic equations". In: *Journal of Computational Physics* 48.2, pp. 200–222. DOI: 10.1016/0021-9991(82)90047-x.

Bills, Bruce G. et al. (2009). "Rotational Dynamics of Europa". In: *Eurosurveillance*, p. 119. URL: https://api.semanticscholar.org/CorpusID:51838705.

Bonneville, Alain and Patrick Capolsini (Dec. 1999). "THERMIC: a 2-D finite-element tool to solve conductive and advective heat transfer problems in Earth Sciences". In: *Computers And Geosciences* 25.10, pp. 1137–1148. ISSN: 0098-3004. DOI: 10.1016/s0098-3004(99)00075-8.

Christensen, Philip R., Bruce M. Jakosky, et al. (2004). "The Thermal Emission Imaging System (THEMIS) for the Mars 2001 Odyssey Mission". In: *Space Science Reviews* 110.1/2, pp. 85–130. DOI: 10.1023/b:spac.0000021008.16305.94.

Christensen, Philip R., John R. Spencer, et al. (May 2024). "The Europa Thermal Emission Imaging System (E-THEMIS) Investigation for the Europa Clipper Mission". In: *Space Science Reviews* 220.4. ISSN: 1572-9672. DOI: 10.1007/s11214-024-01074-1.

Crank, J. and P. Nicolson (Jan. 1947). "A practical method for numerical evaluation of solutions of partial differential equations of the heat-conduction type". In: *Mathematical Proceedings of the Cambridge Philosophical Society* 43.1, pp. 50–67. DOI: 10.1017/s0305004100023197.

Cruz-Mermy et al. (Apr. 2023). "Selection of chemical species for Europa's surface using Galileo/NIMS". In: *Icarus* 394, p. 115379. ISSN: 0019-1035. DOI: 10.1016/j.icarus.2022.115379.

Elachi, C. et al. (2004). "Radar: The Cassini Titan Radar Mapper". In: *The Cassini-Huygens Mission*. Kluwer Academic Publishers, pp. 71–110. DOI: 10.1007/1-4020-3874-7_2.

Ferrari, C., P. Galdemard, et al. (Sept. 2005). "Imaging Saturn's rings with CAMIRAS: thermal inertia of B and C rings". In: *Astronomy And Astrophysics* 441.1, pp. 379–389. ISSN: 1432-0746. DOI: 10.1051/0004-6361:20053100.

Ferrari, C. and A. Lucas (Mar. 2016). "Low thermal inertias of icy planetary surfaces". In: *Astronomy and Astrophysics* 588, A133. DOI: 10.1051/0004-6361/201527625.

Giles, M. (1995). "Stability Analysis of Numerical Interface Boundary Conditions for Parabolic Equations." In: *University of Oxford Research Archive*.

Grasset, O. et al. (Apr. 2013). "JUpiter ICy moons Explorer (JUICE): An ESA mission to orbit Ganymede and to characterise the Jupiter system". In: *Planetary and Space Science* 78, pp. 1–21. DOI: 10.1016/j.pss.2012.12.002.

Gundlach, Bastian and Jürgen Blum (June 2012). "Outgassing of icy bodies in the Solar System – II: Heat transport in dry, porous surface dust layers". In: *Icarus* 219.2, pp. 618–629. DOI: 10.1016/j.icarus.2012.03.013.

Gusarov, A.V. et al. (Mar. 2003). "Contact thermal conductivity of a powder bed in selective laser sintering". In: *International Journal of Heat and Mass Transfer* 46.6, pp. 1103–1109. ISSN: 0017-9310. DOI: 10.1016/s0017-9310(02)00370-8.

Hansen, O.L. (Feb. 1973). "Ten-micron eclipse observations of Io, Europa, and Ganymede". In: *Icarus* 18.2, pp. 237–246. ISSN: 0019-1035. DOI: 10.1016/0019-1035(73)90208-x.

Hayne, P. O. and O. Aharonson (Sept. 2015). "Thermal stability of ice on Ceres with rough topography". In: *Journal of Geophysical Research: Planets* 120.9, pp. 1567–1584. DOI: 10.1002/2015je004887.

Jaeger, J. C. (1950). "Conduction of heat in composite slabs". In: *Quarterly of Applied Mathematics* 8.2, pp. 187–198. DOI: 10.1090/qam/36417.

Janna, William S. (Oct. 2018). *Engineering Heat Transfer*. CRC Press. ISBN: 9781315275383. DOI: 10.1201/9781439883143.

Jennings, D. E. et al. (June 2017). "Composite infrared spectrometer (CIRS) on Cassini". In: *Applied Optics* 56.18, p. 5274. DOI: 10.1364/ao.56.005274.

Kieffer, Hugh H. (Mar. 2013). "Thermal model for analysis of Mars infrared mapping". In: *Journal of Geophysical Research: Planets* 118.3, pp. 451–470. DOI: 10.1029/2012je004164.

Klinger, J. (Sept. 1981). "Some consequences of a phase transition of water ice on the heat balance of comet nuclei". In: *Icarus* 47.3, pp. 320–324. DOI: 10.1016/0019-1035(81)90179-2.

Lage, P. L. C. (Dec. 1996). "Application of the optimized modified strong implicit procedure to nonlinear problems". In: *Numerical Heat Transfer, Part B: Fundamentals* 30.4, pp. 423–435. DOI: 10.1080/10407799608915091.

Langtangen, Hans Petter and Svein Linge (2017). *Finite Difference Computing with PDEs*. Springer International Publishing. DOI: 10.1007/978-3-319-55456-3.

Laskar, J (July 2008). "Chaotic diffusion in the Solar System". In: *Icarus* 196.1, pp. 1–15. ISSN: 0019-1035. DOI: 10.1016/j.icarus.2008.02.017.

Laskar, Jacques (2003). *Frequency map analysis and quasiperiodic decompositions*. DOI: 10.48550/ARXIV.MATH/0305364.

Lehning, Michael et al. (Nov. 2002). "A physical SNOWPACK model for the Swiss avalanche warning". In: *Cold Regions Science and Technology* 35.3, pp. 147–167. DOI: 10.1016/s0165-232x(02)00073-3.

Loeb, Andrew and Christopher Earls (Nov. 2019). "Analysis of heterogeneous computing approaches to simulating heat transfer in heterogeneous material". In: *Journal of Parallel and Distributed Computing* 133, pp. 1–17. DOI: 10.1016/j.jpdc.2019.06.004.

Masson, Roland et al. (Mar. 2020). "Domain decomposition methods to model heat exchanges between a well and a rock mass". In: *Computational Geosciences* 24.3, pp. 1377–1392. DOI: 10.1007/s10596-020-09957-2.

Mazumder, Sandip (2016). "Treatment of the Time Derivative (Parabolic and Hyperbolic PDEs)". In: *Numerical Methods for Partial Differential Equations*. Elsevier, pp. 219–275. DOI: 10.1016/b978-0-12-849894-1.00005-6.

Mergny, Cyril and Frédéric Schmidt (Feb. 2024a). "Gravity-induced ice compaction and subsurface porosity on icy moons". In: *Icarus*, p. 116008. ISSN: 0019-1035. DOI: 10.1016/j.icarus.2024.116008.

— (2024b). "LunaIcy: Exploring Europa's Icy Surface Microstructure through Multiphysics Simulations". In: *submitted*.

Molaro, J. L. et al. (Feb. 2019). "The Microstructural Evolution of Water Ice in the Solar System Through Sintering". In: *Journal of Geophysical Research: Planets* 124.2, pp. 243–277. DOI: 10.1029/2018je005773.

N Putzig, M Mellon (Nov. 2007). "Apparent thermal inertia and the surface heterogeneity of Mars". In: *Icarus* 191.1, pp. 68–94. DOI: 10.1016/j.icarus.2007.05.013.

Nissen, Anna et al. (Dec. 2017). "Heterogeneity preserving upscaling for heat transport in fractured geothermal reservoirs". In: *Computational Geosciences* 22.2, pp. 451–467. DOI: 10.1007/s10596-017-9704-6.

Østerby, Ole (Dec. 2003). "Five Ways of Reducing the Crank–Nicolson Oscillations". In: *BIT Numerical Mathematics* 43.4, pp. 811–822. DOI: 10.1023/b:bitn.0000009942.00540.94.

Pearson, Carl E. (1965). "Impulsive end condition for diffusion equation". In: *Mathematics of Computation* 19.92, pp. 570–576. DOI: 10.1090/s0025-5718-1965-0193765-5.

Phillips, Cynthia B. and Robert T. Pappalardo (May 2014). "Europa Clipper Mission Concept: Exploring Jupiter's Ocean Moon". In: *Eos, Transactions American Geophysical Union* 95.20, pp. 165–167. DOI: 10.1002/2014eo200002.

Piqueux, S. and P. R. Christensen (Sept. 2009a). "A model of thermal conductivity for planetary soils: 1. Theory for unconsolidated soils". In: *Journal of Geophysical Research* 114.E9. DOI: 10.1029/2008je003308.

— (Sept. 2009b). "A model of thermal conductivity for planetary soils: 2. Theory for cemented soils". In: *Journal of Geophysical Research* 114.E9. DOI: 10.1029/2008je003309.

Press, William H. et al. (1992). *Numerical Recipes in C (2nd Ed.): The Art of Scientific Computing*. USA: Cambridge University Press. ISBN: 0521431085.

Rathbun, Julie A., Nathaniel J. Rodriguez, and John R. Spencer (Dec. 2010). "Galileo PPR observations of Europa: Hotspot detection limits and surface thermal properties". In: *Icarus* 210.2, pp. 763–769. DOI: 10.1016/j.icarus.2010.07.017.

Rojek, J., R. Kasztelan, and R. Tharmaraj (June 2022). "Discrete element thermal conductance model for sintered particles". In: *Powder Technology* 405, p. 117521. ISSN: 0032-5910. DOI: 10.1016/j.powtec.2022.117521.

Roubíček, Tomáš (Jan. 1990). "Numerical solution of the nonlinear heat equationin heterogeneous media". In: *Numerical Functional Analysis and Optimization* 11.7-8, pp. 793–810. DOI: 10.1080/01630569008816402.

Rozitis, B. and S. F. Green (July 2011). "Directional characteristics of thermal-infrared beaming from atmosphereless planetary surfaces - a new thermophysical model". In: *Monthly Notices of the Royal Astronomical Society* 415.3, pp. 2042–2062. DOI: 10.1111/j.1365-2966.2011.18718.x.

Schorghofer, Norbert (2022). "Planetary-Code-Collection: Thermal, Ice Evolution, and Exosphere Models for Planetary Surfaces". In: *Zenodo*. DOI: 10.5281/ZENODO.594268.

Shoshany, Yossi, Dina Prialnik, and Morris Podolak (May 2002). "Monte Carlo Modeling of the Thermal Conductivity of Porous Cometary Ice". In: *Icarus* 157.1, pp. 219–227. ISSN: 0019-1035. DOI: 10.1006/icar.2002.6815.

Simon, J.-L. et al. (Aug. 2013). "New analytical planetary theories VSOP2013 and TOP2013". In: *Astronomy and Astrophysics* 557, A49. ISSN: 1432-0746. DOI: 10.1051/0004-6361/201321843.

Spencer, John, Larry Lebofsky, and Mark Sykes (Apr. 1989). "Systematic biases in radiometric diameter determinations". In: *Icarus* 78.2, pp. 337–354. DOI: 10.1016/0019-1035(89)90182-6.

Spencer, John R. et al. (May 1999). "Temperatures on Europa from Galileo Photopolarimeter-Radiometer: Nighttime Thermal Anomalies". In: *Science* 284.5419, pp. 1514–1516. ISSN: 1095-9203. DOI: 10.1126/science.284.5419.1514.

Squyres, Steven W. (Nov. 1980). "Surface temperatures and retention of H2O frost on Ganymede and Callisto". In: *Icarus* 44.2, pp. 502–510. ISSN: 0019-1035. DOI: 10.1016/0019-1035(80)90040-8.

Sundqvist, H. and G. Veronis (Feb. 1970). "A simple finite-difference grid with non-constant intervals". In: *Tellus* 22.1, pp. 26–31. DOI: 10.1111/j.2153-3490.1970.tb01933.x.

Thomas, J. W. (1995). "Stability. In: Numerical Partial Differential Equations: Finite Difference Methods." In: *Texts in Applied Mathematics*. Springer New York, pp. 97–145. DOI: 10.1007/978-1-4899-7278-1_4.

Trumbo, Samantha K., Michael E. Brown, and Bryan J. Butler (Sept. 2018). "ALMA Thermal Observations of Europa". In: *The Astronomical Journal* 156.4, p. 161. ISSN: 1538-3881. DOI: 10.3847/1538-3881/aada87.

Watson, Kenneth (1964). "I. The thermal conductivity measurements of selected silicate powders in vacuum from 150°-350° K. II. An interpretation of the Moon's eclipse and lunation cooling as observed through the Earth's atmosphere from 8-14 microns". en. PhD thesis. DOI: 10.7907/7HDE-1M52.

Wesselink, A. J. (Apr. 1948). "Heat conductivity and nature of the lunar surface material". In: *Bulletin of the Astronomical Institutes of the Netherlands* 10, pp. 351–363.

Williams, S. D. and Donald M. Curry (Jan. 1977). "An implicit-iterative solution of the heat conduction equation with a radiation boundary condition". In: *International Journal for Numerical Methods in Engineering* 11.10, pp. 1605–1619. ISSN: 1097-0207. DOI: 10.1002/nme.1620111010.

Woods-Robinson, Rachel, Matthew A. Siegler, and David A. Paige (July 2019). "A Model for the Thermophysical Properties of Lunar Regolith at Low Temperatures". In: *Journal of Geophysical Research: Planets* 124.7, pp. 1989–2011. DOI: 10.1029/2019je005955.

Young, Leslie A. (Mar. 2017). "Volatile transport on inhomogeneous surfaces: II. Numerical calculations (VT3D)". In: *Icarus* 284, pp. 443–476. DOI: 10.1016/j.icarus.2016.07.021.

Figure 2.10: The name MultIHeaTS stands for Multilayered Implicit Heat Transfer Solver. It is also a wordplay to "multihit", a term used in fighting sports and video games to describe an attack that hits its target multiple times. Illustrated here is a multihit move from the popular Street Fighter franchise.

CHAPTER 3

Gravity-induced Ice Compaction

The work presented in this chapter comes from the article titled *"Gravity-Induced Ice Compaction and Subsurface Porosity on Icy Moons" by C. Mergny and F.Schmidt, Icarus, 2024,* DOI 10.1016/j.icarus.2024.116008

Contents

Foreword

When modeling the thermal properties of icy moons, we need to consider whether density variations could occur within the depths affected by periodic variations of the solar flux. There is substantial evidence suggesting that Europa's surface is highly porous (see Section 3.1 for details). However, the literature does not yet agree on a specific value for this porosity. What exactly does "highly porous" mean—50% porosity, or 90% porosity?

Our goal is not to constrain the porosity, as we currently lack the information to do so, but rather to estimate how it would vary with depth. Regardless of the initial porosity, compaction processes may change the density and thus the porosity of the near-surface ice. Among various compaction processes, the first that comes in mind is the compaction due to overburden pressure exerted by gravity. This raises the question: at what depths does gravity-induced compaction become significant on icy moons? Are these changes substantial enough to be accounted in our thermal model of the near surface?

To address this, we decided to base ourselves on the compaction behavior of snow on Earth. Numerous field studies have been conducted in Earth's cold and snowy regions to investigate snow compaction under gravity (see Figure 3.1 for example). Ice core measurements indicate that within the first dozen meters, gravity causes significant density variations, transitioning from fresh snow to firn, and from firn to bubbled ice.

Figure 3.1: Measurement of snow and firn layers on Suyuparina glacier, southern Peru. Credits: photo by Christian Huggel.

The conditions at the surface of icy moons are very different from those on Earth. We still do not fully understand the scale at which the ice surface compacts on these moons. Such knowledge would be particularly important for designing landers and

selecting landing sites for the Europa lander mission concept (see Figure 3.2). High-porosity ice that does not compact may be challenging to navigate. Additionally, the Cryobot mission concept (Vale Pereira et al., 2023), which involves drilling through Europa's ice shell to reach the subsurface oceans using heat to melt the ice and gravity to descend, will likely be affected by these density changes. Therefore, constraining the evolution of the ice shell properties at these various depths will be crucial for these missions.

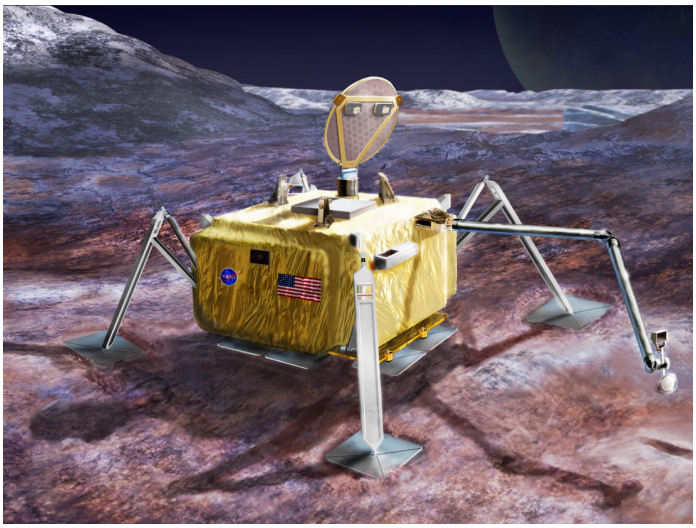

Figure 3.2: Europa lander mission concept. The artist chose to represent a seemingly hard icy surface. Credits: NASA/JPL, slide from Kevin Peter Hand.

The work presented in this Chapter is our attempt to use Earth-based ice measurements to model the evolution of porosity with depth for icy bodies across the Solar System.

Abstract

Our understanding of the surface porosity of icy moons and its evolution with depth remains limited, including the precise scale at which ice compaction occurs under self-weight pressure. This parameter is of crucial interest for the correct interpretation of current remote sensing data (spectroscopy in the visible, infrared to passive microwave) but also for planetary exploration when designing a lander, a rover or a cryobot. In situ exploration of the ice crust would require knowledge about subsurface porosity. This study employs a compaction model solely driven by overburden pressure based on prior research. The formulation for density as a function of depth, incorporates an essential parameter: the ice compaction coefficient. To determine this coefficient, we fit our depth-dependent density model to existing data obtained from Earth-based measurements of ice cores in Antarctica and North Greenland. Our results yield a typical lengthscale for ice compaction on Earth of approximately $20.1 \pm 0.6\,\mathrm{m}$, consistent with the existing literature. We apply the model to Europa, which due to its lower gravity, has a typical ice compaction scale of $150 \pm 4\,\mathrm{m}$, when assuming an Earth-like compaction coefficient. We compare it with the depths scanned by current spaceborne data and find that porosity can be considered constant when accounting only for gravity-induced compaction.

3.1 Introduction

Icy moons, characterized by an icy crust at the surface, present unresolved questions regarding the microscopic properties of their surface and subsurface. Various studies provide compelling evidence that the surface of icy satellites is made of a porous material. One significant piece of evidence comes from brightness temperature measurements, where thermal models obtain a thermal inertia significantly smaller than that of solid ice (Spencer et al., 1989; Rathbun et al., 2010). The most plausible explanation for this reduction in thermal inertia is to introduce porosity into the thermal properties, as it changes the density and conductivity of ice (Ferrari et al., 2016). Other indications are found in spectroscopy measurements of icy moons' surfaces showing improved fits when incorporating a porosity factor (Mishra et al., 2021; Cruz-Mermy et al., 2023) or from the potential existence of O2 molecules trapped in bubbles within Europa's near-surface ice (Oza et al., 2018), indicating the presence of a porous regolith. Various processes may contribute to the development of a porous surface, including the deposition of snow onto the surface or space weathering, which could potentially transform initially solidified ice into a porous material through constant bombardment by micrometeorites and particles.

Specifically, the exact texture of the near-surface remains unclear. Is the ice made of grains with high porosity that compact with increasing depth? Of a granular layer overlaying a denser slab? Or of any other possible configuration? Subsurface porosity is unknown but it constitutes a crucial parameter when building subsurface models for the analysis of spaceborne data, whether aiming to derive thermal properties or optical properties. A common assumption in remote sensing analysis, is that the probed material has a unique thermal inertia (Spencer et al., 1989). This implies that the subsurface is homogeneous, thus having constant porosity through all the depths probed. On Europa, the diurnal skin depth is estimated to be on the order of few centimeters (Ferrari et al., 2016), while the seasonal skin depth may extend to dozens of meters. Hence it is unclear whether Europa porosity changes at the depths probed by brightness temperature retrievals.

On Earth at these depths, notable changes in porosity from ice core measurements have been observed on Antarctica and North Greenland ice, with variations spanning approximately 20 meters (Alley et al., 1982; Hörhold et al., 2011; Gerland et al., 1999). Earlier work (Herron et al., 1980; Alley et al., 1982), identified critical density thresholds, such as $550\,\mathrm{kg\,m^{-3}}$ for the transition from snow to firn and $840\,\mathrm{kg\,m^{-3}}$ from firn to coarse firn, resulting in the proposal of three distinct empirical models to describe the density transitions within the snow structure. However, a more recent investigation (Hörhold et al., 2011), using a comprehensive measurements of 16 ice cores Antarctica and North Greenland did not reveal clear transitions in the ice density profile. This finding suggests the possibility of a unified formulation to describe the entire density variations in these ice cores. Other efforts have been made to model snow compaction more realistically on Earth (Cuffey, 2010), focusing on

complex interactions involving pressure, temperature and sintering. These models (Wilkinson, 1988; KopystyńSki et al., 1993; Arnaud et al., 2000; Meyer et al., 2020) often rely on the fundamental sintering equations first formulated by Swinkels and Ashby (Swinkels et al., 1981).

On Europa, studies (Nimmo et al., 2003; Johnson et al., 2017; Howell et al., 2021) have primarily addressed the dynamic variations of porosity over time within the whole ice shell, predominantly attributed to ice viscosity. However, these studies tend to concentrate on deeper depths ($\sim$ 10s of km), where accurate modeling of the shallow subsurface ($<\sim$10s m) is not required. While exploring other compaction-related processes like sputtering, as observed in some planetary science studies (Raut et al., 2008; Schaible et al., 2017), and late-stage sintering (Molaro et al., 2019), holds promise for future research, our current focus remains on modeling ice compaction under the influence of overburden pressure due to gravity. Hence we address a fundamental question: What is the characteristic lengthscale of ice compaction on icy moons when considering solely the overburden pressure induced by gravity?

The main objective of this study is not to determine the precise surface porosity of icy moons, as the existing data currently available makes it challenging to constrain this parameter. Rather, our focus is to determine what would be the compaction profile of ice for any value of surface porosity. We first adapt the approach undertaken in (Wilson et al., 1994) for the compaction of silicate rock on Earth, Mars and Venus to model the compaction processes of ice on icy worlds. Then, we propose an analogy with a viscous model initially proposed for magma (Fowler, 1985) and used by the planetary science community (Nimmo et al., 2003; Johnson et al., 2017) to study the ice shell. The model will be tested on Earth cases and discussed for icy moons, with a particular focus on Europa.

3.2 Methods

As pointed out by Earth based studies (M. Mellor, 1977), densification of snow under static loading remains unclear. On the one hand, compressive load result in depth-density relations that are almost time-invariant as stated by Sorge's Law (H. Bader, 1954; Bader, 1960), implying that an elastic model would be relevant. On the other hand, snow is known to creep, thus densification can be treated as a continuous time-dependent process, using a viscous flow formulation.

Author's Note

I have maintained the notation from the published article, where depth is denoted by z, instead of x as used in the rest of the thesis.

3.2.1 Compaction Model

3.2.1.1 Generalized Porosity Expression

Following (Wilson et al., 1994), a continuous density function can be used to model the variations of ice density ρ with depth z when compaction of the pore space is solely induced by the overburden pressure. The assumption made by the authors (Wilson et al., 1994) is that the porosity ϕ shows an exponential decay with increasing pressure P, leading to the form:

$$\phi(z,t) = \phi_0 \exp\left(-\lambda(z,t)P(z)\right) \tag{3.1}$$

where ϕ_0 is the top surface porosity value and $\lambda(z,t)$ will be called the compaction coefficient of the considered material. The compaction coefficient, due to its unit in Pa^{-1}, can also be thought as the inverse of the characteristic pressure required for substantial material compaction. Unlike Wilson's approach, this generalized form uses a compaction coefficient $\lambda(z,t)$ which may not be constant with depth or time. This anticipates that factors such as temperature, porosity, compaction time and others can influence the compaction coefficient, thereby affecting the porosity profile $\phi(z,t)$.

3.2.1.2 Density Profile for a Constant Compaction Coefficient

To derive the density profile expression, we follow Wilson's assumption (Wilson et al., 1994) of a constant compaction coefficient λ, with respect to depth. Although the limitations of such an assumption are discussed in 3.4.1, it is necessary in order to obtain a simplified expression of the compaction lengthscale.

It follows from the definitions of the bulk density ρ_b and pore space that the density at any given depth is given by the relation:

$$\rho(z) = \rho_\mathrm{b}(1 - \phi(z)) \tag{3.2}$$

Since the pressure at depth z is given by the weight of the above ice layers, an increase of $\mathrm{d}z$ will increase $\mathrm{d}P$ by the relation

$$\mathrm{d}P(z) = \rho(z) g \,\mathrm{d}z \tag{3.3}$$

where g is the gravity acceleration at the considered body's surface.

Combining Equations (3.1), (3.2) and (3.3), leads to a differential equation for $P(z)$, which after separation of variables and integration takes the form

$$P(z) = \frac{1}{\lambda} \ln\left(\phi_0 + (1-\phi_0)\exp\left(\frac{z}{H}\right)\right). \tag{3.4}$$

and provides the expression for density:

$$\rho(z) = \rho_\mathrm{b}\left(1 + \frac{\phi_0}{1-\phi_0}\exp\left(-\frac{z}{H}\right)\right)^{-1} \tag{3.5}$$

with H the characteristic lengthscale of compaction given by

$$H = \frac{1}{\lambda g \rho_{\mathrm{b}}}. \tag{3.6}$$

Using this formulation, the depth-density profile of an icy layer can be specified in terms of the three model parameters: the top surface porosity ϕ_0, the ice compaction coefficient λ and the gravitational acceleration of the target body g.

3.2.2 Elastic and Viscous Compaction

The assumption of an exponential decay of porosity $\phi(z)$ with rising pressure $P(z)$ made by (Wilson et al., 1994), was revisited in Appendix 3.6. We demonstrated that it can be mathematically derived from both the stress-strain rate relationship of a purely elastic material or of a purely viscous material. The combination of high tidal heating and low gravity of many outer planet satellites leads to conditions where pore close more readily viscously due to high temperatures rather than due only to self gravity. Hence in many studies of Europa's ice shell (Nimmo et al., 2003; Howell et al., 2021), ice compaction is approached by considering it as the compression of a viscous flow, using Fowler's law of porosity (Fowler, 1985):

$$\frac{\partial \phi}{\partial t}(z,t) = -\phi(z,t)\frac{P(z)}{\eta(z,t)} \tag{3.7}$$

where t is the time of compaction, and $\eta(z,t)$ the viscosity of the considered material at a specific depth and time. This differential equation can be derived from the stress-strain rate relationship of a purely viscous material, as demonstrated in Appendix 3.6.2. This leads to the expression of porosity:

$$\phi(z,t) = \phi_i(z)\exp\left(-\frac{t}{\eta(z,t)}P(z)\right) \tag{3.8}$$

where $\phi_i(z)$ is the initial porosity profile at $t = 0$.

It is unclear whether near-surface ice on icy bodies undergoes elastic compaction, viscous creep, or a simultaneous combination of both processes. Determining the dominant compaction mechanism is challenging, primarily due to the poorly constrained viscosity of near-surface porous ice at these conditions, which can vary on multiple orders of magnitude. The main focus of this study is not to quantify which compaction process dominates on icy moons, but rather to understand how each process would behave independently and can be related to single parameter: the compaction coefficient. Elastic compaction and viscous flow are two distinct compaction processes but derivation of compaction from both elastic or viscous processes result in the same general mathematical form of the porosity given by Equation (3.1). The elastic derivation shows a direct inverse relationship between the compaction coefficient and the ice Young's modulus E:

$$\lambda \Leftrightarrow \frac{1}{E}. \tag{3.9}$$

while the viscous flow derivation leads to a relationship between the compaction coefficient λ, the compaction time t, and the viscosity η:

$$\lambda(z,t) \Leftrightarrow \frac{t}{\eta(z,t)}. \tag{3.10}$$

The relationship of Equation (3.10) elucidates that selecting a value for λ on any icy body imposes constraints on a parameter pair: viscosity and compaction time. If we adhere to Wilson's analogy method (Wilson et al., 1994), we must assume that the compaction coefficient for a planetary ice body is comparable to the value observed on Earth. However, if the compaction coefficient deviates from the Earth's measurement, Equation (3.10) provides the relationship between λ, t, and η.

3.3 Results

Number of reasons may lead to changes in the values of the compaction coefficient of ice between Earth and icy moons. The significantly lower temperature, lack of atmosphere and the different environment found on the icy moons could change how ice reacts to compression. To the best of our knowledge, we currently lack a method to properly obtain the compaction coefficient on icy moons. Therefore, in this section we will first describe how ice would compact due to the lower gravity on icy moons assuming the compaction coefficient is the same as on Earth. Then we explore how other compaction mechanisms like viscous creep may come into play, effectively changing the compaction coefficient.

3.3.1 Constant Earth-like Compaction Coefficient

To determine the value of the ice compaction coefficient on Earth, an analysis of density measurements with depth derived from Earth-based data is conducted. This analysis uses a dataset comprising measurements from ice cores located in North Greenland (77.3 S, −49.2 W) (Hörhold et al., 2011), Berkner Island, Antarctica A1 (79.3 S, 45.4 W) (Gerland et al., 1999), and Ridge BC, Antarctica A2 (82.5 S, 136.4 W) (Alley et al., 1982). While sintering and melting occur on Earth, on large ice sheet such as Greenland and Antarctica, they are only confined in the first few meters depths (Alley et al., 1982). Therefore, we conclude that these processes do not significantly impact the density variations spanning dozens of meters observed in these ice cores. Knowing the bulk ice density $\rho_\mathrm{b} = 917\,\mathrm{kg\,m^{-3}}$, we have fitted the depth density profile from Equation (3.2) to the three ice cores shown in Figure 3.3. For example, for the B26 North Greenland ice core, the best fit results in an initial surface porosity $\phi_0 = 48.5 \pm 0.7\%$ and an ice compaction coefficient of $\lambda = 4.9 \pm 1.5 \times 10^{-6}\,\mathrm{Pa^{-1}}$. The average value over the three locations studied here is $\overline{\lambda} = 5.5 \pm 0.2 \times 10^{-6}\,\mathrm{Pa^{-1}}$ and will be used as a reference for the compaction of ice on Earth for the remaining of this chapter.

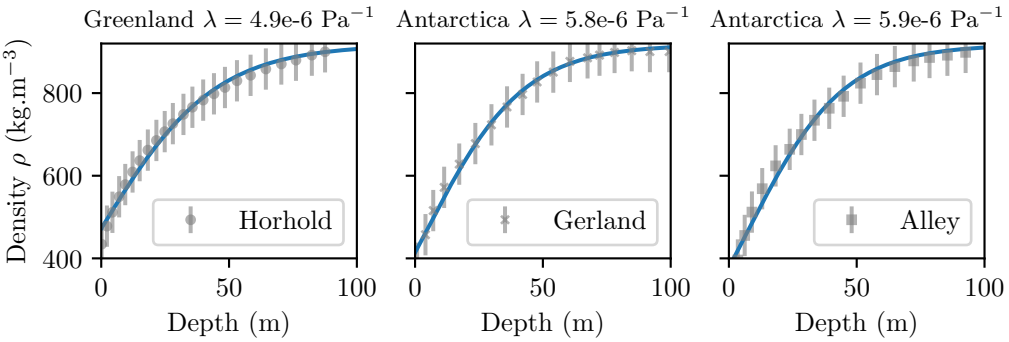

Figure 3.3: Ice depth-density profiles for three ice cores (*Left*) North Greenland (77.3 S,−49.2 W), (*Middle*) Berkner Island, Antarctica A1 (79.3 S, 45.4 W), (*Right*) Ridge BC, Antarctica A2 (82.5 S, 136.4 W). Grey dots depict measured density data with associated error bars (Hörhold et al., 2011; Gerland et al., 1999; Alley et al., 1982), while blue lines represent the best-fit density function using Equation (3.5).

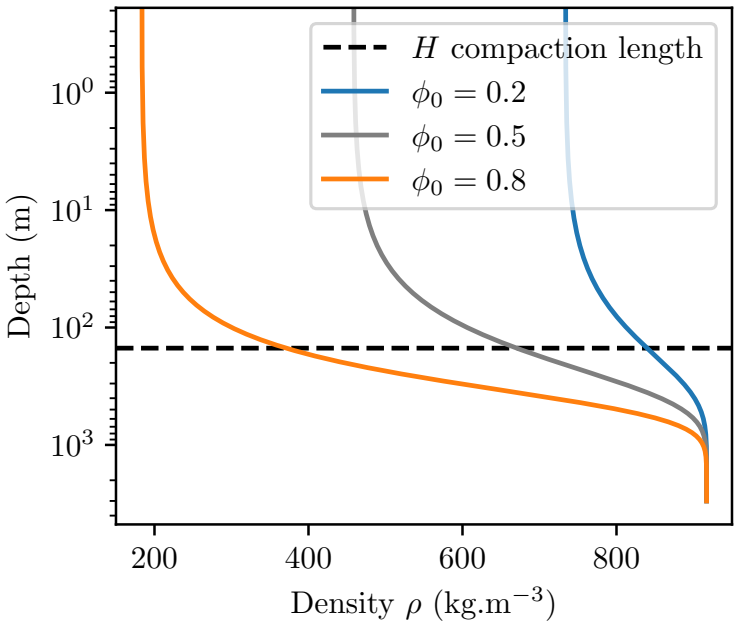

Figure 3.4: Modeled ice densities as function of depth for Europa's ice shell and different starting porosities using Earth's compaction coefficient $\overline{\lambda} = 5.5 \pm 0.2 \times 10^{-6}\,\text{Pa}^{-1}$. For reference, the characteristic compaction length H for Europa is represented by the dotted black line. The orange zone shows the surface layers affected by solar temperature variations, called the seasonal thermal skin depth. We observe that porosity remains nearly constant around the thermal skin depth, due to Europa's low gravity.

Name	Radius (km) (km)	Surface Gravity ($\mathrm{m\,s^{-2}}$)	Gravity-Induced Compaction Length H (m)
Earth	6370	9.81	20
Ganymede	2630	1.43	140
Europa	1560	1.32	150
Callisto	2410	1.24	160
Pluto	1190	0.62	320
Iapetus	1470	0.22	880
Enceladus	250	0.11	1760

Table 3.1: Ice compaction lengthscales under gravity-induced pressure for different bodies in the Solar System assuming a constant Earth-like compaction coefficient of ice $\overline{\lambda} = 5.5 \pm 0.2 \times 10^{-6}\,\mathrm{Pa^{-1}}$. Note that other processes like sputtering or sintering, may also compact the ice leaving to different compaction lengths.

Having obtained Earth's ice compaction coefficient $\overline{\lambda}$, we extend our analysis by applying the density-depth formulation presented in Equation (3.2) to other planetary surfaces. While this method could be applied to any icy moon, our focus lies on Europa, where the surface gravitational acceleration is estimated to be $g = 1.315\,\mathrm{m\,s^{-2}}$ (Anderson et al., 1998). For any given surface porosity, the formulation of Equation (3.5) enables us to determine the density profile at various depths, accounting only for self-weight-induced ice compaction. In Figure 3.4, we present distinct density profiles for a range of initial porosities on Europa for an ice compaction coefficient $\overline{\lambda}$. It is evident that, regardless of the starting porosity, significant compaction effects are not noticeable until reaching depths deeper than 100 meters. This outcome aligns with the prediction from Equation (3.6), which illustrates that the compaction lengthscale is largely independent of the initial porosity, as shown in Figure 3.4.

When evaluating this expression for Europa, we derive a compaction lengthscale of $H = 150 \pm 4\,\mathrm{m}$. At the subsurface, for example for depths under 5 m, the porosity change ranges from approximately 2% to less than 1%, depending on the initial porosity ϕ_0. This result aligns with radar reflectivity models, which suggest that Europa has a surface layer with appreciable porosity that is at least meters thick (Johnson et al., 2017). Visible compaction effects only become prominent at greater depths, near the compaction lengthscale H.

We have applied the same analysis for various icy bodies in the Solar System and present in Table 3.1 their compaction lengthscale (see also additional representation in Section 3.7.2). We found that the lengthscales of gravity-induced compaction range from $\sim 20\,\mathrm{m}$ to $\sim 2000\,\mathrm{m}$ depending on gravity and thus size of the bodies. In general, due to a lower gravitational acceleration, ice compaction lengthscales are considerably higher than those observed on Earth. While our study focused on Solar System icy bodies, it anticipates that exoplanetary icy bodies, potentially discovered

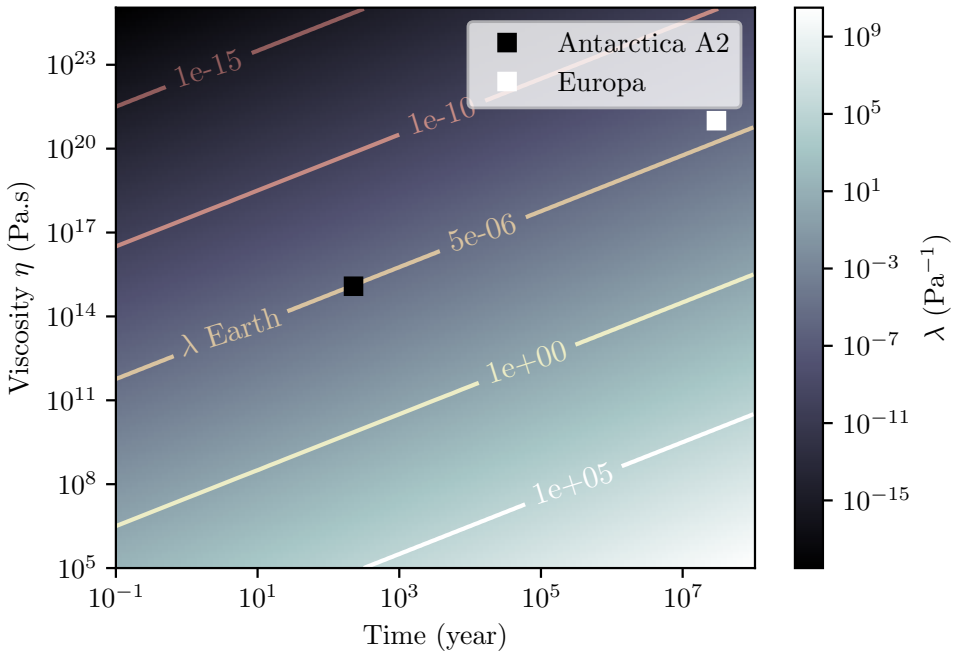

Figure 3.5: Evolution of the compaction coefficient $\lambda(\eta, t)$ with the ice viscosity and the compaction time. The average ice compaction coefficient measured on Earth is given by the yellow line $\overline{\lambda} = 5.5 \times 10^{-6}\,\mathrm{Pa}^{-1}$. Black square represents the location of the Antarctica A2 dataset in this graph, estimated from the local accumulation rate of snow. White square represents our scenario for Europa, where the compaction time is taken to be the ice crust age and for a viscosity of $\eta = 10^{21}\,\mathrm{Pa\,s}$ (Jara-Orué et al., 2011).

in the future, would benefit from these findings in interpreting surface properties through direct imaging (Hu et al., 2012; Berdyugina et al., 2019).

3.3.2 Viscous Creep Scenario

The previous analysis proposed to use the compaction of Earth ice as an analog to the compaction of ice on an icy moons. However it is possible that the compaction coefficient λ for a given planetary ice has a different value than the one measured on Earth $\overline{\lambda}$. If the ice composition or its physical properties like viscosity are different than the one on Earth, the viscous compression model would be helpful to extend the previous work. Also, while the measurements from Earth ice cores have allowed particular time for ice to compact, we remain uncertain about the compaction time on icy moons.

In this model, we can verify that the compaction coefficient λ is coherent with well known values of ice viscosity on Earth. Since glaciers are formed by accumulation

at the top, we propose to relate the elapsed time of compaction at depth z to the accumulation rate of snow A. To achieve this, we use a simplified expression from (H. Bader, 1954; Bader, 1960):

$$t(z) = \frac{z}{A}. \tag{3.11}$$

For the Antarctica A2 ice core, a snow accumulation rate of $A = 100\,\mathrm{mm\,yr^{-1}}$ was estimated (Alley et al., 1982). Applying Equation (3.11) to the characteristic compaction depth $z = H = 19\,\mathrm{m}$ results in a compaction time of $t = 190\,\mathrm{yr}$. Then, from the compaction coefficient of the A2 ice core, we can use Equation (3.10) to estimate the viscosity of the compacted snow in this region as $\eta = 1.0 \times 10^{15}\,\mathrm{Pa\,s}$ (see Figure 3.5, black square). This viscosity value is compatible with the compactive viscosity mentioned by (Mellor, 1974) for Antarctica ice, falling within the range of $10^{14} - 10^{18}\,\mathrm{Pa\,s}$. The viscous ice model is compatible with this data.

In order to apply this model to Europa, we first need to establish a compaction scenario. While an accurate accumulation rate remains to be determined for Europa, we propose considering the compaction time to be the ice crust age, estimated at approximately $t = 30\,\mathrm{Myr}$ (Zahnle et al., 2003). Using the surface age in this way provides an upper boundary value for compaction time.

The viscosity of Europa's subsurface ice remains unknown. It is challenging to model notably due to its high dependency on various parameters including temperature, stress, porosity and grain size. Here we first present a simple analytical form to estimate the viscosity of ice, then in Section 3.4.1 we discuss the relevance and limitations of such approach. Studies focusing on the deeper portion of the ice shell use a temperature-dependent viscosity law (Thomas et al., 1986; Nimmo et al., 2003):

$$\eta(z) = \eta_b \exp\left(\frac{Q}{R}\left[\frac{1}{T(z)} - \frac{1}{T_b}\right]\right) \tag{3.12}$$

where η_b and T_b are the viscosity and temperature at the base of the ice shell, Q is an activation energy and R the gas constant. While this viscosity law is suitable for modeling the base of the ice shell, near the surface, Europa's low temperature $\sim 100\,\mathrm{K}$ results in unrealistically high ice viscosity values exceeding $10^{26}\,\mathrm{Pa\,s}$. As highlighted by Thomas et al. (1986), appropriately modelling the subsurface would require a warmer surface to counterbalance these excessively high viscosity.

To the best of our knowledge, there has not been a comprehensive study modeling the shallow subsurface viscosity of Europa. However, various authors (Jara-Orué et al., 2011; Kihoulou, 2021) have proposed the use of a cut-off value for viscosity to address the exceptionally high values given by Equation (3.12). Following the suggestion by (Jara-Orué et al., 2011) for Europa's lithosphere, we consider $\eta = 10^{21}\,\mathrm{Pa\,s}$ as a potential viscosity for Europa's icy subsurface. Using Equation (3.10), we find that ice with such viscosity, compacted over 30 million years, yields a compaction coefficient value of $\lambda = 0.9 \times 10^{-6}\,\mathrm{Pa^{-1}}$ and a compaction lengthscale of $H = 880\,\mathrm{m}$. It is noteworthy that the compaction coefficient value, λ, although falling within

the large potential range of values given by Equation 3.10, is of the same order of magnitude as Earth's value, as illustrated in Figure (3.5, white square).

Local-scale processes, such as the formation of chaos terrain or cryovolcanism on Europa, could result in more recent and locally warmer ice, thereby changing the compaction lengthscale.

3.4 Discussion

3.4.1 Depth and Time Dependant Viscosity

The viscosity of ice depends on various factors such as temperature, porosity, stress, and grain size. Across the depths considered in this study, these parameters may vary with depth (e.g., temperature due to a thermal gradient) or with time (e.g., porosity due to viscous pore closure). Our model, primarily focused on the near surface of icy moons, assumes a constant viscosity with depth and time. Here, we discuss both the relevance and limitations of this approach.

3.4.1.1 Porosity Dependant Viscosity

We expect the surface of icy Galilean moons to exhibit high porosity (Black, 2001; Johnson et al., 2017) and studies on porous media (Mackenzie, 1950; Sura et al., 1990) suggest that the viscosity decreases non-linearly with increasing porosity. Theses findings imply that the viscosity of the porous subsurface ice on Europa would be significantly lower than the viscosity of bulk ice. In fact, porous snow on Earth, with a viscosity in the range of $10^4 - 10^9$ Pa s (Mellor, 1974; Bartelt et al., 2000; Camponovo et al., 2001), can be orders of magnitude less viscous than compacted ice at Earth's temperatures, which has a viscosity around 10^{12} Pa s (Fowler, 1997).

Assuming that the viscosity changes with depth would be a more realistic approach but it would require solving both the porosity and viscosity evolution as an iterative and coupled process. While this would be valuable for future research, the primary goal in this study is to present a simple yet analytical form that helps making comparative planetology.

Elastic compaction tends to have porosity that decreases exponentially with depth (S. M. Clifford, 1993; S. Clifford, 2001; Wieczorek et al., 2013). This can be intuited from Equation (3.1), when considering a constant compaction coefficient with depth. Although Equation (3.8) has an exponential form, the porosity profile with depth does not necessary follow an exponential curve. Indeed, for deeper portion of the ice shell the viscosity is the primary driver of ice compaction, and not the overburden pressure. Hence viscous flow tends to have a relatively constant porosity until the temperature is great enough at depth to rapidly close porosity in a geologically short period of time (Besserer et al., 2013; Wieczorek et al., 2013; Gyalay et al., 2020).

3.4.1.2 Variations of Temperature with Depth

For modeling the compaction of near-surface ice, our model assumes a constant temperature, though temperatures may fluctuate within these depths due to a thermal gradient. Here, we quantify the variations of temperatures in the near-surface temperatures and explore their impact on viscosity. The temperature profile in the model by (Nimmo et al., 2003) assumes a mean surface temperature of 100 K for Europa, with results indicating a constant temperature within the first kilometer. Similar results are observed at the near surface of Enceladus (Besserer et al., 2013). The authors (Besserer et al., 2013) propose to use the improved model of conduction, where the changes of conductivity with porosity are taken into account (Shoshany et al., 2002). Even with this refined model, their results indicate that temperature variations with depth is less than 5 K within the first hundred meters. At these depths, tidal heating is negligible (Tobie et al., 2003). Although the ice viscosity is strongly dependent on temperature, minor temperature fluctuations in the near surface, here inferior to 5 K, would only result in a change in viscosity of one order of magnitude. Hence in contrast with the substantial uncertainty in viscosity variations with porosity, temperature variations with depth near the surface do not induce significant viscosity changes. We conclude that adding a comprehensive description of the thermal profile would remove the simplicity of the analytical form, without gaining substantial additional information.

3.4.1.3 Constitutive Flow Laws

An important aspect that has not been developed in our model is the rheology of ice under different stress and grain-size conditions. Goldsby and Kohlstedt (Goldsby et al., 2001) have worked on formulating a constitutive equation for the effective viscosity (Besserer et al., 2013) (or strain-rate) under different creep regimes:

$$\eta(T, P, D) = \left[\eta_{\text{diff}}^{-1} + \eta_{\text{disl}}^{-1} + (\eta_{\text{bas}} + \eta_{\text{gbs}})^{-1}\right]^{-1} \tag{3.13}$$

where D is the grain size and the subscripts diff, disl, bas, and gbs refer to different creep regimes, namely diffusion flow, dislocation creep, basal slip, and grain boundary sliding.

Using the parameters from (Goldsby et al., 2001) [see Tables 5 and 6] we found that at 100 K, the viscosity does not vary significantly within the range of stresses inferior to 0.1 MPa, typical of the near surface conditions on icy moons (see Figure 3.6). However, interpreting these results is challenging, as the temperatures used to obtain the activation energies, around 250 K, are significantly higher than those on icy moons, around 100 K. Since the experimental data have been collected at temperatures around 250 K (viscosity around 10^{12} Pa s), it seems difficult to extrapolate these parameters to icy moons cold environment (viscosity of 10^{31} Pa s on Figure 3.6 at 100 K). Conducting experiments to observe creep behavior in an environment with temperatures similar to those found on icy moons would be beneficial. However, it

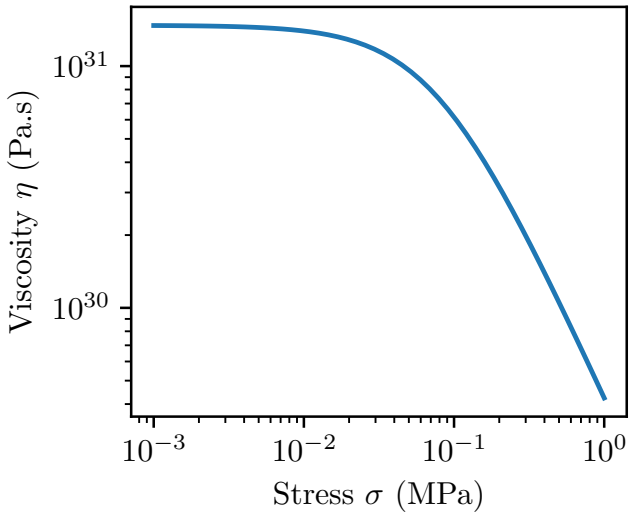

Figure 3.6: Viscosity vs stress using Goldsby's (Goldsby et al., 2001) constitutive equation and parameters for a temperature of 100 K and a grain size of 100 μm.

remains challenging due to the significant timescale for relaxation of ice at such low temperatures.

3.4.2 Comparison with Cold Compaction Experiments

A set of cold compaction experiments (Durham et al., 2005) provided valuable insights into the compaction of cold ice at high pressure (>MPa) over relatively short timescales ($\sim$ 15h). As the authors acknowledged, densification can occur at all pressures, including those lower than the range covered in the experiments. In our study, we have looked at the compaction of ice for lower pressure. At a depth of 100 meters, with, for example, a porous ice density of approximately 500 kg m^{-3}, the overburden pressure is around 0.05 MPa. Although we cannot precisely determine how ice would compact at these pressures, since it is outside the range of the experiments, their results at high pressure suggest that minimal elastic compaction would occur at lower pressure. Such experimental result would mean, that under elastic compression, the compaction coefficient of cold ice $T < 100K$ is significantly lower than the one measured at Earth's temperature, $\overline{\lambda}$. This would lead to a compaction lengthscale significantly higher than the one presented in Table 3.1. If anything, these experiments confirm that it is even more unlikely to see porosity variations at the depth probed by the current remote sensing instruments (except for the upcoming JUNO/MRW data, which may probe depths of dozens of kilometers.).

Another result suggested by these experiments, is that even after high pressure compaction, substantial residual porosity remains. If this is indeed the case, then it would be necessary to change the expression of Equation 3.1 by adding a residual

porosity term:

$$\phi(z) = (\phi_0 - \phi_\infty) \exp(-\lambda P(z)) + \phi_\infty \tag{3.14}$$

where ϕ_∞ is the residual porosity from elastic compaction. Experiments on Earth snow (Cuffey, 2010), suggest that packing can not reduce porosity below 40% and other mechanism must be responsible for further densification. This porosity could be then be removed by viscous creep or by pressure sintering (Cuffey, 2010) over long period of time (millions of years at 120 K). The experiments from (Durham et al., 2005) were conducted over relatively short timescales of about 15 hours, much shorter than the relaxation time of viscous ice at these temperatures. In our study, we looked at the viscous creep of ice over timescales of 200 years on Earth and 30 millions years on Europa. We believe that changes in porosity due to viscous creep over such extended periods could not have been detected in Durham's experiments.

3.5 Conclusion

This study has used Earth ice core measurements to determine a fundamental parameter related to the compaction of ice under the influence of gravity: the ice compaction coefficient. As a result of this analysis, we were able to infer the typical gravity-induced compaction length on Europa of $H = 150 \pm 4$ m, assuming an Earth-like compaction coefficient of ice. By employing the same method, we determined that the compaction lengthscale for icy bodies within the Solar System spans a range from 20 m to 2000 m.

The compaction lengthscale significantly exceeds the wavelengths and penetration depths within the visible and near-infrared ranges, which can extend up to only a few centimeters. Thermal infrared emissions allow to estimate features as deep as the diurnal and seasonal thermal skin depth, which is typically less than ~ 10 cm and less than dozen of meters for Europa, depending on the thermal diffusivity. At such depths, we expect that gravity-induced compaction will lead to relatively minor changes in porosity. Still, recent observations from the JUNO MicroWave Radiometer could probe up to dozens of kilometers deep into the Galilean moons' surfaces (Brown et al., 2023). Incoming analysis of the observations for Europa would reveal new constraints on porosity of the ice shell.

The strength of the models presented in this chapter lies in their simplicity and analytical solutions. Enhancements can be made by considering the strong influence of porosity, temperature, stress and grain size on viscosity and developing a more precise compaction scenario for the crusts of icy moons. Additionally, other compaction mechanisms are likely to come into play near the surface, such as those induced by sputtering or sintering (Schaible et al., 2017; Raut et al., 2008), potentially observable by space instruments. The effect of these mechanisms on the ice porosity profile is not yet fully understood. While dry water ice metamorphism and sputtering-induced sintering have been studied for planetary surfaces (Molaro et al.,

2019; Schaible et al., 2017), their quantitative connection to ice densification is yet to be established.

Given these results, upcoming missions should consider the use of large wavelength radar beams capable of penetrating deep into the subsurface to assess the porosity profile, such as REASON onboard Europa Clipper (Bayer et al., 2019) and RIME onboard JUICE (Bruzzone et al., 2013). Additionally, when considering the potential challenges for landers and rovers (Pappalardo et al., 2013; Hand et al., 2022) to operate on highly porous surfaces and when developing technologies like cryobots (Vale Pereira et al., 2023) for exploring icy crusts and reaching subsurface oceans, it is imperative to account for this substantial compaction lengthscale. Therefore, selecting target locations with low surface porosity would be of major interest in mission planning.

3.6 Appendix on the Rheology of Ice

Standard rheological models, for example the Burgers model (Mellor, 1974), have been used to study the mechanical behavior of snow. Nevertheless, as (Mellor, 1974) pointed at, snow is a much more complicated material than bulk ice, and we currently do not have enough available data to define accurate general constitutive equations. Hence we have to rely on simplifications, such as treating snow as a purely elastic (Wilson et al., 1994) or purely viscous solid (Nimmo et al., 2003).

3.6.1 Purely Elastic Solid

For a a purely elastic solid, the strain is related to the applied stress using Hooke's Law:

$$\epsilon = \frac{\sigma}{E}. \tag{3.15}$$

The strain rate can be expressed as the reduction of the pore radius a as in (Fowler, 1985):

$$\dot{\epsilon} = \frac{da}{dt}\frac{1}{a} \tag{3.16}$$

Then, following (Nimmo et al., 2003), we can express the strain rate as a function of the porosity:

$$\dot{\epsilon} = -\frac{d\phi}{dt}\frac{1}{\phi}. \tag{3.17}$$

Thus, taking the differential of Equation (3.15) and setting the stress equal to the overburden pressure $P(z)$ results in:

$$d\epsilon = -d\phi\frac{1}{\phi} = dP\frac{1}{E} \tag{3.18}$$

where E is the elastic Young modulus. Integrating from $z = 0$ to z:

$$\int_{\phi_0}^{\phi(z)} \frac{1}{\phi} d\phi = -\frac{1}{E}\int_0^{P(z)} dP(z) \tag{3.19}$$

gives the expression of porosity that was assumed by Wilson (Wilson et al., 1994):

$$\phi(z) = \phi_0 \exp\left(-\frac{1}{E}P(z)\right). \tag{3.20}$$

This expression elucidates that the assumption of exponential decay of porosity with pressure can be mathematically derived by assuming that the material is purely elastic. Additionally, using this, we can establish relationship between the compaction coefficient and the inverse of the Young modulus:

$$\lambda = \frac{1}{E}. \tag{3.21}$$

3.6.2 Purely Viscous Solid

For a purely viscous solid, the strain rate of the pores relationship to the stress is given by (Mellor, 1974; Fowler, 1985):

$$\dot{\epsilon} = \frac{\sigma}{\eta} \tag{3.22}$$

By taking the stress to be equal to the overburden pressure $P(z)$, and using (3.17), this leads to the differential equation found in (Fowler, 1985; Nimmo et al., 2003):

$$\frac{d\phi}{dt} = -\phi\frac{P(z)}{\eta} \tag{3.23}$$

Leading to the expression of porosity given by Fowler (Fowler, 1985):

$$\phi(z,t) = \phi_i(z) \exp\left(-\frac{t}{\eta}P(z)\right). \tag{3.24}$$

3.7 Thesis' Supplementary Material

3.7.1 Comparison with other Experiments

A set of experiments by Leliwa-Kopystyński et al. (1995) investigated the compaction behavior of granular ice using a piston-cylinder device under various conditions. Based on their experimental data, they derived the compaction rate of water ice as

$$\frac{\partial \phi}{\partial t} = \mathcal{F}(\phi, P, T) \tag{3.25}$$

where $\mathcal{F}$ is an empirical function, with coefficients for water ice detailed in Leliwa-Kopystyński et al. (1995) (text under Equation 3 of their article).

This expression cannot be directly compared with our formulation, as it does not express porosity as a function of depth; the experiments were conducted under constant pressure. However, we can compare it to Fowler's law, which also expresses the compaction rate as a function of porosity, pressure, and viscosity (see Equation 3.7). By equating the two expressions of the compaction rate from Equation 3.25 and Equation 3.7, we can derive a relationship for viscosity as a function of temperature

$$\eta(T) = -\frac{\phi P}{\mathcal{F}(\phi, P, T)}. \tag{3.26}$$

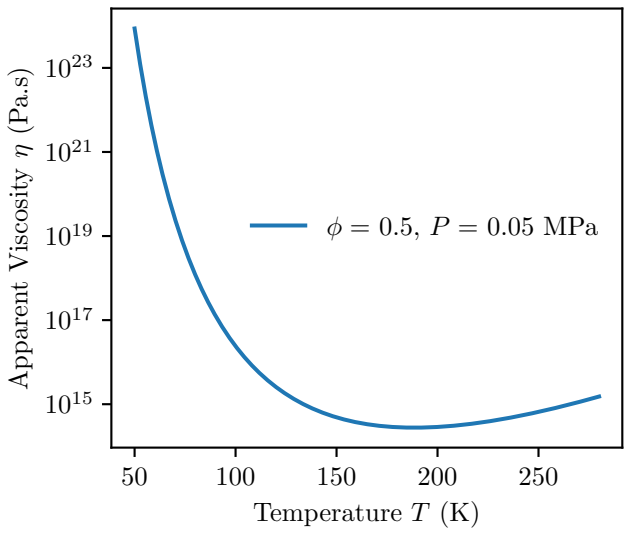

Figure 3.7: Apparent viscosity of the ice as function of temperature based on Leliwa-Kopystyński et al. (1995)'s experiments assuming the compaction rate follows Fowler's law. The porosity and pressure are fixed to typical conditions around 100 m depth on Europa.

Using the empirical function from Leliwa-Kopystyński et al. (1995) at constant pressure, we can deduce the "apparent" viscosity of ice during their experiments.

This is "apparent" in the sense that it represents the viscosity if ice were to follow Fowler's compaction law. Figure 3.7 shows the apparent viscosity as a function of temperature for a constant pressure of $P = 0.05\,\mathrm{MPa}$ and a porosity of $\phi = 50\%$. We chose this pressure, as mentioned in Section 3.4.2, because it is the typical pressure expected around a depth of $\sim 100\,\mathrm{m}$, close to Europa's compaction lengthscale.

We observe that the viscosity in the temperature range of icy moons lies within the expected range for ice in these conditions, between 10^{15} and $10^{23}\,\mathrm{Pa\,s}$. However, above 200 K, the viscosity starts to increase, which is unrealistic and likely indicates a change in the compaction regime. Additionally, around Europa's average surface temperature of 100 K, the apparent ice viscosity from Leliwa-Kopystyński et al. (1995)'s experiments appears to be around $10^{16}\,\mathrm{Pa\,s}$. This value is even lower than our cutoff of $10^{21}\,\mathrm{Pa\,s}$ in Section 3.3.2, suggesting that low-temperature porous ice has a much lower viscosity than the first order estimation by Equation 3.12.

However, it is important to note that this apparent viscosity is highly dependent on porosity and pressure. Since these parameters are not well constrained for the surface of icy moons, the resulting viscosity estimates are also highly uncertain.

3.7.2 Representation of Europa's Gravity-induced Compaction

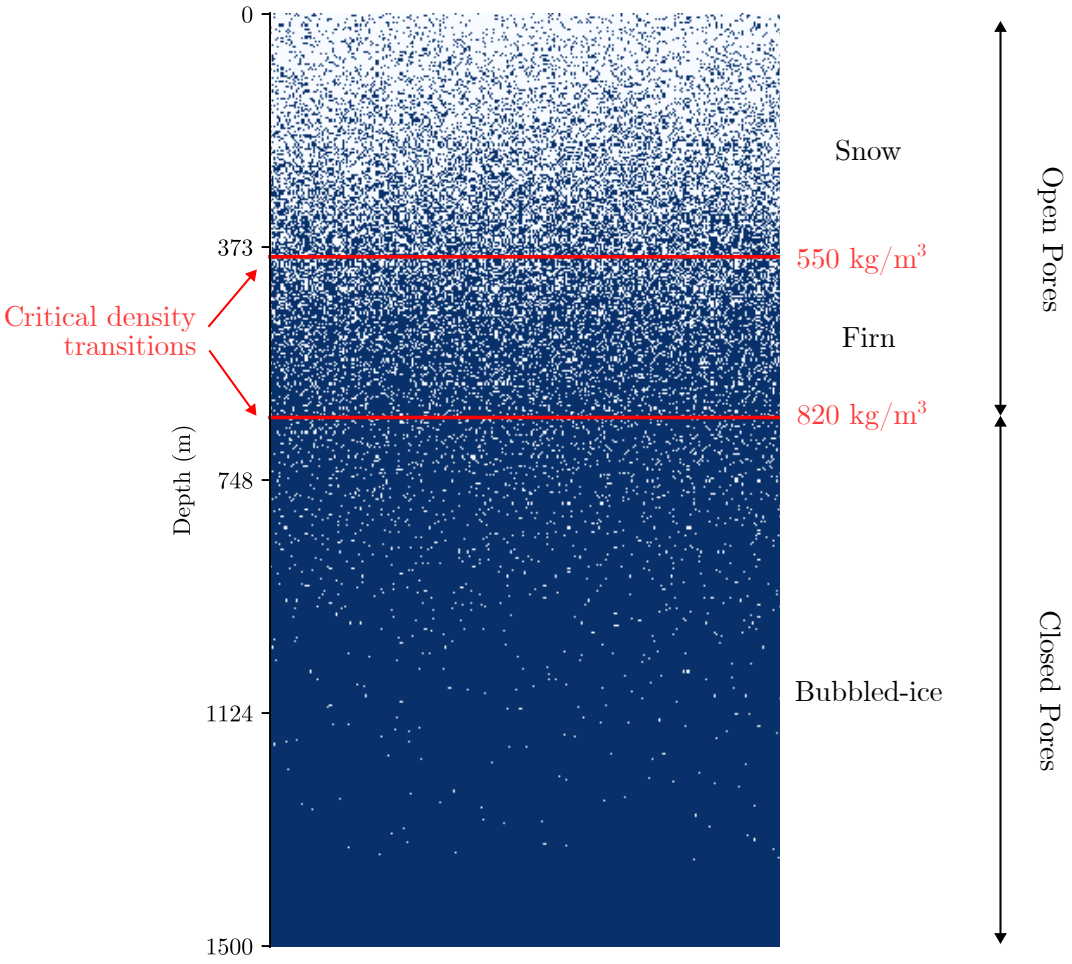

Figure 3.8: Representation of gravity-induced compaction on Europa's surface with an initial surface porosity of 90%. Each row contains a ratio of white pixels to blue pixels corresponding to the porosity value, with pixels randomly distributed on the row. Critical transitions from snow to firn and from firn to bubbled ice are highlighted in red.

Bibliography for Chapter 3

Alley, Richard B., John F. Bolzan, and Ian M. Whillans (1982). "Polar Firn Densification and Grain Growth". In: *Annals of Glaciology* 3, pp. 7–11. DOI: 10.3189/s0260305500002433.

Anderson, J. D. et al. (Sept. 1998). "Europa's Differentiated Internal Structure: Inferences from Four Galileo Encounters". In: *Science* 281.5385, pp. 2019–2022. DOI: 10.1126/science.281.5385.2019.

Arnaud, Laurent, J-M. Barnola, and Paul Duval (2000). "Physical modeling of the densification of snow/firn and ice in the upper part of polar ice sheets". In: *Physics of Ice Core Records*. URL: https://api.semanticscholar.org/CorpusID:55280031.

Bader (1960). "Theory of Densificatioof Dry Snow on HighPolar Glaciers". In: *U. S. ARMY SNOW ICE AND PERMAFROST RESEARCH ESTABLISHMENT*.

Bader, Henri (1954). "Sorge's Law of densification of snow on high polar glaciers". In: *SNOW, ICE AND PERMAFROST RESEARCH ESTABLISHMENT*.

Bartelt, Perry and Markus Von Moos (2000). "Triaxial tests to determine a microstructure-based snow viscosity law". In: *Annals of Glaciology* 31, pp. 457–462. ISSN: 1727-5644. DOI: 10.3189/172756400781819761.

Bayer, Todd et al. (Mar. 2019). "Europa Clipper Mission: Preliminary Design Report". In: *2019 IEEE Aerospace Conference*. IEEE. DOI: 10.1109/aero.2019.8741777.

Berdyugina, S. V. and J. R. Kuhn (Nov. 2019). "Surface Imaging of Proxima b and Other Exoplanets: Albedo Maps, Biosignatures, and Technosignatures". In: *The Astronomical Journal* 158.6, p. 246. ISSN: 1538-3881. DOI: 10.3847/1538-3881/ab2df3.

Besserer, J. et al. (May 2013). "Convection-driven compaction as a possible origin of Enceladus's long wavelength topography". In: *Journal of Geophysical Research: Planets* 118.5, pp. 908–915. ISSN: 2169-9100. DOI: 10.1002/jgre.20079.

Black, G (June 2001). "Icy Galilean Satellites: 70 cm Radar Results from Arecibo". In: *Icarus* 151.2, pp. 160–166. ISSN: 0019-1035. DOI: 10.1006/icar.2001.6615.

Brown, Shannon et al. (June 2023). "Microwave Observations of Ganymede's Sub-Surface Ice: I. Ice Temperature and Structure". In: *Journal of Geophysical Research: Planets* 128.6. ISSN: 2169-9100. DOI: 10.1029/2022je007609.

Bruzzone, L. et al. (July 2013). "RIME: Radar for Icy Moon Exploration". In: *2013 IEEE International Geoscience and Remote Sensing Symposium - IGARSS*. IEEE. DOI: 10.1109/igarss.2013.6723686.

Camponovo, Christian and Jürg Schweizer (2001). "Rheological measurements of the viscoelastic properties of snow". In: *Annals of Glaciology* 32, pp. 44–50. ISSN: 1727-5644. DOI: 10.3189/172756401781819148.

Clifford, S (Nov. 2001). "The Evolution of the Martian Hydrosphere: Implications for the Fate of a Primordial Ocean and the Current State of the Northern Plains". In: *Icarus* 154.1, pp. 40–79. ISSN: 0019-1035. DOI: 10.1006/icar.2001.6671.

Clifford, Stephen M. (June 1993). "A model for the hydrologic and climatic behavior of water on Mars". In: *Journal of Geophysical Research: Planets* 98.E6, pp. 10973–11016. ISSN: 0148-0227. DOI: 10.1029/93je00225.

Cruz-Mermy et al. (Apr. 2023). "Selection of chemical species for Europa's surface using Galileo/NIMS". In: *Icarus* 394, p. 115379. ISSN: 0019-1035. DOI: 10.1016/j.icarus.2022.115379.

Cuffey, Kurt M. (2010). *The Physics of Glaciers*. Ed. by W. S. B. Paterson. 4th ed. Description based on publisher supplied metadata and other sources. San Diego. 1721 pp. ISBN: 9780080919126.

Durham, William B., William B. McKinnon, and Laura A. Stern (Sept. 2005). "Cold compaction of water ice". In: *Geophysical Research Letters* 32.18, n/a–n/a. DOI: 10.1029/2005gl023484.

Ferrari, C. and A. Lucas (Mar. 2016). "Low thermal inertias of icy planetary surfaces". In: *Astronomy and Astrophysics* 588, A133. DOI: 10.1051/0004-6361/201527625.

Fowler, A. C. (Sept. 1985). "A mathematical model of magma transport in the asthenosphere". In: *Geophysical and Astrophysical Fluid Dynamics* 33.1-4, pp. 63–96. DOI: 10.1080/03091928508245423.

— (1997). "Glaciers and ice sheets". In: *The Mathematics of Models for Climatology and Environment*. Springer Berlin Heidelberg, pp. 301–336. ISBN: 9783642606038. DOI: 10.1007/978-3-642-60603-8_9.

Gerland, S. et al. (1999). "Density log of a 181 m long ice core from Berkner Island, Antarctica". In: *Annals of Glaciology* 29, pp. 215–219. DOI: 10.3189/172756499781821427.

Goldsby, D. L. and D. L. Kohlstedt (June 2001). "Superplastic deformation of ice: Experimental observations". In: *Journal of Geophysical Research: Solid Earth* 106.B6, pp. 11017–11030. ISSN: 0148-0227. DOI: 10.1029/2000jb900336.

Gyalay, Szilárd et al. (Aug. 2020). "Constraints on Thermal History of Mars From Depth of Pore Closure Below InSight". In: *Geophysical Research Letters* 47.16. ISSN: 1944-8007. DOI: 10.1029/2020gl088653.

Hand, K. P. et al. (Jan. 2022). "Science Goals and Mission Architecture of the Europa Lander Mission Concept". In: *The Planetary Science Journal* 3.1, p. 22. DOI: 10.3847/psj/ac4493.

Herron, Michael M. and Chester C. Langway (1980). "Firn Densification: An Empirical Model". In: *Journal of Glaciology* 25.93, pp. 373–385. ISSN: 1727-5652. DOI: 10.3189/s0022143000015239.

Hörhold, M. W. et al. (Jan. 2011). "The densification of layered polar firn". In: *Journal of Geophysical Research: Earth Surface* 116.F1, n/a–n/a. DOI: 10.1029/2009jf001630.

Howell, S. M. et al. (Mar. 2021). "Fomenting Chaos: Formation on Europa Through Dry Porous Compaction". In: *52nd Lunar and Planetary Science Conference*. Lunar and Planetary Science Conference, 2423, p. 2423. URL: https://ui.adsabs.harvard.edu/abs/2021LPI....52.2423H.

Hu, Renyu, Bethany L. Ehlmann, and Sara Seager (May 2012). "Theoretical Spectra of Terrestrial Exoplanet Surfaces". In: *The Astrophysical Journal* 752.1, p. 7. ISSN: 1538-4357. DOI: 10.1088/0004-637x/752/1/7.

Jara-Orué, Hermes M. and Bert L.A. Vermeersen (Sept. 2011). "Effects of low-viscous layers and a non-zero obliquity on surface stresses induced by diurnal tides and non-synchronous rotation: The case of Europa". In: *Icarus* 215.1, pp. 417–438. DOI: 10.1016/j.icarus.2011.05.034.

Johnson, Brandon C. et al. (Dec. 2017). "Porosity and Salt Content Determine if Subduction Can Occur in Europa's Ice Shell". In: *Journal of Geophysical Research: Planets* 122.12, pp. 2765–2778. DOI: 10.1002/2017je005370.

Kihoulou, Martin (2021). "Impact crater relaxation throughout the Solar System". In: *Masters Thesis*.

KopystyńSki, J. Leliwa and N. Maeno (1993). "Ice/rock porous mixtures: compaction experiments and interpretation". In: *Journal of Glaciology* 39.133, pp. 643–655. DOI: 10.3189/s0022143000016543.

Leliwa-Kopystyński, J. and K.J. Kossacki (July 1995). "Kinetics of compaction of granular ices H2O, CO2 and (NH3)x(H2O)1 -x at pressures of 2–20 MPa and in temperatures of 100–270 K. Application to the physics of the icy satellites". In: *Planetary and Space Science* 43.7, pp. 851–861. DOI: 10.1016/0032-0633(94)00215-d.

Mackenzie, J K (Jan. 1950). "The Elastic Constants of a Solid containing Spherical Holes". In: *Proceedings of the Physical Society. Section B* 63.1, pp. 2–11. DOI: 10.1088/0370-1301/63/1/302.

Mellor (1974). "A review of basic snow mechanics." In: *The International Symposium on Snow Mechanics*.

Mellor, Malcolm (1977). "Engineering Properties of Snow". In: *Journal of Glaciology* 19.81, pp. 15–66. DOI: 10.3189/s002214300002921x.

Meyer, Colin R. et al. (May 2020). "A model for French-press experiments of dry snow compaction". In: *The Cryosphere* 14.5, pp. 1449–1458. DOI: 10.5194/tc-14-1449-2020.

Mishra, Ishan et al. (Sept. 2021). "A Comprehensive Revisit of Select Galileo/NIMS Observations of Europa". In: *The Planetary Science Journal* 2.5, p. 183. ISSN: 2632-3338. DOI: 10.3847/psj/ac1acb.

Molaro, J. L. et al. (Feb. 2019). "The Microstructural Evolution of Water Ice in the Solar System Through Sintering". In: *Journal of Geophysical Research: Planets* 124.2, pp. 243–277. DOI: 10.1029/2018je005773.

Nimmo, F, R.T Pappalardo, and B Giese (Nov. 2003). "On the origins of band topography, Europa". In: *Icarus* 166.1, pp. 21–32. DOI: 10.1016/j.icarus.2003.08.002.

Oza, Apurva V., Robert E. Johnson, and François Leblanc (May 2018). "Dusk/-dawn atmospheric asymmetries on tidally-locked satellites: O2 at Europa". In: *Icarus* 305, pp. 50–55. ISSN: 0019-1035. DOI: 10.1016/j.icarus.2017.12.032.

Pappalardo, R.T. et al. (Aug. 2013). "Science Potential from a Europa Lander". In: *Astrobiology* 13.8, pp. 740–773. DOI: 10.1089/ast.2013.1003.

Rathbun, Julie A., Nathaniel J. Rodriguez, and John R. Spencer (Dec. 2010). "Galileo PPR observations of Europa: Hotspot detection limits and surface thermal properties". In: *Icarus* 210.2, pp. 763–769. DOI: 10.1016/j.icarus.2010.07.017.

Raut, U. et al. (Nov. 2008). "Cosmic Ray Compaction of Porous Interstellar Ices". In: *The Astrophysical Journal* 687.2, pp. 1070–1074. DOI: 10.1086/592193.

Schaible, M.J. et al. (Mar. 2017). "High energy electron sintering of icy regoliths: Formation of the PacMan thermal anomalies on the icy Saturnian moons". In: *Icarus* 285, pp. 211–223. DOI: 10.1016/j.icarus.2016.08.033.

Shoshany, Yossi, Dina Prialnik, and Morris Podolak (May 2002). "Monte Carlo Modeling of the Thermal Conductivity of Porous Cometary Ice". In: *Icarus* 157.1, pp. 219–227. ISSN: 0019-1035. DOI: 10.1006/icar.2002.6815.

Spencer, John, Larry Lebofsky, and Mark Sykes (Apr. 1989). "Systematic biases in radiometric diameter determinations". In: *Icarus* 78.2, pp. 337–354. DOI: 10.1016/0019-1035(89)90182-6.

Sura, Vivek M. and Prakash C. Panda (Sept. 1990). "Viscosity of Porous Glasses". In: *Journal of the American Ceramic Society* 73.9, pp. 2697–2701. DOI: 10.1111/j.1151-2916.1990.tb06748.x.

Swinkels, F.B. and M.F. Ashby (Feb. 1981). "A second report on sintering diagrams". In: *Acta Metallurgica* 29.2, pp. 259–281. DOI: 10.1016/0001-6160(81)90154-1.

Thomas, Paul J. and Gerald Schubert (Mar. 1986). "Crater relaxation as a probe of Europa's interior". In: *Journal of Geophysical Research: Solid Earth* 91.B4, pp. 453–459. DOI: 10.1029/jb091ib04p0d453.

Tobie, Gabriel, Gaël Choblet, and Christophe Sotin (Nov. 2003). "Tidally heated convection: Constraints on Europa's ice shell thickness". In: *Journal of Geophysical Research: Planets* 108.E11. ISSN: 0148-0227. DOI: 10.1029/2003je002099.

Vale Pereira, Paula do et al. (May 2023). "Experimental Validation of Cryobot Thermal Models for the Exploration of Ocean Worlds". In: *The Planetary Science Journal* 4.5, p. 81. DOI: 10.3847/psj/acc2b7.

Wieczorek, Mark A. et al. (Feb. 2013). "The Crust of the Moon as Seen by GRAIL". In: *Science* 339.6120, pp. 671–675. ISSN: 1095-9203. DOI: 10.1126/science.1231530.

Wilkinson, D.S. (1988). "A Pressure-sintering Model for the Densification of Polar Firn and Glacier Ice". In: *Journal of Glaciology* 34.116, pp. 40–45. DOI: 10.3189/s0022143000009047.

Wilson, Lionel and James W. Head (1994). "Mars: Review and analysis of volcanic eruption theory and relationships to observed landforms". In: *Reviews of Geophysics* 32.3, p. 221. DOI: 10.1029/94rg01113.

Zahnle, Kevin et al. (June 2003). "Cratering rates in the outer Solar System". In: *Icarus* 163.2, pp. 263–289. ISSN: 0019-1035. DOI: 10.1016/s0019-1035(03)00048-4.

Figure 3.9: What is the surface of Europa like? There is currently not enough data to tell, but models show that it's likely very porous for at least several meters. Could we just drop down a man from space? Probably not, but one can always dream. Original creation for this thesis from the artist @FMdessine, representing an "astronaut" resting on the snowy surface of Europa.

CHAPTER 4

Ice Sintering

The work presented in this chapter comes from the article titled *"LunaIcy: Exploring Europa's Icy Surface Microstructure through Multiphysics Simulations" by C. Mergny and F. Schmidt, 2024* The Planetary Science Journal, DOI 10.3847/PSJ/ad6d6d

Contents

Foreword

Ice Sintering, Metamorphism, Annealing — Dry snow consist of an ice network with interstitial pores filled with a mixture of air/void and water vapor (see Figure 4.1). Over time, "bonds" or "necks" form between particles in a process known as sintering. This inter-granular bonding of snow grains influences the material's strength, viscosity, creep, and thermal, optical, and electromagnetic properties (Adams et al., 2001). The study of ice sintering was initiated by Kingery et al. (1955), who measured the growth of necks formed between two ice spheres in contact as functions of time, temperature, and sphere radius.

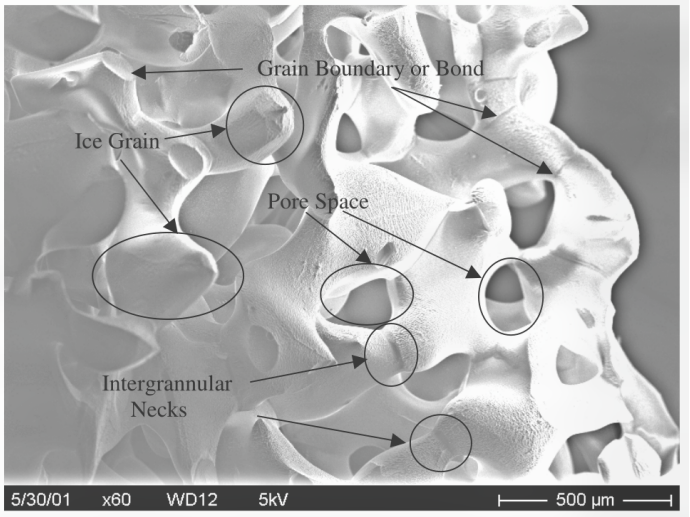

Figure 4.1: Scanning Electron Microscope (SEM) image identifying typical microstructural features of snow that has been kept under macroscopically isothermal conditions. Figure from D. A. Miller (2002).

Six mass-transport mechanisms were assumed to contribute simultaneously and independently to the growth of bonds between particles ((Figure 4.2): surface diffusion from a surface source (Kuczynski, 1949), lattice diffusion from a surface source (Kuczynski, 1949), vapor transport from a surface source (Hobbs et al., 1964), boundary diffusion from a grain boundary source (Johnson, 1969; Colbeck, 1998; Adams et al., 2001), lattice diffusion from a grain boundary source (Ashby, 1974), and lattice diffusion from dislocation sources (Ashby, 1974). Particular diffusion mechanisms may dominate the sintering rates during different stages, under varying temperature and atmospheric conditions, at depth or on the surface, or in different materials.

Diffusion by Vapor Transport... — A question that arises is which mechanisms, if any, are predominant and whether any can be neglected. Several theoretical and experimental studies have addressed this issue. Hobbs et al. (1964) presented convincing arguments pointing to vapor diffusion as the dominant sintering mechanism.

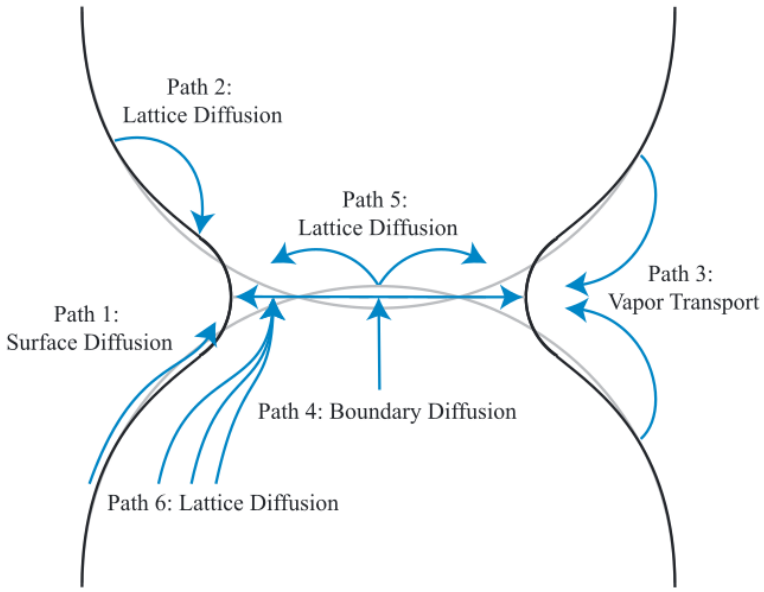

Figure 4.2: Two spherical grains forming a bond by different types of diffusion mechanisms. Figure from Molaro et al. (2019).

Maeno et al. (1983) later confirmed that vapor transport is dominant, except under certain temperature and geometric conditions where surface diffusion may be significant. Until recently, the scientific consensus for at least the previous 40 years has been that vapor diffusion is the primary sintering mechanism ; other mechanisms are probably at work but at rates much lower than vapor diffusion. This also applies to planetary conditions. The review on ice sintering for planetary surfaces by Blackford (2007) shows that for the low temperatures and pressures of icy planetary surfaces, vapor transport is still the dominant diffusion process of ice metamorphism (see Figure 10 of their paper).

This process of diffusion by vapor transport was described by Colbeck (1980) as “radius of curvature metamorphism". At a given temperature, vapor pressures over convex surfaces are greater than those over a flat surface, while vapor pressures over concave surfaces are lower than those over a flat surface. As a result, molecules sublimate from the convex surfaces, travel through the pore space, and deposit on the concave neck between grains (see Figure 4.3). More details and fundamental equations are given in this Chapter.

... Does not Lead to Densification. — This diffusion by vapor transport is termed a "non-densifying" mechanism: it redistributes mass from grains to bonds without reducing pore size. For some reasons, it is commonly assumed by the planetary science community that sintering leads to densification of the ice layer. While vapor transport creates bonds that make the ice structure more cohesive, it does not

increase the ice's density in any way. Also, smaller grains sublimate faster than large ones, which can lead to a sorting phenomenon. Among the other diffusion mechanisms previously presented, some lead to densification, but as discussed, there are not expected to be efficient in planetary conditions.

Although work by Eluszkiewicz (J. Eluszkiewicz, 1990; Eluszkiewicz, 1991; Eluszkiewicz, 1993) presents some form of ice densification through sintering, their expressions are derived from "an unpublished internal report by Ashby 1988," which existence cannot be verified (Molaro et al., 2019). Without a way to verify these equations or understand their origin, we cannot rely on these studies. Therefore, it is important to remember that the expected dominant sintering mechanism for planetary icy surfaces, vapor transport, does not lead to any ice compaction.

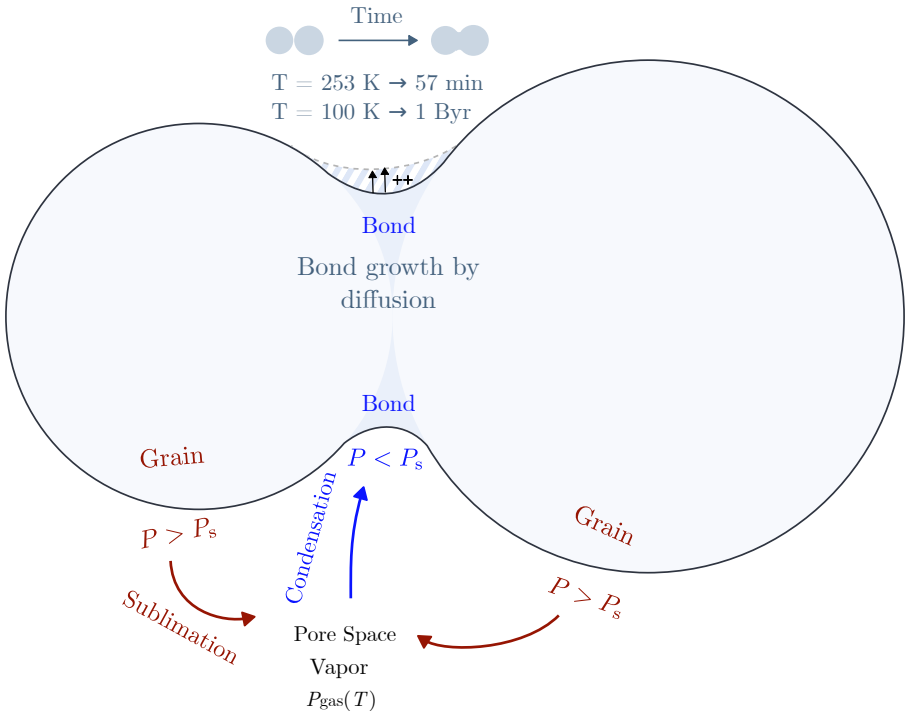

Figure 4.3: Diffusion through vapor transport. Due to curvature matter sublimates from the convex grain surfaces, diffuses through the pore space and then condenses on the concave bond surfaces.

Existing Models and Motivations for Refinements — To our knowledge, all the existing literature in planetary science that has modeled the sintering of ice (Eluszkiewicz, 1991; Kossacki et al., 1994; Gundlach et al., 2018; Molaro et al., 2019) is based on the fundamental equations from Swinkels et al. (1981). Swinkels et al. (1981) studied the sintering of metals, an important process in metallurgy to

assess the strength, density, and other bulk properties of the metal. Their article established a foundational basis for the study of sintering and as such, has been widely used by the planetary community to study similar processes on icy surfaces.

The initial plan of this PhD was to directly integrate the diffusion equation used in the literature into our multiphysics model. To adapt these equations to our geometry, we have look for the mathematical justification for the curvature difference in the vapor transport equation (Equation 3 of Table 2 of (Swinkels et al., 1981)). In fact, the concept of curvature difference was first mentioned in 1974 by Ashby (1974). In this first report, the authors state, "*Mechanisms which transport matter from one part of the pore to another are driven by the differences in curvature around the pore itself: between the [grain and the bond].*" They then proceed to cite Kingery et al. (1955) as the source of the vapor transport equation.

However, upon examining the details of Kingery et al. (1955), such a difference in curvature between grains and bonds never appears in their pioneering article (see their Equations 2-5). The two fundamental equations used are Kelvin Equation and the Langmuir Equation, also known as Hertz-Knudsen Equation (see details in Section 4.2.2.1), where only the bond curvature intervenes. In a sense, it is understandable that Ashby and Swinkels intuitively linked the sublimation of grains to the condensation rate of the neck and vice versa, as they likely influence each other. However, the origin of the difference of curvature in (Ashby, 1974) and all subsequent articles based on it has, to our knowledge, never been mathematically justified.

This chapter presents our efforts to 1) refine the sintering model to include a more accurate description of the exchange with the pore space and 2) couple the sintering model to a thermal solver to study its effects on Europa's surface over a million-year timescale.

Abstract

A multiphysics simulation model incorporating a sintering model coupled with the MultIHeaTS thermal solver, was developed to study the evolution of icy moons' microstructure. The sintering process is highly dependent on temperature, and this study represents the first attempt in planetary science to examine the coupled interaction between heat transfer and sintering. Our approach to ice sintering is based upon the literature, while offering a refined description of the matter exchange between grains, bonds, and the pore space. By running the numerical framework, we simulate the evolution of ice microstructure on Galilean satellites, specifically tracking the changes in the ice grain and bond radii over time. LunaIcy, our multiphysics model, was applied to study the evolution of Europa's ice microstructure over a million years along its orbit, with a parameter exploration to investigate the diverse configurations of the icy surface. Our results indicate that effective sintering can take place in regions where daily temperatures briefly surpass 115 K, even during short intervals of the day. Such sintering could not have been detected without the diurnal thermal coupling of LunaIcy, due to the cold daily mean temperature. In these regions, sintering occurs within timescales shorter than Europa's ice crust age, suggesting that, in present times, their surface is made of an interconnected ice structure.

Author's Note

Some of the work presented in this chapter is currently going under revision. While some modifications to the sintering model suggested by the reviewers may lead to slightly different results, they will not change the overall conclusions.

4.1 Introduction

The surfaces of icy moons have a microstructure shaped by a complex interplay of physical processes. Among them, ice *sintering*, also known as *annealing* or *metamorphism*, transports material from ice grains into their bond region, resulting in changes in the thermal, optical and mechanical properties of the ice (Adams et al., 2001; Blackford, 2007).

On Earth, the sintering process is typically studied using ice samples of snow, firn or ice. Using these ice core measurements, snow metamorphism is implemented in a phenomenological way through a set of quantitative laws describing the evolution rate of bond and grain radii. The state of the ice or snow, whether it is dry or wet, if it possesses a temperature gradient or not, significantly influences the conditions of sintering, resulting in different types of rate equations (Vionnet et al., 2012). From these empirical laws, multiphysics snow cover models such as SNTHERM (Jordan, 1991), CROCUS (Brun et al., 1992; Vionnet et al., 2012) or SNOWPACK (Lehning et al., 2002), can simulate the evolution of the ice microstructure as a function of the environmental conditions.

While the sintering process of snow on Earth has been extensively studied, there is a scarce amount of information regarding the alteration of ice in planetary surface environments characterized by low temperatures and pressures. In the planetary science community, the basis for the sintering equations originates from (Swinkels et al., 1981), where the sintering of grains is studied for metallurgy. These equations have been applied to the sintering process on comet surfaces (Kossacki et al., 1994), Mars (J. Eluszkiewicz, 1993) and the surfaces of icy moons (Eluszkiewicz, 1991; Eluszkiewicz, 1993; Schaible et al., 2017; Gundlach et al., 2018; Molaro et al., 2019; Choukroun et al., 2020).

The kinetics of sintering are highly dependent on temperature (Molaro et al., 2019), so achieving a precise temperature estimation is essential for accurately characterizing this process. However, such investigation has not been conducted primarily due to a significant challenge: the substantial difference between the surface temperature variations timescale and the sintering timescale under cold conditions. In this study, we introduce a multiphysics model to investigate how thermal coupling influences the sintering process in simulations covering a timeframe of one million years.

While the sintering process and the methodology used here can be applied to any

icy surface in the Solar System, our primary focus is to investigate the evolution of Europa's ice microstructure. An estimation of the sintering timescale on Europa at constant temperature leads to a lower limit of 10^4 years and upper limit of 10^9 years (Molaro et al., 2019). The authors suggested that, in reality, the daily variations of temperature would need to be taken into account to obtain the accurate sintering timescale falling between these two limits. This aspect is particularly intriguing given Europa's estimated ice crust age of 30 million years (R. T. Pappalardo et al., 1998) leading the question: Does Europa's ice microstructure evolve on a timescale shorter than its ice crust age? If so, what are the conditions on specific parameters (albedo, grain size, latitude, ...) necessary for sintering? Answering these questions would provide valuable insights into the current state of Europa's ice microstructure.

Inspired by snow cover models used on Earth, we developed a first-generation multiphysics model to simulate ice microstructure on planetary surfaces. The following section is dedicated to the description of the sintering model, the third section to the multiphysics coupling, and results and discussion are presented in the fourth section.

4.2 Sintering Model

Early studies on sintering (Kingery et al., 1955; Hobbs et al., 1964; Swinkels et al., 1981; Maeno et al., 1983) have identified six mechanisms of diffusion for the sintering process. In the conditions of low temperatures found on icy moons, the dominant mechanism is diffusion by vapor transport between the grain and bond surfaces via the pore space (Kossacki et al., 1994; Blackford, 2007; Gundlach et al., 2018; Molaro et al., 2019). The convex grain surface sublimates matter into the pore space, which then condenses on the concave bond surface. This diffusion of water vapor occurs as a result of the different curvatures of the grain and bond surfaces, which changes the local saturation pressure. In order to quantify this process, we have developed a model to describe the evolution of gas mass within the pore space over time.

The focus of this approach is to accurately describe the exchange of matter between the grain, the bond and the pore space. Previous models used in planetary science, directly compute the mass flux from the grain surface to the bond surface, as it was suggested by Swinkels et al., 1981. However this difference of curvature between the grains and bonds, does not appear in any of the analytical models of sintering used on Earth (D. Miller et al., 2003; Flin et al., 2003; Flanner et al., 2006). The evaporation-condensation laws may have been incorrectly used for planetary cases, as they do not seem to properly described the exchange of matter between the ice and the gas in the pore space. To address this, in our model, we calculate both mass fluxes separately, the flux of matter from the grain surface to the pore space and the flux between the pore space and the bond.

4.2.1 Model Geometry

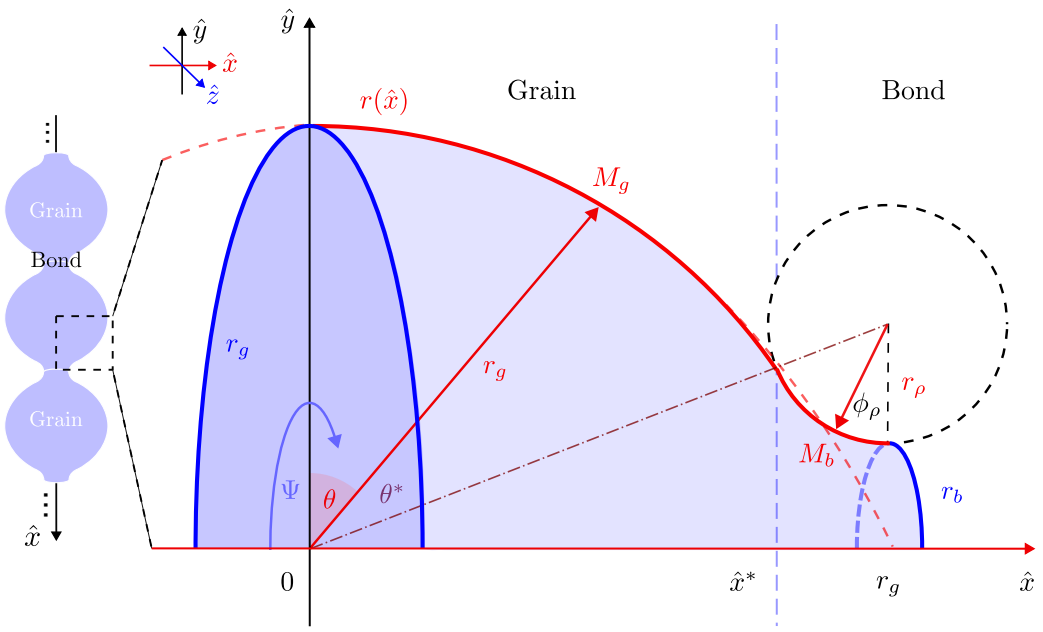

Figure 4.4: (*Left*) Grain/bond pattern repeated periodically along the $\hat{x}$ axis. Each grain is connected to its neighbors by top and bottom bonds. (*Right*) Schematic representation of the grain/bond geometry. Due to symmetry along two axes represented here, our model only needs to represent a quarter of total grain/bond volume. The red line follows the curvature of the vapor/ice interface along the $\hat{x}$ axis, while the blue line follows the curvature in the $\hat{y}\hat{z}$ plane.

The model assumes that grains are completely spherical, with a radius r_g, connected with concave bonds of radius r_b. The initial bond radius is set by the radius of contact when two grains come into contact. For ice grains, this adhesion stage occurs due to the Van der Waals interaction between particles, leading to the expression of the bond radius (Molaro et al., 2019):

$$r_\mathrm{b} \approx \left(\frac{\gamma r_\mathrm{g}^2}{10\mu}\right)^{1/3} \tag{4.1}$$

where γ is surface tension of water ice and μ its shear modulus given in Table 4.2.

Following Swinkels et al., 1981; Molaro et al., 2019 with no densification, the radius of the imaginary circle between grains (see Figure 4.4) is geometrically defined as

$$r_\rho = \frac{r_\mathrm{b}^2}{2(r_\mathrm{g} - r_\mathrm{b})}. \tag{4.2}$$

The $\hat{x}$ axis follows the direction from the grain center towards the bond center. The model considers the grain and bond separately; the transition between the two

occurring at a distance $\hat{x}^*$ from the grain center:

$$\hat{x}^* = r_\mathrm{g} \sin \theta^* \tag{4.3}$$

where θ^* is given by:

$$\theta^* = \arctan \frac{r_\mathrm{g}}{r_\mathrm{b} + r_\rho}. \tag{4.4}$$

The surface curvature is defined as the inverse of the radius of curvature. The grain area, left of $\hat{x}^*$, is considered to have a constant curvature K_g, given by

$$K_\mathrm{g} = \frac{2}{r_\mathrm{g}}. \tag{4.5}$$

The bond area, right of $\hat{x}^*$, is assumed to have a constant curvature K_b calculated by the sum of curvatures along the two relevant axes ($\hat{x}$ in red and $\hat{y}$ in blue on Figure 4.4)

$$K_\mathrm{b} = \frac{1}{r_\mathrm{b}} - \frac{1}{r_\rho}. \tag{4.6}$$

In reality, the transition between the grain and bond is smooth, with local changes in curvature near the interface. However, given the smaller bond radius compared to the grain radius, the surface affected by such changes is relatively small and thus not considered. Nonetheless, exploring this aspect in further studies could prove valuable, particularly when the bond radius approaches the size of the grains.

4.2.2 Vapor Transport Diffusion

The pore space is modeled as a reservoir of volume V_p and an initial gas pressure $P_\mathrm{gas}(t = 0)$ (see Figure 4.5). The relationship between the gas pressure P_gas and total mass of matter in the box, m_gas, is given by the ideal gas law

$$P_\mathrm{gas} = \frac{m_\mathrm{gas} R T}{V_\mathrm{p} M}. \tag{4.7}$$

The gas mass variations in the pore space result from the flux of matter coming from the neighboring grain and bond and will continue to change until reaching a steady state.

One of the key benefits of such modelization is that no assumptions are made regarding the initial gas pressure. For example if the initial gas pressure is zero, both the grain and bond will sublimate to fill the pore space. The model does not enforce a particular direction of transport, it is only when the gas pressure in the pore space approaches the saturation vapor pressure over a flat surface that matter will naturally sublimate from the convex grain surface and condense on the concave bond surface.

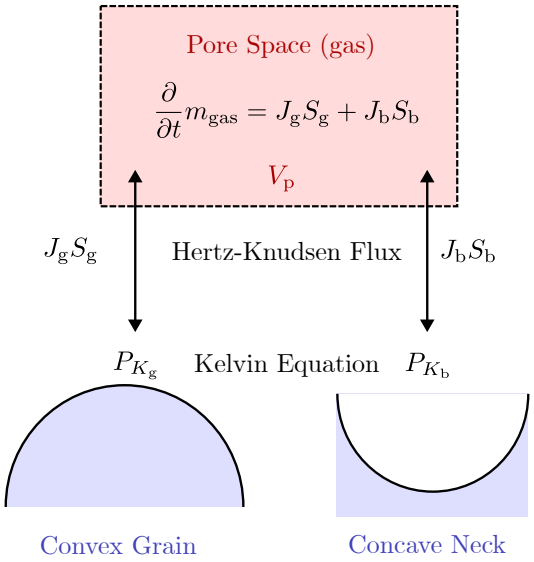

Figure 4.5: Schematic representation of diffusion by vapor transport. The grain and bond surfaces exchange matter with the surrounding gas in the pore space.

4.2.2.1 Reaching the steady state

Our model computes the gas mass variations over time using the sum of the Hertz–Knudsen flux (J_{g}, J_{b}) multiplied by their respective area of exchange (S_{g}, S_{b})

$$\frac{\partial}{\partial t} m_{\text{gas}} = J_{\text{g}} S_{\text{g}} + J_{\text{b}} S_{\text{b}}. \tag{4.8}$$

The mass fluxes arriving in the gas phase are calculated using the Hertz–Knudsen equation (Schrage, 1953; Jones, 2018), from the difference between the gas vapor pressure $P_{\text{gas}}(t)$ and the modified saturated vapor pressure due to curvature $P_{K_{\text{j}}}$:

$$J_{\text{j}} = \alpha \left(P_{K_{\text{j}}} - P_{\text{gas}}(t) \right) \sqrt{\frac{M}{2\pi R T}} \tag{4.9}$$

where the subscript j represent the grain or bond, α is the sticking coefficient, M is the molar mass of water, R the gas constant. The modified saturated vapor pressure due to curvature $P_{K_{\text{j}}}$ is obtained from Kelvin equation (Butt, 2003)

$$P_{K_{\text{j}}} \approx P_{\text{s}}(T) \left(1 + \frac{\gamma M}{R T \rho_0} K_{\text{j}} \right). \tag{4.10}$$

where ρ_0 is the bulk ice density and $P_{\text{s}}(T)$ is the saturated water vapor pressure over a flat surface, given by Feistel et al. (2007).

Using Equations 4.9 and 4.10 we can re-write Equation 4.8 as

$$\frac{\partial}{\partial t} m_{\text{gas}} = \alpha P_{\text{s}}(T) \left[S_{\text{b}} + S_{\text{g}} + \frac{\gamma M}{RT\rho_0} \left(S_{\text{b}} K_{\text{b}} + S_{\text{g}} K_{\text{g}} \right) \right] \frac{2}{\pi \langle v \rangle} - \alpha P_{\text{gas}}(t)(S_{\text{b}} + S_{\text{g}}) \frac{2}{\pi \langle v \rangle}. \tag{4.11}$$

where $\langle v \rangle = \sqrt{8RT/M\pi}$ is the mean velocity of gas particles following a Boltzmann distribution. Using Equation 4.7, this leads to a first-order differential equation for the gas mass

$$\frac{\partial}{\partial t} m_{\text{gas}} + \frac{m_{\text{gas}}}{\tau_{\text{gas}}} = \frac{m_\infty}{\tau_{\text{gas}}} \tag{4.12}$$

with general solutions of the form

$$m_{\text{gas}}(t) = C\, e^{-t/\tau_{\text{gas}}} + m_\infty \tag{4.13}$$

where C is a constant to be determined. From this formulation, appears a characteristic timescale for the gas mass variations τ_{gas}, expressed as

$$\tau_{\text{gas}} = \frac{4V_{\text{p}}}{\alpha(S_{\text{g}} + S_{\text{b}})\langle v \rangle} \tag{4.14}$$

and the gas mass at the steady state m_∞ given by

$$m_\infty = \alpha \tau_{\text{gas}} P_{\text{s}}(T) \left[S_{\text{b}} + S_{\text{g}} + \frac{\gamma M}{RT\rho_0} \left(S_{\text{b}} K_{\text{b}} + S_{\text{g}} K_{\text{g}} \right) \right] \frac{2}{\pi \langle v \rangle} \tag{4.15}$$

By obtaining m_∞ we get access to the gas pressure at the steady state as computed in Appendix 4.7, which will be used to compute the mass transfer in the steady regime.

4.2.3 Incrementing the Grain and Bond Masses

Now that the gas pressure in the steady state has been obtained, the sublimation and condensation flux can be calculated using Hertz–Knudsen flux (Equation 4.9) and the vapor pressure Kelvin Equation (4.10) for the grain or bond curvature. To maintain numerical stability, it is necessary that the sintering timestep is significantly smaller than the characteristic bond growth timescale: $\Delta t_{\text{sint}} << \tau_{\text{sint}}(r_{\text{b}})$. This ensures that only a small fraction of grain and bond mass is altered, allowing us to assume constant grain geometry throughout a single iteration. The updated grain and bond masses m_{g} and m_{b} are calculated using

$$m_{\text{j}}(t + \Delta t_{\text{sint}}) = m_{\text{j}}(t) - J_{\text{j}}(t) S_{\text{j}} \Delta t_{\text{sint}} \tag{4.16}$$

where J_{j} is the Hertz–Knudsen flux in the steady state, with a negative sign because it represents mass entering the pore space and S_{j} is the surface area in contact with the interface. The analytical expression of the surfaces areas in contact with the phase exchange are determined using geometrical considerations (see Appendix 4.6.1), knowing that due to symmetry only a quarter of the total grain/model system needs to be represented.

4.2.4 Updating the geometry

Once new masses have been calculated for the grain and bond, the corresponding volumes $V_\mathrm{g}, V_\mathrm{b}$ are numerically obtained by multiplying these masses with the bulk density of ice

$$V_\mathrm{j}(t + \Delta t_\mathrm{sint}) = \frac{m_\mathrm{j}(t + \Delta t_\mathrm{sint})}{\rho_0} \tag{4.17}$$

To retrieve the resulting new grain and bond radii r_g, r_b, we need to obtain the relationship between the radii and volumes. Using geometrical considerations, we can derive the analytical relationship between the grain and bond radii and their respective volumes v_g, v_b (see Appendix 4.6.1).

The issue is that there is no direct analytical equation that gives the grain or bond radii $r_\mathrm{g}, r_\mathrm{b}$ as functions of their volumes. To address this, from the analytical expression of the grain volume (Equation 4.40) and bond volume (Equation 4.44) we use the Newton-Raphson method to find the updated values of r_g and r_b. This method finds the roots of the difference between the numerically computed volumes V and the analytically obtained volumes v:

$$r_\mathrm{g}(t + \Delta t_\mathrm{sint}) = \min_{r_\mathrm{g}} |V_\mathrm{g}(t + \Delta t_\mathrm{sint}) - v_\mathrm{g}(r_\mathrm{g}, r_\mathrm{b}(t))| \tag{4.18}$$

$$r_\mathrm{b}(t + \Delta t_\mathrm{sint}) = \min_{r_\mathrm{b}} |V_\mathrm{b}(t + \Delta t_\mathrm{sint}) - v_\mathrm{b}(r_\mathrm{g}(t), r_\mathrm{b})| \,. \tag{4.19}$$

Once the Newton-Raphson algorithm gives the updated values of the grain and bond radii, the other geometric parameters r_ρ, θ^*, $\hat{x}^*$, K_g and K_b are updated accordingly. Upon finding the updated geometry, the algorithm is ready to determine a new steady state and repeat the process iteratively.

4.2.5 Comparison with Experimental Data

To confront our analytical model against real-world sintering scenarios, we compare it to a well-known experiment on ice sintering conducted by Hobbs et al. (1964). This comprehensive study involved spherical particles ranging from 50 to 700 µm in diameter, exposed to temperatures between −3 °C and −20 °C. After approximately one hour, bond growth was observed, regulated by the vapor supply originating from nearby regions (Blackford, 2007). Based on their findings, the authors concluded that vapor transport serves as the dominant mechanism in the sintering process.

The evolution of the relative bond radius from the −3 °C experiments, conducted for grain radii of 35 µm, 100 µm, and 200 µm, is illustrated in Figure 4.6 (marked with crosses). To compare our model with the experiments, we need to assign a value to the sticking coefficient α, which is poorly known but we take the advantage of thesei experimental data to estimate it. By setting our sticking coefficient value to $\alpha = 0.03$, we are able to effectively fit all the experiments, regardless of grain size.

The sticking coefficient value used in our model is notably low compared to values reported in the literature, such as 0.75 at 140 K (Haynes et al., 1992). According to

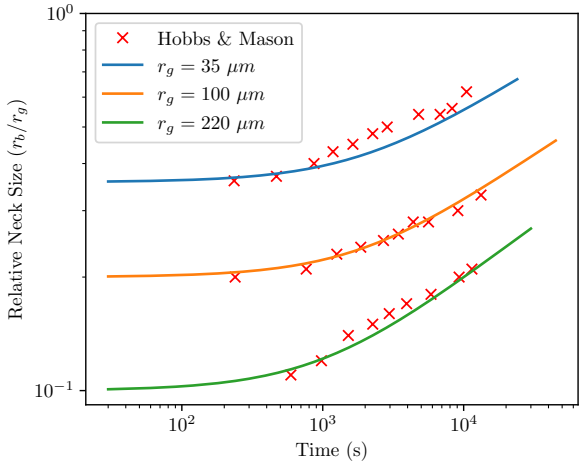

Figure 4.6: Evolution of the relative bond radius $r_\mathrm{b}/r_\mathrm{g}$ in Hobbs et al. (1964) experiments (crosses) for different grain sizes at a constant temperature $-3\,^\circ\mathrm{C}$. With a single value of the sticking coefficient $\alpha = 0.03$, the model (lines) can accurately compute the relative bond radius evolution for the three experiments.

the extrapolation of Haynes et al. (1992), the sticking coefficient would be expected to be around 0.5 at the temperature of the experiment of $-3\,^\circ\mathrm{C}$ used in Figure 4.6. Despite also fitting the data at $-10\,^\circ\mathrm{C}$, $-15\,^\circ\mathrm{C}$, and $-20\,^\circ\mathrm{C}$, the sticking coefficient remains very low without a clear trend as the temperature decreases. Therefore, in our model, the sticking coefficient functions more as a fitting parameter rather than reflecting a physical property. We anticipate that future experimental and theoretical research will provide further insights into this issue.

However, the ability to use a single value of the sticking coefficient to fit the three experiments conducted under different grain size conditions is indicative of a consistent physical description, demonstrating robustness in the model's approach across varying grain sizes. This agreement also validates our approach.

4.2.6 Varying Number of Bonds per Grain

The previously defined geometry assumed that each grain is connected to its neighbors by two bonds, while in real cases, the number of bonds per grain may vary. To estimate this influence, we adapted our model to three scenarios: a grain connected by a single bond, by two bonds as initially presented, and by six bonds (two in each direction). These modifications change the geometry of the grain-bond system, with detailed surface and volume derivations provided in Appendix 4.6.

Using a reference scenario at a fixed temperature of $T = 150\,\mathrm{K}$ and a grain size of $r_\mathrm{g} = 100\,\mu\mathrm{m}$, we plotted the different evolutions of the grain and bond radii over time for varying bonds-per-grain values in Figure 4.7 (*Left*). Firstly, the results

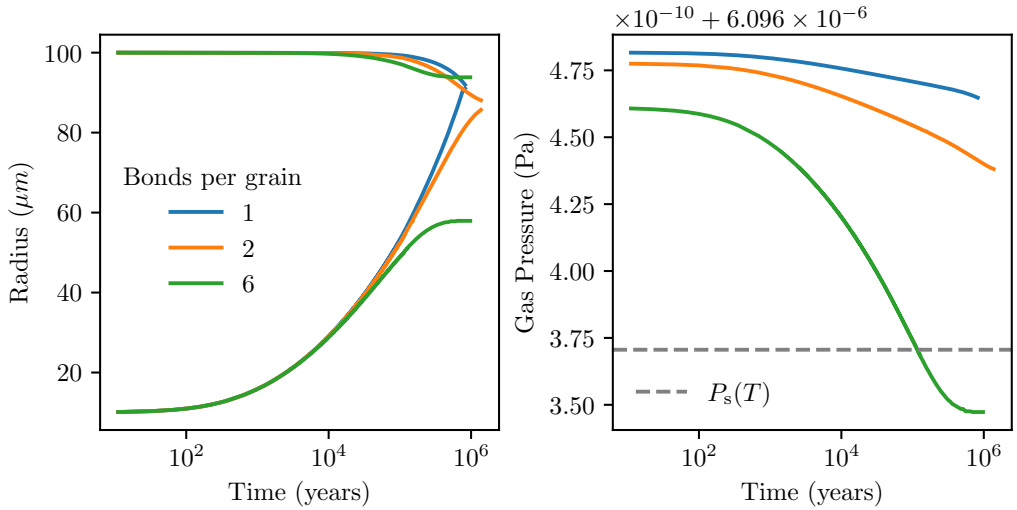

Figure 4.7: (*Left*) Evolution of grain radius (top) and bond radius (bottom) over time at $T = 150\,\mathrm{K}$ for different bond-per-grain scenarios (1, 2, and 6). (*Right*) Evolution of gas pressure P_{gas} over time for different bond-per-grain scenarios (1, 2, and 6). The gray dashed line represents the saturated vapor pressure over a flat surface at $T = 150K$.

show that up to about half of the bond's final size, its evolution does not depend on the number of bonds per grain. However, in the late stage of sintering, differences emerge. For the two bonds per grain case, after significant time, the surface of the bond-grain system becomes almost completely flat with the bond radius nearing that of the grain. In the six bonds per grain scenario, the late stage of sintering is limited by competition among bonds for condensation, resulting in an equilibrium where the bond radius is smaller than the final grain radius. In the single bond per grain scenario, the bond growth does not follow an asymptote. Our explanation is that while one hemisphere of the grain connected to the bond will eventually flatten, the other hemisphere, not connected to a bond, remains spherical. Thus, sublimation of the unconnected hemisphere continues to provide matter for condensation over the flat bond. Note that, simulations were stopped when the bond radius reached values too close to the grain radius, as this induces computational errors.

The simulations also allow us to track the evolution of gas pressure over time in the pore space for different bonds per grain scenarios, as shown in Figure 4.7 (*Right*). Firstly, we observe that the equilibrium gas pressure is always different from the saturated vapor pressure over a flat surface. In most scenarios, the gas pressure is higher than the saturated vapor pressure, with fewer bonds per grain leading to more convex surfaces and consequently higher gas pressure. Interestingly, in the case of six bonds per grain, when the bonds reach a critical radius (after around 100,000 years in Figure 4.7), the gas vapor pressure drops below the saturated vapor

pressure over a flat surface. In this case, the system becomes dominated by concave surfaces formed by the bonds, resulting in lower gas pressure.

While these late-stage evolution scenarios provide new results on the sintering behavior under different grain environment, they should be considered with caution, as other diffusion mechanisms could become predominant at this stage (further discussed in Section 4.3.1), and vapor transport sintering may become irrelevant after a certain bond threshold (Molaro et al., 2019).

4.2.7 Sintering Timescales

The equivalent behavior of the different bond-per-grain scenarios in the initial to mid stages of sintering allows us to define a unique characteristic sintering timescale irrespective of the number of bonds per grain. We choose to define the sintering timescale as the time it takes for the bond radius to reach 50% of the grain radius, in a two bond-per-grain case:

$$r_{\mathrm{b}}(\tau_{\mathrm{sint}_{50}}) = \frac{1}{2} r_{\mathrm{g}}(\tau_{\mathrm{sint}_{50}}). \tag{4.20}$$

By running the sintering model, we can retrieve the sintering timescales for different grain sizes and temperatures, as shown in Figure 4.8. Note that the results depend on the arbitrary definition of the sintering timescale. If we defined this timescale as the time it takes for the bonds to reach 90% of the grain radius or or the time it takes for the bonds to double their initial size, the timescales would differ significantly. These definitions provide first-order estimates at a fixed temperature, but more detailed and accurate results require simulating sintering coupled with a thermal solver.

Another way to analytically estimate a characteristic timescale for sintering $\tau_{\mathrm{sint_V}}$, would be to defined it as the time for condensation to significantly change the bond volumes:

$$\tau_{\mathrm{sint_V}}(r_{\mathrm{b}}) = V_{\mathrm{b}} \left| \frac{\partial t}{\partial V_{\mathrm{b}}} \right|. \tag{4.21}$$

The variations of the bond volume due to condensation can then be related to the condensation flux on the bond surface

$$\frac{\partial V_{\mathrm{b}}}{\partial t} = \frac{1}{\rho_0} \frac{\partial m_{\mathrm{b}}}{\partial t} = \frac{J_{\mathrm{b}} S_{\mathrm{b}}}{\rho_0}. \tag{4.22}$$

Developing the Hertz–Knudsen equation once the gas has reached steady state, and using the approximation from Appendix 4.7: $P_{\mathrm{gas}}(t >> \tau_{\mathrm{gas}}) = P_{\mathrm{s}}$, leads to an analytical expression of the characteristic bond growth timescale

$$\tau_{\mathrm{sint_V}}(r_{\mathrm{b}}) = \sqrt{2\pi} \frac{\rho_0^2}{\alpha \gamma P_{\mathrm{s}} |K_{\mathrm{b}}|} \frac{V_{\mathrm{b}}}{S_{\mathrm{b}}} \left(\frac{RT}{M} \right)^{3/2}. \tag{4.23}$$

However, the explicit dependence on the bond radius underscores that this characteristic time is not constant throughout the sintering process. Rather, it provides an indication of the time required to observe noticeable growth of the bond volume.

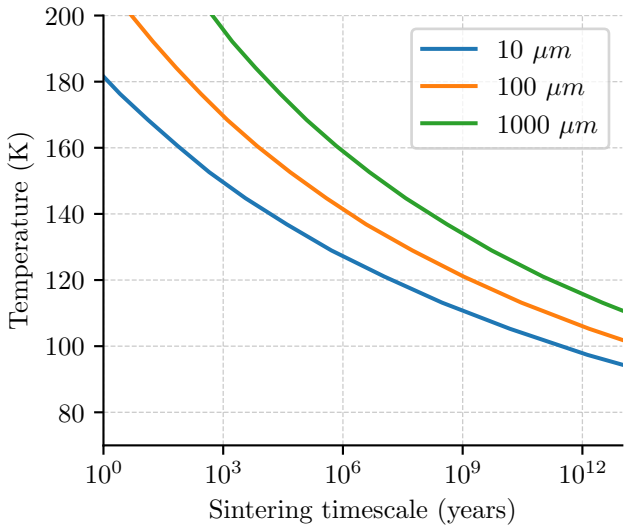

Figure 4.8: Sintering timescales for different temperatures and initial grain radii, computed based on simulations with two bonds per grain. The timescale is determined when the bond radius reaches half of the grain radius.

While, two analytical timescales ($\tau_{\mathrm{sint_V}}(r_\mathrm{b}), \tau_\mathrm{gas}$) appear in our description of the sintering process, they characterize different physics and vary on vastly different scales. For instance, at a temperature of 140 K, with a grain radius of $r_\mathrm{g} = 100\,\mu\mathrm{m}$, a bond radius of $r_\mathrm{b} = 10\,\mu\mathrm{m}$, and a sticking coefficient of $\alpha = 0.03$, the characteristic bond growth timescale is $\tau_{\mathrm{sint_V}}(r_\mathrm{b}) \sim 3600$ years, while the characteristic timescale of gas mass variations is $\tau_\mathrm{gas} \sim 10^{-11}$ s. Hence while the steady state is reached almost instantly, the sintering timescale takes much longer to occur.

4.3 Multiphysics Coupling with LunaIcy

To accurately simulate the temperature-dependent sintering process, the sintering model is coupled with the thermal solver MultiHeaTS (Mergny et al., 2024b) creating our multiphysics simulations model, LunaIcy (see Figure 4.9). The model consist of a uni-dimensional bloc of ice made of grains, with a certain porosity and thermal properties for each depth. In this numerical model, we use an irregular spatial grid consisting of n_x points, which we iterated for a total of n_t iterations. Here the vertical axis x is the same as the $\hat{x}$ axis of the sintering model. However, the variables have different names to clearly indicate the important distinction: x represents the depth, while $\hat{x}$ represents the distance to the grain center in the sintering model.

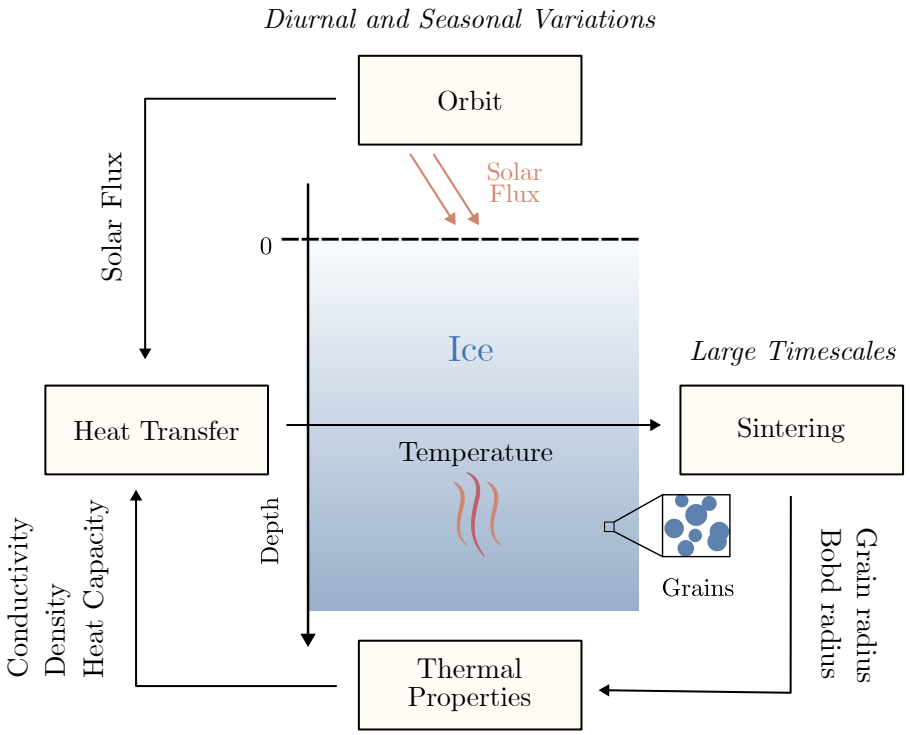

Figure 4.9: Block diagram of the proposed multi-physics simulation model LunaIcy.

The spatial and temporal parameters are discretized as follows:

$$\begin{cases} x \to x_n & = x_{n-1} + \Delta x_n \\ t \to t^i & = t^{i-1} + \Delta t^i. \end{cases} \tag{4.24}$$

Here, n is an integer such that $n \in \{0, \dots, n_x - 1\}$, representing the nth element in the spatial dimension, and i is an integer such that $i \in \{0, \dots, n_t - 1\}$, representing the ith element in the time dimension. It is worth noting that both the spatial Δx_n and temporal Δt^i increments may not be constant. This flexibility is advantageous as it allows for the use of irregular spatial grids and optimization of the timestep to be more computationally efficient.

By calculating the orbit of the target body, we determine the solar flux heating the ice surface. Then, our thermal solver MultIHeaTS, computes the heat transfer throughout the material's depth for each timestep. At each depth, the sintering module assesses the microstructure changes corresponding to the current temperature, and then updates the ice's thermal properties accordingly. Since the pore spaces do not communicate, the grain/bond system forms a closed system. Therefore, each layer of LunaIcy contains a grain/bond system that computes sintering independently based on its layer properties. This iterative process is repeated throughout the simulation. A summary of the thermal modules is provided here, with a detailed description available in the joint paper (Mergny et al., 2024b).

4.3.1 Heat Transfer

Temperature — MultiHeaTS proposes to solve numerically the heat equation where all thermal properties can vary continuously over space and time, and with non-constant time and space increments. The derivation of the fully implicit scheme and additional details can be found in Mergny et al., 2024b. In one dimension, the heat equation for conduction transfer can be expressed as:

$$\rho(x,t)c_{\mathrm{p}}(x,t)\frac{\partial T(x,t)}{\partial t} = \frac{\partial}{\partial x}\left(k(x,t)\frac{\partial}{\partial x}T(x,t)\right) + Q(x,t) \tag{4.25}$$

where ρ is the density, c_{p} is heat capacity, k is thermal conductivity, and Q denotes an optional source or sink term. The upper boundary condition (i.e., the flux leaving the surface) is determined by the energy equilibrium between the solar flux and the gray body emission from the surface (Spencer et al., 1989):

$$\forall t, k(0,t)\left.\frac{\partial T(x,t)}{\partial x}\right|_{x=0} = -F_{\mathrm{solar}}(t) + \epsilon \cdot \sigma_{\mathrm{SB}} \cdot T(0,t)^4 \tag{4.26}$$

where ϵ is the thermal emissivity and σ_{SB} the Stefan-Boltzmann constant.

The expression of the solar flux is based on Spencer et al., 1989 as a function of latitude λ and longitude ψ:

$$F_{\mathrm{solar}}(t,\lambda,\psi) = (1 - A(\lambda,\psi))\,\frac{G_{\mathrm{SC}}}{d(t)^2}\cos(\theta_i(t,\lambda,\psi)) \tag{4.27}$$

where A is the surface albedo, G_{SC} the solar constant, θ_i the solar incidence angle and d the distance to the Sun in AU, estimated using harmonic functions as described in Mergny et al., 2024b.

By default, and hereafter, the thermal solver is set without considering eclipses, which is strictly valid for the anti-Jovian hemispheres of the Galilean moons. However, it is possible to extend these results to any longitude by accounting for the eclipse effect at first order using an equivalent albedo (Mergny et al., 2024b) (Equation 40 of the cited article, with less than 0.5% error on the temperature distribution).

Porosity — While sintering could lead in some cases to a change of density, it remains unclear when such densification occurs. The sintering mechanism mostly studied under planetary conditions is diffusion by vapor transport, a non-densifying mechanism (Swinkels et al., 1981; Blackford, 2007; Molaro et al., 2019). This process redistributes mass from grains to bond areas but does not reduce pore space. While it strengthens the mechanical properties of the ice by cementing grains together, it does not change density.

If densification does occur, it would likely involve a different diffusion mechanism like grain boundary diffusion (Kaempfer et al., 2007), particle-induced compaction (Raut et al., 2008; Schaible et al., 2017) or what is referred as "late-stage" sintering by Molaro et al. (2019), possibly operating over longer timescales than vapor diffusion.

Although work by Eluszkiewicz, 1991 proposed a model for ice densification through sintering, their expression is derived from "an unpublished internal report by Ashby 1988" which existence could not be verified (Molaro et al., 2019). On Earth, some forms of sintering can typically increases density due to the recrystallization of liquid water in the pore space. However, in dry sintering, it is not clear if a densification happens. Therefore, while various other compaction mechanisms can intervene (e.g. sputtering or late stage sintering) we currently lack the ability to quantify their link to densification.

For these reasons, to model the density profile, we refer to our previous work (Mergny et al., 2024a), that specifically focuses on ice compaction driven by overburden pressure. Given that the thermal skin depth on Europa is estimated to be a few centimeters (Mergny et al., 2024b), whereas the compaction length scale is on the order of hundreds of meters (Mergny et al., 2024a), it is reasonable to assume that the porosity remains constant at the depths relevant to our thermal analysis. This lead to the simplified expression for the density of porous ice

$$\rho(\phi) = \rho_0(1 - \phi). \tag{4.28}$$

Conductivity — In contrast, sintering drastically changes the thermal conductivity of ice. As bond growth occurs, the surface area of solid to solid increases leading to an increase in conductivity.

Expressions found in the literature place significant importance in the effect of the bond radius on the effective conductivity of the material (Adams et al., 2001; Gundlach et al., 2018; Lehning et al., 2002). For these reasons, following (Mergny et al., 2024b), we use the expression of the porous conductivity:

$$k(\phi, r_\mathrm{b}, r_\mathrm{g}) = k_0(T)\,(1 - \phi)\,\frac{r_\mathrm{b}}{r_\mathrm{g}}. \tag{4.29}$$

where the bulk crystalline ice conductivity for a given temperature is computed using the expression $k_0 = 567/T$ (Klinger, 1981). Updating the temperature-dependent conductivity for each iteration would slow down computation significantly, so we maintain a constant bulk ice conductivity based on the surface equilibrium temperature. While temperature variations on Europa do not have a significant impact on conductivity compared to porosity and grain contact changes, it would be valuable to include in other applications.

Europa's icy surface is expected to be a mixture of crystalline and amorphous phases, at least in the first millimeter depth (Hansen, 2004; Ligier et al., 2016; Berdis et al., 2020). However, consistency among different lab measurements on amorphous ice conductivity has not been reliable (Murthy et al., 2013), likely due to the wide range of porosity and structural diversity in these experiments (Prialnik et al., 2022). For porosity-independent modeling, it would be helpful to experimentally measure the thermal conductivity of ice before and after amorphization or thermal relaxation. In the absence of such data, we consider only crystalline ice and will address model improvements in future versions of LunaIcy.

As the bond and grain radii evolve due to sintering throughout the simulation, the conductivity is adjusted according to Equation 4.29 to reflect these microstructural changes. This updated conductivity is then accounted in the thermal module, closing the two-way coupling between sintering and heat transfer.

4.3.2 Initialization and parameters

The LunaIcy model is run over a range of parameters to simulate the evolution of Europa's icy surface microstructure under various conditions. While temperature variations occur within the diurnal period, sintering progresses over large timescales under Europa's conditions, leading to a numerical challenge that can be handled with LunaIcy.

To capture temperature variations, the simulations require a precise timestep $\Delta t = p_{\mathrm{E}}/n_{\mathrm{spd}}$, where $p_{\mathrm{E}} = 3.55\,\mathrm{days}$ is Europa's orbital period and here $n_{\mathrm{spd}} = 30$. Over the one million year timescale, this results in a total number of iterations $n_t > 3 \times 10^9$. To address this, the unconditional stability property of the implicit scheme used in MultIHeaTS, coupled with its capability to use an irregular grid, decrease the computation time of each iteration. In these simulations, the spatial increments Δx_n are computed on an irregular grid given by the relation

$$\forall n \in \{0, \ldots, n_x - 1\},\ x_n = \left(\frac{n}{n_x - 1}\right)^5 L \tag{4.30}$$

where L is the maximum depth computed in the model. Given that sintering progresses much slower than temperature variations, the grain and bond radii are only updated after significant amount of time has elapsed, set to $\Delta t_{\mathrm{sint}} = 0.01 \times \tau_{\mathrm{sint_V}}(r_{\mathrm{b}})$. This enables calling the heat transfer module more frequently than the module responsible for updating thermal properties, as shown in Figure 4.9. Thanks to such optimization, particularly due to the thermal solver, the computation time of a one million year simulation was reduced to around 4 days on an 6 cores Intel i7-10750H CPU at 3.6 GHz.

Given the large number of iterations n_t, saving the ice state frequently would take significant storage space. To solve this problem, the properties are saved periodically, every $p_{\mathrm{save}} = 10.1 \times p_{\mathrm{J}}$, where $p_{\mathrm{J}} = 11.86\,\mathrm{years}$ is Jupiter's current orbital period. This ensures that we capture all diurnal and orbital variations while maintaining a manageable file size, typically around 1 GB per simulation.

The determination of initial ice structure is difficult due to lack of information on Europa. The origin of the surface porosity is not clear; it could be the product of a plume deposit or the result of crushed ice by space weathering. Here, we propose to assume a relatively loose granular material, with parameters in agreement with observed surface temperature from infrared measurement (Rathbun et al., 2010; Trumbo et al., 2018) and grain size in agreement with near-infrared spectroscopic measurement (Hansen, 2004; Cruz-Mermy et al., 2023). As a reference warm scenario, we choose a typical grain radius of $r_{\mathrm{g}}(t = 0) = 100\,\mu\mathrm{m}$, an albedo 0.4 and

porosity 0.8 leading to the mean surface temperature of 114 K and a maximum of 141 K, close to the highest values obtained from Galileo photopolarimeter–radiometer (Rathbun et al., 2010). The complete list of parameters is given in Table 4.1.

Parameter	Value
Final time t_f	1 My
Timestep Δt	170 min
Steps per day n_spd	30
Grid points n_x	30
Max depth L	50 m
Latitude λ	0
Longitude ψ	0
Emissivity ϵ	0.9
Albedo A	0.4 (0.4 - 0.8)
Porosity ϕ	0.8 (0.2 - 0.9)
Sticking coefficient α	0.03
Initial grain radius $r_\mathrm{g}(x, 0)$	100 µm

Table 4.1: Physical and numerical parameters used for our simulations. The reference warm scenario is for an albedo of 0.4 and porosity of 0.8.

Parameter	Value	Unit	Reference
Bulk ice density ρ_0	917	$\mathrm{kg\,m^{-3}}$	Molaro et al. (2019)
Ice heat capacity c_p	839	$\mathrm{J\,kg^{-1}\,K^{-1}}$	Klinger (1981)
Water surface tension γ	0.06	$\mathrm{J\,m^{-2}}$	Molaro et al. (2019)
Ice shear modulus μ	10^9	$\mathrm{N\,m^{-2}}$	Molaro et al. (2019)

Table 4.2: Constant properties used in our model.

4.4 Results and Discussion

4.4.1 Results

We first present the results of a simulation under reference warm conditions with a porosity of $\phi = 0.8$ and an albedo of $A = 0.4$, with solar flux set at the equator, $\lambda = 0$. Using the set of parameters found in Table 4.1, we obtain a mean temperature of 114 K and a maximum daily temperature of 141 K. The evolution of the top layer grain $r_\mathrm{g}(x = 0, t)$, and bond $r_\mathrm{b}(x = 0, t)$ radii throughout the simulation can be found in Figure 4.10. These findings indicate that significant sintering occurs under

these conditions, with the top layer bond radius increasing from 0.39 µm to 23.05 µm over one million years. In contrast, the grain radius decreases from 100.00 µm to 99.96 µm during the same period. This difference can be explained by the fact that although the matter condensing on the bonds originates from the grains, the initial volume of the grains is five orders of magnitude larger than that of the bonds. Thus, even minor observable changes in the grain radius result in significant increases in the bond radius.

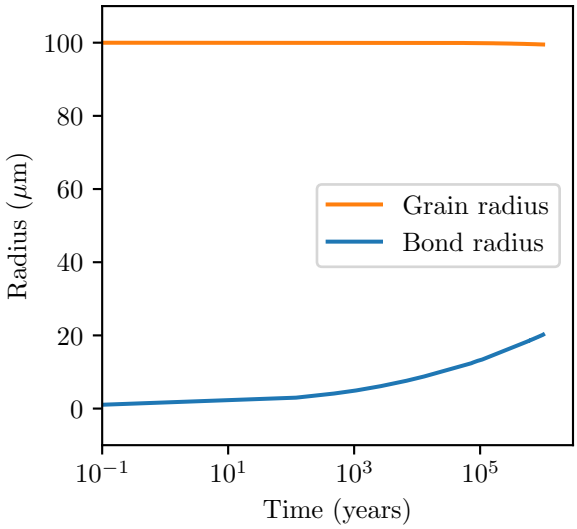

Figure 4.10: Top layer grain and bond radii evolution over one million years in a warm simulation scenario with a porosity of $\phi = 0.8$ and an albedo of $A = 0.4$, resulting in a mean temperature of 114 K and a maximum daily temperature of 141 K. The bond radius has increased by 59 times its initial value, leading to significant changes in the thermal, mechanical and optical properties of the ice.

These results highlights the necessity of the thermal coupling; without it, relying on constant temperatures would lead to inaccurate sintering estimates. For instance, with bond size $r_b = 10$ µm, at the max daily temperature of 141 K, the characteristic sintering time is $\tau_{\text{sint}_V} \sim 2700$ years while at the mean temperature of 114 K, $\tau_{\text{sint}_V} \sim 51$ My.

However, sintering extends beyond the top layer, and the numerical simulations enable us to investigate its effects throughout the ice depth. In Figure 4.11 is plotted the bond radius profile versus depth after one million years, revealing significant sintering at depths shallower than the diurnal thermal skin depth (around 25 cm in this case). While the simulations started with an homogeneous structure, due to the damping of the thermal wave, sintering creates heterogeneity in the ice microstructure. Such changes of the microstructure, influences the macroscopic properties like the thermal conductivity as described by Equation 4.29.

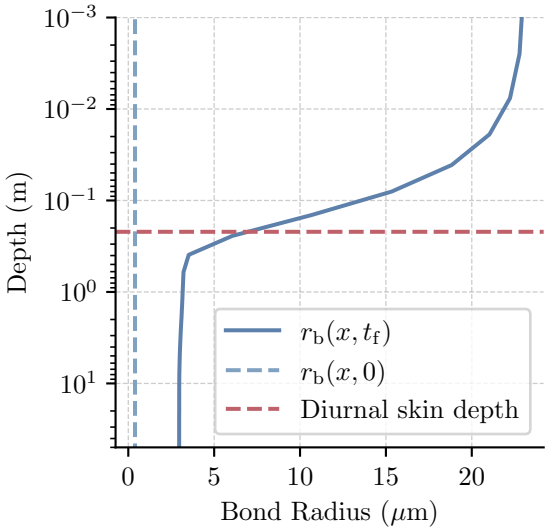

Figure 4.11: Bond radius versus depth after one million years of sintering with an albedo of $A = 0.4$ and a porosity of $\phi = 0.8$. The initial bond radius $r_b(x, 0) \approx 0.4\,\mu m$, is indicated by blue dashed lines for reference. Significant sintering is observed up to the diurnal thermal skin depth.

These results are of primordial importance when modeling the thermal properties of Europa for remote sensing; in warm regions, sintering is expected to occur and lead to an heterogeneous ice profile up to the thermal skin depth. As discussed in Mergny et al., 2024b, this bilayer case could be observed by thermal infra-red observation. This highlights the necessity of using multilayered thermal solvers, such as MultIHeaTS (Mergny et al., 2024b) or the Planetary Code Collection (Schorghofer, 2022), to derive the thermal properties of the surface.

The strength of this numerical approach is its ability to explore the evolution of an icy surface under different sets of parameters. Europa's past and present surface properties are not well constrained, so this parameter exploration allow us to study the surface under different conditions. In this study, we first conducted 25 simulations, varying porosities from 0.2 to 0.9 and albedo from 0.4 to 0.8, typical for Europa (McEwen, 1986; Belgacem et al., 2020).

Figure 4.12 shows the sintering heatmap of the top layer for this set of simulations; for each pair of the porosity and albedo parameters, is represented the ratio of the final bond radius to the initial one $r_b(x = 0, t_f)/r_b(x = 0, t = 0)$. As expected, lowering the albedo or increasing the porosity, which yields a less conductive material, increases the surface temperature thereby enhancing sintering. Only situations of very high albedo $A > 0.8$, do not see any effect of sintering during the one million year period. For the warmest regions, the top layer bond radius grows by almost two

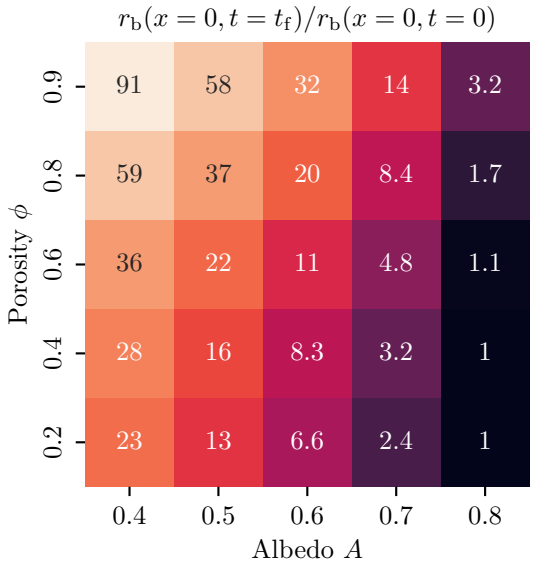

Figure 4.12: Sintering efficiency heatmap for the top layer as a function of porosity and albedo. Colors indicate the ratio of the top layer bond radius after one million years $r_b(t = t_f)$ to the initial bond radius $r_b(t = 0)$. In the majority of scenarios, the bond radius more than doubles after one million years, except for very high albedo.

orders of magnitude its initial size, resulting in the same increase factor for the ice thermal conductivity (Equation 4.29).

In most conditions represented here, except for very high albedo, the bond radius at least double its size after one million years. A consistent trend suggests that regions reaching a maximum daily temperature exceeding 115 K will experience noticeable sintering over this period. While the mean temperature of these surfaces is too cold for effective sintering, the probability distribution of temperature (Mergny et al., 2024b) reveals that even when less than 5% of the time is spent above 115 K, noticeable sintering can occur over one million years.

The effect of longitude on the anti-jovian hemisphere is trivial and null given that it does not alter the solar flux. In contrast, on the sub-Jovian hemisphere, the surface experiences eclipses by Jupiter, which partially obstruct the incoming solar flux. A detailed investigation of this phenomenon is provided in the companion article (Mergny et al., 2024b), which offers a first-order approximation of the eclipse effects using a modified expression of the Bond albedo, A'.

Latitude, however, has a straightforward effect: there is simply less solar flux on average but also at noon. Since the obliquity is near zero, the duration of the day is homogeneous over the moon, whatever the latitude. The influence of the latitude λ can be approximated at first order by introducing an equivalent albedo A_λ defined

as:

$$A_\lambda = 1 + (A - 1)\cos(\lambda). \tag{4.31}$$

For instance, the reference albedo used previously $A = 0.4$ would change to $A_\lambda = 0.58$ at latitude $\lambda = \pm 45°$ and $A_\lambda = 0.79$ at latitude $\lambda = \pm 70°$. Thus, using the results from Figure 4.12, limited sintering is expected for latitude poleward 70° on Europa. As a conclusion, the albedo map of Europa is expected to control the sintering of the ice, with an effective reduction toward the poles due to latitude effects.

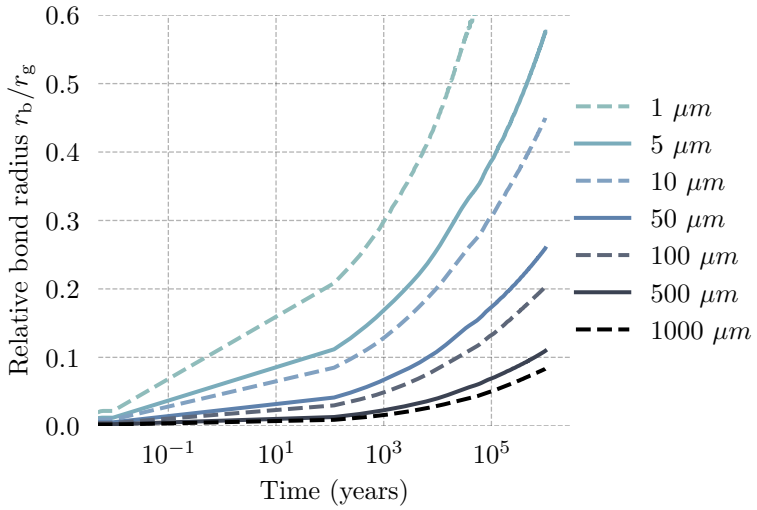

Figure 4.13: Evolution of the top layer relative bond radius r_b/r_g for different initial grain radius $r_g(t = 0)$. Smaller grains show more efficient sintering due to their higher surface curvature. In situations of intense sintering, numerical instabilities start to appear after reaching a critical threshold $r_b > 0.6 r_g$.

A set of simulations was conducted to investigate the effect of grain sizes on the efficiency of sintering. The albedo and porosity were fixed to their values in the reference warm scenario outlined in Table 4.1. Seven simulations were run with varying grain radii ranging from 1 µm to 1 mm. In Figure 4.13, we present the evolution of the relative bond radius r_b/r_g for the different grain sizes, focusing on the top layer, at $x = 0$. As anticipated, the sintering timescale shows a significant dependence on the grain size, with smaller grains undergoing faster sintering due to their higher surface curvature (Blackford, 2007; Molaro et al., 2019). While the exact grain size of Europa's surface remains unknown, thanks to such parameter exploration, we can predict the evolution of the various possible surface configurations.

The time of our simulations is shorter than the estimated ice crust age of approximately 30 My (R. T. Pappalardo et al., 1998), suggesting that, in present times, warm regions on Europa should have experienced significant sintering. These numerical results are consistent with polarimetric comparisons of Europa with pure ice particles

(Poch et al., 2018), suggesting that Europa is possibly covered by relatively coarse and sintered grains. This is particularly noteworthy, as if these areas are made of an interconnected grain structures due to sintering, it drastically changes the thermal, optical and mechanical properties of the surface. Incorporating these effects would be pertinent in designing a lander for Europa's surface.

4.4.2 Discussion

4.4.2.1 Irregular grain shapes

The current model simplifies the sintering system to two curvatures: the grain curvature K_g and the bond curvature K_b. However, near the grain/bond interface (see Figure 4.4, around $\hat{x}^*$), the curvature is a mix of these two profiles (Swinkels et al., 1981; Molaro et al., 2019). Additionally, in reality, shape irregularities can induce local curvatures that influence sintering. To account for such irregular shapes, rather than considering separate curvatures for the grain and bond, the model could be expanded to incorporate a continuous curvature function along the surface $\mathcal{S}$ of the system . For instance, in Figure 4.4, $r(\hat{x})$ describes the system's shape along the y-axis, and by calculating the second derivatives of r, one could derive the local curvature.

A similar approach can be found in the numerical scheme proposed by (Flin et al., 2003) for irregular 3D-shaped grains. At each iteration, the surface normal of every voxel is calculated to determine its local curvature, which is then used to compute the local Hertz-Knudsen flux. In our model, such scenario would lead to the modification of the gas mass variations (Equation 4.8) to:

$$\frac{\partial}{\partial t} m_\mathrm{gas} = \int_{\hat{x}\in\mathcal{S}} J(\hat{x})\,\mathrm{d}S(\hat{x}) \tag{4.32}$$

where $\hat{x}$ are the points along the surface $\mathcal{S}$. While such a precise formulation is essential for terrestrial studies, its relevance for icy moons is limited due to our lack of information about their current microstructure. For Europa, even constraining grain sizes is challenging, so estimating the potential shape of the grains would be even more difficult. Additionally, calculating surface normals and local curvatures, even in a 2D model, would add significant computational overhead. Given the need to compute sintering on million of year timescales and our current resources, implementing such a model would be very challenging.

4.4.2.2 Grain size distribution

Our current model of sintering only considers a uniform distribution of grain sizes, leading to bond growth at the expense of the grains. Experimental observations show that in granular ice media with a nonuniform grain distribution, grain growth and mass redistribution occur due to grain absorption (Kuroiwa, 1961; Molaro et al.,

2019). Smaller grains, with higher radii of curvature, experience a higher sublimation flux. As grains become smaller, sublimation rapidly removes mass at an increasing rate. Consequently, smaller grains tend to be absorbed by larger ones, leading to an increase in the mean grain size over time. This complex behavior is not captured by the model's idealized uniform grain size distribution.

However, while the grain radius decreases in our current model, the newly formed grain-and-bond system optically appears as a larger agglomerate structure. A light ray penetrating a sintered medium may traverse through multiple grains before reaching a pore space, depending on the bond size. As a consequence, these grain-and-bond systems would be interpreted as larger grains with an effectively increased radius in spectroscopy or reflectance models. The exact relationship between bond radius and effective optical grain size is complex, as it also depends on the bonds' orientation within the observed surface. Further work would be necessary to properly model the optical behavior of sintered particles in spectroscopy models.

4.4.2.3 Alternative transport mechanisms

In this study, we have looked at the sintering through vapor transport diffusion where grains can only exchange matter with their neighboring bonds. While the thermal properties considered may vary, the heat transfer simulations presented in the joint publication (Mergny et al., 2024b) reveal temperature fluctuations of up to 15 K within the first 10 cm. This exceeds the $10\,\mathrm{K\,m^{-1}}$ threshold, beyond which temperature gradient metamorphism becomes significant in Earth-based studies (Colbeck, 1983). However, it remains unclear how much this threshold is modified in the cold, near-vacuum conditions found on the surfaces of icy moons. Temperature gradients metamorphism could potentially play a crucial role in the surfaces of icy moons, and it an aspect that has yet to be undertaken by the planetary science community. In this study, we have deliberately restricted pore communication to not account for this effect. Yet, Europa's surface is expected to be highly porous, with ice made of open pores that may have a vapor pressure gradient with depth. The main difference with terrestrial modeling is that the top layer is not in contact with the atmosphere but with the vacuum - more precisely, the near vacuum pressure of the exosphere. Given these factors, temperature gradients could play a significant role in the sintering of ice grains but its implementation would require additional modeling work.

4.4.2.4 Electron-induced sintering

The surface of Saturnian satellites undergoes radiation-induced sintering (Schaible et al., 2017), which may also affect Europa, as this process is closely linked to the distribution of high-energy electrons (> MeV). The flux of high-energy electrons is higher on Europa than on Saturnian moons Cooper (2001) and Schaible et al. (2017), suggesting radiation-induced sintering likely occurs on Europa as well. However, the high surface temperatures of Europa, especially near the equator where

most high-energy electrons impact (Paranicas et al., 2009), suggest that sintering is likely dominated by thermal diffusion. It remains unclear if this process is significant for colder regions and if electrons below MeV can contribute to grain sintering. The most notable difference for Europa is that grain sizes are expected to be much larger than those on Saturnian satellites. For radiation-induced sintering to occur in ~ 30 kyrs on Mimas and Tethys, grain sizes need to be smaller than 5 µm, while for 25 µm grains, it takes 10 Myr (Schaible et al., 2017). Near-infrared spectroscopic measurements on Europa (Hansen, 2004; Cruz-Mermy et al., 2023) indicate that most models require grain sizes > 20 µm. Therefore, over the million-year simulation time, at comparable plasma flux, such sintering is unlikely to be significant, even in polar regions, unless the grain sizes are much smaller than expected. However, due to the higher electron flux on Europa and the likely non-uniform grain size distribution, smaller grains of a few microns could be affected by electron-induced sintering. Detailed modeling of such interactions would be beneficial but is beyond the scope of this paper and may be addressed in future versions of LunaIcy.

4.5 Conclusion and Perspectives

We have developed a multiphysics simulation model to study the evolution of planetary ice microstructure. Our approach includes MultiHeaTS an efficient heat transfer solver, as described in our joint paper (Mergny et al., 2024b), particularly adapted for scenarios with long timescales and small timesteps. Solar flux at the surface is calculated using Europa's orbital parameters. Coupled to the heat transfer, we have built a new model, called LunaIcy, for the sintering of ice grain, that is based on the literature but with refinement of the diffusion process. As changes in ice microstructure affect the thermal properties we have expressed the heat conductivity with a formulation that consider microstructure and porosity which enables a two-way coupling between sintering and heat transfer.

Our simulations spanned a million years, allowing us to thoroughly explore the evolution of Europa's icy surface microstructure. Results show that the hottest regions experience significant sintering, even if high temperatures are only reached during a brief portion of the day. This process takes place on timescales shorter than Europa's ice crust age, suggesting that these regions should currently have surface ice composed of interconnected grains. For further studies, it would be valuable to extend this simulation time to the age of Europa's ice crust, estimated to be around 30 My (R. T. Pappalardo et al., 1998), but it would necessitate further optimization and available resources for computation.

Other parameters describing the ice microstructure, such as crystallinity, roughness or porosity, may evolve due to processes such as space weathering, compaction or crystallisation. In a future work, we would like to expand LunaIcy by including more physical processes. Just as General Circulation Models (GCMs) have become essential tools for studying the climate evolution of planetary atmospheres, we anticipate

further development of such multiphysics simulation tools for studying planetary surfaces.

Accurately simulating these highly coupled processes, such as sintering, provides valuable insights into the evolution of Europa's ice microstructure. These insights, in turn, contribute to the refinement of surface measurements like spectroscopy, enabling improved constraints on grain size. Such advancements play a crucial role in accurately determining the microstructure and quantitative composition of Europa's surface, a key objective for upcoming missions such as JUICE and Europa Clipper, and lander/cryobot missions (R. Pappalardo et al., 2013; Hand et al., 2022; Vale Pereira et al., 2023) in a more distant future.

4.6 Appendix: Geometry of the Sintering Model

The surface areas in contact with phase exchange are determined using geometrical considerations based on the 1/4 grain-and-bond system of Figure 4.4.

4.6.1 One grain connected by two bonds

The main scenario investigated in this article is the case of two bonds per grain where the total volume is obtained by multiplying the surfaces and volumes of the 1/4 system by a factor 4. To begin, we consider the grain surface which is in contact with the pore space. The grain's surface is given by the integral

$$S_{\mathrm{g}} = 4 \int_0^{\theta^*} \int_0^{\pi} (r_{\mathrm{g}}\, d\theta)(r_{\mathrm{g}} \cos\theta\, d\Psi) \tag{4.33}$$

where Ψ is the angle made by rotation along the $\hat{y}\hat{z}$ plane as shown in Figure4.4. After performing the integration, we arrive at the simplified expression

$$S_{\mathrm{g}} = 4\pi r_{\mathrm{g}} \hat{x}^* \tag{4.34}$$

Next, we consider the bond surface, which is in contact with the pore space. The bond's surface is given by the integral:

$$S_{\mathrm{b}} = 4 \int_0^{\pi} \int_0^{\phi_\rho^*} (r(\phi_\rho)\, d\Psi)(r_\rho\, d\phi_\rho). \tag{4.35}$$

where $r(\phi_\rho) = r_\rho + r_{\mathrm{b}} - r_\rho \cos\phi_\rho$, is obtained from trigonometry (see Figure 4.4). After integration, this leads to the expression

$$S_{\mathrm{b}} = 4\pi r_\rho \left((r_\rho + r_{\mathrm{b}})\phi_\rho^* - r_\rho \sin\phi_\rho^* \right), \tag{4.36}$$

knowing that $\phi_\rho^* = \theta^*$.

Similarly, we can derive the analytical relationship between the grain and bond radii and their respective volumes $v(r_\mathrm{g}, r_\mathrm{b})$. The grain volume is defined by the integral:

$$v_\mathrm{g} = 4\left(\frac{1}{2}\int_0^{\hat{x}^*} \pi r(\hat{x})^2 \, d\hat{x}\right). \tag{4.37}$$

By introducing a change of variable to the angle θ given by

$$\begin{cases} \hat{x} & = r_\mathrm{g}\sin\theta \\ d\hat{x} & = r_\mathrm{g}\cos\theta \, d\theta \end{cases} \tag{4.38}$$

and knowing that $r(\hat{x}) = r_\mathrm{g}\cos\theta$, we can express the integral as:

$$v_\mathrm{g} = 2\int_0^{\theta^*} \pi r_\mathrm{g}^3 \cos^3\theta \, d\theta \tag{4.39}$$

After integration over θ, we get the following expression of the grain volume

$$v_\mathrm{g} = \frac{\pi}{6} r_\mathrm{g}^3 \left(9\sin\theta^* + \sin 3\theta^*\right). \tag{4.40}$$

Next, we consider the bond volume, which is defined by the integral:

$$v_\mathrm{b} = 4\left(\frac{1}{2}\int_{\hat{x}^*}^{r_\mathrm{g}} \pi r(\hat{x})^2 \, d\hat{x}\right). \tag{4.41}$$

By introducing a change of variable

$$\begin{cases} \hat{x} & = r_\mathrm{g} - r_\rho\sin\phi_\rho \\ d\hat{x} & = -r_\rho\cos\phi_\rho \, d\phi_\rho \end{cases} \tag{4.42}$$

we can express the integral as

$$v_\mathrm{b} = 2\pi\int_0^{\phi_\rho^*} (r_\rho + r_\mathrm{b} - r_\rho\cos\phi_\rho)^2 r_\rho\cos\phi_\rho \, d\phi_\rho. \tag{4.43}$$

after integration it leads to the expression of the bond volume

$$v_\mathrm{b} = 2\pi r_\rho\left[\sin\phi_\rho\left((r_\rho + r_\mathrm{b})^2 + \frac{9}{12}r_\rho^2\right) - \frac{1}{2}\sin 2\phi_\rho\left(r_\rho^2 + r_\rho r_\mathrm{b}\right) + \sin 3\phi_\rho\,\frac{r_\rho^2}{12} - \phi_\rho\left(r_\rho^2 + r_\mathrm{b} r_\rho\right)\right]. \tag{4.44}$$

Now that analytical expressions of the grain and bond volumes were obtained, the Newton-Raphson method can be called to retrieve the bond and grain radii. Finally, it is worth mentioning that the pore volume is not required by the algorithm, as the expression of the gas pressure in the steady state is independent of V_p. However, if one wants to estimate the timescale of gas mass variations τ_gas, the pore volume can be approximated, at first order, to

$$V_\mathrm{p} = \frac{4}{3}\pi r_\rho^3. \tag{4.45}$$

4.6.2 One grain connected by a single bond

For a grain with a single bond, the total surface and volume of the bonds are simply divided by 2 from Equation 4.36 and Equation 4.44. The total grain surface is obtained by adding half the surface of a sphere to half the surface of the two-bonds case (see Equation 4.34):

$$S_{\mathrm{g}} = 2\pi r_{\mathrm{g}}^2 + 2\pi r_{\mathrm{g}} \hat{x}^*. \tag{4.46}$$

Similarly, the total grain volume is found by adding half the volume of a sphere to half the volume calculated in the two-bonds case (see Equation 4.40):

$$v_{\mathrm{g}} = \frac{2}{3}\pi r_{\mathrm{g}}^3 + \frac{\pi}{12} r_{\mathrm{g}}^3 \left(9 \sin\theta^* + \sin 3\theta^*\right). \tag{4.47}$$

4.6.3 One grain connected by six bonds

For a grain with six bonds, the total surface area and volume of the bonds are simply multiplied by 3 from Equation 4.36 and Equation 4.44. The total grain surface is calculated by subtracting the areas of the six caps removed by the bonds from the area of a sphere. The surface of a single cap is given by

$$S_{\mathrm{cap}} = \int_0^{2\pi} \int_{\theta^*}^{\frac{\pi}{2}} (r_{\mathrm{g}}\, d\theta)(r_{\mathrm{g}} \cos\theta\, d\Psi) = 2\pi r_{\mathrm{g}}(r_{\mathrm{g}} - \hat{x}^*) \tag{4.48}$$

resulting in the total grain surface of

$$S_{\mathrm{g}} = 4\pi r_{\mathrm{g}}^2 - 12\pi r_{\mathrm{g}}(r_{\mathrm{g}} - \hat{x}^*). \tag{4.49}$$

The total grain volume is calculated by subtracting the volume of the six caps removed by the bonds from the volume of a sphere. The volume of a single cap is given by

$$v_{\mathrm{cap}} = \int_{\hat{x}^*}^{r_{\mathrm{g}}} \pi r(\hat{x})^2\, d\hat{x} = \frac{\pi}{12} r_{\mathrm{g}}^3 \left(8 - 9\sin\theta^* - \sin 3\theta^*\right) \tag{4.50}$$

resulting in the total grain volume of

$$v_{\mathrm{g}} = \frac{4}{3}\pi r_{\mathrm{g}}^3 - \frac{\pi}{2} r_{\mathrm{g}}^3 \left(8 - 9\sin\theta^* - \sin 3\theta^*\right). \tag{4.51}$$

4.7 Appendix: Steady State Fluxes

Using Equation 4.15 and the ideal gas law (Equation 4.7), the gas pressure at the equilibrium simplifies to

$$P_\infty = P_{\mathrm{s}}(T) \left[1 + \frac{\gamma M}{SRT\rho_0} \left(S_{\mathrm{b}} K_{\mathrm{b}} + S_{\mathrm{g}} K_{\mathrm{g}}\right)\right]. \tag{4.52}$$

By recognizing the limited development of the exponential function

$$P_\infty = P_\mathrm{s}(T) \exp\left(\frac{\gamma M}{SRT\rho_0}\left(S_\mathrm{b}K_\mathrm{b} + S_\mathrm{g}K_\mathrm{g}\right)\right) \tag{4.53}$$

this lead to a simpler expression of P_∞

$$P_\infty = \left(P_{K_\mathrm{b}}^{S_\mathrm{b}} P_{K_\mathrm{g}}^{S_\mathrm{g}}\right)^{1/S}. \tag{4.54}$$

This expression clearly shows that at the steady state, the gas pressure is not the saturated vapor pressure.

Injecting the gas pressure at the steady state into equation Equation 4.9, we obtain the surface flux at the steady state

$$J_\mathrm{j} = P_\mathrm{s}(T)\frac{\alpha\gamma}{\sqrt{2\pi}S\rho_0}\left(\frac{M}{RT}\right)^{\frac{3}{2}}\left(K_\mathrm{j}S - K_\mathrm{b}S_\mathrm{b} - K_\mathrm{g}S_\mathrm{g}\right) \tag{4.55}$$

Due to conservation of mass, at the steady-state Equation (4.8) shows that the total mass sublimating from the grains should be equal to the total mass condensing on the bonds:

$$J_\mathrm{b}S_\mathrm{b} + J_\mathrm{g}S_\mathrm{g} = 0 \tag{4.56}$$

So we can first compute the surface mass flux entering the pore space from the bonds (it's negative)

$$J_\mathrm{b} = P_\mathrm{s}(T)\frac{\alpha\gamma}{\sqrt{2\pi}S\rho_0}\left(\frac{M}{RT}\right)^{\frac{3}{2}} S_\mathrm{g}\left(K_\mathrm{b} - K_\mathrm{g}\right) \tag{4.57}$$

and the grain flux is simply retrieved using Equation 4.56.

4.8 Thesis' Supplementary Material

4.8.1 Comparison with Choukroun's Experiments

Choukroun et al. (2020) investigated the strength evolution of ice samples allowed to sinter over extended periods. They measured the mechanical resistance of granular ice by penetrating a cone into samples made of grains approximately 12 µm in size, which were left at different temperatures for varying durations. The authors proposed using an Arrhenius law to model the strengthening rate S as a function of temperature:

$$\dot{S} = \dot{S}_0 \exp\left(-\frac{Q}{RT}\right) \tag{4.58}$$

where $\dot{S}_0$ is the intercept of the rate of strengthening and Q is the activation energy. While the paper provides upper and lower bounds for the activation energy based on the experiments ($Q = 24.3 \pm 3.3\,\mathrm{kJ\,mol^{-1}}$), the intercept rate was not specified. We manually estimated it from the article's figures as $\dot{S}_0 \approx 2 \times 10^5\,\mathrm{Pa\,s^{-1}}$.

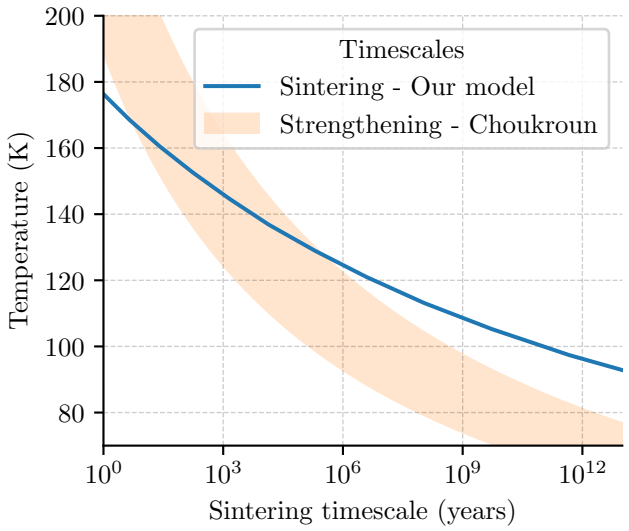

Figure 4.14: (*Blue curve*) Sintering timescale based on our model for an initial grain radius of 6 µm. (*Orange area*) Strengthening timescale from Choukroun et al. (2020)'s experiments, representing the time required for an ice sample to reach a mechanical resistance of $S_{\mathrm{mech}} \approx 10\,\mathrm{MPa}$. The upper and lower bounds reflect the uncertainties in the activation energy.

The authors goal was not to measure the evolution of bond and grain radii through sintering, but rather on the increase in mechanical strength. Their paper presents a strengthening rate, which is measurable and linked to sintering, but it is difficult to compare it directly with our model. Still, they mention a mechanical

resistance threshold around $S_{\text{mech}} \sim 10\,\text{MPa}$, where the ice samples are "well consolidated". Based on this, we can arbitrarily define a strengthening timescale as the time it takes for an ice sample to reach this resistance threshold:

$$\tau_{\text{mech}} = S_{\text{mech}}/\dot{S} \tag{4.59}$$

This strengthening timescale is related to our sintering timescale, but the exact relationship between changes in microstructure due to bond formation and the resulting mechanical behavior of the sample is not straightforward and beyond the scope of this thesis.

In Figure 4.14, is plotted the strengthening timescales using Equation 4.59 alongside our sintering timescale based on Figure 4.8 for the mean grain radius used in their experiments $\sim 6\,\mu\text{m}$. We observe that between 170 K and 120 K, the sintering timescale falls within the same error bars as Choukroun's strengthening timescales. However, at lower temperatures, our predicted sintering is significantly slower than Choukroun's.

One possibility is that the timescales are defined using different stopping points. We arbitrarily chose to stop when the bond radius reaches the grain radius, while Choukroun's timescale stops when the ice sample reaches a mechanical resistance threshold, like 10 MPa. There is no way to ascertain if these two stopping points occur are the same time. Additionally, we used the mean grain sizes from Choukroun et al. (2020)'s experiments, as we do not have access to the grain size distribution. Since sintering rates are highly dependent on grain size, this will also impact the sintering timescales shown in Figure 4.14

However, at low temperature there is still a significant gap between these two timescales, which could be attributed to the unexpected activation energy measured in Choukroun's experiments. While the literature, based on sintering experiments (Hobbs et al., 1964; Blackford, 2007; Molaro et al., 2019), agrees that vapor transport is likely the dominant form of sintering, Choukroun et al. (2020) derived an activation energy of $Q = 24.3 \pm 3.3\,\text{kJ}\,\text{mol}^{-1}$, which is consistent with a process dominated by surface diffusion rather than vapor transport. An exponential fit of our sintering timescale for a grain radius of $6\,\mu\text{m}$ yields an activation energy of $Q \sim 37\,\text{kJ}\,\text{mol}^{-1}$. So for reasons yet unknown, the strengthening timescales appear to be governed by surface diffusion rather than vapor transport, highlighting our incomplete understanding of the sintering process. Further research is needed to clarify these mechanisms and reconcile the discrepancies between different models and experimental results.

4.8.2 Sublimation versus Sintering

As the surface of icy moons is in contact with their exosphere, sublimation and condensation of the ice top layers will occur. This sublimation may be faster than the sintering rates and therefore needs to be considered to accurately estimate the

surface microstructure. Models of Europa's exosphere have primarily focused on the contribution of sputtering by energetic particles. However, Hayne (2016) suggest that low- to mid-latitudes that experience temperatures above 130 K, contribute significantly to the sublimation rates. To model the sublimation flux, we used the Hertz-Knudsen equation over a flat surface in contact with the vacuum:

$$J_{\text{sub}} = (P_{\text{s}}(T) - 0)\sqrt{\frac{M}{2\pi RT}}. \tag{4.60}$$

Note that the sticking coefficient was set to 1, not 0.03, because the value 0.03 was used to fit our sintering model, not to model the sublimation process.

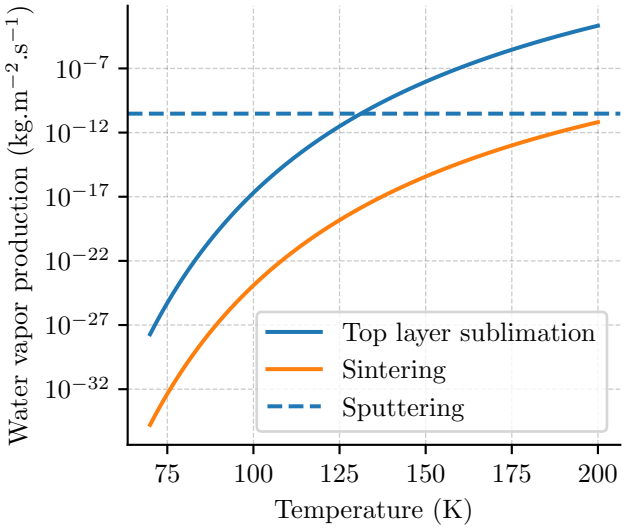

Figure 4.15: Water vapor production flux from three different sources: (1) (*blue curve*) sublimation of ice in direct contact with a complete vacuum, (2) (*blue dashes*) estimated water production rate from sputtering (Hayne, 2016), and (3) (*orange curve*) for comparison, the sintering flux in the steady state for a grain geometry with $r_{\text{g}} = 100\,\mu\text{m}$ and $r_{\text{b}} = 10\,\mu\text{m}$.

In Figure 4.15, is plotted the dependency of the sublimation flux as a function of temperature. To compare it with the sintering flux, we used the expression of the grain flux in the steady state from Equation 4.55. Additionally, the expected sputtering rate of approximately $\sim 10^{15}\,\text{H}_2\text{O}\,\text{m}^{-2}\,\text{s}^{-1}$ (Hayne, 2016) is shown for comparison. As noted by Hayne (2016), for temperatures above 130 K, the sublimation flux contributes more to the production of water vapor in Europa's exosphere than sputtering. In comparison, the sintering flux is orders of magnitude lower.

To investigate this, we define a sublimation timescale, τ_{sub}, as the time it takes for a spherical grain to completely sublimate. This time is obtained by iteratively

removing the sublimation volume to the grain:

$$\frac{4}{3}\pi r_{\mathrm{g}}^3(t+\Delta t) = \frac{4}{3}\pi r_{\mathrm{g}}^3(t) - 4\pi r_{\mathrm{g}}^2(t)\frac{J_{\mathrm{sub}}}{\rho_0}\Delta t, \tag{4.61}$$

until $r_{\mathrm{g}}(\tau_{\mathrm{sub}}) = 0$. In Figure 4.16, is plotted the sublimation timescales alongside the sintering timescales (see Section 4.2.7) for different grain sizes. The results show that sublimation of an ice layer in direct contact with the vacuum is much faster than sintering across the range of temperatures found at the surface of icy moons.

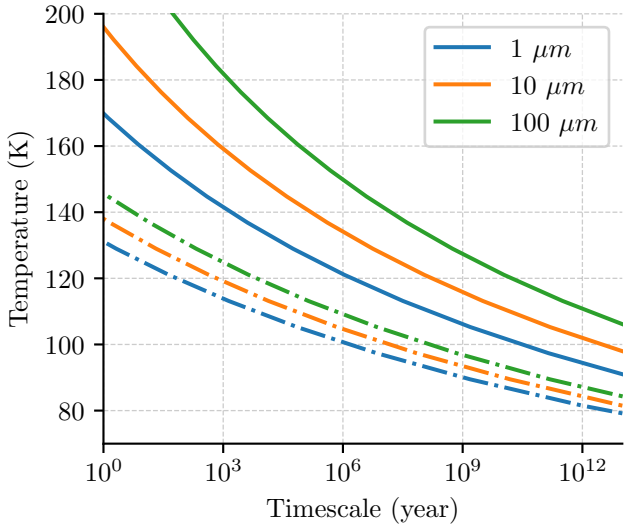

Figure 4.16: Comparison of the sintering timescales (*plain curves*) with the sublimation timescales (*dashes*) for three different grain sizes. Note that the sublimation timescales are only valid for a surface in direct contact with the vacuum.

Does this mean that sintering does not occur in the near surface? Not really. The computed sublimation flux here is an upper boundary of the real sublimation rate. First, in reality, the surface of icy moons has an exosphere which varies in pressure depending on location, slowing sublimation rates.

More importantly, layers that are not in direct contact with the surface will sublimate in the pore space, which has its own pressure. If the pore structure is closed, then there is simply no exchange of vapor with the exosphere under the top layer. If the pore structure is open, pores can communicate, allowing for an exchange of matter. On one hand, sublimation fills the pores with matter; on the other hand, the top layer evacuates this matter into the exosphere. Depending on porosity, tortuosity, temperature, depth etc., the pore pressure may vary greatly. While the top layer grains in contact with the exosphere are likely to sublimate, we do not know exactly to what depths this sublimation is faster than sintering. Is it only a few grains deep, or much deeper? Computing this pressure is complex and

requires a precise formulation of the fluid dynamics within the pore space, which is beyond the scope of this thesis but is briefly discussed in Section 6.3.2.

Bibliography for Chapter 4

Adams, E. E., D. A. Miller, and R. L. Brown (Dec. 2001). "Grain boundary ridge on sintered bonds between ice crystals". In: *Journal of Applied Physics* 90.11, pp. 5782–5785. DOI: 10.1063/1.1410889.

Ashby, M.F (Mar. 1974). "A first report on sintering diagrams". In: *Acta Metallurgica* 22.3, pp. 275–289. DOI: 10.1016/0001-6160(74)90167-9.

Belgacem, Ines, Frédéric Schmidt, and Grégory Jonniaux (Mar. 2020). "Regional study of Europa's photometry". In: *Icarus* 338, p. 113525. ISSN: 0019-1035. DOI: 10.1016/j.icarus.2019.113525.

Berdis, Jodi R. et al. (May 2020). "Europa's surface water ice crystallinity: Discrepancy between observations and thermophysical and particle flux modeling". In: *Icarus* 341, p. 113660. ISSN: 0019-1035. DOI: 10.1016/j.icarus.2020.113660.

Blackford, Jane R (Oct. 2007). "Sintering and microstructure of ice: a review". In: *Journal of Physics D: Applied Physics* 40.21, R355–R385. DOI: 10.1088/0022-3727/40/21/r02.

Brun, E. et al. (1992). "A numerical model to simulate snow-cover stratigraphy for operational avalanche forecasting". In: *Journal of Glaciology* 38.128, pp. 13–22. ISSN: 1727-5652. DOI: 10.3189/s0022143000009552.

Butt, Hans-Jürgen (2003). *Physics and chemistry of interfaces*. Ed. by Karlheinz Graf and Michael Kappl. Physics textbook. Includes bibliographical references and index. Weinheim: Wiley-VCH. 1361 pp. ISBN: 9783527606405.

Choukroun, M. et al. (Aug. 2020). "Strength Evolution of Ice Plume Deposit Analogs of Enceladus and Europa". In: *Geophysical Research Letters* 47.15. DOI: 10.1029/2020gl088953.

Colbeck, S. C. (1980). "Thermodynamics of snow metamorphism due to variations in curvature". In: *Journal of Glaciology* 26.94, pp. 291–301. ISSN: 1727-5652. DOI: 10.3189/s0022143000010832.

— (June 1983). "Theory of metamorphism of dry snow". In: *Journal of Geophysical Research: Oceans* 88.C9, pp. 5475–5482. DOI: 10.1029/jc088ic09p05475.

— (Oct. 1998). "Sintering in a dry snow cover". In: *Journal of Applied Physics* 84.8, pp. 4585–4589. ISSN: 1089-7550. DOI: 10.1063/1.368684.

Cooper, J (Jan. 2001). "Energetic Ion and Electron Irradiation of the Icy Galilean Satellites". In: *Icarus* 149.1, pp. 133–159. DOI: 10.1006/icar.2000.6498.

Cruz-Mermy et al. (Apr. 2023). "Selection of chemical species for Europa's surface using Galileo/NIMS". In: *Icarus* 394, p. 115379. ISSN: 0019-1035. DOI: 10.1016/j.icarus.2022.115379.

Eluszkiewicz (1991). "On the microphysical state of the surface of Triton". In: *Journal of Geophysical Research: Space Physics*.

— (1993). "Thesis". PhD thesis.

Eluszkiewicz, Janusz (Mar. 1990). "Compaction and internal structure of Mimas". In: *Icarus* 84.1, pp. 215–225. ISSN: 0019-1035. DOI: 10.1016/0019-1035(90)90167-8.

— (May 1993). "On the Microphysical State of the Martian Seasonal Caps". In: *Icarus* 103.1, pp. 43–48. DOI: 10.1006/icar.1993.1056.

Feistel, Rainer and Wolfgang Wagner (2007). "Sublimation pressure and sublimation enthalpy of H2O ice Ih between 0 and 273.16K". In: *Geochimica et Cosmochimica Acta* 71.1, pp. 36–45. ISSN: 0016-7037. DOI: https://doi.org/10.1016/j.gca.2006.08.034. URL: https://www.sciencedirect.com/science/article/pii/S0016703706020461.

Flanner, Mark G. and Charles S. Zender (2006). "Linking snowpack microphysics and albedo evolution". In: *Journal of Geophysical Research* 111.D12. DOI: 10.1029/2005jd006834.

Flin, Frédéric et al. (Apr. 2003). "Full three-dimensional modelling of curvature-dependent snow metamorphism: first results and comparison with experimental tomographic data". In: *Journal of Physics D: Applied Physics* 36.10A, A49–A54. DOI: 10.1088/0022-3727/36/10a/310.

Gundlach, B et al. (July 2018). "Sintering and sublimation of micrometre-sized water-ice particles: the formation of surface crusts on icy Solar System bodies". In: *Monthly Notices of the Royal Astronomical Society* 479.4, pp. 5272–5287. DOI: 10.1093/mnras/sty1839.

Hand, K. P. et al. (Jan. 2022). "Science Goals and Mission Architecture of the Europa Lander Mission Concept". In: *The Planetary Science Journal* 3.1, p. 22. DOI: 10.3847/psj/ac4493.

Hansen, Gary B. (2004). "Amorphous and crystalline ice on the Galilean satellites: A balance between thermal and radiolytic processes". In: *Journal of Geophysical Research* 109.E1. DOI: 10.1029/2003je002149.

Hayne, Paul O. (Oct. 2016). "Sublimation as a Continuous and Transient Source of Water in Europa's Exosphere". In: *AAS/Division for Planetary Sciences Meeting Abstracts #48*. Vol. 48. AAS/Division for Planetary Sciences Meeting Abstracts, 517.06, p. 517.06. URL: https://ui.adsabs.harvard.edu/abs/2016DPS....4851706H.

Haynes, D. R., N. J. Tro, and S. M. George (Oct. 1992). "Condensation and evaporation of water on ice surfaces". In: *The Journal of Physical Chemistry* 96.21, pp. 8502–8509. ISSN: 1541-5740. DOI: 10.1021/j100200a055.

Hobbs, P. V. and B. J. Mason (Feb. 1964). "The sintering and adhesion of Ice". In: *Philosophical Magazine* 9.98, pp. 181–197. DOI: 10.1080/14786436408229184.

Johnson, D. Lynn (Jan. 1969). "New Method of Obtaining Volume, Grain-Boundary, and Surface Diffusion Coefficients from Sintering Data". In: *Journal of Applied Physics* 40.1, pp. 192–200. ISSN: 1089-7550. DOI: 10.1063/1.1657030.

Jones, Frank E. (2018). *Evaporation of Water With Emphasis on Applications and Measurements*. 1st ed. Milton: CRC Press. 1201 pp. ISBN: 9781351080415.

Jordan, Rachel E. (1991). "A One-dimensional temperature model for a snow cover". In: *Technical Documentation for SNTHERM.89*. URL: https://api.semanticscholar.org/CorpusID:126628105.

Kaempfer, T. U. and M. Schneebeli (Dec. 2007). "Observation of isothermal metamorphism of new snow and interpretation as a sintering process". In: *Journal of Geophysical Research: Atmospheres* 112.D24. ISSN: 0148-0227. DOI: 10.1029/2007jd009047.

Kingery, W. D. and M. Berg (Oct. 1955). "Study of the Initial Stages of Sintering Solids by Viscous Flow, Evaporation-Condensation, and Self-Diffusion". In: *Journal of Applied Physics* 26.10, pp. 1205–1212. DOI: 10.1063/1.1721874.

Klinger, J. (Sept. 1981). "Some consequences of a phase transition of water ice on the heat balance of comet nuclei". In: *Icarus* 47.3, pp. 320–324. DOI: 10.1016/0019-1035(81)90179-2.

Kossacki, Konrad J. et al. (May 1994). "The influence of grain sintering on the thermoconductivity of porous ice". In: *Planetary and Space Science* 42.5, pp. 383–389. DOI: 10.1016/0032-0633(94)90127-9.

Kuczynski, G. C. (Dec. 1949). "Study of the Sintering of Glass". In: *Journal of Applied Physics* 20.12, pp. 1160–1163. ISSN: 1089-7550. DOI: 10.1063/1.1698291.

Kuroiwa, Daisuke (May 1961). "A Study of Ice Sintering". In: *Tellus* 13.2, pp. 252–259. ISSN: 2153-3490. DOI: 10.1111/j.2153-3490.1961.tb00082.x.

Lehning, Michael et al. (Nov. 2002). "A physical SNOWPACK model for the Swiss avalanche warning". In: *Cold Regions Science and Technology* 35.3, pp. 147–167. DOI: 10.1016/s0165-232x(02)00073-3.

Ligier, N. et al. (May 2016). "VLT/SINFONI observations of Europa: new insights into the surface composition". In: *The Astronomical Journal* 151.6, p. 163. ISSN: 1538-3881. DOI: 10.3847/0004-6256/151/6/163.

Maeno, Norikazu and Takao Ebinuma (Oct. 1983). "Pressure sintering of ice and its implication to the densification of snow at polar glaciers and ice sheets". In: *The Journal of Physical Chemistry* 87.21, pp. 4103–4110. ISSN: 1541-5740. DOI: 10.1021/j100244a023.

McEwen, Alfred S. (July 1986). "Exogenic and endogenic albedo and color patterns on Europa". In: *Journal of Geophysical Research: Solid Earth* 91.B8, pp. 8077–8097. ISSN: 0148-0227. DOI: 10.1029/jb091ib08p08077.

Mergny, Cyril and Frédéric Schmidt (Feb. 2024a). "Gravity-induced ice compaction and subsurface porosity on icy moons". In: *Icarus*, p. 116008. ISSN: 0019-1035. DOI: 10.1016/j.icarus.2024.116008.

Mergny, Cyril and Frédéric Schmidt (2024b). "MultIHeaTS: a Fast and Stable Thermal Solver for Multilayered Planetary Surfaces". In: *submitted*.

Miller, D.A., E.E. Adams, and R.L. Brown (Nov. 2003). "A microstructural approach to predict dry snow metamorphism in generalized thermal conditions". In: *Cold Regions Science and Technology* 37.3, pp. 213–226. DOI: 10.1016/j.coldregions.2003.07.001.

Miller, Daniel August (2002). "An integrated microstructural study of dry snowmetamorphism under generalized thermal conditions". PhD thesis. MONTANA STATE UNIVERSITY.

Molaro, J. L. et al. (Feb. 2019). "The Microstructural Evolution of Water Ice in the Solar System Through Sintering". In: *Journal of Geophysical Research: Planets* 124.2, pp. 243–277. DOI: 10.1029/2018je005773.

Murthy, S. Gudipati and Castillo-Rogez Julie (2013). *The Science of Solar System Ices*. Springer New York. ISBN: 9781461430766. DOI: 10.1007/978-1-4614-3076-6.

Pappalardo, R. T. et al. (Jan. 1998). "Geological evidence for solid-state convection in Europa's ice shell". In: *Nature* 391.6665, pp. 365–368. DOI: 10.1038/34862.

Pappalardo, R.T. et al. (Aug. 2013). "Science Potential from a Europa Lander". In: *Astrobiology* 13.8, pp. 740–773. DOI: 10.1089/ast.2013.1003.

Paranicas, C. et al. (Jan. 2009). "Europa's Radiation Environment and Its Effects on the Surface". In: *Europa*.

Poch, O. et al. (Oct. 2018). "Polarimetry of Water Ice Particles Providing Insights on Grain Size and Degree of Sintering on Icy Planetary Surfaces". In: *Journal of Geophysical Research: Planets* 123.10, pp. 2564–2584. ISSN: 2169-9100. DOI: 10.1029/2018je005753.

Prialnik, Dina and David Jewitt (2022). *Amorphous ice in comets: evidence and consequences*. DOI: 10.48550/ARXIV.2209.05907.

Rathbun, Julie A., Nathaniel J. Rodriguez, and John R. Spencer (Dec. 2010). "Galileo PPR observations of Europa: Hotspot detection limits and surface thermal properties". In: *Icarus* 210.2, pp. 763–769. DOI: 10.1016/j.icarus.2010.07.017.

Raut, U. et al. (Nov. 2008). "Cosmic Ray Compaction of Porous Interstellar Ices". In: *The Astrophysical Journal* 687.2, pp. 1070–1074. DOI: 10.1086/592193.

Schaible, M.J. et al. (Mar. 2017). "High energy electron sintering of icy regoliths: Formation of the PacMan thermal anomalies on the icy Saturnian moons". In: *Icarus* 285, pp. 211–223. DOI: 10.1016/j.icarus.2016.08.033.

Schorghofer, Norbert (2022). "Planetary-Code-Collection: Thermal, Ice Evolution, and Exosphere Models for Planetary Surfaces". In: *Zenodo*. DOI: 10.5281/ZENODO.594268.

Schrage, Robert W. (Dec. 1953). *A Theoretical Study of Interphase Mass Transfer*. Columbia University Press. ISBN: 9780231877367. DOI: 10.7312/schr90162.

Spencer, John, Larry Lebofsky, and Mark Sykes (Apr. 1989). "Systematic biases in radiometric diameter determinations". In: *Icarus* 78.2, pp. 337–354. DOI: 10.1016/0019-1035(89)90182-6.

Swinkels, F.B. and M.F. Ashby (Feb. 1981). "A second report on sintering diagrams". In: *Acta Metallurgica* 29.2, pp. 259–281. DOI: 10.1016/0001-6160(81)90154-1.

Trumbo, Samantha K., Michael E. Brown, and Bryan J. Butler (Sept. 2018). "ALMA Thermal Observations of Europa". In: *The Astronomical Journal* 156.4, p. 161. ISSN: 1538-3881. DOI: 10.3847/1538-3881/aada87.

Vale Pereira, Paula do et al. (May 2023). "Experimental Validation of Cryobot Thermal Models for the Exploration of Ocean Worlds". In: *The Planetary Science Journal* 4.5, p. 81. DOI: 10.3847/psj/acc2b7.

Vionnet, V. et al. (May 2012). "The detailed snowpack scheme Crocus and its implementation in SURFEX v7.2". In: *Geoscientific Model Development* 5.3, pp. 773–791. DOI: 10.5194/gmd-5-773-2012.

Figure 4.17: Original creation from the artist @FMdessine.

CHAPTER 5

Crystallization and Amorphization

The work presented in this chapter comes from the article titled *"Crystallinity of Europa's Surface" by C. Mergny, F.Schmidt and F. Keil, 2024* which will soon be submitted for publication.

Contents

Foreword

Hexagonal vs Amorphous Ice — The surfaces of icy moons are expected to consist notably of a mixture of crystalline and amorphous water ice (Hansen, 2004; Ligier et al., 2016; Cruz-Mermy et al., 2023). Both types of ice display distinct optical behaviors across different wavelengths, making them potentially distinguishable through remote sensing. Our particular interest lies in the Near- to Mid-infrared range (0.8-25 µm), which is commonly used by remote sensing instruments for spectroscopic observations.

Various experimental investigations have explored how amorphous and crystalline ice behave optically within this wavelength range, as illustrated in Figure 5.1. Comparing amorphous to crystalline H_2O ice, the 2.0 µm and 1.5 µm bands shift to shorter wavelengths, and the 1.65 µm and 1.56 µm bands decrease in strength (Figure 5.1, *Left*). The band at 3.1 µm is greatly weakened in warm crystalline or cold amorphous ice (Grundy et al., 1998; B. Schmitt, 1998), as illustrated in Figure 5.1, (*Right*). This fundamental absorption near 3.1 µm may appears as a reflection peak for some spectra. It is broad and weak for amorphous and warm ice (Hagen et al., 1981; Wood et al., 1982; Warren, 1984), and stronger with a triplet structure for cold crystalline ice (Mastrapa et al., 2008).

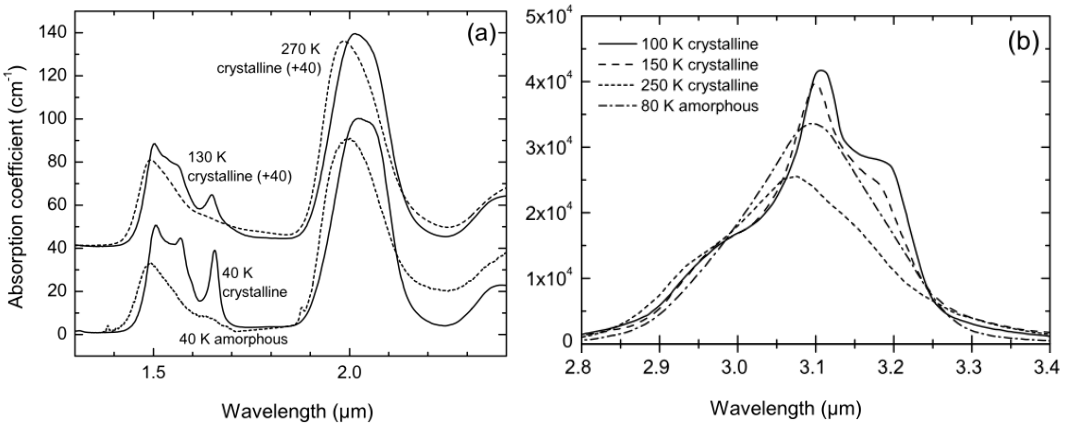

Figure 5.1: **(a)** Near-infrared absorption spectra of water ice where for visibility, the upper curves are offset by $+40\,\mathrm{cm}^{-1}$. *Upper curves* : crystalline ice at 130 K (*solid line*) and 270 K (*dashes*). *Lower curves* : crystalline (*solid line*) and amorphous water ice (*dotted line*), both at 40 K(Grundy et al., 1998; B. Schmitt, 1998). **(b)** Absorption spectra of water ice in the region of the fundamental absorption centered near 3.1 µm. The four examples shown are for crystalline ice at 100K, 150K and 250 K and for amorphous ice at 80 K. Figures adapted from Mastrapa et al. (2008)

As shown in Figure 5.1, the absorption spectrum of hexagonal water ice is very sensitive to the temperature. In both 1.65 µm and 3.1 µm bands, the amorphous spectrum is going toward the shape of the warm temperature ice spectrum. However,

for the Galilean satellites, all the ice is at temperatures colder than 150 K, so it is not possible to confuse amorphous ice with warm ice (Hansen, 2004).

Europa Ice-Rich Spectra — The conditions found on the surfaces of icy moons may be more favorable for the formation and stability of amorphous water ice (B. Schmitt, 1998). When water vapor freezes at the such cold temperatures, the ice forms an amorphous structure characterized by high porosity, with temperature and condensation rate being the key factors influencing it. Knowing whether the surface stays amorphous or crystallizes may have important consequences on its properties. An amorphous surface is expected to have a higher gas retention (Jenniskens et al., 1998) which could better explain the trapping of molecules, necessary in some models of the Europa's exosphere (Oza et al., 2018).

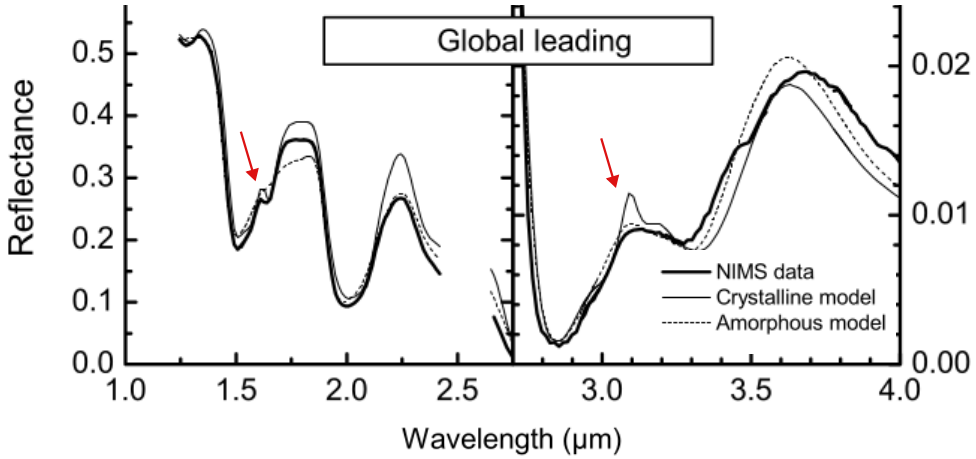

Figure 5.2: Average Europa ice-rich reflectance spectra and model fits on the leading hemisphere. The average spectra are plotted as heavy, solid lines. Shortwave segment on the left (1.0 – 2.75 µm) and a longwave segment on the right (2.7 – 4.0 µm) with different vertical scales. On each panel, the thin solid line represents a model with the best band shape using crystalline ice while the thin dashed line represents the same model with amorphous ice. Red arrows show the 1.65 µm and 3.1 µm bands. Figure adapted from (Hansen, 2004).

The majority of Europa's surface spectra have been acquired by the Near-Infrared Mapping Spectrometer (NIMS) aboard the Galileo spacecraft, operating within the $0.7 - 5.2\,\mu m$ range. Based on this data, Hansen (2004) have compared the ice-rich spectra of Europa, with models of crystalline and amorphous ice (see Figure 5.2). On one hand, the longwave segment with a focus on the characteristic 3.1 µm band shows that, for the top micrometer of the surface (i.e., the depth probed by near-infrared observations), water ice on Europa is predominantly amorphous. On the other hand, the shortwave segment with a focus on the characteristic 1.65 µm band shows a better fit with the crystalline model for ice at $\sim 1\,mm$ depth and deeper.

These results suggest that a positive vertical crystallinity gradient exists in the near surface.

Ligier et al. (2016) observed and modeled the abundance of amorphous ice using Earth-based observations with the VLT. Their study presents separate maps for amorphous ice and crystalline ice. To determine the crystalline fraction, we would need to compute the ratio between the two. However, the significant presence of non-ice chemicals on the trailing hemisphere complicates interpretations in this region. Nonetheless, on a global scale, they derived that crystalline ice is approximately twice as abundant as amorphous ice based on the analysis of the 1.65 µm band. This results in an amorphous-to-crystalline water ice ratio suggesting a crystallinity of 64%.

In the end, Hansen and Ligier results are in agreement. Hansen uses both the 3.1 µm band, which probes the very shallow surface and was found to be more amorphous, and the 1.65 µm band, which probes deeper depths and shows predominantly crystalline ice. Ligier focuses solely on the 1.65 µm band and similarly finds a higher proportion of crystalline ice. However, in the interpretation of the icy moons surfaces, the presence of a band near 1.65 µm does not exclusively indicate a surface that is entirely crystalline, as it can also be present in predominantly amorphous compositions. Mastrapa et al. (2008) have shown that only a 20 percent fraction of crystalline ice is sufficient to make a sample's spectra look nearly fully crystalline. This can greatly change our interpretation of Europa's spectra and show the limitations of linear mixture spectroscopy models for estimating compositions. One more recent attempt, using non-linear radiative transfer have shown that a mixture of crystalline and amorphous ice is present at the surface of Europa (Cruz-Mermy et al., 2023).

A Competition for Crystallinity — Hansen proposed that the mixture of amorphous and crystalline ice phases observed on Europa's surface results from a delicate balance between thermal and radiolytic processes. On one hand, the surface of Europa reaches temperatures where thermal crystallization can occur over reasonable timescales. On the other hand, the intense radiation from Jupiter's magnetosphere is likely responsible for amorphizing the surface ice. Despite their observations, neither Hansen (2004) nor Ligier et al. (2016) have put forward a theoretical model to explain the crystallinity they derived.

To address this issue, Berdis et al. (2020) conducted a numerical modeling of the competition between ion radiations and thermal crystallization. However, their model assumes a fixed average temperature for Europa's surface. As for the sintering process, thermal crystallization rates are extremely sensitive to temperature, and neglecting the full temperature history can lead to significant errors in crystallization rates. Furthermore, Berdis et al. (2020) neglected the effects of electrons and UV radiation on the ice surface, while these are known to induce amorphization at least for low temperatures (see Section 5.2.2 for details). Finally, their study does not

explain the vertical crystallinity gradient observed by Hansen (2004).

This chapter details our efforts to model the competition between thermal crystallization and radiation-induced amorphization, and their integration into LunaIcy to produce a detailed crystallinity map of Europa.

Author's Note

The work presented here first started during the internship of Master's student Felix Keil, which I co-supervised during my second year of PhD. During this internship, Felix focused on modeling the thermal crystallization process and assisted in gathering the literature review on amorphization processes.

Abstract

The surface of Europa experiences a competition between thermally-induced crystallization and radiation-induced amorphization processes, leading to changes of its crystalline structure. The non-linear crystallization and temperature-dependent amorphization rate, incorporating ions, electrons and UV doses, are integrated into our multiphysics model LunaIcy, enabling simulations of coupled processes on icy surfaces.

Thirty simulations spanning 100 000 years, covering the ranges of albedo and latitude values on Europa, explore the competition between crystallization and irradiation, providing insights into the evolution of crystalline fraction at varying depths. Using an interpolated albedo map of Europa, our set of simulations generates a crystallinity map consistent with spectroscopic observations, showing, within the top millimeter, highly crystalline ice near the equator, amorphous ice at the poles, and a mix of the two at mid-latitudes. Regions/depths with balanced competition between crystallization and amorphization rates are of high interest due to their periodic fluctuations in crystalline fraction. Our interpolated map reveals periodic variations, with seasonal amplitudes reaching up to 35% of crystalline fraction. These are observable near the millimeter depth and we propose a plan to observe these variations by spectroscopy in forthcoming missions.

Author's Note

The manuscript presented here is still under construction. It will soon be ready for submission, but some of the sections / even the article's name may change after the peer-review process.

5.1 Introduction

The surface of icy moons consists of water ice that can exist in either a crystalline or amorphous phase. For the typical temperature range of the Galilean moons, around 100 K, water ice tends to form in its amorphous phase (Kouchi, Yamamoto, et al., 1994).

Amorphous ices are metastable, meaning that there exist a crystalline phase with lower energy. The process that slowly transforms amorphous ice into its crystalline forms (cubic or hexagonal) is called thermal crystallization. The rate of crystallization is extremely sensitive to temperature, taking for example 5 minutes at 150 K but up to 5 billion years at 80 K (Bernard Schmitt et al., 1989). Thus, depending on the conditions, the surface of icy moons may have crystallized or remained locked in its amorphous state. Acting in the opposite direction, the constant bombardment of energetic particles on the surfaces increases the disorder in ice crystals, leading to amorphization (Cooper, 2001; Raúl A. Baragiola, 2003; Berdis et al., 2020). However, the exact mechanisms behind this radiation-induced amorphization remains unclear.

The complex balance between thermal crystallization and radiation-induced amorphization, may lead to various crystallinity on Europa depending on the dominant process. To determined the current state of Europa's surface, space-observation based study have brought valuable insights on the crystallinity. Hansen (2004) compared Galileo Near-Infrared Mapping Spectrometer (NIMS) ice-rich spectra of Europa's surface with models of crystalline and amorphous ice. The longwave segment, focusing on the 3.1 µm band, shows that at depths close to 1 mm and deeper, water ice on Europa is found to be predominantly crystalline. The shortwave segment, focusing on the 1.65 µm band, indicates a better fit with the amorphous model above this depth. Complementary to this study, Ligier et al. (2016) used VLT observations to produce separate maps of the abundance of amorphous and crystalline ice. However, they do not directly provide a crystallinity map and the non-ice chemicals on the trailing hemisphere complicate interpretations. Globally, they found crystalline ice to be about twice as abundant as amorphous ice based on the 1.65 µm band. Ultimately, both studies are in agreement and suggest that there exist a positive vertical crystallinity gradient near the surface. However, the presence of a band near 1.65 µm does not exclusively indicate a fully crystalline surface, as it can also appear in predominantly amorphous compositions. Mastrapa et al. (2008) demonstrated that an ice mixture made of 80% amorphous ice can make a sample's spectra appear

nearly fully crystalline. This highlights the limitations of linear mixture spectroscopy models for estimating compositions (Cruz-Mermy et al., 2023).

Numerical work can also be very valuable for simulating the intricate competition that leads to Europa's crystallinity. Berdis et al. (2020) conducted modeling of the interaction between ion radiations and thermal crystallization. However, their model assumes a fixed average temperature for Europa's surface. Given the strong temperature dependency of crystallization kinetics (Kouchi, Yamamoto, et al., 1994), it would be important to consider the daily temperature variations, as even brief temperature peaks within the day can significantly impact crystallization over long timescales. Additionally, the impact of electrons (Heide, 1984; Lepault et al., 1983; Jacques Dubochet et al., 1988) and UV photons (Kouchi and Kuroda, 1990; Leto and Baratta, 2002; Leto, Gomis, et al., 2005) remains unexplored specifically on icy moons despite their significant flux (Cooper, 2001).

As a result, modeling studies have not yet been able to explain the vertical crystallinity gradient observed by Hansen (2004), leaving several questions unanswered: How does crystallinity of the near surface varies for different locations on Europa? What are the typical depths of variations of the crystalline fraction? The solar flux heating the surface varies periodically, influencing the intensity of thermal crystallization. Could there be observable periodic changes in the surface crystallinity of Europa?

To accurately model crystallinity, these two competing processes must be 1) computed simultaneously 2) coupled to a thermal solver, given their temperature-dependency. To so, they are integrated into multiphysics model LunaIcy (Mergny and Schmidt, 2024b; Mergny and Schmidt, 2024a) that incorporates a precise orbit description of Europa over long timescales, along with a fast and stable thermal solver, MultIHeaTS (Mergny and Schmidt, 2024b), and additional physics describing the evolution of the thermal properties of the ice.

In the first section, we present the derivation of crystallization timescales and irradiation dose rates for ions, electrons, and UV radiation, and their integration into our multiphysics model. We then present the results of simulations conducted over 100 kyr, covering the range of possible parameter configurations on Europa. This allow us to create an expected crystallinity map of Europa and study the temporal and depth-dependent variations in crystallinity profiles under various conditions.

5.2 Methods

5.2.1 Thermal Crystallization of Ice

The Johnson–Mehl–Avrami–Kolmogorov equation, also known as Avrami equation, describes the kinetics of crystallisation (Avrami, 1939; Avrami, 1940; Avrami, 1941). According the Avrami equation, the crystalline fraction, defined as the volume

fraction of crystalline ice, is given after a relaxation time t by

$$\theta(t) = 1 - \exp\left(-\left(\frac{t}{\tau}\right)^n\right) \tag{5.1}$$

where n is the Avrami constant, an integer depending on the crystallization conditions, and τ is the characteristic crystallization time. There is no consensus in the literature regarding the exact choice of Avrami exponent n for ice crystallization on planetary surfaces. While, for example, Kouchi, Yamamoto, et al. (1994) solves the differential equation with an exponent $n = 1$, Steckloff et al. (2023) opts to solve the Avrami equation with an exponent $n = 4$. The selection of this exponent depends on the conditions under which our ice crystallizes. Rao et al. (1980) compiled a table encompassing various values obtained experimentally of the exponent n found in the literature. However, it is important to note that the characteristic crystallization time does not depend on this Avrami exponent.

The crystallization timescale has been expressed by Kouchi, Yamamoto, et al. (1994) based on work from (Seki et al., 1981), as

$$\tau = \left(\frac{1}{2\pi\alpha}\right)^{1/4} \left(\frac{k_B T}{s}\right)^{1/8} \frac{\Omega^{2/3}}{D_0} \exp\left(\frac{1}{k_B T}\left[E_\alpha + \frac{4\pi\sigma^3}{3L^2}\left(\frac{T_m}{T_m - T}\right)^2\right]\right) \tag{5.2}$$

where T is the temperature, k_B the Boltzmann constant, and the other parameters are taken from Kouchi, Yamamoto, et al. (1994) and Bernard Schmitt et al. (1989) : $\alpha = 2$ is a geometric factor dependent on the growth type, $\Omega = 3.25 \times 10^{-29}\,\mathrm{m}^3$ is the effective volume of a water molecule, $D_0 = 6.1 \times 10^{-7}\,\mathrm{m}^2\,\mathrm{s}^{-1}$ is the ice self-diffusion coefficient, $E_a = 7635 \times 10^{-23}\,\mathrm{J}$ is the activation energy of self-diffusion, $L = 2.6 \times 10^{-21}\,\mathrm{J}$ is the crystallization enthalpy per molecule, $T_m = 273\,\mathrm{K}$ is the ice-water melting temperature, $\gamma = 70 \times 10^{-3}\,\mathrm{N\,m}^{-1}$ is the surface tension of water and $s = \frac{2}{3}\Omega\gamma$. For reference, the crystallization timescale is close to one billion years at 80 K, around a thousand years at 100 K and less than one Europa's day at 130 K (see additional Figure in this thesis Section 5.5.1) . These key timescales (Bernard Schmitt et al., 1989) are within the temperature range found on Europa, highlighting the necessity to accurately estimate the temperature variations.

While the Avrami Equation (5.1) allows us to understand the evolution of the ice crystalline fraction under a constant temperature T, under more realistic conditions, the ice temperature varies over time, especially due to diurnal oscillations in solar flux. In such situations, it is no longer possible to use the analytical expression derived by Avrami. To answer this, Kouchi, Yamamoto, et al. (1994) suggested to approximate the the crystalline fraction expression from the maximum temperature (Kouchi, Yamamoto, et al., 1994). This method assumes that only the maximum temperature affects crystallization, disregarding the entire temperature history, which significantly contributes to crystallization, particularly when temperatures are lower but close to to the maximum temperature. Another drawback is the necessity to know in advance the maximum temperature before initiating calculations.

To improve upon this, inspired by Steckloff et al. (2023), we propose here to discretize the differential equation that lead to Equation (5.1) under the exponent $n = 1$

$$\theta(t + \Delta t) = \theta(t) + \frac{1 - \theta(t)}{\tau(T)}\Delta t, \tag{5.3}$$

where Δt is the timestep, chosen to be greatly inferior to the crystallization timescale. Thanks to such formulation, the crystallization rate can be computed for each iteration coupled to a thermal solver, taking into account the complete temperature history.

5.2.2 Radiation-Induced Amorphization

5.2.2.1 Amorphization Evolution

The surface of icy moons is continuously bombarded by a range of charged ions, electrons and photons that breaks its crystalline structure. Following experimental results (Moore et al., 1992; Strazzulla et al., 1992; Leto and Baratta, 2002), the amorphization of the crystalline fraction, when no crystallization occurs, is given by

$$\theta(t) = \exp\left(-k(T)D(t)\right) \tag{5.4}$$

where D is a dose (in Joules), the radiation energy accumulated per molecule after some time t and $k(T)$ is the amorphization factor.

Although energy deposition comes from different excitation sources, k shows similar temperature dependence for ions (Famá et al., 2010; R. A. Baragiola et al., 2013), referred to as $k_+(T)$ in this article. Using various experimental values under different radiation sources and temperatures (Strazzulla et al., 1992), we obtained an exponential fit

$$k(T) = \exp\left(-A_k T + B_k\right) \tag{5.5}$$

with, for ions, $A_{k+} = 1.826 \times 10^{-2}\,\mathrm{eV^{-1}K^{-1}}$ and $B_{k+} = -2.691 \times 10^{-1}\,\mathrm{eV^{-1}}$.

In contrast, experimental results suggest that for electrons and UV photons, ice becomes extremely resistant to irradiation above $\sim 77\,\mathrm{K}$ (Lepault et al., 1983; J. Dubochet et al., 1984; Heide, 1984; Kouchi and Kuroda, 1990; Moore et al., 1992; Leto and Baratta, 2002). It is not clear whether amorphization by electrons above this temperature is simply impossible or requires very high doses. While Moore et al. (1992) mentionned that Heide (1984) achieved amorphization at 120 K with a dose of approximately $2000\,\mathrm{ev\,molecules^{-1}}$, this information is not explicitly provided in the original paper. We choose to also adopt an exponential fit of the amorphization factor for electrons (Equation (5.5)) based on the experimental results from Heide (1984), leading the constants $A_{k-} = 7.494 \times 10^{-2}\,\mathrm{eV^{-1}K^{-1}}$ and $B_{k-} = 1.699 \times 10^{-1}\,\mathrm{eV^{-1}}$. Photons induced amorphization lack sufficient data with temperature (Kouchi and Kuroda, 1990; Leto and Baratta, 2002) but they show a similar trends and resistance at high temperature as electron (Famá et al., 2010; R. A. Baragiola

et al., 2013). For these reasons, with assume electrons and photons to share the same amorphization factor, referred to as $k_{-}(T)$, The implications of not making amorphization by electrons impossible at high temperature but instead requiring very high dose, is discussed later in the paper.

There is no reason to expect the dose to remain constant with time. Here we also discretize the temporal variations for amorphization $D(t+\Delta t) = D(t) + D(\Delta t)$. Using a timestep small enough such that with $kD(\Delta t) \ll 1$, Equation (5.4) can be approximated to

$$\theta(t+\Delta t) \approx -\exp\left(-k(T)D(t)\right)\left(1-k(T)D(\Delta t)\right) \tag{5.6}$$

leading to the expression

$$\theta(t+\Delta t) = \theta(t)\left(1-k(T)D(t,\Delta t)\right). \tag{5.7}$$

By combining (5.3) and (5.7), the crystalline fraction can be obtained at each iteration, for any given temperature and dose. The dose can be obtained by computing the quantity of energy E_r absorbed by water molecules N

$$D(x) = \frac{E_r}{N} \tag{5.8}$$

In a box of thickness h and cross-section S, the energy received by the radiation flux F after a time Δt is given by

$$E_r = S\left(F(x) - F(x+h)\right)\Delta t \tag{5.9}$$

where the radiation flux is considered constant in time between t and $t+\Delta t$. The considered box, has a number of molecules equals to $N = h \times S \times n_{H_2O}$, where n_{H_2O} is the number density of H_2O molecules in the ice given by

$$n_{H_2O}(\phi) = \rho_0(1-\phi)\frac{\mathcal{N}_a}{M} \tag{5.10}$$

with ϕ the porosity, ρ_0 the density of bulk ice, M the molar mass of water and $\mathcal{N}_a$ the Avogrado's constant. By taking the limit when the thickness of the box h tends to zero, the expression of the dose absorbed by molecules in an infinitesimal layer at depth x becomes

$$D(x,\Delta t) = -\frac{\partial F(x)}{\partial x}\frac{\Delta t}{n_{H_2O}} \tag{5.11}$$

Hence by computing the radiation flux with depth for the different radiations sources we get access to the absorbed dose which leads to the amorphization rate.

5.2.2.2 Charged particles radiations

The flux of charged particles penetrating the surface and subsurface of Europa, has been the subject of various articles (Cooper, 2001; Paranicas, R. W. Carlson,

et al., 2001; T. A. Nordheim et al., 2018). Measures of the ion intensity by Galileo Energetic Particle Detector lead to the the fit from (Mauk et al., 2004; Paranicas, John Cooper, et al., 2009) of the ion spectrum near Europa,

$$j(E) = cE\left(E + K_T(1+\gamma_1)\right)^{-1-\gamma_1}\left(1+\left(\frac{E}{E_T}\right)^{\gamma_2}\right)^{-1} \tag{5.12}$$

where j is the ion intensity ($\mathrm{cm}^{-2}\mathrm{sr}^{-1}\mathrm{keV}^{-1}$) at the proton energy E(keV), and the constants for each individual ion are given in Table 1 of Paranicas, John Cooper, et al. (2009). The same type of measurement lead to the fit of the electron spectrum near Europa

$$j(E) = j_0 E^{-a}\left(1+\frac{E}{E_0}\right)^{-b} \tag{5.13}$$

where j is the ion intensity ($\mathrm{cm}^{-2}\mathrm{sr}^{-1}\mathrm{MeV}^{-1}$) at the proton energy E(MeV), and the constants are $j_0 = 4.23\times10^6$, $E_0 = 3.11\,\mathrm{MeV}$, $a = 1.58$ and $b = 1.86$.

To first order, we assume that the deposition of energetic particles is nearly uniform over Europa's surface. For ion fluxes, the difference between hemispheres is only a few times larger on the trailing hemisphere (Paranicas, Ratliff, et al., 2002). However, electrons show a stronger tendency: electrons with energies less than 25 MeV preferentially impact Europa's trailing hemisphere, while those with energies greater than 25 MeV preferentially impact the leading hemisphere (Cooper, 2001; Paranicas, John Cooper, et al., 2009; T. A. Nordheim et al., 2018). Although accounting for the distribution of charged particles over Europa's surface would be valuable for further studies, it would necessitate running different simulations for each latitude/longitude pair, which is beyond the scope of this paper.

If we consider that the measured ion intensity in upstream regions is also present on the magnetic field lines connected to Europa, the uniform flux of energy deposited by particles at the surface is

$$F_\mathrm{p}(0) = \pi\int_E j(E)E\mathrm{d}E. \tag{5.14}$$

Then the energetic flux of a particle penetrating depth x is given by

$$F_\mathrm{p}(x) = \pi\int_E j(E)E\exp\left(-\alpha'_\mathrm{p}(E)x\right)\mathrm{d}E \tag{5.15}$$

where α'_p is the absorption coefficient of a particle at energy E in porous ice. Particles of different energies will have different stopping range. Using Cooper (2001) Figure 13, we have access to the stopping range of ions and electrons in water ice as function of their energy. The stopping range L is expressed in $\mathrm{g\,cm}^{-2}$ to simplify discussion of porosity. Then in our model, the ice absorption coefficient is expressed as

$$\alpha'_\mathrm{p}(E) = \frac{\rho(\phi)}{L(E)} = \frac{\rho_0(1-\phi)}{L(E)}. \tag{5.16}$$

The stopping range for electrons provided by Cooper (2001) covers only electrons with energies greater than 10 keV. To include the full electron spectrum found near Europa, we fit the stopping range L_{e-} (in g cm^{-2}) using the function:

$$\log L_e(E) = A_e \log(E) + B_e \tag{5.17}$$

with E the electron energy in keV, $A_{e-} = 1.4762$ SI, $B_{e-} = -11.3245$ and a coefficient of determination $R^2 = 0.9934$. It remains unclear whether low-energy electrons can amorphize ice, as there are, to our knowledge, no experimental studies on this subject. Even if the complete energy range of electrons is included in this study, lower-energy electrons can only penetrate very shallow depths, where high amorphization rates are already observed. For instance, electrons with energies below 1 keV are absorbed within the first few µm of depth.

Finally, the particle-induced dose at depth is obtained from Equation (5.11),

$$D(x, \Delta t) = \frac{\Delta t}{n_{H_2O}} \pi \int_E \alpha'_p(E) j(E) E \exp\left(-\alpha'_p(E) x\right) \mathrm{d}E \tag{5.18}$$

and can be computed for protons, helium, oxygen, sulfur and electrons.

5.2.2.3 UV radiations

Kouchi and Kuroda (1990) and later Leto and Baratta (2002) have experimentally observed UV-induced amorphization of water ice. However to our knowledge, there has not been any investigation of the effect of UV on the crystalline structure of Europa's icy surface. In order to obtained the UV-induced dose at depth, we first define the emitted solar flux at the surface of the sun

$$F_{\odot_{\lambda_{1,2}}}(\lambda_1, \lambda_2) = \int_{\lambda_1}^{\lambda_2} B_\lambda(\lambda, T_\odot) \mathrm{d}\lambda \tag{5.19}$$

where B_λ is the spectral radiance in W m^{-3} given by Planck' law

$$B_\lambda(\lambda, T_\odot) = \frac{2\pi h c^2}{\lambda^5} \frac{1}{\exp\left(\dfrac{hc}{\lambda k_B T_\odot}\right) - 1}. \tag{5.20}$$

The solar flux received at the target body's surface, is then given by

$$F(0, \lambda, t) = \frac{R_\odot^2}{d(t)^2} (1 - A_\lambda) \cos\theta_i(t) F_{\odot_{\lambda_{1,2}}} \tag{5.21}$$

where $d(t)$ is the distance to the sun, $\theta_i(t)$ the solar incidence angle and A_λ is the albedo for each specific wavelength. Europa's surface albedo in the UV spectrum was obtained from Becker et al. (2018) (Figure 8 of the article) using measurements from the International Ultraviolet Explorer, HST, and Galileo data (Hendrix et al., 2005) and then interpolated over the available wavelength range of $120 - 320$ nm.

Note that the UV spectrum extends from $100 - 400\,\mathrm{nm}$, meaning our modeling does not account for some photons outside the considered range that could also induce amorphization. Additionally, it is unclear if other types of photons (visible, infrared, ...) could induce amorphization, and if not, why this would be the case. The amorphization rate is also likely wavelength-dependent. This underscore the fact that the amorphization process is still poorly understood, and we currently work with the limited available data at our disposal.

Using Beer-Lambert law, the flux received at depth x is (Lee et al., 2013)

$$F(x,t) = \frac{R_\odot^2}{d(t)^2}\cos\theta_i(t)\int_{\lambda_1}^{\lambda_2}(1-A_\lambda)B_\lambda \exp\left(-\frac{\alpha'_\lambda x}{\cos\theta_i(t)}\right) \tag{5.22}$$

where α'_λ is the spectral absorption coefficient of porous water ice

$$\alpha'_\lambda = \frac{\rho(\phi)}{\rho_0}\alpha_\lambda = (1-\phi)\alpha_\lambda \tag{5.23}$$

obtained from the reference absorption coefficient of water ice

$$\alpha_\lambda = \frac{4\pi\,\mathrm{Im}(n(\lambda))}{\lambda} \tag{5.24}$$

where $n(\lambda)$ is the complex index of refraction of ice Ih (Warren, 1984).

Finally, the UV-induced dose at depth is obtained from Equation (5.11),

$$D_{UV}(x,\Delta t) = \frac{R_\odot^2}{d(t)^2}\frac{\Delta t}{n_{\mathrm{H_2O}}(\phi)}\int_{\lambda_1}^{\lambda_2}\alpha'_\lambda(1-A_\lambda)B_\lambda \exp\left(-\frac{\alpha'_\lambda x}{\cos\theta_i(t)}\right)\mathrm{d}\lambda \tag{5.25}$$

which is coherent with the expression found in Cook et al. (2007).

5.2.3 Coupling with LunaIcy

The thermal crystallization process is highly dependent of the temperature. As both crystallization and amorphization processes occurs competitively on the surface and subsurface of icy moons, it is necessary to compute them simultaneously. Therefore, to accurately simulate the crystalline evolution, we have integrated the crystallization and amorphization modules into our multiphysics simulation model LunaIcy (Mergny and Schmidt, 2024a). The model consist of a uni-dimensional bloc of ice made of grains, with a certain porosity and thermal properties for each depth. In this numerical model, we use an irregular spatial grid consisting of n_x points, which we iterated for a total of n_t iterations.

By calculating the orbit of the target body, we determine the solar flux heating the ice surface. Then, our thermal solver MultIHeaTS computes the heat transfer throughout the material's depth for each timestep. At each depth, the crystalline module assesses the crystallinity changes corresponding to the current temperature and radiation flux. This iterative process is repeated throughout the simulation.

A complete description of LunaIcy is presented in details in (Mergny and Schmidt, 2024b; Mergny and Schmidt, 2024a).

The LunaIcy model is run over a range of parameters to simulate the evolution of Europa's icy surface crystallinity under various conditions for 100 kyr. While temperature variations occur within the diurnal period, crystallization and amorphization processes can occur over large timescales under Europa's conditions. To capture temperature variations, the simulations require a precise timestep $\Delta t = p_e/n_{\mathrm{spd}}$, where $p_e = 3.55$ days is Europa's orbital period and here $n_{\mathrm{spd}} = 30$.

The determination of initial ice structure is difficult due to lack of information on Europa. As a reference scenario, we choose to impose a constant thermal inertia of $95\,\mathrm{m^2Ks^{1/2}}$ everywhere on the moon, following results from Trumbo, Brown, and Butler (2018) and Rathbun et al. (2010). Also, we make the assumption that ice is formed in its amorphous phase at the surface of Europa, leading to an initial value of the crystalline fraction of $\theta = 0$.

Please note that some aspects of the coupling have been neglected. Studies, such as Murthy et al. (2013), have found that the thermal conductivity of amorphous ice is lower than that of crystalline ice, although it is unclear if this is due to differences in porosity. Additionally, Raut et al. (2008) showed that nanoporous ice compacts due to ionizing radiation in laboratory results and Palumbo et al. (2010) indicate that both ion and UV irradiation could slightly alter the porosity of amorphous water ice. Finally, Steckloff et al. (2023) also mentioned that the transition from amorphous to crystalline ice is exothermic, which should be included in the heat budget. While we acknowledge these differences between crystalline and amorphous ice, they do lead to important changes in the thermal properties and will be addressed in future refinements of the model.

5.3 Results

5.3.1 Radiation Dose Profiles

The computation of the dose with depth accumulated after one-year of irradiation from different sources (see Section 5.2.2) is shown in Figure 5.3. Over the full range of depths, the electron dose clearly dominates over any form of radiation for the surface of Europa. Therefore it would be important to better constrain the efficiency of electrons in amorphizing the ice, especially at temperatures above 70K.

However, even if electrons cannot induce amorphization, the total ion dose is comparable to the electron dose from millimeter to meter depths. These depths are actually the most impactful ones because, at shallower depths, amorphization would be too superficial, and at greater depths, the dose is too low to be significant. Therefore, ions play a significative role in the amorphization of Europa's surface. Among ions, protons and sulfur ions deliver the highest energy doses, while oxygen and helium ion doses are at least one order of magnitude lower.

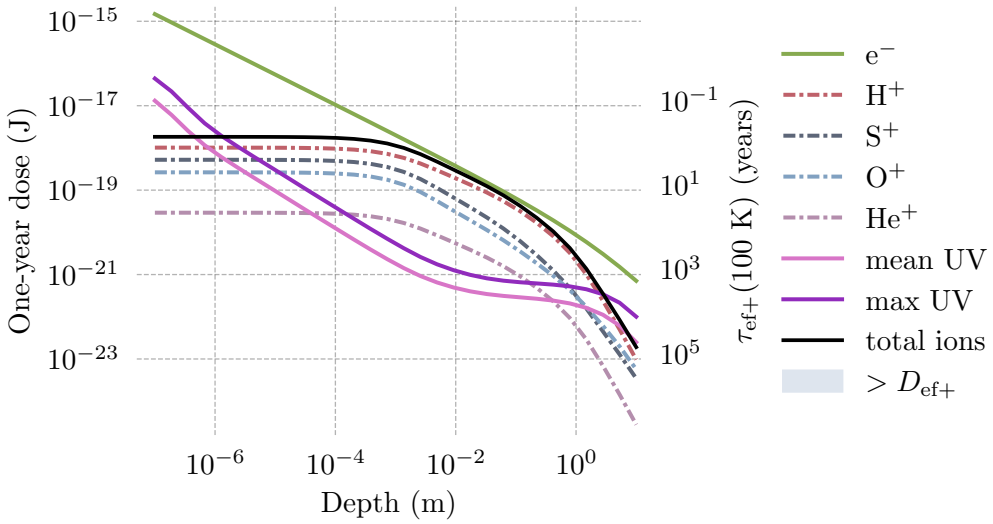

Figure 5.3: One-year irradiation dose penetrating the depths of a pure H_2O surface on Europa. Particle-induced doses are represented by dash dots. UV doses are computed at the equator using Europa's mean distance to the Sun 5.20 AU, with the maximum UV corresponding to the highest daily value and the mean UV to the average over the day. The total ion dose is represented by the black line and can be compared with the efficient dose for amorphization $D_{\mathrm{ef+}}$, illustrated by the blue area.

UV-induced doses are also shown for a reference case at the equator using Europa's mean distance to the Sun 5.20 AU, considering both the highest daily value and the average over the day. Due to the high absorption of Europa's surface in the UV spectrum (Becker et al., 2018), UV radiations is absorbed in the first few layers, resulting in high doses at very shallow depths ($< 1\,\mu m$). It remains unclear whether UV radiation can amorphize ice at temperatures above 70 K (Kouchi and Kuroda, 1990). If not, the UV dose results should be disregarded for mid and low latitudes where temperatures exceed 70 K. Nevertheless, while the UV dose is significant, it only affects a very superficial layer of the ice.

The contribution from all sources is summed at each iteration to determine the total dose, which is then used to compute the amorphization rate using Equation 5.7. For comparison purposes, we define the necessary dose for efficient amorphization, denoted as D_{ef+}, as the dose at which $k(T)D_{ef+} = 1$. Considering that the amorphization factor $k(T)$ varies with temperature, we chose a reference temperature of $T = 100\,K$, close to the mean surface temperature of Europa (Ashkenazy, 2019), to compute the efficient dose. This computation leads to an efficient dose of $D_{ef+} = 1.33 \times 10^{-18}\,J = 8.33\,eV$. One-year doses above the efficient dose will lead to significant amorphization ($\theta = 1/e \approx 0.36$) and are shown by the blue area in Figure 5.3.

Note, however, that doses in Figure 5.3 are computed after only one year of irradiation. Apart from UVs, charged particles dose rates are constant with time, so the computed dose after a time Δt (in years) is simply $D(\Delta t) = D(1yr)\Delta t/1yr$. As a consequence, after a time of 30 Myr (the estimated age of Europa's surface (Pappalardo et al., 1998)) most doses under the meter depth fall within the efficient amorphization zone.

We also define an efficient timescale for amorphization, t_{ef}, as the time it takes to accumulate enough dose for efficient amorphization, calculated as $t_{ef} = D_{ef}/D(1yr) \times 1yr$. The right y-axis of Figure 5.3 illustrates that maximum UV doses and electrons doses are efficient at the very near surface on a timescale close to 10^{-2} years, while ion doses take a few years to induce significant amorphization. Above the meter depth, the total dose requires more than 100 years to amorphize. However, this does not imply that the ice is currently amorphous at these depths, due to the counter effect of thermal crystallization.

Finally it's important to remember that charged particles are deposited on Europa's surface with a spatial distribution that varies based on their energy and type. Although we have assumed a uniform distribution of particles, in reality, different locations on the surface receive particles of varying energies (Addison et al., 2023). Since penetration depth is energy-dependent (Teolis et al., 2017), this would result in different doses profiles at different locations.

5.3.2 Parameter Exploration

Thanks to the numerical model LunaIcy, we can simulate all conditions affecting crystallinity on Europa by conducting a parameter exploration. While the charged particles flux is considered uniform in this study, the UV dose changes with latitude. Moreover, thermal crystallization is temperature dependent and hence will depend on the solar flux, surface albedo and thermal properties. To investigate this parameter dependency, a set of simulation is run with varying albedo values from 0.3 to 0.8 with a step of 0.1, covering the range found on Europa (Rathbun et al., 2010). Simultaneously, solar flux is latitude dependent, so latitude values are varied from 0 to 80 degrees with a step of 20 degrees, as negative latitudes do not need to be computed due to the symmetry of the solar flux on Europa. The ice thermal properties is fixed, with the reference thermal inertia $95\,\mathrm{m^2Ks^{1/2}}$ (Trumbo, Brown, and Butler, 2018). This parameter exploration results in 30 different simulations, representing various thermal configurations found on Europa. The final crystalline fraction profiles after 100 kyr for the 30 albedo/latitude pairs is shown in Figure 5.4.

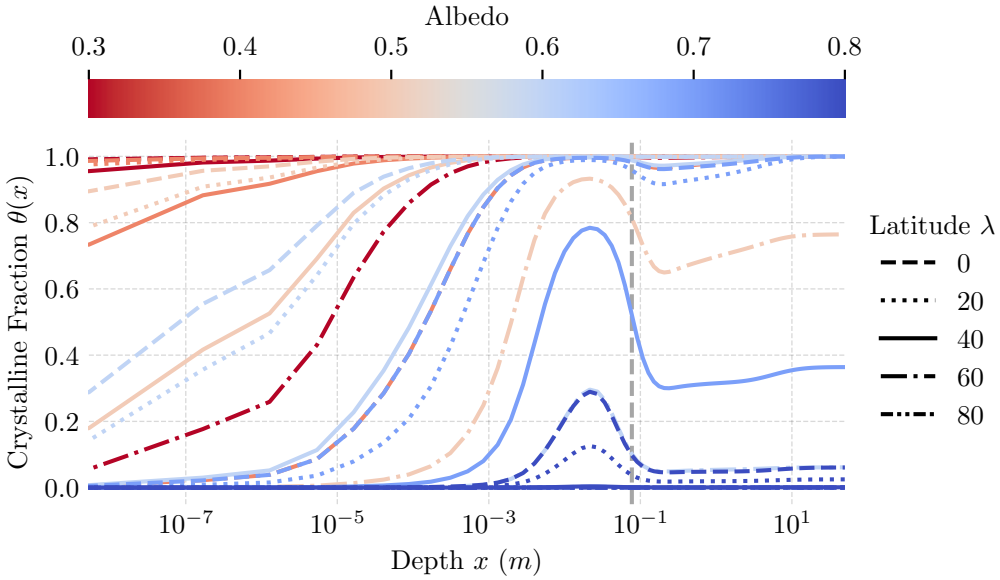

Figure 5.4: Crystalline fraction profiles after 100 kyr for the set of simulations of Europa. We vary the albedo from 0.3 to 0.8 with a step of 0.1, while latitude ranges from 0 to 80 degrees with a step of 20 degrees, leading to 30 different simulations. The diurnal thermal skin depth is indicated by the grey dashes at $\sim 7\,\mathrm{cm}$.

As expected, coldest regions, high latitudes and high albedo, maintain completely amorphous ice. Due to computational constraints, simulations are run for 100k years; however, within this timeframe, some of the coldest regions may not have sufficient time to crystallize. Indeed, for temperatures below 92 K, the crystallization timescale

(see Equation 5.2) exceeds 100k years. Nevertheless, this limitation does not significantly impact our understanding, as ice at temperatures below 84 K takes longer to crystallize than the estimated age of Europa's surface, approximately 30 Myr (Pappalardo et al., 1998).

Also anticipated, hottest regions, at low latitudes and low albedo, present an almost completely crystalline profile after 100 kyr. However it is interesting to note, that even in these regions, at very shallow depths ($< 1\,\mu m$), the UV-induced amorphization is high enough to compete with the crystallization process. It remains uncertain whether UV radiation can reliably amorphize ice at temperatures above 77 K (Kouchi and Kuroda, 1990; Leto and Baratta, 2002). However, if such amorphization is prevented due to a "restoration mechanism" (Lepault et al., 1983; J. Dubochet et al., 1984), then this fails to explain why protons can amorphize ice at higher temperatures than UV or electrons (Strazzulla et al., 1992), despite receiving equal doses.

Regions of particular interest, are where a balanced competition between thermal crystallization and amorphization can happen. Such scenario is often seen at mid latitudes, for example for the simulation $\lambda = 40°$, $A = 0.6$ (see Figure 5.4, light blue full line). The radiation dose predominates at shallow depths ($< 1\,\mu m$), with the transition from UV-dominated amorphization to particle-dominated amorphization being particularly evident in the simulation with $\lambda = 0°$ and $A = 0.6$ (see Figure 5.4, light blue dashes). The dose then gradually decreases with depth (see Figure 5.3) to allow for a balanced competition with thermal crystallization. Around the $\sim 1\,mm$ depth, the dose shows a steeper decline, allowing thermal crystallization to dominate, leading to the crystallization peak at the $\sim 1\,mm$ depth (see Figure 5.4). This result is particularly interesting because it is in agreement with spectroscopy-based model (Hansen, 2004) that found ice at the 1 mm depth on Galilean moons to be predominantly crystalline. Beyond the diurnal thermal skin depth ($> 7\,cm$), high daily temperatures cannot penetrate, significantly reducing thermal crystallization. Although the radiation dose is significantly lower than at the surface, amorphization once again dominates beyond the thermal skin depth due to the lower temperature, shown by the second trough on Figure 5.4. Finally, at depths exceeding several meters, most of the radiation has been absorbed, and ice crystallizes slowly through deep, steady thermal processes.

5.3.3 Crystallinity Map

Various observable quantities can be derived from the crystallization profiles shown in Figure 5.4. Interpretation of the infrared spectra from the Near Infrared Mapping Spectrometer on Galileo (Hansen, 2004), led to estimations of the crystalline structure of Europa, with a critical depth $\sim 1\,mm$ where a transition from amorphous to crystalline ice is observed. To compare with spectroscopy measurements, we derive the average crystalline fraction after 100 kyr on the first $d = 1\,mm$

depth:

$$\langle\theta\rangle(d) = \frac{1}{d}\int_0^d \theta(x)dx. \tag{5.26}$$

The averaged crystalline fraction within the first millimeter, denoted as $\langle\theta\rangle_{\mathrm{mm}}$, is displayed for the albedo/latitude parameter exploration in Figure 5.5 (*Top Left*). Consistent with Figure 5.4, crystallinity decreases from fully crystalline to entirely amorphous with increasing latitude and albedo.

Then, the first-millimeter averaged crystalline fraction $\langle\theta\rangle_{\mathrm{mm}}$ computed for discrete values (Figure 5.5, *Top Left*), is interpolated over a continuous range of albedos $A \in [0.3, 0.8]$ and latitudes $\lambda \in [-90°, 90°]$. This interpolation allows for the computation for all albedo/latitude pair values found on Europa's reconstructed albedo map, as illustrated in Figure 5.5 (*Bottom*). The fitted albedo map of Europa was previously generated (Mergny, Schmidt, et al., 2024) through the calculation of bond albedo across 19 regions of interest on Europa (Belgacem et al., 2020), combined with data from the USGS Galileo SSI Global Mosaic (see thesis' SupMat 5.5.2). Note that a data gap exist in the Europa mosaic at the south pole, with no coverage below latitude -83°, and only low-resolution data cover the north pole and many high latitudes in both the north and south.

Results show that, at the first millimeter depth, near equator regions $\lambda \in [-30°, 30°]$ of the trailing hemisphere are fully crystalline, whereas the leading hemisphere displays more variability due to higher albedo. Irrespective of longitude, high-latitude regions $|\lambda| > 50°$ are characterized by entirely amorphous ice, attributed to the slow thermal crystallization at these temperatures. Regions displaying a mixed amorphous/crystalline ratio are particularly noticeable at mid latitudes $\lambda \sim 45°$, experiencing a balance between thermal crystallization and irradiation-induced amorphization. Notable high albedo features, like Pwyll crater (25.2 °S 271.4 °W) have locally lower crystallinity due to the lower temperature.

The crystallinity map shown in Figure 5.5, is of particular interest for the analysis of existing spectroscopy measurements and the suggestion of target spots for the upcoming spatial missions. We suggest comparing spectroscopy measurements between low latitude, low albedo regions like Dyfed Regio (10°N, 250°W) and high latitude regions like Balgatan Regio (50°S, 30°W). Our model would be confirmed if distinct crystallinity profiles are observed, with completely amorphous ice at the poles and fully crystalline ice near the equator. However, due to the different composition and microstructure of the ice at different regions, cautious work must be made to properly estimate the crystallinity from spectroscopy measurements. As shown by Cruz-Mermy et al. (2023), various mix of materials can explain the same spectrum and thus can lead to different abundance of crystalline/amorphous H_2O. Also, as the authors have shown, a mix between amorphous and crystalline ice result in non linear optical properties, and thus one must be careful when estimating a crystalline fraction. Still our numerical modeling is in great agreement with the observation of a vertical crystallinity gradient by spectroscopy of the surface (Hansen, 2004; Ligier

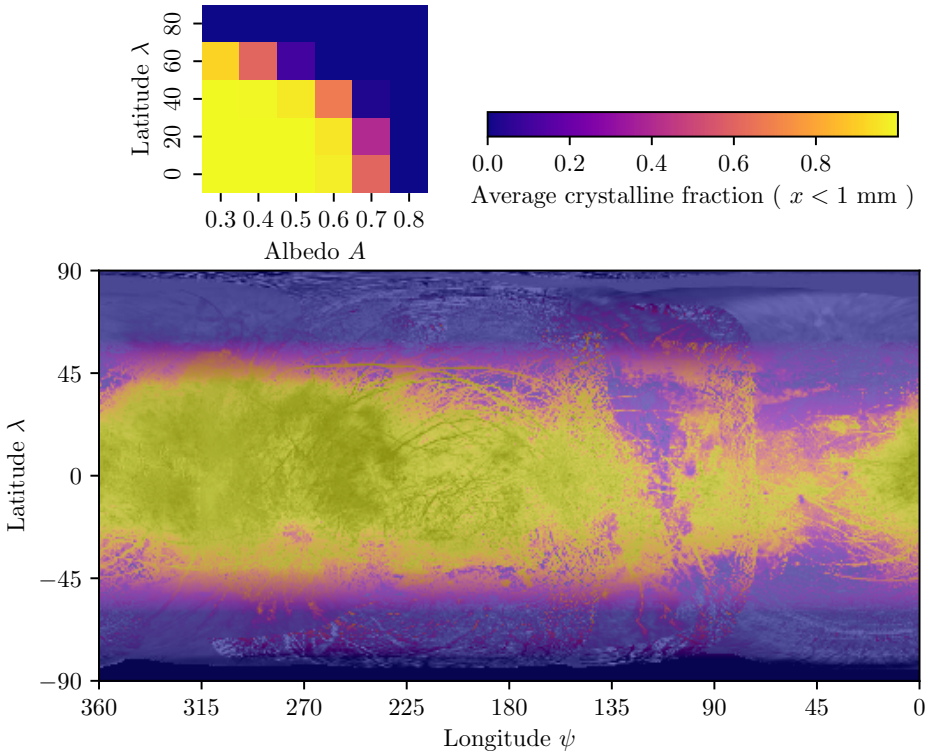

Figure 5.5: (*Top Left*) Average crystalline fraction heatmap for depths $< 1\,\text{mm}$ computed on Europa for a uniform flux of particles as function of albedo and latitude. (*Bottom*) Interpolation of the averaged crystalline fraction heatmap to the albedo map of Europa.

et al., 2016). For non-equatorial regions, particle radiation are high enough to induce significantly alter the ice up to the 1 mm depth where most radiations have already been absorbed. This is shown by the 3.1 µm band on Europa's ice-rich spectra, that is better fitted with an amorphous model (Hansen, 2004). Deeper than 1 mm, thermal crystallization is prevalent, and coherent with the 1.65 µm band, all ice under this depth is found to be crystalline (Hansen, 2004; Ligier et al., 2016).

It would be highly unexpected to observe any significant crystallinity near the poles since crystallization is inefficient in those regions, unless our understanding of Europa's surface temperature is significantly mistaken, which seems unlikely. The presence of high crystallinity at the poles would necessitate two conditions to be met: first, significantly lower radiation levels or a less efficient amorphization process than anticipated, and second, mechanisms such as surface recycling or deposition of ice at high enough temperature to be formed in its crystalline state.

If low crystallinity is detected in the first millimeter near the equator of the trailing hemisphere, the first potential explanation would be to consider the high flux of low-energy electrons ($< 10\,\mathrm{keV}$) as a factor inducing amorphization. To verify this explanation, the crystallinity of the near-equator leading hemisphere, for example in Tara Regio (10 °S 75°W), could also be measured, where it is assumed that no low-energy electrons reach the surface (Paranicas, John Cooper, et al., 2009; T. Nordheim et al., 2017). If amorphous ice is also observed in that region, it would suggest that other sources of amorphization, such as ions or UV radiation, may be more numerous or efficient than expected or, less likely, that our current estimations of Europa's surface temperatures (Rathbun et al., 2010; Ashkenazy, 2019) and thermal properties (Trumbo, Brown, and Butler, 2018) are significantly different from reality.

Finally, it is important to acknowledge that several assumptions were made in this theoretical modeling, which may result in a crystallinity map shown in Figure 5.5 distinct from reality. For instance, we assumed a constant flux of charged particles, yet several studies (Paranicas, John Cooper, et al., 2009; Teolis et al., 2017; T. Nordheim et al., 2017) suggest significant variations in electron flux reaching icy moons surfaces across different locations, with only MeV-energy electrons able to reach the leading hemisphere, resulting in less amorphization at shallow depths there. Although variations in ion flux with latitude/longitude exist, they are less pronounced and would induce minor fluctuations in crystallinity. Moreover, the amorphization factor is poorly constrained $k(T)$, particularly for UV and electrons at higher temperatures; if no amorphization occurs above 77K, this would increase the overall surface crystallinity.

Additionally, Europa's surface is not made of pure H_2O ice (McCord et al., 1999; R. Carlson et al., 2005; Ligier et al., 2016; Cruz-Mermy et al., 2023), which lead to different radiation penetration depths in reality. Furthermore, the temperature profiles computed here are only rough approximations of reality. The reconstructed albedo map has regions of very low resolution, where albedo estimation is unreli-

able, and the fit of albedo to pixel values in the USGS map is imperfect. Also our understanding of surface thermal properties remains uncertain; thermal inertia is not uniform across the surface, resulting in local variations that affect crystallization timescales. Notably, regions with temperature anomalies will see corresponding changes in crystallinity. We anticipate that upcoming missions JUICE (Grasset et al., 2013) and Europa Clipper (Phillips et al., 2014) will provide better surface observations, enabling better constraints on these parameters and lead to improved modeling.

5.3.4 Periodic Variations

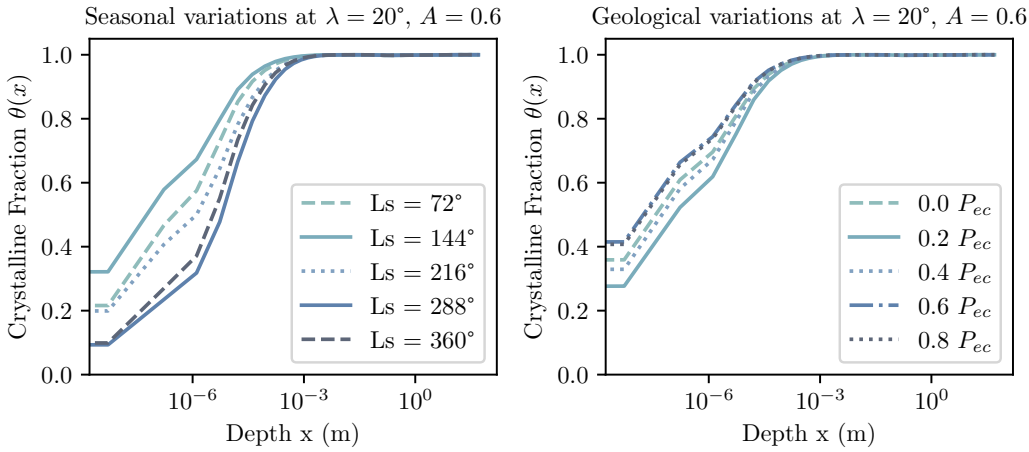

Figure 5.6: (*Left*) Crystalline fraction profiles for various solar longitude, for a surface at latitude $\lambda = 20°$, albedo $A = 0.6$ and $Lt = 0°$. Seasonal variations are observable at greater depth and amplitude for mid-latitude regions where there exist an equilibrium between particle amorphization and crystallization. (*Right*) Crystalline fraction profiles of the same surface for different locations during the eccentricity oscillation period P_{ec} at the same local time and solar longitude $Ls = Lt = 0°$. LunaIcy's orbital model captures Europa's eccentricity period of about $P_{\text{ec}} \sim 55\,000$ years, leading to temperature fluctuations that affect the crystalline profiles.

The solar flux heating the surface of Europa has diurnal, seasonal and geological fluctuations that lead to varying efficiency of the thermal crystallization. An unprecedented implication of this, is that thanks to the simulated competition between crystallization and radiation, we can observe periodic variations of the crystallinity profile.

Diurnal Variations — On the diurnal timescale, significant changes in crystallinity require very high doses. To align the efficient amorphization timescale with Europa's period, $t_{\text{ef}} \sim 3.55$ days, a one-year dose of approximately $\sim 1.37 \times 10^{-16}$ J is needed.

According to Figure 5.3, such doses are never achieved, except in the special case where maximum UV doses reach high values near the surface, but this is for very superficial depths $< 1 \times 10^{-7}$ m at the equator. Therefore, in the current scenario, no noticeable daily variations in crystallinity would be observed. However, if the high flux of low-energy electrons were capable of amorphizing ice, periodic fluctuations in crystallinity on the diurnal period could occur. Specifically, during the night, if the amorphization rate of low-energy electrons is sufficient, it would amorphize the cold surface of the moon. In contrast, during the day, regions experiencing temperatures above 130 K undergo thermal crystallization within a timescale shorter than Europa's day length, leading to an increase in crystallinity on the surface, unless electron-induced amorphization dominates. Such a scenario is possible for regions reaching such high temperatures and on the trailing hemisphere where low-energy electrons land, such as the Dyfed Regio.

Seasonal Variations — While Jupiter's tilt is only 3°, due to its eccentricity $e = 0.048$, the surfaces of Galilean moons experience seasonal variations of the solar flux. These variations can lead to surface temperatures variations of up to 5 K on Europa (Ashkenazy, 2019) and lead to significant changes on the crystallization rate. For regions where there is a delicate balance between crystallization and radiations, this can lead to important changes of the crystallinity profiles. On Figure (5.6, *Left*), is shown the crystallinity profiles for various locations in Jupiter's orbit, for the same surface of Europa, compared at the same local time. From the surface to the first millimeter depth, we see considerable variations of the crystalline fraction (up to 35%) at different solar longitudes.

To anticipate comparison with spectroscopy measurements, we calculate the average variations in crystallinity at the first $d = 1$ mm depth:

$$\langle \Delta\theta \rangle(d) = \frac{1}{d} \int_0^d \max_{\text{Ls}} |\Delta\theta(x)| dx. \tag{5.27}$$

This represents the average over the first millimeter of the maximum peak-to-peak difference between crystalline fraction profiles of different solar longitudes. These seasonal fluctuations are illustrated in Figure (5.5, *Top Left*) as part of the albedo/latitude parameter exploration.

Following the previous method, the seasonal variation heatmap is then interpolated over a continuous range of albedos $A \in [0.3, 0.8]$ and latitudes $\lambda \in [-90°, 90°]$. This allow us to generate a map of mean seasonal crystallinity variations in the first millimeter depth across Europa, as shown by Figure (5.7, *Bottom*). It is evident from this map, that regions with pronounced seasonal fluctuations are globally situated at mid-latitudes, around $\lambda \sim 45°$ and for the leading hemisphere, also at low-latitudes. While equatorial regions of the trailing hemisphere are dominated by high thermal crystallization locking the ice into its crystalline state, the higher albedo leading hemisphere experiences high seasonal variations due to a more balanced competition

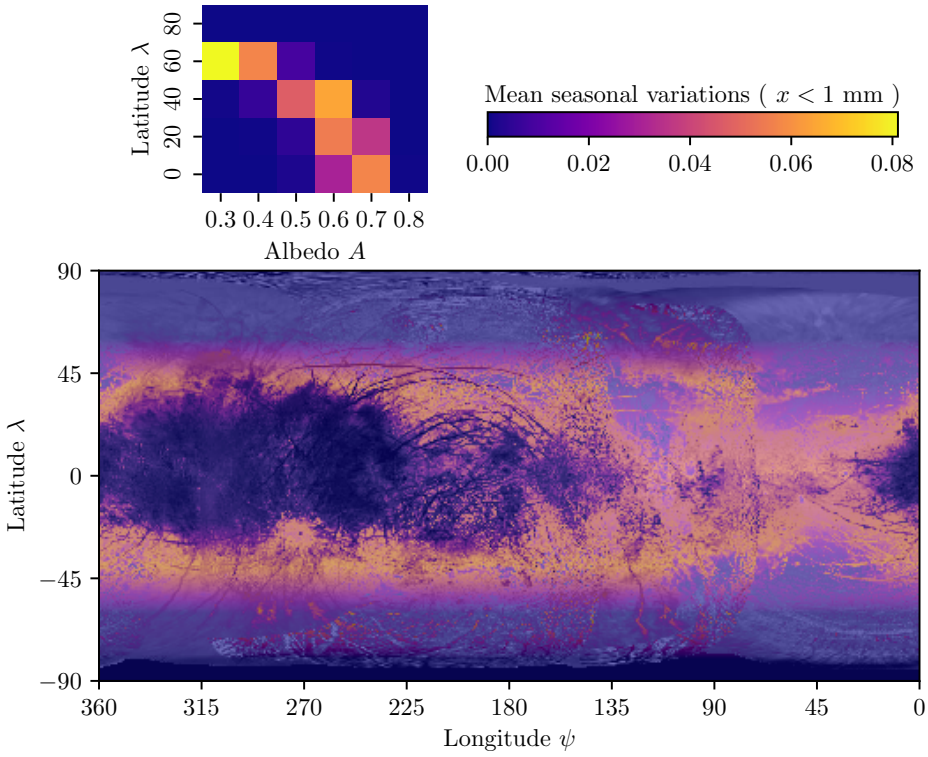

Figure 5.7: (*Top Left*) Heatmap of the mean seasonal variations for depths $< 1\,\text{mm}$ computed on Europa as function of albedo and latitude. (*Bottom*) Interpolation of the seasonal variations heatmap to the albedo map of Europa.

with radiations. However, as discussed previously, it is important to acknowledge the simplifications in our model, which may lead to differences between the presented map and the actual seasonal variations on Europa's surface. Given the delicate balance required for seasonal variations, errors in modeling are even more particularly sensitive here. Nonetheless, considering the fast crystallization rate of near equator areas and the locked amorphous state at the poles, mid-latitude regions likely represent the most likely areas of balanced competition.

This is particularly interesting for the upcoming missions, as the Europa Clipper's expected lifespan of 4 years aligns well with the potential observability of these variations. Given Jupiter's orbital period of $p_j = 11.86$ years, the highest crystallinity variations occur over approximately 5.43 years (half a period). This means that considerable variations could be detected within the Europa Clipper's operational timeframe. For example we suggest conducting multiple observations over several years at the same local time within regions like the Pwyll crater (25.2° S, 271.4° W) or the Tara Regio (10° S, 75° W). These areas are expected to show significant seasonal variations and are also of particular interest for other scientific purposes (Villanueva et al., 2023; Trumbo and Brown, 2023).

Geological Variations — Over large timescales, some of the orbital parameters, notably the eccentricity of the Galilean system, fluctuate with periods ranging from 27,000 to 1.1 million years (Laskar, 2008), which is accounted in LunaIcy's orbital module (Mergny and Schmidt, 2024b). The most pronounced period occurs approximately every $P_{\text{ec}} \sim 55.000$ years and induces small variations of the solar flux. Given that crystallization strongly depends on temperature, these fluctuations lead to noticeable changes in crystallinity profiles. Figure (5.6, *Right*) shows the crystalline fraction profiles at various locations over the eccentricity oscillation period P_{ec}, at latitude $\lambda = 20°$, albedo $A = 0.6$, and local time $Lt = 0°$. Variations of up to 10 % in crystallinity are noticeable between these different locations. While these fluctuations are not observable within our lifespan, they suggest that crystallinity profiles could provide insights on the surface's thermal history.

5.4 Conclusion and Perspectives

Many processes affecting the surfaces of icy moons, such as thermal crystallization, are highly temperature-dependent and cannot be accurately estimated with a fixed temperature. For theses reasons, they must be coupled with a precise temperature evolution, which is why LunaIcy was developed. Competing with this process, radiation of charged particles can lead to amorphization of ice, but also from electrons and UV on whose effect on crystallinity have not been explored for Europa yet. Our results indicate that dose penetration is primarily dominated by electrons and protons, with UV radiation having the most significant effect in the first micron of depth.

To better understand which process dominates on Europa, we conducted a set of simulations where both thermal crystallization and radiation-induced amorphization are integrated into LunaIcy. Through a parameter exploration covering relevant latitudes and albedo values, we explored various configurations of the icy moon. Interpolating these results allowed us to generate a crystallinity map for the first millimeter depth across Europa. Our current model reveals a transition from amorphous ice at the poles to fully crystalline at the equator, with a mixture of the two at mid-latitudes. Although our model assumes a uniform distribution of charged particles, in reality, electrons are mainly concentrated on the trailing hemisphere. Accounting for this asymmetry in future studies may lead to a decrease in crystallinity on the trailing hemisphere and an increase on the leading hemisphere.

Remarkably, the simulations of these competing process have reveal periodic variations in the crystallinity profiles. Notably, seasonal variations have the highest amplitudes, reaching crystallinity fluctuations of up 35 % in mid latitude regions. This is significant, as upcoming missions like Europa Clipper and JUICE could potentially observe these seasonal variations during their operational lifetimes. Additionally, smaller yet noticeable variations are expected on timescales of $\sim 55\,000$ years and daily variations could be observable if radiation-induced amorphization locally exceeds the levels accounted for in our current model.e.

This study represents one of the initial attempts at coupled modeling of Europa's crystallinity, necessitating several simplifications that may introduce discrepancies with reality. We propose the observation of key regions—Dyfed Regio, Balgatan Regio, Pwyll Crater, and Tara Regio—during upcoming missions Europa Clipper and JUICE to validate or refine our model. Improved spectroscopy models will also be essential for accurately estimating crystallinity within acceptable error margins, given the nonlinear nature of the process.

5.5 Thesis' Supplementary Material

5.5.1 Crystallization versus Temperature Plot

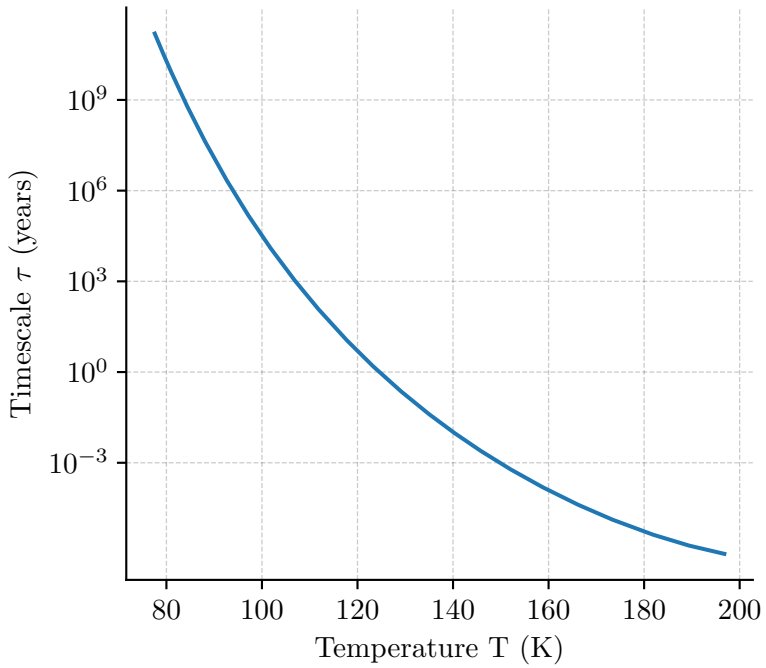

Figure 5.8: Thermal crystallization timescale as a function of temperature based on Equation 5.2.

5.5.2 Europa Bond Albedo Map

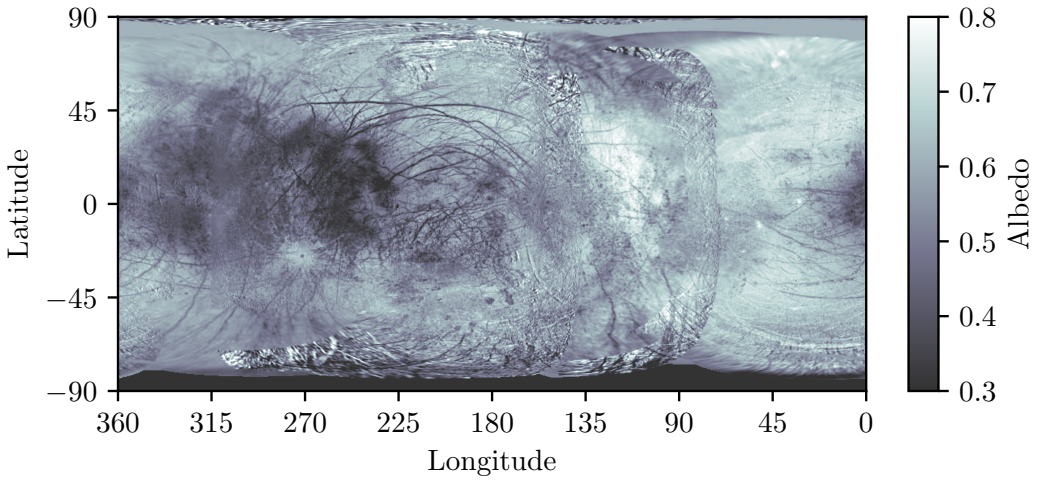

Figure 5.9: Computed Europa bond albedo map. Note that a data gap exist in the Europa mosaic at the south pole, with no coverage below latitude -83°, and only low-resolution data cover the north pole and many high latitudes in both the north and south.

The albedo map presented in this chapter is based on a short letter that is currently being written (not included in this thesis). The letter aims to propose a Bond albedo map with the highest possible spatial resolution for various applications, such as preparing for quantitative measurements of future space missions and estimating the quantitative energy balance at the surface of Europa.

A new absolute Bond albedo map has been created by incorporating the complete set of angular observations from Voyager, Galileo, and New Horizons, combined with the highest resolution images available. We used 20 Regions of Interest (ROI) with known photometric behavior from Belgacem et al. (2020). These locations were used as tie-points to the grayscale Voyager/Galileo global mosaic of Europa (USGS, 2002). By fitting a linear relationship between the pixel values in the image at the ROIs and the Bond albedo tie-points, we produced a high-resolution albedo map from the mosaic (see Figure 5.9).

Bibliography for Chapter 5

Addison, Peter, Lucas Liuzzo, and Sven Simon (Aug. 2023). "Surface-Plasma Interactions at Europa in Draped Magnetospheric Fields: The Contribution of Energetic Electrons to Energy Deposition and Sputtering". In: *Journal of Geophysical Research: Space Physics* 128.8. ISSN: 2169-9402. DOI: 10.1029/2023ja031734.

Ashkenazy, Yosef (June 2019). "The surface temperature of Europa". In: *Heliyon* 5.6, e01908. ISSN: 2405-8440. DOI: 10.1016/j.heliyon.2019.e01908.

Avrami, Melvin (Dec. 1939). "Kinetics of Phase Change. I General Theory". In: *The Journal of Chemical Physics* 7.12, pp. 1103–1112. ISSN: 1089-7690. DOI: 10.1063/1.1750380.

— (Feb. 1940). "Kinetics of Phase Change. II Transformation-Time Relations for Random Distribution of Nuclei". In: *The Journal of Chemical Physics* 8.2, pp. 212–224. ISSN: 1089-7690. DOI: 10.1063/1.1750631.

— (Feb. 1941). "Granulation, Phase Change, and Microstructure Kinetics of Phase Change. III". In: *The Journal of Chemical Physics* 9.2, pp. 177–184. ISSN: 1089-7690. DOI: 10.1063/1.1750872.

Baragiola, R. A. et al. (Apr. 2013). "Radiation Effects in Water Ice in the Outer Solar System". In: *Astrophysics and Space Science Library*. Springer New York, pp. 527–549. ISBN: 9781461430766. DOI: 10.1007/978-1-4614-3076-6_16.

Baragiola, Raúl A. (Dec. 2003). "Water ice on outer solar system surfaces: Basic properties and radiation effects". In: *Planetary and Space Science* 51.14–15, pp. 953–961. ISSN: 0032-0633. DOI: 10.1016/j.pss.2003.05.007.

Becker, T. M. et al. (May 2018). "The Far-UV Albedo of Europa From HST Observations". In: *Journal of Geophysical Research: Planets* 123.5, pp. 1327–1342. ISSN: 2169-9100. DOI: 10.1029/2018je005570.

Belgacem, Ines, Frédéric Schmidt, and Grégory Jonniaux (Mar. 2020). "Regional study of Europa's photometry". In: *Icarus* 338, p. 113525. ISSN: 0019-1035. DOI: 10.1016/j.icarus.2019.113525.

Berdis, Jodi R. et al. (May 2020). "Europa's surface water ice crystallinity: Discrepancy between observations and thermophysical and particle flux modeling". In: *Icarus* 341, p. 113660. ISSN: 0019-1035. DOI: 10.1016/j.icarus.2020.113660.

Carlson, R.W. et al. (Oct. 2005). "Distribution of hydrate on Europa: Further evidence for sulfuric acid hydrate". In: *Icarus* 177.2, pp. 461–471. ISSN: 0019-1035. DOI: 10.1016/j.icarus.2005.03.026.

Cook, Jason C. et al. (July 2007). "Near-Infrared Spectroscopy of Charon: Possible Evidence for Cryovolcanism on Kuiper Belt Objects". In: *The As-*

trophysical Journal 663.2, pp. 1406–1419. ISSN: 1538-4357. DOI: 10.1086/518222.

Cooper, J (Jan. 2001). "Energetic Ion and Electron Irradiation of the Icy Galilean Satellites". In: *Icarus* 149.1, pp. 133–159. DOI: 10.1006/icar.2000.6498.

Cruz-Mermy et al. (Apr. 2023). "Selection of chemical species for Europa's surface using Galileo/NIMS". In: *Icarus* 394, p. 115379. ISSN: 0019-1035. DOI: 10.1016/j.icarus.2022.115379.

Dubochet, J. and J. Lepault (Sept. 1984). "CRYO-ELECTRON MICROSCOPY OF VITRIFIED WATER". In: *Le Journal de Physique Colloques* 45.C7, pp. C7-85-C7–94. ISSN: 0449-1947. DOI: 10.1051/jphyscol:1984709.

Dubochet, Jacques et al. (May 1988). "Cryo-electron microscopy of vitrified specimens". In: *Quarterly Reviews of Biophysics* 21.2, pp. 129–228. ISSN: 1469-8994. DOI: 10.1017/s0033583500004297.

Famá, M. et al. (May 2010). "Radiation-induced amorphization of crystalline ice". In: *Icarus* 207.1, pp. 314–319. ISSN: 0019-1035. DOI: 10.1016/j.icarus.2009.11.001.

Grasset, O. et al. (Apr. 2013). "JUpiter ICy moons Explorer (JUICE): An ESA mission to orbit Ganymede and to characterise the Jupiter system". In: *Planetary and Space Science* 78, pp. 1–21. DOI: 10.1016/j.pss.2012.12.002.

Grundy, W. M. and B. Schmitt (Oct. 1998). "The temperature-dependent near-infrared absorption spectrum of hexagonal H2O ice". In: *Journal of Geophysical Research: Planets* 103.E11, pp. 25809–25822. ISSN: 0148-0227. DOI: 10.1029/98je00738.

Hagen, W., A.G.G.M. Tielens, and J.M. Greenberg (Apr. 1981). "The infrared spectra of amorphous solid water and ice Ic between 10 and 140 K". In: *Chemical Physics* 56.3, pp. 367–379. ISSN: 0301-0104. DOI: 10.1016/0301-0104(81)80158-9.

Hansen, Gary B. (2004). "Amorphous and crystalline ice on the Galilean satellites: A balance between thermal and radiolytic processes". In: *Journal of Geophysical Research* 109.E1. DOI: 10.1029/2003je002149.

Heide, H.-G. (Jan. 1984). "Observations on ice layers". In: *Ultramicroscopy* 14.3, pp. 271–278. ISSN: 0304-3991. DOI: 10.1016/0304-3991(84)90095-0.

Hendrix, Amanda R., Deborah L. Domingue, and Kimberly King (Jan. 2005). "The icy Galilean satellites: ultraviolet phase curve analysis". In: *Icarus* 173.1, pp. 29–49. ISSN: 0019-1035. DOI: 10.1016/j.icarus.2004.06.017.

Jenniskens, P., D. F. Blake, and A. Kouchi (1998). "Amorphous Water Ice". In: *Solar System Ices*. Springer Netherlands, pp. 139–155. ISBN: 9789401152525. DOI: 10.1007/978-94-011-5252-5_7.

Kouchi, Akira and Toshio Kuroda (Mar. 1990). "Amorphization of cubic ice by ultraviolet irradiation". In: *Nature* 344.6262, pp. 134–135. ISSN: 1476-4687. DOI: 10.1038/344134a0.

Kouchi, Akira, Tetsuo Yamamoto, et al. (1994). "Conditions for condensation and preservation of amorphous ice and crystallinity of astrophysical ices". In: *Astronomy and Astrophysics* 290, pp. 1009–1018. URL: https://api.semanticscholar.org/CorpusID:55034175.

Laskar, J (July 2008). "Chaotic diffusion in the Solar System". In: *Icarus* 196.1, pp. 1–15. ISSN: 0019-1035. DOI: 10.1016/j.icarus.2008.02.017.

Lee, Zhongping et al. (Sept. 2013). "Penetration of UV-visible solar radiation in the global oceans: Insights from ocean color remote sensing". In: *Journal of Geophysical Research: Oceans* 118.9, pp. 4241–4255. ISSN: 2169-9291. DOI: 10.1002/jgrc.20308.

Lepault, J., R. Freeman, and J. Dubochet (Dec. 1983). "Electron beam induced "vitrified ice"". In: *Journal of Microscopy* 132.3. ISSN: 1365-2818. DOI: 10.1111/j.1365-2818.1983.tb04590.x.

Leto, G. and G. A. Baratta (Dec. 2002). "Ly-alpha photon induced amorphization of Ic water ice at 16 Kelvin". In: *Astronomy and Astrophysics* 397.1, pp. 7–13. ISSN: 1432-0746. DOI: 10.1051/0004-6361:20021473.

Leto, G., O. Gomis, and G. Strazzulla (Jan. 2005). "The reflectance spectrum of water ice: Is the 1.65 mu msp peak a good temperature probe?." In: *Memorie della Societa Astronomica Italiana Supplementi* 6, p. 57. URL: https://ui.adsabs.harvard.edu/abs/2005MSAIS...6...57L.

Ligier, N. et al. (May 2016). "VLT/SINFONI observations of Europa: new insights into the surface composition". In: *The Astronomical Journal* 151.6, p. 163. ISSN: 1538-3881. DOI: 10.3847/0004-6256/151/6/163.

Mastrapa, R et al. (Sept. 2008). "Optical constants of amorphous and crystalline H2O-ice in the near infrared from 1.1 to 2.6 um". In: *Icarus* 197.1, pp. 307–320. ISSN: 0019-1035. DOI: 10.1016/j.icarus.2008.04.008.

Mauk, B. H. et al. (July 2004). "Energetic ion characteristics and neutral gas interactions in Jupiter's magnetosphere". In: *Journal of Geophysical Research: Space Physics* 109.A9. ISSN: 0148-0227. DOI: 10.1029/2003ja010270.

McCord, Thomas B. et al. (May 1999). "Hydrated salt minerals on Europa's surface from the Galileo near-infrared mapping spectrometer (NIMS) investigation". In: *Journal of Geophysical Research: Planets* 104.E5, pp. 11827–11851. ISSN: 0148-0227. DOI: 10.1029/1999je900005.

Mergny, Cyril and Frédéric Schmidt (2024a). "LunaIcy: Exploring Europa's Icy Surface Microstructure through Multiphysics Simulations". In: *submitted*.

— (2024b). "MultIHeaTS: a Fast and Stable Thermal Solver for Multilayered Planetary Surfaces". In: *submitted*.

Mergny, Cyril, Frédéric Schmidt, et al. (2024). "Photometric Map of Europa". In: *in writing*.

Moore, Marla H. and Reggie L. Hudson (Dec. 1992). "Far-infrared spectral studies of phase changes in water ice induced by proton irradiation". In: *The Astrophysical Journal* 401, p. 353. ISSN: 1538-4357. DOI: 10.1086/172065.

Murthy, S. Gudipati and Castillo-Rogez Julie (2013). *The Science of Solar System Ices*. Springer New York. ISBN: 9781461430766. DOI: 10.1007/978-1-4614-3076-6.

Nordheim, T. A., K. P. Hand, and C. Paranicas (July 2018). "Preservation of potential biosignatures in the shallow subsurface of Europa". In: *Nature Astronomy* 2.8, pp. 673–679. ISSN: 2397-3366. DOI: 10.1038/s41550-018-0499-8.

Nordheim, T.A. et al. (Apr. 2017). "The near-surface electron radiation environment of Saturn's moon Mimas". In: *Icarus* 286, pp. 56–68. ISSN: 0019-1035. DOI: 10.1016/j.icarus.2017.01.002.

Oza, Apurva V., Robert E. Johnson, and François Leblanc (May 2018). "Dusk/-dawn atmospheric asymmetries on tidally-locked satellites: O2 at Europa". In: *Icarus* 305, pp. 50–55. ISSN: 0019-1035. DOI: 10.1016/j.icarus.2017.12.032.

Palumbo, M.E. et al. (May 2010). "H bonds in astrophysical ices". In: *Journal of Molecular Structure* 972.1–3, pp. 64–67. ISSN: 0022-2860. DOI: 10.1016/j.molstruc.2009.12.017.

Pappalardo, R. T. et al. (Jan. 1998). "Geological evidence for solid-state convection in Europa's ice shell". In: *Nature* 391.6665, pp. 365–368. DOI: 10.1038/34862.

Paranicas, C., R. W. Carlson, and R. E. Johnson (Feb. 2001). "Electron bombardment of Europa". In: *Geophysical Research Letters* 28.4, pp. 673–676. ISSN: 1944-8007. DOI: 10.1029/2000gl012320.

Paranicas, C., John Cooper, et al. (Jan. 2009). "Europa's Radiation Environment and Its Effects on the Surface". In: *Europa*.

Paranicas, C., J. M. Ratliff, et al. (Mar. 2002). "The ion environment near Europa and its role in surface energetics". In: *Geophysical Research Letters* 29.5. ISSN: 1944-8007. DOI: 10.1029/2001gl014127.

Phillips, Cynthia B. and Robert T. Pappalardo (May 2014). "Europa Clipper Mission Concept: Exploring Jupiter's Ocean Moon". In: *Eos, Transactions American Geophysical Union* 95.20, pp. 165–167. DOI: 10.1002/2014eo200002.

Rao, C. N. R. and K. J. Rao (Mar. 1980). "Phase transitions in solids". In: *Acta Crystallographica Section A* 36.2, pp. 332–333. ISSN: 0567-7394. DOI: 10.1107/s0567739480000708.

Rathbun, Julie A., Nathaniel J. Rodriguez, and John R. Spencer (Dec. 2010). "Galileo PPR observations of Europa: Hotspot detection limits and surface thermal properties". In: *Icarus* 210.2, pp. 763–769. DOI: 10.1016/j.icarus.2010.07.017.

Raut, U. et al. (Nov. 2008). "Cosmic Ray Compaction of Porous Interstellar Ices". In: *The Astrophysical Journal* 687.2, pp. 1070–1074. DOI: 10.1086/592193.

Schmitt, B. (1998). *Solar System Ices. Based on Reviews Presented at the International Symposium "Solar System Ices" held in Toulouse, France, on March 27-30, 1995*. Ed. by C. Bergh and M. Festou. Astrophysics and Space Science Library 227. Dordrecht: Springer. 810 pp. ISBN: 9789401152525.

Schmitt, Bernard et al. (Nov. 1989). "Laboratory studies of cometary ice analogues". In: *Physics and Mechanics of Cometary Materials* 302, pp. 65–69.

Seki, J. and H. Hasegawa (Sept. 1981). "Origin of Amorphous Interstellar Grains". In: *Progress of Theoretical Physics* 66.3, pp. 903–912. ISSN: 1347-4081. DOI: 10.1143/ptp.66.903.

Steckloff, Jordan K., Gal Sarid, and Brandon C. Johnson (Jan. 2023). "The Effects of Early Collisional Evolution on Amorphous Water Ice Bodies". In: *The Planetary Science Journal* 4.1, p. 4. DOI: 10.3847/psj/aca75a.

Strazzulla, G et al. (Mar. 1992). "Ion-Beam–Induced Amorphization of Crystalline Water Ice". In: *Europhysics Letters (EPL)* 18.6, pp. 517–522. ISSN: 1286-4854. DOI: 10.1209/0295-5075/18/6/008.

Teolis, B. D. et al. (Oct. 2017). "Water Ice Radiolytic O2, H2, and H2O2 Yields for Any Projectile Species, Energy, or Temperature: A Model for Icy Astrophysical Bodies". In: *Journal of Geophysical Research: Planets* 122.10, pp. 1996–2012. ISSN: 2169-9100. DOI: 10.1002/2017je005285.

Trumbo, Samantha K. and Michael E. Brown (Sept. 2023). "The distribution of CO 2 on Europa indicates an internal source of carbon". In: *Science* 381.6664, pp. 1308–1311. ISSN: 1095-9203. DOI: 10.1126/science.adg4155.

Trumbo, Samantha K., Michael E. Brown, and Bryan J. Butler (Sept. 2018). "ALMA Thermal Observations of Europa". In: *The Astronomical Journal* 156.4, p. 161. ISSN: 1538-3881. DOI: 10.3847/1538-3881/aada87.

USGS (2002). "Controlled photomosaic map of Europa". In: *Je 15M CMN: U.S. Geological Survey Geologic Investigations Series I–2757, available at https://pubs.usgs.gov/imap/i2757/.*

Villanueva, G. L. et al. (Sept. 2023). "Endogenous CO 2 ice mixture on the surface of Europa and no detection of plume activity". In: *Science* 381.6664, pp. 1305–1308. ISSN: 1095-9203. DOI: 10.1126/science.adg4270.

Warren, Stephen G. (Apr. 1984). "Optical constants of ice from the ultraviolet to the microwave". In: *Applied Optics* 23.8, p. 1206. ISSN: 1539-4522. DOI: 10.1364/ao.23.001206.

Wood, BE and JA Roux (1982). "Infrared optical properties of thin H 2 O, NH 3, and CO 2 cryofilms". In: *JOSA* 72.6, pp. 720–728.

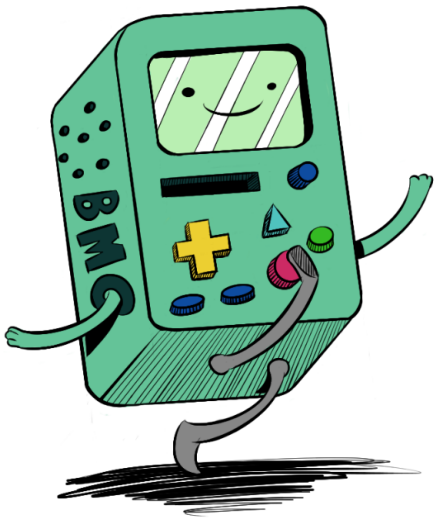

Figure 5.10: The supercomputer that conducted LunaIcy simulations is named "BMO," a reference to the character from the Adventure Time cartoon. BMO is a living prototype portable electrical outlet, computer, music player, video game console system, VCR, video player, video editor, roommate, camera, alarm clock, toaster, flashlight, strobe light, skateboarder, soccer player, tape player, chef, detective and friend. Credits: Scketch from OwenOak95 on Deviant art.

CHAPTER 6

Conclusion and Perspectives

Contents

The various works presented in this thesis focus on the evolution of Europa's icy surface microstructure. In this last chapter, we summarize the main findings from these studies and place them in the context of current research on Europa. Finally, we address the remaining unanswered questions from this thesis and suggest potential future research directions to advance this field.

6.1 General Conclusion

Numerous processes affect the surface of Europa, and I hope that after reading this thesis you are now convinced that they must be considered simultaneously and coupled together. In this PhD project, we have adopted a numerical modeling approach to study the surface ice, inspired by snowpack models on Earth (Brun et al., 1992; Vionnet et al., 2012; Lehning et al., 2002; Sauter et al., 2020). These models, used for avalanche forecasting, typically integrate one-dimensional equations governing heat transfer, water transport, vapor diffusion, and mechanical deformation of the snow. Although the processes on the surface of icy moons are different, the concept is similar: the surface is subject to heating, radiation, bombardment, sintering, and more. All these processes are interdependent and must be modeled together (see Figure 6.1).

Heat Transfer — The heat transfer module is at the core of our simulations, as it controls the kinetics of most surface processes. While various thermal solvers have been developed in the literature, none met the five requirements essential for our multiphysics model: stability, multi-layered, compatibility with Stefan-Boltzmann boundary conditions, modularity, and efficiency.

To address this, we have developed the thermal solver MultIHeaTS, which we have made available to the planetary science community as an open source code. This model accommodates heterogeneous media and is efficient enough to simulate daily heat variations over timescales of millions of years. This capability makes possible the study of Europa's icy surface evolution over long timescales within a reasonable computation time.

MultIHeaTS does not only consist of a thermal solver, but also incorporates a detailed description of Europa's orbital evolution. This integration allows, for the first time, to simulate the variations of solar flux not only over several seasons but over hundreds of thousands of Jupiter's orbits around the Sun. Overall, the development of MultIHeaTS has allowed for unprecedented simulations, providing better insights on the icy moons surface heat budget.

Density and Compaction — The modeling of heat transfer could not be achieved without a preliminary study of the thermal properties. Given Europa's highly porous surface, we asked ourselves whether compaction due to overburden pressure could occur at depths relevant for thermal analysis. To address this, we have developed a

gravity-induced compaction model based on Earth measurements of snow compaction and two different compaction models. We have found that on Europa, significant density changes occur only after at least a hundred meters, well beyond the diurnal and seasonal thermal skin depths. Therefore, for the near-surface, Europa's low gravity allows us to consider density and porosity as constant. Other compaction processes might be involved and would require further modeling, but they might not be quite efficient near the surface. A very recent interpretation of ALMA observations by (Thelen et al., 2024) finds no evidence of significant changes in porosity over the first dozen centimeters.

Sintering — Ice sintering has long been expected to affect the surface of icy moons, but its efficiency has never been accurately estimated. Two primary reasons contribute to this: 1) sintering is extremely sensitive to temperature, and 2) the full temperature history has never been considered for planetary surface sintering. This is mainly due to technical constraints: at Europa's temperatures, sintering can take at least tens of thousands of years, while temperature variations occur on a daily basis.

Thanks to the speed of MultIHeaTS and its integration with our multiphysics model LunaIcy, we have been able to simulate the coupled effects of sintering and heat transfer on Europa. The proposed sintering model not only includes mathematical refinements from the literature but also incorporates a description of the thermal conductivity of sintered grains, allowing for a two-way coupling with heat transfer.

We have conducted a parameter exploration to estimate the sintering efficiency across various configurations and regions of Europa. LunaIcy has revealed that the hottest regions, typically near the equator, are likely composed of well-sintered grains, whereas the colder regions at high latitudes do not experience sufficient sintering within Europa's estimated crust age.

Crystallinity — The multiphysics model LunaIcy investigates the effects of surface processes on multiple scales: at the macroscopic scale (e.g., temperature), at the grain scale (sintering), and at the molecular-arrangement scale (crystallinity). As for sintering, thermal crystallization is highly temperature dependent and had never been coupled to a thermal solver before. The surface is also influenced by the competing process of amorphization due to irradiation by charged particles and UVs, for which we have developed a new analytical model.

Integration of these processes into LunaIcy allowed to simulate the crystallinity profiles of the surface over various scenarios. This work represents the first attempt to model crystallinity profiles with depth on icy moons. Thanks to this parameter exploration and the reconstructed albedo map of Europa, we have produced the crystallinity map of the observable surface. Our results are promising, explaining some of the vertical crystallinity gradients observed by space missions and even showing periodic variations over seasons, which could potentially be observed by the upcom-

ing Europa Clipper and JUICE missions.

So what is the current state of Europa's ice microstructure?

The microstructure of Europa's surface appears to be heterogeneous, influenced by the varying balance of surface processes. Crystallinity shows variability in location, depth, and over time, ranging from predominantly amorphous to fully crystalline ice. The porosity is likely high and does not compact under its own weight near the surface. Sintering likely occurs on most of Europa's surface, resulting in a multi-layered ice with interconnected grains at the surface and a vertical gradient in sintering intensity with depth.

We have gained many insights from these numerical models, yet there is also much left to be discovered. While experimental investigations and space observations contribute to answering this question, they are limited by time and resources. There are still six years to pass before the first spacecraft in human-history orbits Europa, elucidating some of the surface microstructure mysteries. In the meantime, a lot of research can be done to advance the field. Developing and improving numerical models will greatly help us refine the values of the unconstrained parameters describing the microstructure of Europa. These numerical models work in complement to experimental and observational studies. Experiments improves our understanding of physical processes, enabling us to develop and validate theoretical models. Observations, can also validate and refine these models, and in return they significantly benefit from modeling advancements. A better understanding of Europa's surface through numerical modeling enhance the interpretation of space-based data, and will be crucial for the upcoming mission JUICE and Europa Clipper.

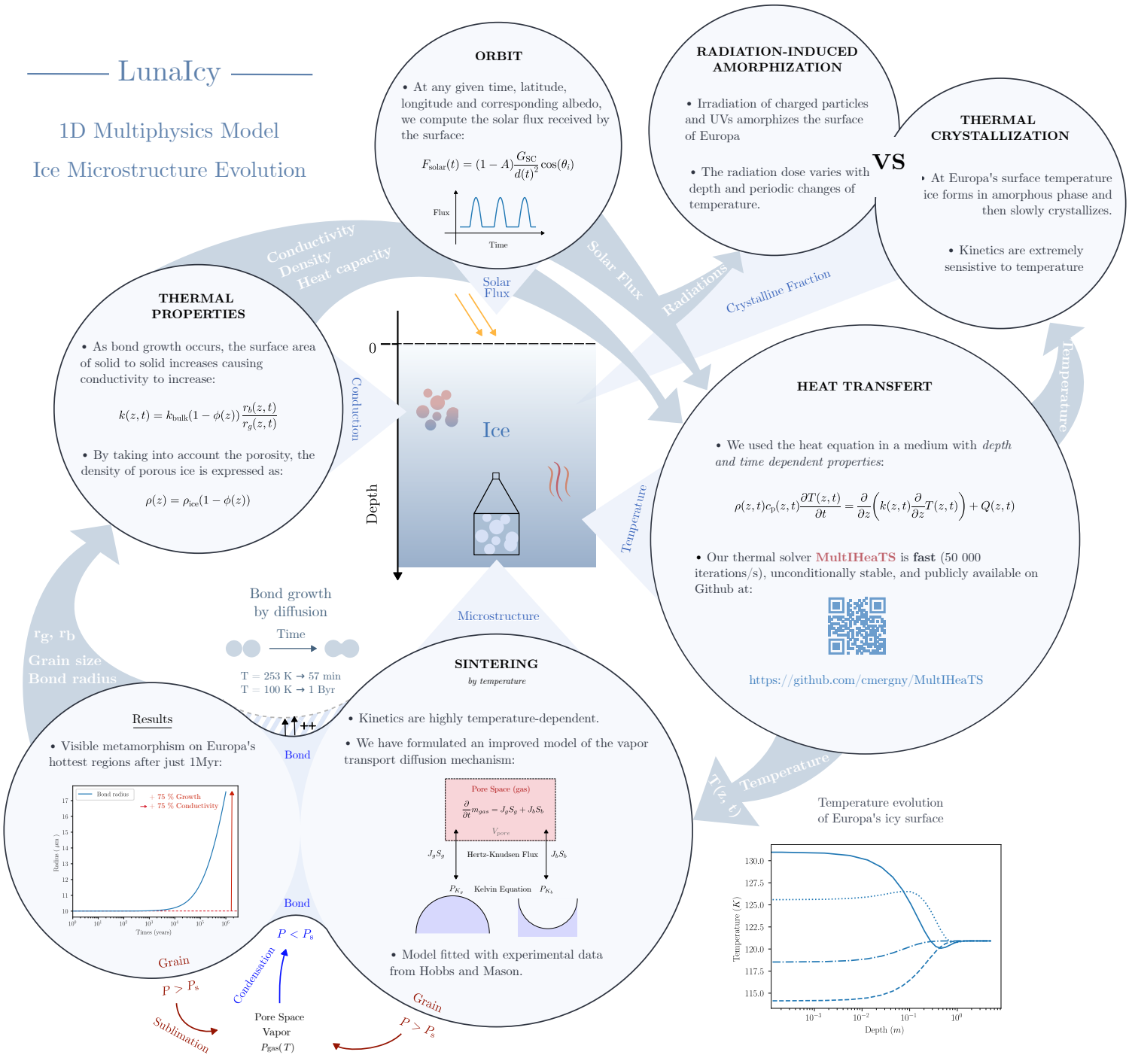

Figure 6.1: Summary of the physics modules implemented in the current version of LunaIcy and their interactions. This updated figure is adapted from a poster that I presented at the 2023 Workshop on the Origins and Habitability of the Galilean Moons.

While LunaIcy already gave us valuable insights on Europa's microstructure, significant potential development remains for further advancement. Notably, there are three research axes that I aim to expand upon, each requiring analytical, experimental, and/or observational approaches.

6.2 Axis 1: Applications to Other Planetary Surfaces

In Chapter 1, we listed the various planetary bodies in our solar system where ices have been found. To some extent, LunaIcy could be applied to any of these surfaces, with varying degrees of modification to adapt to the different conditions compared to Europa. The multiphysics model was developed with the goal of being a general tool capable of simulating any icy surface. Given the limited time of this PhD, we focused on Europa due to its potential habitability and its importance among upcoming missions. However, I plan to apply the model to other bodies after this PhD. Instead of listing all potential applications here, we will focus on a few detailed examples.

6.2.1 Ganymede

As the primary target of the JUICE mission, which will conduct 12 flybys of Ganymede around 2032 and then will be on orbit around it, this moon will be at the center of the planetary science community for the coming years. Conducting numerical simulations of its surface evolution will be highly valuable for better interpreting the surface observations from JUICE.

Direct Application of LunaIcy — Ganymede's environment is not drastically different from that of its sister moon, Europa, allowing us to use the current version of LunaIcy without additional modules to study Ganymede's microstructure. However, some notable differences must be considered.

Ganymede's surface is less active and much older than Europa's, dating back around 4 billion years, and features two distinct types of terrain. The lighter regions, covering about two-thirds of the surface, are marked by grooves and ridges, while the darker regions, covering one-third, are saturated with impact craters.

As for Europa, Ganymede's leading hemisphere has a brighter surface albedo than its trailing hemisphere. However, unlike Europa's bright surface with a bond albedo of 0.68, Ganymede's is much darker at 0.44, resulting in surface temperatures up to 20 Kelvin higher (Pater et al., 2014). This implies that temperature-dependent processes like sintering and thermal crystallization are going to more efficient on Ganymede. Additionally, with its less active crust dating back 4 billion years, Ganymede's surface has had ample time for sintering and crystallization to

occur.

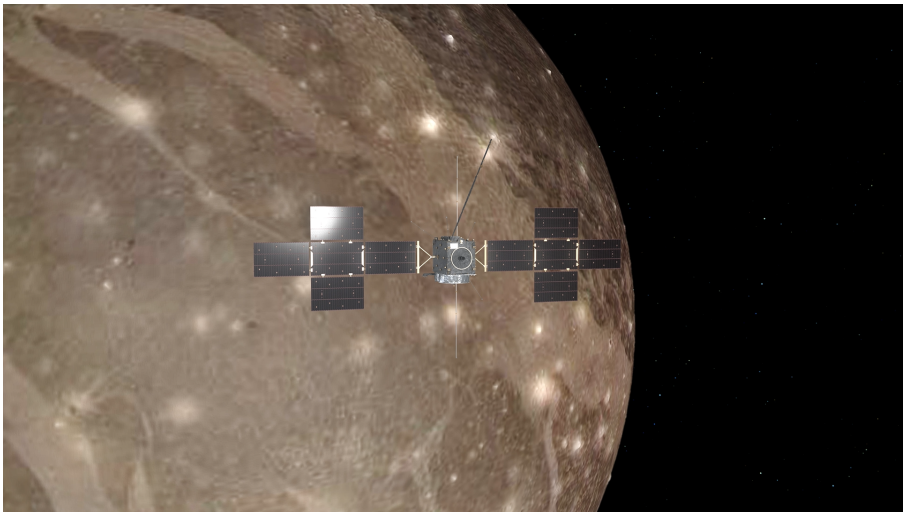

Figure 6.2: Artist's impression of JUICE flyby around Ganymede. Credits: ESA / ATG medialab

Also important to account, Ganymede is the only moon in the Solar System with a substantial magnetic field. This magnetic field protects the equatorial regions from much of the radiation. Additionally, being farther from Jupiter, the radiation levels at Ganymede's surface are much lower than those on Europa. As a result, Ganymede's surface composition at low latitudes is likely more endogenous, with limited alteration by space weathering. Therefore, apart from the polar regions where heavy ions continuously precipitate, amorphization will likely be less effective, especially since the amorphization rate decreases with higher temperatures.

Validating Compaction Lengthscales — In June 2021, Juno MWR mapped Ganymede's ice shell at six frequencies ranging from 0.6 to 22 GHz (S. Brown et al., 2023; Zhang et al., 2023). Notably, the study by S. Brown et al. (2023) revealed that brighter regions have high reflectivity compared to darker regions, likely due to the presence of numerous subsurface structures (fracturing, density heterogeneity).

An additional strength of MWR data lies in its ability to compare measurements across different frequencies. Multi-frequency radiometry enables the measurement of subsurface ice structure and composition at various depths, due to changes of density, purity, and potentially liquid water reservoirs. For solid ice at 100 K, the emission penetration depths range up to 24 km at MWR's longest frequency (0.6 GHz) and 15 m at the shortest frequency (22 GHz). These fall within the depth of noticeable density changes induced by gravity derived in Chapter 3 for Ganymede of $\sim 150\,\mathrm{m}$ (see Table 3.1).

While the study by (S. Brown et al., 2023) assumed constant porosity, it would be interesting to explore potential variations in density with depth based on this data

and compare them with our obtained compaction lengthscale for Ganymede. Also, it would be valuable to analyze Europa MWR data using the same methodology to validate our compaction lengthscales from these multi-frequency measurements.

6.2.2 Mars

Mars has two permanent polar ice caps consisting primarily of water ice, whereas the south cap has a permanent dry ice cover about eight meters thick. During local winter, carbon dioxide but also H_2O condenses and accumulates as a thin layer, called seasonal cap, over both polar regions. The seasonal north and south cap develops a CO_2 layer about one meter thick during the local winter. When the poles are again exposed to sunlight during spring, the frozen CO_2 sublimes, transporting large amounts of dust and water vapor.

Mars has been a potential target for our model since the beginning of LunaIcy's development (see F.Schmidt HDR (Schmidt, 2014)). However, due to the Martian atmosphere and the high presence of dust, further work is needed for full applicability. Here, we review two outstanding problems that LunaIcy could help address.

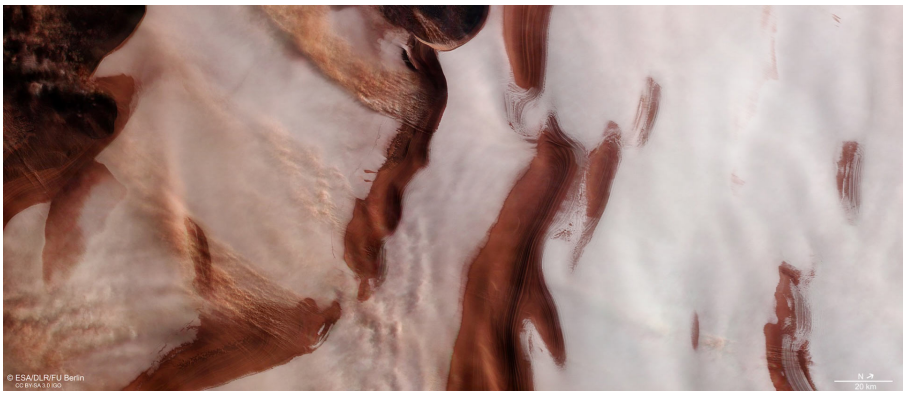

Figure 6.3: Satellite imagery of Mars' north pole, featuring bright ice patches, dark troughs, depressions, and signs of strong winds and storms. Data from the High Resolution Stereo Camera (HRSC) with a ground resolution of approximately 15 m/pixel, centered at (85°N, 244°E). Credit: ESA/DLR/FU Berlin.

Polar caps — The major source of water in the Martian atmosphere at present is related to the Northern permanent cap (Madeleine et al., 2014) (see Figure 6.3), but the net annual mass balance of the polar cap is not well constrained. Water cold-trapped by the seasonal frost is released at the end of spring when the CO_2 entirely sublimates. So, is the polar cap in a net ablation or accumulation? Additionally, the permanent Northern polar cap of Mars shows an increase in grain size during the summertime (Langevin et al., 2005). The absorbed solar energy by the ice can be: (i) converted to sublimate the H_2O ice, enriching Mars' atmosphere (Langevin et al.,

2005), (ii) converted into heat to increase the temperature and/or the intensity of ice sintering (Eluszkiewicz, 1993), or (iii) absorbed by dust grains that will gradually sink (Portyankina et al., 2010). To date, near-infrared spectroscopy investigations have not conclusively distinguished between sintering or relative ablation (A. J. Brown et al., 2016). The relative proportions of these phenomena and the overall microphysics of the cap surface remain open questions. Answering these questions would provide new insights into the age and formation of Mars' polar cap. By deciphering the layers within the permanent cap, we can unlock the climate record stored in it (Smith et al., 2020).

The mass balance of the ice polar cap cannot be retrieved by direct observations but through analytic and numeric modeling (Schmidt, 2014). Further development of LunaIcy and coupling with atmosphere models (GCM) (Forget et al., 1999; Way et al., 2017) could help us link the surface balance and microstructure characteristics (grain size, impurities, compaction).

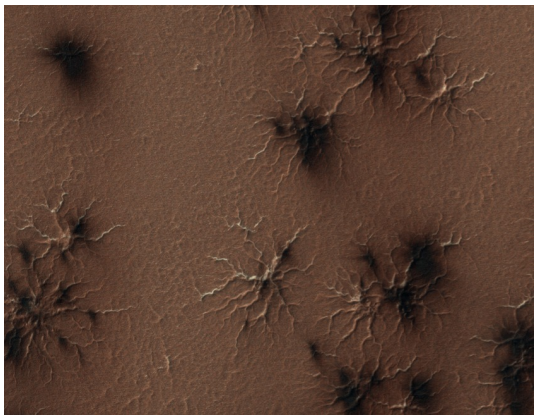

Figure 6.4: The dark spots in this image are the sign of 'spiders' scattered across the southern polar region of Mars. Credits: Hirise image at ($-87.0°$N, $127.2°E$) / LPL Arizona.

Evolution of CO_2 Slab Ice — Satellite imagery of Mars seasonal caps at $\sim 10\,\mathrm{m}$ resolution reveal "spiders" and "dark spots" patterns (see Figure 6.4), first discovered by the MOC instrument (Malin et al., 1998) and then confirmed by the HiRISE instrument (C. Hansen et al., 2010). The classic model (Kieffer et al., 2006) suggests that after a dust-cleaning phenomenon, CO_2 ice becomes transparent (Andrieu et al., 2018) to visible light down to the regolith, allowing the substrate to absorb solar energy and create a solid-state greenhouse effect. During the southern spring, the CO_2 ice receives enough solar energy to start sublimating from the bottom, creating a gas pocket that builds up pressure and cracks the ice. When the gas is ejected it drags dark material to the surface and shatters layers of ice up to a meter thick, carving the spiderweb-like network of grooves. This dark material falls back to the

surface and may be carried up slope by wind, creating dark wind streak patterns on the ice cap. These dark spots are a sign that spiders may be lurking below.

Sintering appears to be the key mechanism governing the translucency of the Martian ice slab. Conducting laboratory experiments to study the behavior of sintering in various types of ices would be highly valuable. It would be beneficial to examine how sintering rates differ between water ice and carbon dioxide ice under the same conditions. Additionally, since many planetary ices contain impurities, investigating how these impurities affect sintering rates would be interesting. Modeling the sintering process has never been done for CO_2 ice, and it could also help us understand the conditions for slab formation on Mars (Schmidt, 2014).

6.2.3 Other Bodies

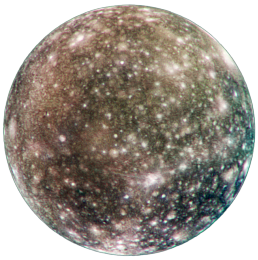

Among the other potential applications of LunaIcy, there is obviously Callisto, the third icy Galilean moon left to study. Due to its low albedo, Callisto's surface temperature can peak at up to 160 K, making it warmer even than Ganymede. Combined with lower radiation levels from being further from Jupiter, Callisto's surface is likely well-sintered and composed of crystalline ice. Simulating the surfaces of all three Galilean moons—Europa, Ganymede, and Callisto—would be highly valuable for comparative studies. These simulations could be linked to observations like those from G. B. Hansen (2004), which noted an increase in crystallinity from Europa to Ganymede to Callisto. Given the similar environments of these moons, they represent the most feasible applications for LunaIcy at present without requiring additional modeling.

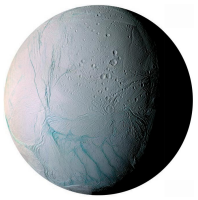

Going into the Saturnian system, as discussed in section 2, we have an ongoing collaboration with Dr. Le Gall and PhD student Raza Salman, applying our thermal solver to study Iapetus and Enceladus. Beyond the use of our thermal solver, it would be interesting to explore the effects of other physic modules, particularly sintering, on the Saturnian moons. Being farther from the Sun than Jupiter, the solar flux is insufficient to induce significant sintering. However, Enceladus experiences strong internal heating, leading to high surface temperatures along the Tiger Stripes. While Enceladus' surface is much colder than Europa's at around 70 K (J. R. Spencer et al., 2006), Cassini's Composite Infrared Spectrometer (CIRS) measurements indicate temperatures reaching up to at least 167 K near the Tiger Stripes (John R. Spencer et al., 2009). Sintering is thus likely to occur in these regions, and as we have shown in Chapter 4, this would result in a heterogeneous surface. As a result, it would be interesting to see if including a vertical thermal inertia gradient would

lead to better match of the brightness temperature observed Cassini.

Enceladus orbits within the inner regions of Saturn's magnetosphere, where the particle flux is high (R. H. Brown et al., 2006). Despite the low surface temperature that should result in amorphous ice formation, most of the surface ice is found to be crystalline, with some amorphous ice mixed in (Grundy, 1999; R. H. Brown et al., 2006). This phenomenon is not unique to Enceladus. Many ice bodies in the outer solar system are observed to be crystalline, even though they should form as amorphous ice at these temperatures (Clark, Carlson, et al., 2012). This paradox remains unexplained, highlighting the need for further experiments on ice formation to understand this discrepancy between observations and theory.

I did not list all potential applications of our multiphysics model here, but instead provided some examples. The long-term goal for LunaIcy is to be applicable to any icy moon and, more broadly, to any icy surface in our solar system, from planets, to moons, to comets. In the future, it could even be used to simulate the surface environment of potential icy exomoons, much like how GCMs simulate the atmospheres of exoplanets.

6.3 Axis 2: Modeling Improvements

The LunaIcy model has significantly enhanced our understanding of Europa's microstructure, though it required some simplifications. Here, we discuss the most critical simplifications and suggest ways to refine our modeling in future studies.

6.3.1 MultIHeaTS

The heat transfer is already quite efficient, but there are areas for potential improvement in future studies.

Firstly, refining the computation of solar flux incident on the surface could benefit from adopting Schorghofer (2022)'s more stable and efficient upper boundary conditions, particularly beneficial for simulations involving solar flux discontinuities such as eclipses. Further studies focusing on detailed descriptions of incoming flux should also consider factors like shadows, reflected light, and other photometric properties that influence the input flux.

Additionally, for surfaces where ice is near its evaporation or melting point, implementing phase changes and the associated enthalpy would be valuable. Also, the phase transition from crystalline to amorphous ice, which releases heat, should be included in the heat budget.

To save computation time, our current simulations consider that the thermal properties do not change with temperature. However, a more accurate description of the ice bulk conductivity, heat capacity and density as functions of temperature could be obtained by integrating the SeaFreeze tool within our framework (Journaux et

al., 2020). The SeaFreeze implementation is supposed to be computationally efficient and suitable for use in intensive simulations, such as LunaIcy (Journaux et al., 2020). Despite this, updating the thermal properties at each iteration, would still result in slower computation time, which will need to be addressed in future work.

Furthermore, our current model uses a simple analytical expression for the conduction of granular sintered media. More sophisticated formulations of conductivity exist (Piqueux et al., 2009; Ferrari et al., 2016; Gundlach et al., 2018; Rojek et al., 2022), which account for conduction through ice grains, radiation, and convection through pore spaces. Integrating these formulations would be more realistic and it would be interesting to see how they influence our results.

The thermal solver itself is already numerically efficient, and improving it further is not currently a priority as it is not the limiting factor in LunaIcy simulations. However, the computation of orbital parameters and resulting solar flux was implemented without specific attention to speed efficiency due to time constraints, making it the current bottleneck. A small amount of work on optimizing this part could accelerate simulations. It is important because faster computations also means improving resolution in both grid and time domains. Furthermore, more significant speed enhancements could allow us to run simulations on a detailed latitude/longitude grid to account for the spatial distribution of thermal properties, of charged particles radiations and of solar flux.

6.3.2 Ice Sintering

The accurate modeling ice sintering for planetary surface is a complex task, and this thesis represents only the beginning. Due to inconsistencies in the formulations found in the literature, we had to rebuild a model of diffusion through vapor transport from scratch.

Vapor Transport Improvements — Several improvements can still be made to our vapor diffusion model. One important point is understanding why we obtain such a small sticking coefficient ($\alpha \sim 0.003$). Currently, this parameter is used as a fitting parameter with experimental data, but ideally, we would set the sticking coefficient to a value found in the literature, typically between 0.5 and 1. Understanding what changes in our modeling can be made to fit experimental data with a realistic sticking coefficient value would be a significant advancement.

Our model currently considers a closed system where grains sublimate and the material condenses only on neighboring bonds. However, in highly porous ice, the pore structure is open, allowing pore spaces to communicate with each other. One crucial next step of development, is to model vapor transport between pores due to pressure gradients. In Europa's tenuous exosphere, water vapor will migrate from the bottom to the top, causing some bonds to gain more material from condensation while others lose material from their emptied pore spaces. Given Europa's expected

high surface porosity, modeling the influence of communicating pores on sintering would provide a more realistic representation, though it poses significant challenges as it has never been modeled in such conditions before.

If pores can communicate with each other, a form of sintering known on Earth as "temperature gradient metamorphism" or also "kinetic growth metamorphism" could occur. Unlike equi-temperature metamorphism, which is the process modeled in LunaIcy, temperature gradient metamorphism involves matter sublimating from warmer layers and condensing on colder ones (see Figure 6.5). Temperature differences produce water vapor concentration gradients within the pore space. If there is a large enough pore space, a substantial vapor flux from warmer to colder regions develops. This flux results in unique ice morphologies. As the temperature gradient increases, the snow microstructure changes from smooth, rounded grains with smooth interconnections to large, highly faceted, angular crystals, with large surrounding pore spaces and poor bonding characteristic of "depth hoar" .

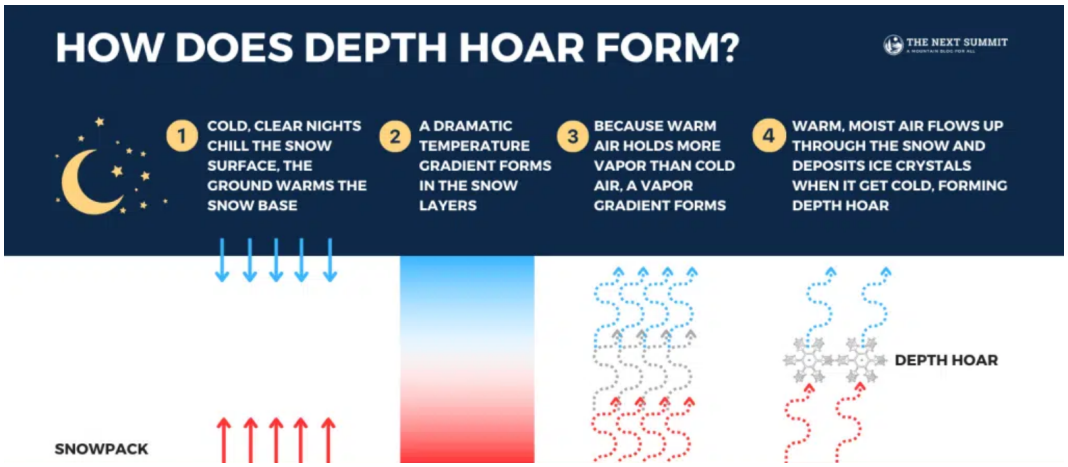

Figure 6.5: Depth hoar forms when there is a significant temperature gradient in the snow. Water vapor moves from the warmer layers to the colder layers, creating a vapor gradient. As the vapor reaches the colder snow layers, it turns into ice, resulting in the formation of faceted ice crystals called "depth hoar". Credits: Modified Figure from The Next Summit.

This temperature-induced concentration gradient will be balanced by the evacuation of matter through the surface exposed to the exosphere, making it unclear in which areas open-pore sintering will be favorable. Given the complexity of these interactions and the fact that such sintering have never been modeled under Europa's conditions, conducting laboratory experiments would be valuable for developing a model of temperature gradient sintering for icy moons. For example, one could conduct experiments in which a porous granular ice layer of a certain thickness is placed at low pressure and heated from the top. By measuring the sintering efficiency with varying parameters—such as grain size, temperature gradients, and porosity—these

experiments would provide valuable insights in our understanding of sintering under icy moons conditions.

Moreover, multiple sintering experiments have demonstrated that larger grains grow at the expense of smaller ones. Therefore, we aim to adapt our model to incorporate grains of varying sizes. In a communicating pore system, it would be interesting to see if the theoretical model can replicate these experimental observations.

Finally, while the sintering of pure ice has been well studied due to its presence on Earth, the sintering of other ice types remains largely unexplored. Impurities such as dust and salts in the ice could alter sintering rates. Since Europa's surface is not composed of completely pure water ice, especially on the trailing hemisphere, it is crucial to understand these effects. Additionally other planetary surfaces consist of different ices, such as carbon dioxide on Mars, and we aim to also model sintering for these volatiles. This project could build on the preliminary work of Clark, Fanale, et al. (1983) and Sandford et al. (1993), who evaluated the annealing efficiency of various ices. It would be very valuable to conduct comparative experiments for different types of ice and varying amounts of impurities to see how these changes affect the sintering rates.

Other Diffusion Mechanisms — Vapor diffusion is expected to be the most dominant mechanism for sintering under most planetary conditions. However, it is not clear if vapor transport is also the dominant mechanism for other types of ice, or if other mechanisms play a significant role. Vapor transport is non-densifying, meaning the "densification" expected from sintering does not occur through this process. Other diffusion mechanisms that could be intervene include grain boundary diffusion from a boundary source, lattice diffusion from a boundary source, or lattice diffusion from dislocation sources (Swinkels et al., 1981). Even for water ice, these processes, though less efficient, may become significant under high temperatures and long timescales. For this reason, Molaro et al. (2019) refers to these densifying mechanisms as "late-stage" sintering. Estimating the efficiency of these mechanisms under icy moon conditions would be valuable, and allow us to include the most significant ones in LunaIcy to complete the sintering module.

To conclude, accurately modeling the various mechanisms involved in ice sintering still requires a lot of development, but it will be crucial for estimating the properties of icy planetary surfaces.

6.3.3 Crystallinity

The work presented in Chapter 5 is the first attempt to couple thermal crystallization, radiation-induced amorphization with a thermal solver, to study their effect over geological timescales. While providing valuable insights, the first version of this model required several simplifications, that we would like to develop in further studies.

The main area needing improvement is the assumption of uniformity of charged particles bombardment. On Europa, the majority of radiation impacts the trailing hemisphere in a lens-shaped pattern (Paranicas et al., 2009; Nordheim et al., 2018) (see Figure 6.6), with fewer ions and only very high-energy electrons reaching the leading hemisphere. This non-uniform particle distribution significantly influences the crystallinity map of Europa. Future efforts should focus on integrating this non-uniform distribution into our models to enhance the accuracy of the crystallinity mapping process.

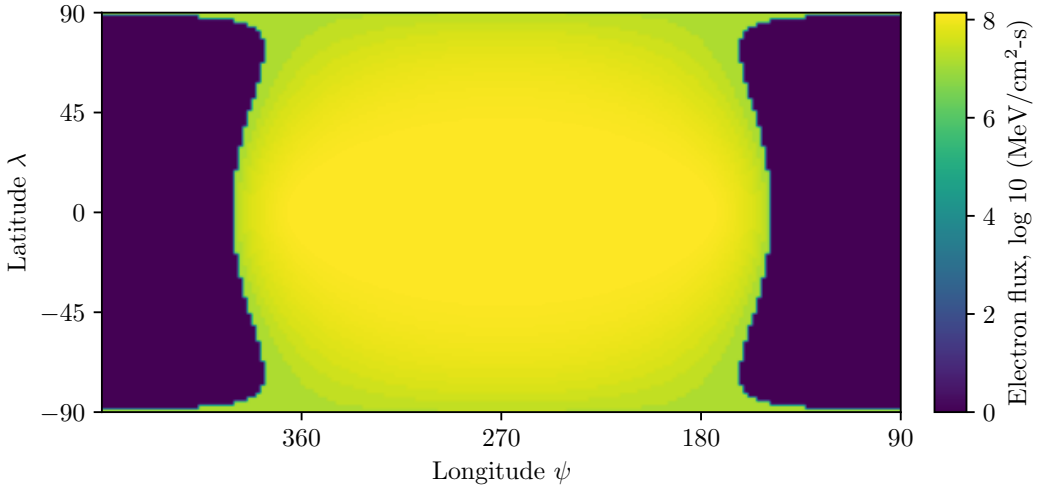

Figure 6.6: Power per unit area into Europa surface for 10 keV to ∼ 25 keV electrons. Computation based on Paranicas et al. (2009) data, with the most intense flux at the center of the trailing hemisphere of Europa at 270°W.

However, this development would be quite challenging because calculating the dose with depth requires knowledge of the non-integrated surface flux for each energy level and for each particle type. Unfortunately, most studies provide only the flux distributions on Europa integrated over all energies (see Figure 6.6). Nonetheless, our work has initiated discussions with experts such as Dr. Paranicas and Dr. Nordheim at Johns Hopkins University Applied Physics Laboratory, who could provide such flux distributions and potentially lead to collaborations in the near future. Furthermore, this would require running simulations for each longitude/latitude pair to accurately reproduce the crystallinity map, significantly increasing the computational cost.

Additionally, there are other areas that could benefit from improvement. The inclusion of Jupiter eclipses on the sub-jovian hemisphere will affect crystallization rates, and this will be implemented in the near future using the equivalent albedo from Chapter 5, possibly even before this thesis defense. Moreover, Europa's surface is not made of pure ice, so the penetration length of charged particles may be affected by the presence of impurities. Heterogeneity in composition could lead to varying doses with depth at different locations on the surface. Furthermore, the amorphiza-

tion rates, particularly for electrons and UV, are not well constrained. Conducting experiments on UV/electron irradiation of crystalline ice at various temperatures and photon energy would be valuable in constraining these rates. Finally, there is still no consensus on a theoretical model to explain the process of amorphization. Current models fail to explain why ice becomes very resistant to electrons and UV above 70K but not to ions. While challenging, developing such a model and comparing it to experimental results would be valuable.

The modeling work presented in Chapter 5, could be extended far beyond the study of crystallinity. The radiation and penetration of charged particles within the ice are responsible for sputtering and various exogenous chemical reactions. Electron bombardment is also thought to induce ice sintering, as shown by Schaible et al. (2017), and it would be interesting to see how our refined model affects their results. Therefore, further development of these models would not only better our understanding of crystallinity but also be valuable for different scientific field of interest on Europa's surface.

6.4 Axis 3: New Modules

Here we present examples of planned modules for both short-term and long-term implementation in LunaIcy, along with the development of new models to account for the microstructure of ice when interpreting space observations.

6.4.1 Micrometeorites Gardening

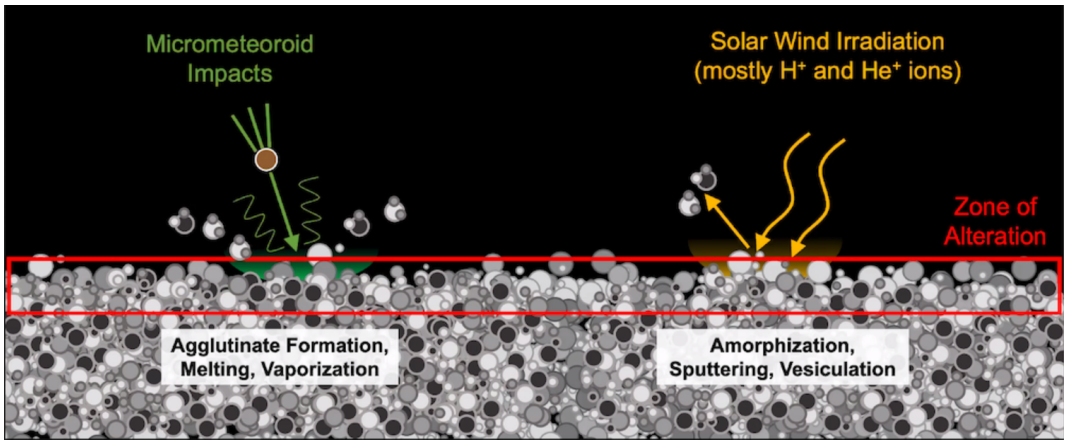

Figure 6.7: Space weathering causes the alteration of surface material due to exposure to interplanetary space. Credits: slide from Michelle Thompson on AAS Nova.

The surface of Europa is constantly bombarded by micrometeorites, which leads to gardening and mixing of the near surface (see Figure 6.7). This process notably

affects the crystallinity of the surface, as micrometeorites can bury irradiation products below the optical surface, changing the crystallinity profiles. Additionally, the impact of micrometeorites could break bonds between ice grains, counter-balancing the sintering process. Lastly, this constant bombardment could lead to densification of the near surface, a compaction process that we have yet to account for, affecting the thermal properties of the ice. This effect might be particularly noticeable on the leading hemisphere, which is especially exposed to bombardment. A modeling effort, based on existing literature, is needed to estimate the rate and penetration depth of such bombardment and integrate it into LunaIcy. It would be interesting to couple this bombardment with other modules to examine the resulting changes in crystallinity, sintering, and thermal properties of the icy surface at various locations on Europa.

6.4.2 Atmosphere Coupling

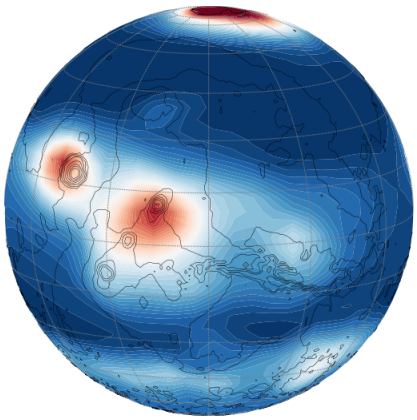

Figure 6.8: Result of GCM simulations outputting Mars water ice column, conducted at the Laboratoire de Météorologie Dynamique (Forget et al., 1999). Color bar values range from $2.07 \times 10^{-6}\,\mathrm{kg\,m^{-2}}$ to $7.00 \times 10^{-3}\,\mathrm{kg\,m^{-2}}$. Credits: Mars Climate Database.

Another important aspect to consider for long-term improvement of our model is the surface-atmosphere interaction. On Mars, the majority of the CO_2 atmosphere condenses in the polar cap during winter and sublimates during spring and summer. The formation and evolution of seasonal caps are intrinsically linked to their interaction with the atmosphere (see Figure 6.8). While challenging, coupling LunaIcy with existing GCM models, similar to how snowpack models are linked to climate models on Earth, would be highly beneficial for understanding Mars surface and climate.

Although Europa's exosphere is tenuous, its interaction with the surface is also important. As previously discussed, due to high porosity, the ice could consist of open pores exposed to the low-pressure exosphere which will affect sintering rates.

Additionally, an aspect overlooked in our modeling due to the lack of data, is how formation of ice occurs on Europa. Modeling vapor condensation on the surface and phase changes at the interface may provide crucial information about the current state of the microstructure. On one hand, radiation of charged particles sputters the H_2O surface, creating O_2 and H_2, which mainly compose Europa's exosphere. On the other hand, gas molecules, particularly O_2, may become trapped in the ice as clathrate hydrates and later released into the atmosphere (Oza et al., 2018). Coupling the atmosphere-surface interaction model could help us better understand the composition and evolution of Europa's exosphere and surface.

6.4.3 Improving Space-Data Interpretation

The future of LunaIcy lies not only in developing and refining new modules but also in its application for interpreting spaceborne data. As mentioned earlier, the model is already employed in collaboration with IPSL/LATMOS to enhance the interpretation of CASSINI brightness temperature measurements using a multi-layered surface model. Furthermore, investigating the effects of sintering and bombardment on the near surface results would result in new model of thermal inertia profiles, which could be used to better fit the brightness temperature data.

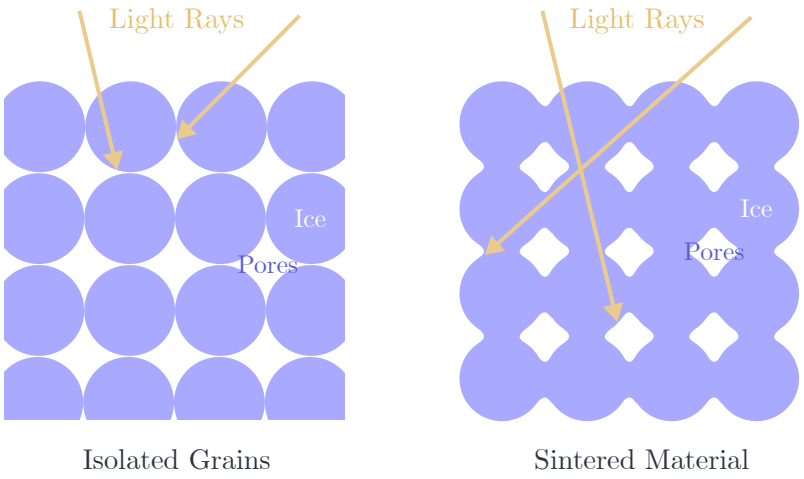

Figure 6.9: Light rays passing through isolated grains are more likely to encounter an ice/pore interface compared to sintered material, due to the increased grain-to-grain contact area in sintered material. As a result, although sintered grains are smaller, due to their bonds they appear as larger "grains" through spectroscopy.

An essential objective that we aim to collaborate closely with Dr. Andrieu's expertise at GEOPS, and with Dr. Cruz-Mermy's expertise at ESAC, is to refine the connection between surface microstructure, radiative transfer and spectroscopic models. The sintering of a surface leads to important variations of the optical properties, which we would like to confirm through observations from space. However,

establishing the relationship between microstructure and observed spectra is not straightforward.

Sintering is expected to increase grain sizes, but the vapor diffusion process detailed in Chapter 4 leads to a growth of bonds at the expense of grains. Why this unexpected behavior? The explanation is that sintering results in a complex structure composed not only of grains but also of bonds between them. From an optical point-of-view, this complicates the definition of "grain size" for sintered materials. When light passes through such a structure made of grain-bond-grain arrangements, in terms of radiative transfer, the mean free path of photon is increasing, and thus it appears as a larger "grain". Commonly used radiative transfer model, such as the Hapke model, assumes a granular media, i.e.: an arrangement of grains without bonds. As a result, a sintered material, with its increased grain-to-grain contact area, may appear to have increased its grain sizes when analyzed through spectroscopic techniques (see Figure 6.9).

It remains unclear how these microstructural changes specifically correlate with optical parameters in the Hapke model. Establishing a relationship between the growth of bond radius and the effective grain size observed by spectroscopy instruments would be very valuable. By comparing space observations of surfaces expected to sinter, such as equatorial regions, with those less likely to sinter, such as polar regions, we can assess if these variations in grain size are systematic, potentially confirming ongoing sintering processes on Europa.

The implications of this PhD project gains significant relevance when compared to the work of Dr. Cruz-Mermy. Connecting our numerical simulations with Dr. Cruz-Mermy's spectroscopic modeling represents the next logical advancement toward a better understanding of Europa's microstructure.

The prospects for LunaIcy are numerous, and I have likely outlined enough possibilities for the next decade here. Developing the various modules presented in this study required understanding of diverse physical processes, and it is this ongoing renewal that has sustained my motivation throughout the PhD. Integrating literature from multiple fields has been a valuable experience, and I have enjoyed bridging gaps between these disciplines and communities, that should probably communicate a bit more (Planetary Science, Earth Science, Physics, Mathematics, and Computer Science). I believe experts from each domain could contribute significantly to the development of such multiphysics simulations. So, hopefully, the future of LunaIcy will not be isolated but rather with various collaborators contributing in an open-source manner to each module of the project.

*
* *

Bibliography for Chapter 6

Andrieu, François et al. (Nov. 2018). "Ice state evolution during spring in Richardson crater, Mars". In: *Icarus* 315, pp. 158–173. ISSN: 0019-1035. DOI: 10.1016/j.icarus.2018.06.019.

Brown, Adrian J. et al. (Oct. 2016). "Martian north polar cap summer water cycle". In: *Icarus* 277, pp. 401–415. ISSN: 0019-1035. DOI: 10.1016/j.icarus.2016.05.007.

Brown, Robert H. et al. (Mar. 2006). "Composition and Physical Properties of Enceladus' Surface". In: *Science* 311.5766, pp. 1425–1428. ISSN: 1095-9203. DOI: 10.1126/science.1121031.

Brown, Shannon et al. (June 2023). "Microwave Observations of Ganymede's Sub-Surface Ice: I. Ice Temperature and Structure". In: *Journal of Geophysical Research: Planets* 128.6. ISSN: 2169-9100. DOI: 10.1029/2022je007609.

Brun, E. et al. (1992). "A numerical model to simulate snow-cover stratigraphy for operational avalanche forecasting". In: *Journal of Glaciology* 38.128, pp. 13–22. ISSN: 1727-5652. DOI: 10.3189/s0022143000009552.

Clark, Roger N., Robert Carlson, et al. (Apr. 2012). "Observed Ices in the Solar System". In: *Astrophysics and Space Science Library*. Springer New York, pp. 3–46. ISBN: 9781461430766. DOI: 10.1007/978-1-4614-3076-6_1.

Clark, Roger N., Fraser P. Fanale, and Aaron P. Zent (Nov. 1983). "Frost grain size metamorphism: Implications for remote sensing of planetary surfaces". In: *Icarus* 56.2, pp. 233–245. ISSN: 0019-1035. DOI: 10.1016/0019-1035(83)90036-2.

Eluszkiewicz (1993). "Thesis". PhD thesis.

Ferrari, C. and A. Lucas (Mar. 2016). "Low thermal inertias of icy planetary surfaces". In: *Astronomy and Astrophysics* 588, A133. DOI: 10.1051/0004-6361/201527625.

Forget, François et al. (Oct. 1999). "Improved general circulation models of the Martian atmosphere from the surface to above 80 km". In: *Journal of Geophysical Research: Planets* 104.E10, pp. 24155–24175. ISSN: 0148-0227. DOI: 10.1029/1999je001025.

Grundy, W (Dec. 1999). "Near-Infrared Spectra of Icy Outer Solar System Surfaces: Remote Determination of H2O Ice Temperatures". In: *Icarus* 142.2, pp. 536–549. ISSN: 0019-1035. DOI: 10.1006/icar.1999.6216.

Gundlach, B et al. (July 2018). "Sintering and sublimation of micrometre-sized water-ice particles: the formation of surface crusts on icy Solar System bodies". In: *Monthly Notices of the Royal Astronomical Society* 479.4, pp. 5272–5287. DOI: 10.1093/mnras/sty1839.

Hansen, C.J. et al. (Jan. 2010). "HiRISE observations of gas sublimation-driven activity in Mars' southern polar regions: I. Erosion of the surface". In: *Icarus*

205.1, pp. 283–295. ISSN: 0019-1035. DOI: 10.1016/j.icarus.2009.07.021.

Hansen, Gary B. (2004). "Amorphous and crystalline ice on the Galilean satellites: A balance between thermal and radiolytic processes". In: *Journal of Geophysical Research* 109.E1. DOI: 10.1029/2003je002149.

Journaux, B. et al. (Jan. 2020). "Holistic Approach for Studying Planetary Hydrospheres: Gibbs Representation of Ices Thermodynamics, Elasticity, and the Water Phase Diagram to 2,300 MPa". In: *Journal of Geophysical Research: Planets* 125.1. ISSN: 2169-9100. DOI: 10.1029/2019je006176.

Kieffer, Hugh H., Philip R. Christensen, and Timothy N. Titus (Aug. 2006). "CO2 jets formed by sublimation beneath translucent slab ice in Mars' seasonal south polar ice cap". In: *Nature* 442.7104, pp. 793–796. ISSN: 1476-4687. DOI: 10.1038/nature04945.

Langevin, Y. et al. (Mar. 2005). "Summer Evolution of the North Polar Cap of Mars as Observed by OMEGA/Mars Express". In: *Science* 307.5715, pp. 1581–1584. ISSN: 1095-9203. DOI: 10.1126/science.1109438.

Lehning, Michael et al. (Nov. 2002). "A physical SNOWPACK model for the Swiss avalanche warning". In: *Cold Regions Science and Technology* 35.3, pp. 147–167. DOI: 10.1016/s0165-232x(02)00073-3.

Madeleine, J.-B. et al. (July 2014). "Recent Ice Ages on Mars: The role of radiatively active clouds and cloud microphysics". In: *Geophysical Research Letters* 41.14, pp. 4873–4879. ISSN: 1944-8007. DOI: 10.1002/2014gl059861.

Malin, M. C. et al. (Mar. 1998). "Early Views of the Martian Surface from the Mars Orbiter Camera of Mars Global Surveyor". In: *Science* 279.5357, pp. 1681–1685. ISSN: 1095-9203. DOI: 10.1126/science.279.5357.1681.

Molaro, J. L. et al. (Feb. 2019). "The Microstructural Evolution of Water Ice in the Solar System Through Sintering". In: *Journal of Geophysical Research: Planets* 124.2, pp. 243–277. DOI: 10.1029/2018je005773.

Nordheim, T. A., K. P. Hand, and C. Paranicas (July 2018). "Preservation of potential biosignatures in the shallow subsurface of Europa". In: *Nature Astronomy* 2.8, pp. 673–679. ISSN: 2397-3366. DOI: 10.1038/s41550-018-0499-8.

Oza, Apurva V., Robert E. Johnson, and François Leblanc (May 2018). "Dusk/-dawn atmospheric asymmetries on tidally-locked satellites: O2 at Europa". In: *Icarus* 305, pp. 50–55. ISSN: 0019-1035. DOI: 10.1016/j.icarus.2017.12.032.

Paranicas, C. et al. (Jan. 2009). "Europa's Radiation Environment and Its Effects on the Surface". In: *Europa*.

Pater, Imke de and Jack J. Lissauer (Dec. 2014). *Planetary Sciences*. Cambridge University Press. ISBN: 9781316165270. DOI: 10.1017/cbo9781316165270.

Piqueux, S. and P. R. Christensen (Sept. 2009). "A model of thermal conductivity for planetary soils: 2. Theory for cemented soils". In: *Journal of Geophysical Research* 114.E9. DOI: 10.1029/2008je003309.

Portyankina, Ganna et al. (Jan. 2010). "HiRISE observations of gas sublimation-driven activity in Mars' southern polar regions: III. Models of processes involving translucent ice". In: *Icarus* 205.1, pp. 311–320. ISSN: 0019-1035. DOI: 10.1016/j.icarus.2009.08.029.

Rojek, J., R. Kasztelan, and R. Tharmaraj (June 2022). "Discrete element thermal conductance model for sintered particles". In: *Powder Technology* 405, p. 117521. ISSN: 0032-5910. DOI: 10.1016/j.powtec.2022.117521.

Sandford, Scott A. and Louis J. Allamandola (Dec. 1993). "The Condensation and Vaporization Behavior of Ices Containing SO2, H2S, and CO2: Implications for Io". In: *Icarus* 106.2, pp. 478–488. ISSN: 0019-1035. DOI: 10.1006/icar.1993.1186.

Sauter, Tobias, Anselm Arndt, and Christoph Schneider (Nov. 2020). "COSIPY v1.3 – an open-source coupled snowpack and ice surface energy and mass balance model". In: *Geoscientific Model Development* 13.11, pp. 5645–5662. DOI: 10.5194/gmd-13-5645-2020.

Schaible, M.J. et al. (Mar. 2017). "High energy electron sintering of icy regoliths: Formation of the PacMan thermal anomalies on the icy Saturnian moons". In: *Icarus* 285, pp. 211–223. DOI: 10.1016/j.icarus.2016.08.033.

Schmidt, Frédéric (Jan. 2014). "Echanges de volatils entre surface et atmosph'ere sur mars". Habilitation à diriger des recherches. HDR, Paris-Sud XI. URL: https://theses.hal.science/tel-01085029.

Schorghofer, Norbert (2022). "Planetary-Code-Collection: Thermal, Ice Evolution, and Exosphere Models for Planetary Surfaces". In: *Zenodo*. DOI: 10.5281/ZENODO.594268.

Smith, Isaac B. et al. (May 2020). "The Holy Grail: A road map for unlocking the climate record stored within Mars' polar layered deposits". In: *Planetary and Space Science* 184, p. 104841. ISSN: 0032-0633. DOI: 10.1016/j.pss.2020.104841.

Spencer, J. R. et al. (Mar. 2006). "Cassini Encounters Enceladus: Background and the Discovery of a South Polar Hot Spot". In: *Science* 311.5766, pp. 1401–1405. ISSN: 1095-9203. DOI: 10.1126/science.1121661.

Spencer, John R. et al. (2009). "Enceladus: An Active Cryovolcanic Satellite". In: *Saturn from Cassini-Huygens*. Springer Netherlands, pp. 683–724. ISBN: 9781402092176. DOI: 10.1007/978-1-4020-9217-6_21.

Swinkels, F.B. and M.F. Ashby (Feb. 1981). "A second report on sintering diagrams". In: *Acta Metallurgica* 29.2, pp. 259–281. DOI: 10.1016/0001-6160(81)90154-1.

Thelen, Alexander E. et al. (Feb. 2024). "Subsurface Thermophysical Properties of Europa's Leading and Trailing Hemispheres as Revealed by ALMA". In: *The Planetary Science Journal* 5.2, p. 56. ISSN: 2632-3338. DOI: 10.3847/psj/ad251c.

Vionnet, V. et al. (May 2012). "The detailed snowpack scheme Crocus and its implementation in SURFEX v7.2". In: *Geoscientific Model Development* 5.3, pp. 773–791. DOI: 10.5194/gmd-5-773-2012.

Way, M. J. et al. (July 2017). "Resolving Orbital and Climate Keys of Earth and Extraterrestrial Environments with Dynamics (ROCKE-3D) 1.0: A General Circulation Model for Simulating the Climates of Rocky Planets". In: *The Astrophysical Journal Supplement Series* 231.1, p. 12. ISSN: 1538-4365. DOI: 10.3847/1538-4365/aa7a06.

Zhang, Zhimeng et al. (June 2023). "Microwave Observations of Ganymede's Sub-surface Ice: 2. Reflected Radiation". In: *Geophysical Research Letters* 50.11. ISSN: 1944-8007. DOI: 10.1029/2022gl101565.

Synthèse

Le travail accompli au cours de cette thèse est présenté dans ce manuscrit rédigé en anglais. Conformément aux règlements de l'Université Paris Saclay et de l'école doctorale SMEMaG, une synthèse de ce travail, rédigée en français, est également proposée ci-dessous pour les lecteurs francophones intéressés.

Contexte Général

Les Glaces dans le Système Solaire et sur Europe

Sur Terre, le terme "glace" désigne communément l'eau figée sous forme solide, généralement à des températures inférieures à 0 °C ou 273.15 K, à la pression atmosphérique. En astrophysique et en science planétaire, le terme "glaces" a une signification plus large : il désigne des composés chimiques modérément à hautement volatils à l'état solide (Schmitt, 1998). Dans le système solaire, ces glaces incluent principalement l'eau (H_2O), l'ammoniac (NH_3), le dioxyde de soufre (SO_2), le dioxyde de carbone (CO_2), le méthane (CH_4), le monoxyde de carbone (CO), et l'azote (N_2), et constituent une part significative de la masse du système solaire externe (Schmitt, 1998).

Les glaces sont répandues dans tout le système solaire, allant de Mercure aux objets transneptuniens lointains. À mesure que notre technologie d'observation s'améliore, nous découvrons de plus en plus de glaces dans des endroits divers à travers le système solaire. La plupart des glaces identifiées par observations télescopiques et missions spatiales se trouvent à la surface des corps planétaires.

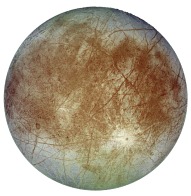

Étudier et caractériser les propriétés de ces glaces est important car cela nous aide à comprendre les processus impliqués dans l'évolution des surfaces planétaires. Bien que toutes ces surfaces glacées suscitent un grand intérêt, dans le cadre de cette thèse de doctorat, nous avons choisi de concentrer nos efforts de modélisation sur la surface d'Europe, qui est sujet de nombreuses questions. Europe est l'un des principaux candidats pour la recherche de l'habitabilité potentielle et est au centre des prochaines missions phares de l'ESA et de la NASA. Une meilleure compréhension de la microstructure de surface d'Europe contribuera grandement à l'analyse des données de ces missions et à la sélection des sites d'atterrissage potentiels pour des concepts tels que "Europa Lander".

Europe, tout comme les quatre lunes galiléennes, est en rotation synchrone avec Jupiter, ce qui signifie qu'une hémisphère fait toujours face à la planète. Cet hémisphère est appelé l'hémisphère sub-jovien, tandis que l'hémisphère opposé est connu sous le nom d'hémisphère anti-jovien. De même, on distingue l'hémisphère dit "leading", qui fait face à la direction de l'orbite de la lune, et l'hémisphère dit "trailing", dans la direction opposée.

Europe a notamment été visitée par la sonde Galileo de 1995 à 2003 qui a fourni la plupart des informations que nous avons actuellement à son sujet. Les mesures de son moment d'inertie suggèrent une différenciation interne avec un noyau métallique entouré par un manteau silicaté et une couche externe d'eau de 80 à 170 km d'épaisseur (J. D. Anderson et al., 1998) (voir Figure 6.10). Des observations d'un champ magnétique induit indiquent la présence d'un océan global sous une épaisse couche de glace, avec une atmosphère ténue d'oxygène et des caractéristiques géologiques variées. La composition de surface, dominée par la glace d'eau, révèle une complexité due à divers processus locaux.

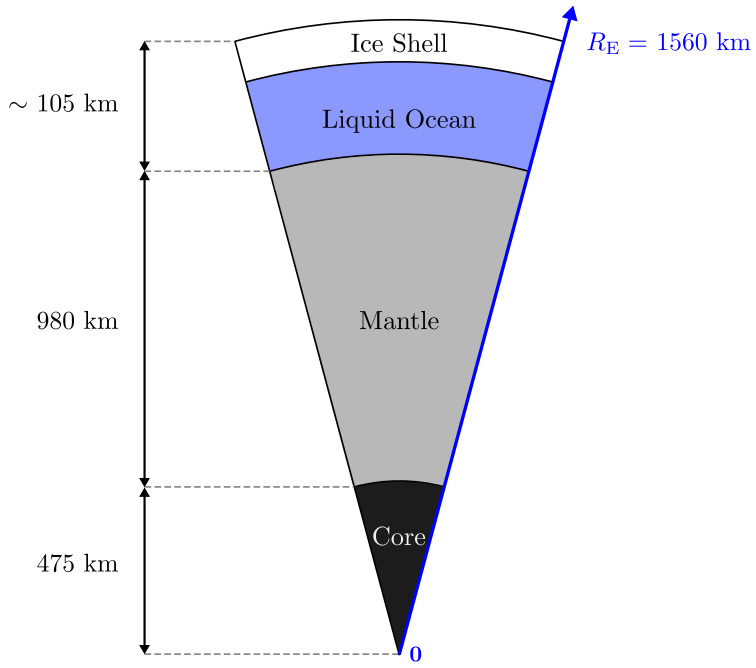

Figure 6.10: Représentation schématique de l'intérieur d'Europe selon les épaisseurs proposées par (Vance et al., 2018). Les épaisseurs et les matériaux sont déduits des mesures du moment d'inertie d'Europe et des contraintes de densité. La spectroscopie indique que la surface est composée de glace d'eau, et les mesures d'un champ magnétique induit fournissent des preuves d'un océan intérieur d'eau liquide.

La Microstructure de la Glace sur Europe

Quel est l'état actuel de la microstructure de la glace sur Europe ? Par microstructure de la glace, on fait référence à l'arrangement et aux caractéristiques microscopiques de la glace sur les corps planétaires, comme les lunes glacées. Cela inclut la taille, la forme, l'orientation et la distribution des grains de glace, la cristallinité de la phase de glace, ainsi que la présence de pores, d'impuretés, de rugosités et d'autres caractéristiques à petite échelle qui influencent les propriétés physiques de la glace.

Comprendre la microstructure d'un matériau est crucial car elle influence significativement ses propriétés physiques, telles que l'absorption de la lumière, la conductivité thermique, la résistance, la dureté, ainsi que d'autres propriétés optiques, thermiques et mécaniques. Cette connaissance améliore notre compréhension de la surface d'Europe, affine les modèles spectroscopiques, spectrophotométriques, thermophysiques et le choix de sites d'atterrissage potentiels, entre autres applications.

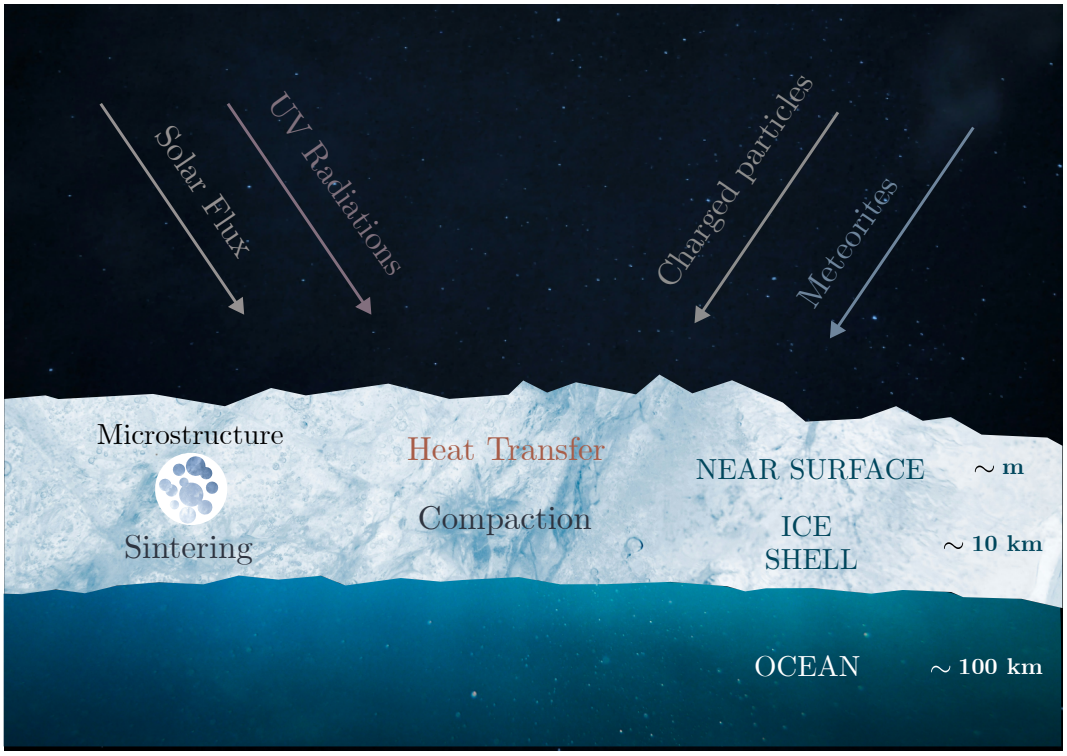

Figure 6.11: La surface glacée et la proche-surface d'Europe sont influencés par divers processus physiques couplés : flux solaire, conduction de la chaleur, compaction induite par la gravité, métamorphisme de la glace, cristallisation thermique, amorphisation induite par le rayonnement, et bombardement météoritique (non encore modélisé). Cette thèse se concentre sur la modélisation et le couplage de ces phénomènes physiques afin de mieux comprendre l'évolution de la microstructure de la glace.

Actuellement, notre connaissance de la microstructure d' Europe est limitée, avec la meilleure résolution d'images satellite de la surface étant d'environ 10 mètres par pixel. Par conséquent, nous manquons d'informations détaillées sur les propriétés de la surface. Divers processus physiques peuvent altérer la microstructure de la surface glacée, comme illustré dans la Figure 6.11. Parmi eux : le transfert de chaleur, la compaction induite par la gravité, le métamorphisme de la glace, la cristallisation thermique et l'amorphisation induite par le rayonnement seront développés dans cette thèse. Ces processus ont un effet notable seulement sur la proche-surface proche d' Europe, donc nous avons concentré notre étude sur les premiers mètres de profondeur.

Motivations pour des Simulations Multiphysiques

Sur Terre, notre compréhension de la surface est considérablement aidée par la possibilité de mener des études de terrain. Les échantillons collectés sont analysés en laboratoire, fournissant des contraintes robustes pour les modèles géologiques. Cependant, pour d'autres corps planétaires, de telles analyses ne sont pas encore possibles. Comment étudier ces surfaces glacées ?

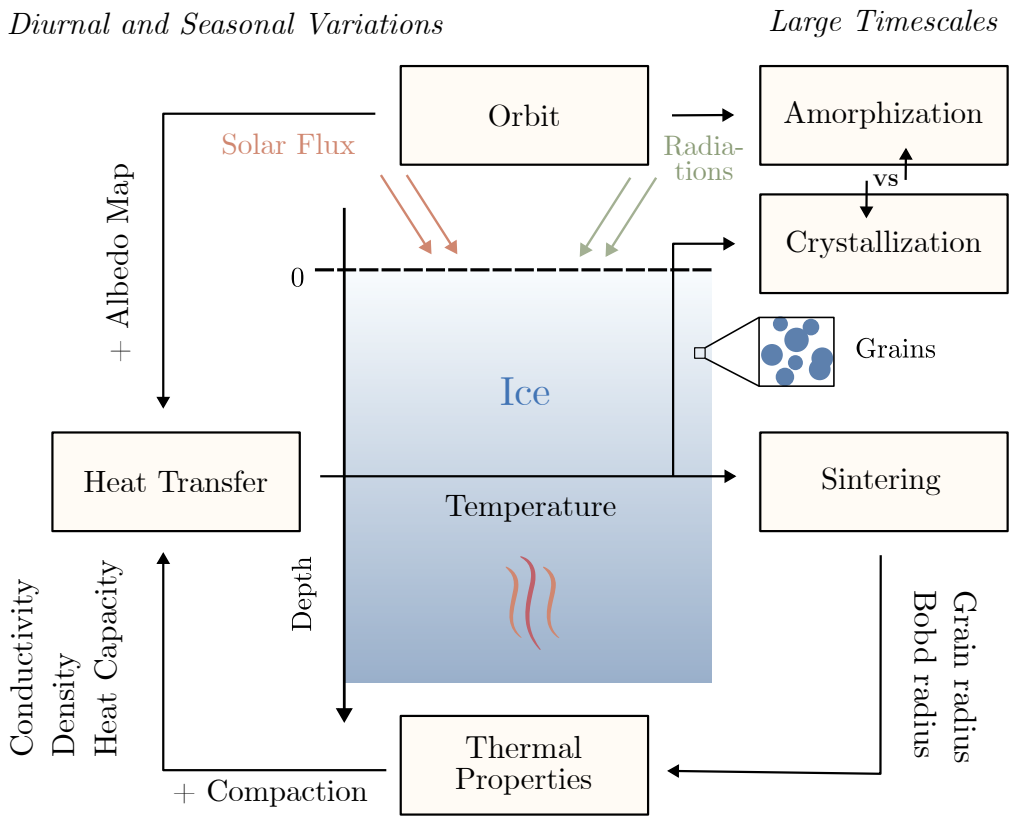

Figure 6.12: Diagramme bloc du modèle de simulation proposé LunaIcy montrant le couplage multiphysique entre chaque module.

Une possibilité est de développer des modèles analytiques/numériques, de les valider en les confrontant à des données spatiales ou expérimentales, puis de les utiliser pour étudier l'évolution de ces surfaces. Les modèles existants abordent traditionnellement la description de ces processus physiques de manière indépendante, tels que la modélisation du transfert de chaleur (Spencer et al., 1989), le métamorphisme de la glace (Molaro et al., 2019) et la cristallinité (Berdis et al., 2020), entre autres. Bien qu'utiles pour fournir des estimations de premier ordre des effets de chaque processus, il existe en réalité un fort couplage entre ces phénomènes physiques (voir Figure 6.12):

La température de la proche-surface d'Europe est calculée en fonction du transfert de chaleur, reposant sur nos connaissances des propriétés thermiques et du flux solaire entrant. Les propriétés thermiques, comme la densité, sont affectées par les processus de compaction et le calcul du flux solaire nécessite un calcul détaillée de l'orbite d'Europe. D'une part, le métamorphisme est extrêmement sensible à la température, nécessitant une connaissance précise de l'évolution thermique. D'autre part, le métamorphisme forme des liaisons qui modifient les propriétés thermiques de la glace, affectant ainsi la température en retour. Enfin, la cristallisation et l'amorphisation de la glace dépendent également fortement de la température et peuvent induire des fluctuations dans ses propriétés thermiques.

Étant donné la nature couplée de ces phénomènes physiques, peut-on réellement estimer leurs effets de manière indépendante ?

Le concept central de cette thèse est d'intégrer les divers phénomènes physiques qui affectent la microstructure de la glace sur Europe et de les coupler dans un modèle de simulation multiphysiques unidimensionnel nommé "LunaIcy" (voir Figure 6.12). Tout comme il a été développé des modèles de circulation générale (GCM) pour les études climatiques, l'étude des surfaces glacées planétaires bénéficierait de la création de modèles numériques multiphysiques. Ce type de simulation serait analogue aux modèles de manteau neigeux utilisés pour la prédiction des avalanches, mais ici pour les glaces du système solaire.

Transferts de Chaleur

La température est le principal paramètre qui régit la cinétique des processus physiques interagissant sur la microstructure de la glace. Pour cette raison, le premier objectif de cette thèse a été d'estimer avec précision l'évolution de la température en fonction de la profondeur et du temps d'une surface glacée. La surface d'Europe est chauffée par le flux solaire et/ou une source de chaleur interne, cette chaleur peut être tranmise en profondeur par conduction ou réémise sous forme de radiations à longue longueur d'onde depuis la surface (voir Figure 6.13).

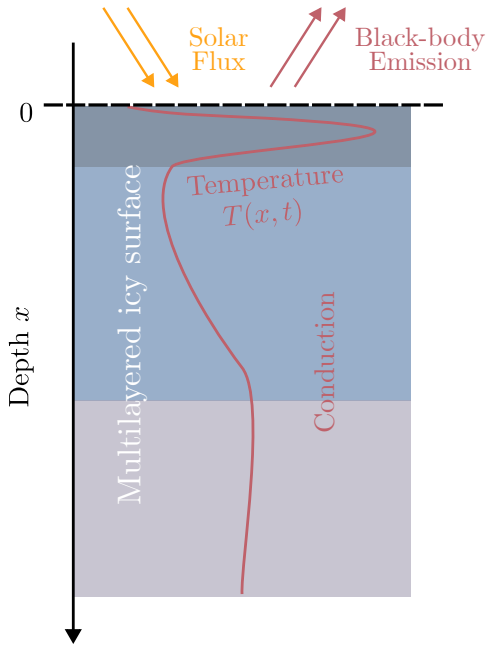

Figure 6.13: Conduction thermique à travers une surface glacée multicouche. Les lunes glacées, comme Europe, ont probablement des propriétés thermiques variables avec la profondeur. Ces gradients peuvent provenir de différences de composition, comme une fine couche de poussière recouvrant la surface, ou de processus de surface comme le métamorphisme qui modifient la microstructure de la glace.

Près de la surface, le transfert de chaleur se fait par conduction et est influencé par les propriétés thermiques : la conductivité thermique, la capacité calorifique spécifique, la densité, l'émissivité thermique et l'albédo. Les mesures de la température de brillance du photopolarimètre-radiomètre (PPR) de Galileo et des observations depuis la Terre ont été utilisées pour déterminer l'inertie thermique du sous-sol d'Europe (Spencer et al., 1989; Rathbun et al., 2010; Trumbo et al., 2018). Ces études ont utilisé des modèles thermophysiques en supposant une surface glacée homogène. Cependant, des mesures télescopiques (O. Hansen, 1973) pendant les éclipses induites par Jupiter ont montré que la surface d'Europe semble fortement stratifié : les quelques millimètres supérieurs ont une faible inertie thermique, tan-

dis que la couche sous-jacente a une inertie thermique beaucoup plus élevée. Ces résultats soulèvent des questions importantes : comment la température de surface est-elle affectée par un modèle multicouches ? Quel est l'effet des éclipses solaires de Jupiter sur l'hémisphère sub-jovien ? De plus, la modélisation sur de longues périodes nécessite de considérer les variations du flux solaire sur ces périodes étendues : quel est l'effet des variations à long terme de l'orbite d'Europe sur les profils de température ?

Pour répondre à cela, il existe de nombreux solveurs thermiques disponibles dans la littérature, couvrant divers domaines. Ils ne se trouvent pas seulement en sciences planétaires (Spencer et al., 1989), mais sont également largement utilisés en géophysique (Bonneville et al., 1999), en science des matériaux (Rojek et al., 2022), en ingénierie mécanique et électrique (D. A. Anderson et al., 2020), et en dynamique des fluides computationnelle (Janna, 2018), entre autres.

Alors, pourquoi en développer un autre ? La raison en est que les conditions uniques nécessaires pour modéliser les surfaces planétaires complexes nécessitent des traitements spéciaux qui ne sont pas correctement abordés dans la littérature existante. Ces exigences sont les suivantes :

- **Stabilité :** un schéma implicite procure une stabilité inconditionnelle, plus efficace que les schémas de pas de temps explicites traditionnels dans les modèles thermiques planétaires.
- **Compatibilité avec les Surfaces Hétérogènes :** Cette approche gère plusieurs couches, contrairement à de nombreux modèles supposant l'homogénéité, ce qui la rend applicable à divers scénarios planétaires.
- **Équilibre de l'Émission Thermique :** Le solveur traite la nature non linéaire de l'équilibre de l'émission thermique dû à la loi de Stefan-Boltzmann, conditions spécifiques aux surface planétaires.
- **Modularité :** Les modules sont écrits en Python pour faciliter leur utilisation, la collaboration et l'intégration avec les modules du modèle de simulations.
- **Vitesse :** Le solveur est optimisé pour son temps de calcul afin de gérer les grandes échelles de temps requises pour les simulations de surfaces planétaires.

Nous avons donc développé un algorithme efficace et open-source avec un schéma implicite appelé MultIHeaTS, qui utilise les différences finies pour résoudre l'équation de la chaleur sur des médias hétérogènes 1D avec une grille irrégulière. Bien que notre objectif principal soit la science planétaire, notre algorithme est adaptable et peut gérer différents types de conditions aux limites et de surfaces.

Pour les cas homogènes, l'algorithme a été validé à l'aide d'une solution analytique connue. Cette validation, qui utilisait une condition initiale discontinue, a montré la robustesse de MultIHeaTS face à des conditions rigides, contrairement à la méthode de Crank-Nicolson. Pour les cas hétérogènes, MultIHeaTS a été validé par

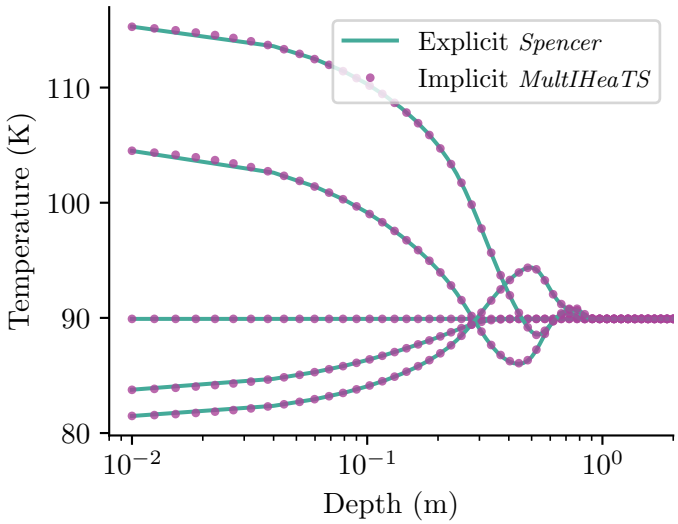

Figure 6.14: Validation de MultIHeaTS par rapport à l'algorithme explicite de Spencer. Les profils de température pour différents moments sont tracés à $i = 0$, 200, 14050, 34959, 49000. MultIHeaTS est aussi précis que le solveur explicite de Spencer avec l'avantage de la stabilité. L'espacement inégal de la grille de MultiHeaTS, plus dense à la surface est montré par l'axe horizontal logarithmique.

comparaison avec un algorithme explicite bien établi en science planétaire (Spencer et al., 1989) (voir Figure 6.14). Notre schéma implicite est resté précis et stable, produisant des résultats proches de ceux du modèle explicite de Spencer. Grâce à sa stabilité avantageuse, MultIHeaTS peut calculer la même température pour un temps donné jusqu'à 100 fois plus rapidement que la méthode explicite de Spencer. Cela est particulièrement avantageux pour simuler des processus se déroulant sur de grandes échelles de temps.

La capacité de MultIHeaTS à simuler des surfaces complexes a été illustrée par le calcul d'une surface bicouche. D'après nos résultats, nous recommandons une stratégie d'observation : mesurer la température de surface au lever du soleil, à midi et à minuit pour caractériser les profils de surface bicouche et homogène. Une deuxième application a tiré parti de la capacité de calcul rapide de MultIHeaTS en estimant le profil de température d'une surface anti-jovienne sur Europe pendant un million d'années, incluant les variations diurnes et les variations des éléments orbitaux de la lune galiléenne. Cela nous a permis de tracer pour la première fois la distribution de température en fonction de la profondeur sur une telle échelle de temps. Enfin, l'effet des éclipses de Jupiter sur l'hémisphère sub-jovien a été exploré, nous permettant de proposer une équivalence en utilisant un albédo modifié avec des erreurs limitées. Grâce à sa formulation par différences finies, le solveur peut être facilement couplé à d'autres processus, tels que le métamorphisme ou les changements de phase.

Compaction

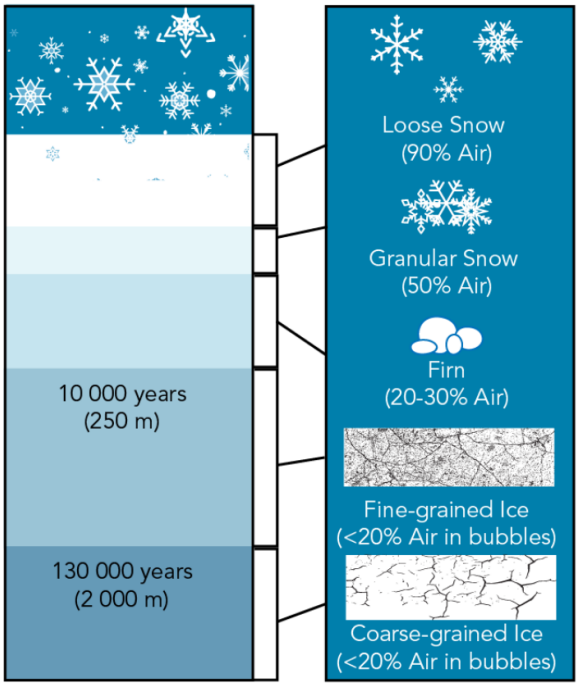

Figure 6.15: Compaction de la neige avec la profondeur sur Terre. Figure de Let's Talk Science 2021, inspirée par une image de Marshak (2012).

Plusieurs études fournissent des preuves convaincantes que la surface des satellites glacés est constituée d'un matériau poreux (Spencer et al., 1989; Rathbun et al., 2010; Ferrari et al., 2016; Cruz-Mermy et al., 2023; Oza et al., 2018). Sur Terre, des changements notables de la porosité à partir de mesures de carottes de glace ont été observés en Antarctique et dans le nord du Groenland, avec une échelle de variation d'environ 20 mètres (Alley et al., 1982; Hörhold et al., 2011; Gerland et al., 1999). Cette compaction conduit à des variations de densité, passant de la neige fraîche au névé, puis du névé à de la glace avec quelques bulles (voir Figure 6.15).

Les conditions en surface des lunes glacées, comme la gravité de surface et la température sur Europe, sont très différentes de celles sur Terre. Cela soulève la question : Comment la compaction sur les lunes glacées diffère-t-elle de celle sur Terre ? Quelle est l'échelle typique de compaction de la glace poreuse sur Europe ? De plus, pour modéliser les propriétés thermiques en surface, on peut se demander : La gravité induit-elle des changements notables de densité d'Europe ? Une telle connaissance serait particulièrement importante pour la sélection des sites d'atterrissage pour des concepts tel que "Europa Lander".

Pour aborder cette question, nous avons décidé de nous baser sur le comportement

de compaction de la neige sur Terre. De nombreuses études de terrain ont été menées dans les régions froides et enneigées de la Terre pour étudier la compaction de la neige sous l'effet de la gravité. Les mesures de carottes de glace indiquent qu'au cours des premiers dizaines de mètres, la gravité provoque des variations significatives de densité, passant de la neige fraîche au névé, puis du névé à la glace à bulles.

Nous avons utilisé les mesures de carottes de glace terrestres pour déterminer un paramètre fondamental lié à la compaction de la glace sous l'influence de la gravité : le coefficient de compaction de la glace. Grâce à cette analyse, nous avons pu déduire la longueur typique de compaction induite par la gravité sur Europe, soit $H = 150 \pm 4\,\mathrm{m}$, en supposant un coefficient de compaction de la glace similaire à celui de la Terre (voir Figure 6.16). En appliquant la même méthode, nous avons déterminé que l'échelle de longueur de compaction pour les corps glacés du Système Solaire varie de 20 m à 2000 m.

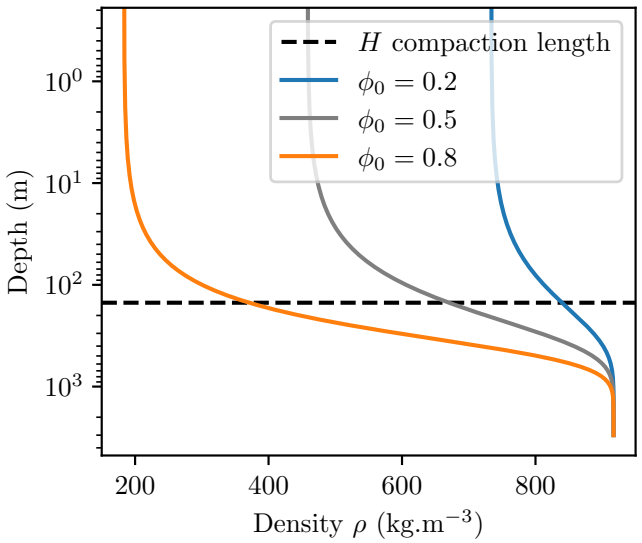

Figure 6.16: Profils de densités de glace en fonction de la profondeur pour la surface d'Europe et différentes porosités initiales en utilisant le coefficient de compaction de la Terre $\overline{\lambda} = 5.5 \pm 0.2 \times 10^{-6}\,\mathrm{Pa}^{-1}$. Pour référence, la longueur caractéristique de compaction H pour Europe est représentée par la ligne pointillée noire. La zone orange montre les couches superficielles affectées par les variations de température solaire, appelée profondeur de peau saisonnière. Nous observons que la porosité reste presque constante autour de la profondeur de peau saisonnière, en raison de la faible gravité d'Europe.

L'échelle de longueur de compaction dépasse largement les longueurs d'onde et les profondeurs de pénétration dans les gammes visible et proche infrarouge, qui ne peuvent s'étendre que sur quelques centimètres seulement. Les émissions infrarouges thermiques permettent d'estimer des caractéristiques aussi profondes que la pro-

fondeur thermique diurne et saisonnière, qui est typiquement inférieure à $\sim 10\,\mathrm{cm}$ et à moins d'une dizaine de mètres pour Europe, selon la diffusivité thermique. À de telles profondeurs, nous nous attendons à ce que la compaction induite par la gravité entraîne des changements relativement mineurs de la porosité. Cependant, les observations récentes du Radiomètre Micro-onde de JUNO pourraient sonder jusqu'à des dizaines de kilomètres de profondeur dans les surfaces des lunes galiléennes (Brown et al., 2023). L'analyse des observations pour Europe pourrait révéler de nouvelles contraintes sur la porosité de la couche de glace.

La force des modèles que nous avons utilisé réside dans leur simplicité et leurs solutions analytiques. Des améliorations peuvent être apportées en considérant l'influence importante de la porosité, de la température, des contraintes et de la taille des grains sur la viscosité, et en développant un scénario de compaction plus précis pour les croûtes des lunes glacées. De plus, d'autres mécanismes de compaction sont susceptibles de jouer un rôle près de la surface, tels que ceux induits par le jardinage spatial ou le métamorphisme de glace (Schaible et al., 2017; Raut et al., 2008), potentiellement observables par des instruments spatiaux. L'effet de ces mécanismes sur le profil de porosité de la glace n'est pas encore complètement compris.

À la lumière de ces résultats, les prochaines missions devraient envisager l'utilisation de faisceaux radar à grandes longueurs d'onde capables de pénétrer profondément dans le sous-sol pour évaluer le profil de porosité, comme REASON à bord d'Europe Clipper (Bayer et al., 2019) et RIME à bord de JUICE (Bruzzone et al., 2013). De plus, pour considérer les défis potentiels pour les atterrisseurs et les rovers (Pappalardo et al., 2013; Hand et al., 2022) pour opérer sur des surfaces très poreuses, et lors du développement de technologies telles que les cryobots (Vale Pereira et al., 2023) pour explorer les croûtes glacées et atteindre les océans souterrains, il est impératif de tenir compte de cette échelle de longueur de compaction substantielle. Par conséquent, sélectionner des sites cibles avec une faible porosité de surface serait d'un grand intérêt dans la planification de ces missions.

Métamorphisme de Glace

La neige sèche se compose d'un réseau de grains avec des pores interstitiels remplis d'un mélange d'air ou de vide et de vapeur d'eau. Au fil du temps, des "ponts" ou "cols" se forment entre les particules dans un processus appelé métamorphisme de glace, ou aussi "frittage" ou "recuit". Ce processus est principalement induit par la réduction de l'énergie de surface du système. Cette liaison intergranulaire des grains influence la résistance du matériau, sa viscosité, son fluage, ainsi que ses propriétés thermiques, optiques et électromagnétiques (Adams et al., 2001).

La cinétique du métamorphisme est très sensible à la température et à la taille des grains, les taux les plus rapides étant observés à des températures plus élevées et avec des grains plus petits. La Figure 6.17 montre le métamorphisme de deux grains à 253 K, où la formation d'un pont de taille notable se fait en environ ~ 1 h (Molaro et al., 2019). Sur les surfaces des lunes glacées, en raison des températures beaucoup plus basses, il n'est pas évident si le mécanisme de métamorphisme est efficace.

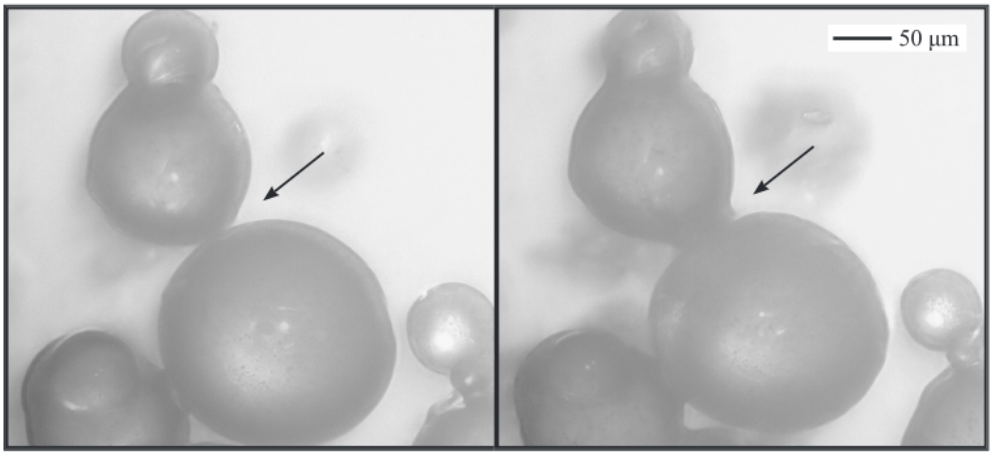

Figure 6.17: Les grains de glace d'eau subissent un métamorphisme à 253 K lors de la première observation (*à gauche*) et après 57 minutes (*à droite*), montrant la croissance du pont (*flèche*) de 33 à 65 µm. Les grains avaient initialement des rayons de 101 et 73 µm, rétrécissant respectivement de 3% et 4% après 57 minutes. Figure issue de Molaro et al. (2019).

La théorie du métamorphisme utilisée dans la communauté des sciences planétaires est fondée sur des études de métallurgie (Swinkels et al., 1981). Les estimations de l'échelle de temps du métamorphisme sur Europe, basées sur les températures de surface et les tailles de grains, ont été fournies par Molaro et al. (2019), avec des valeurs allant d'une limite inférieure de 10^4 ans à une limite supérieure de 10^9 ans (Molaro et al., 2019). La différence entre ces deux échelles de temps est significative. Savoir si l'échelle de temps du métamorphisme se situe vers la limite inférieure ou supérieure peut avoir un impact considérable sur notre compréhension des propriétés

de la surface, ce qui soulève les questions suivantes : Les conditions sur Europe sont-elles favorables au métamorphisme ? Comment les tailles de grains et les propriétés thermiques influencent-elles quantitativement les taux de métamorphisme ? De plus, la formation de ponts augmente la zone de contact entre les grains, améliorant la conduction de la chaleur au sein de la glace (Piqueux et al., 2009). Comment la conduction de la chaleur évolue-t-elle avec les variations microstructurales induites par le métamorphisme ? En anticipation d'un projet d'atterrissage en surface : Quelles régions d'Europe sont actuellement composées de grains de glace isolés ou interconnectés ?

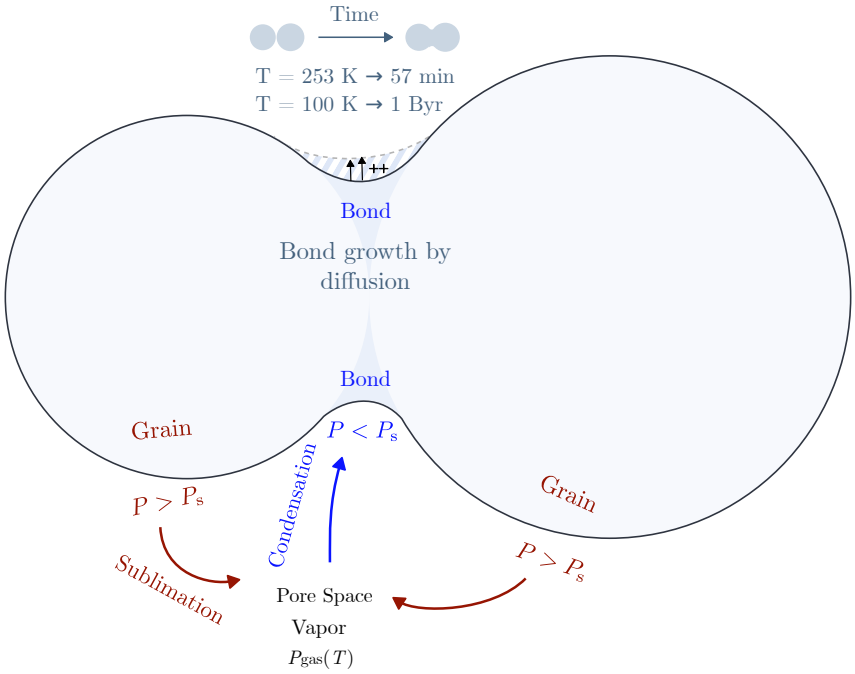

Figure 6.18: Diffusion par transport de la vapeur. En raison de la courbure, la matière sublime depuis les surfaces convexes des grains, puis se diffuse à travers l'espace poreux, et se condense sur les surfaces concaves des ponts.

Dans cette thèse, nous avons 1) affiné le modèle de métamorphisme pour inclure une description plus précise des échanges avec l'espace poreux (voir Figure 6.18) , et 2) couplé ce modèle à un solveur thermique pour étudier ses effets sur la surface d'Europe sur une échelle de temps d'un million d'années. Le modèle de métamorphisme proposé non seulement intègre des raffinements mathématiques issus de la littérature, mais inclut également une description de la conductivité thermique des grains métamorphosés, permettant un couplage bidirectionnel avec le transfert de chaleur.

Ce modèle de métamorphisme a été couplé au solveur thermique MultIHeaTS, aboutissant à la première version de notre modèle multiphysiques appelé LunaIcy. Nos simulations couvrent une durée d'un million d'années, nous permettant d'explorer en profondeur l'évolution de la microstructure glacée de la surface d'Europe. Les résultats montrent que les régions les plus chaudes subissent un métamorphisme significatif, même si des températures élevées ne sont atteintes que pendant une brève période de la journée. Ce processus se déroule sur des échelles de temps plus courtes que l'âge de la croûte de glace d'Europe, suggérant que ces régions devraient actuellement présenter une glace de surface composée de grains interconnectés.

Crystallinité

Les conditions trouvées à la surface des lunes glacées sont favorables à la formation et stabilité de glace d'eau amorphe (Schmitt, 1998) (voir Figure 6.19). Lorsque la vapeur d'eau gèle à de si basses températures, la glace forme une structure amorphe. Savoir si la surface d'Europe reste amorphe ou se cristallise peut avoir des conséquences importantes sur ses propriétés.

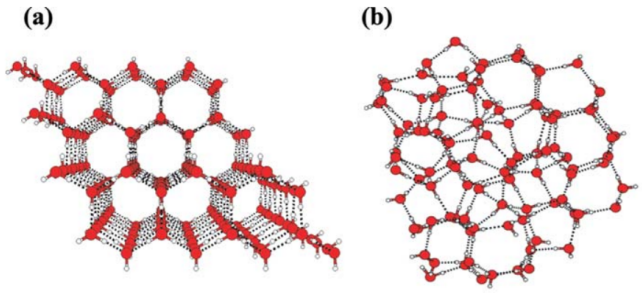

Figure 6.19: Arrangement moléculaire de (a) la glace Ih et (b) la glace amorphe de faible densité (LDA). Presque toutes les molécules s'intègrent dans le réseau de liaisons hydrogène (tirets noirs). Figure tirée de Belosludov et al. (2008).

La majorité des spectres de surface d'Europe ont été obtenus par le spectromètre de cartographie en proche infrarouge (NIMS) à bord de la sonde Galileoc. Sur la base de ces données, G. B. Hansen (2004) ont comparé les spectres riches en glace d'Europe avec des modèles de glace cristalline et amorphe. La bande caractéristique à 3.1 µm montre que, à une profondeur d'environ 1 mm, la glace d'eau sur Europe est principalement cristalline. En revanche, la bande à 1.65 µm s'ajuste mieux au modèle amorphe pour les glaces situées à moins de 1 mm de profondeur. Ces résultats suggèrent un gradient de cristallinité positif près de la surface.

Hansen a proposé que le mélange de phases de glace amorphe et cristalline observé à la surface d'Europe résulte d'un équilibre délicat entre les processus thermiques et radiolytiques. D'une part, la surface d'Europe atteint des températures où la cristalli-

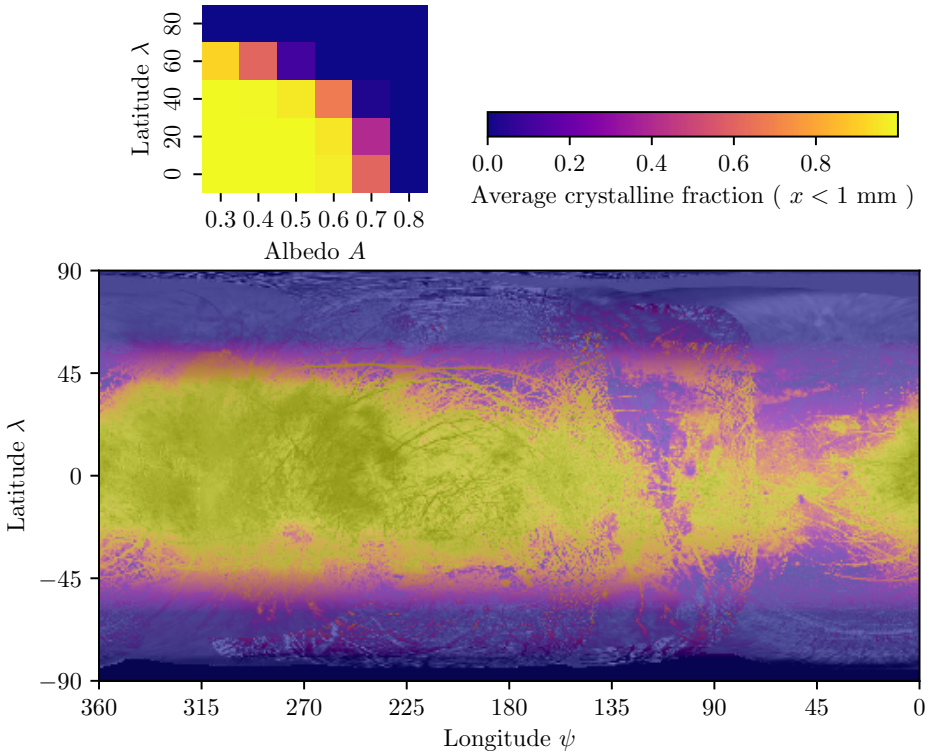

Figure 6.20: (*En haut*) Carte thermique de la fraction cristalline moyenne pour des profondeurs $< 1\,\text{mm}$ calculée sur Europe pour un flux uniforme de particules en fonction de l'albédo et de la latitude. (*En bas*) Interpolation de la carte thermique de la fraction cristalline moyenne sur la carte d'albédo d'Europe.

sation thermique peut se produire sur des échelles de temps raisonnables. D'autre part, l'intense radiation provenant de la magnétosphère de Jupiter est probablement responsable de l'amorphisation de la glace en surface. Malgré leurs observations, aucune des précédentes études G. B. Hansen, 2004; Ligier et al., 2016; Cruz-Mermy et al., 2023 n'ont proposé de modèle théorique pour expliquer la cristallinité qu'ils ont dérivée. Ce point soulève les questions suivantes : Comment la cristallinité des surfaces glacées d'Europe change-t-elle en fonction de la de la profondeur et du lieu ? Pourrait-il y avoir des changements périodiques observables de la cristallinité de la surface d'Europe ?

Pour mieux comprendre quel processus domine sur Europe, nous avons intégré la cristallisation thermique et l'amorphisation induite par radiations dans LunaIcy. En explorant divers paramètres de latitude et d'albédo, nous avons généré une carte de la cristallinité du premier millimètre de profondeur (voir Figure 6.20). Notre modèle révèle qu'aux pôles la glace est totalement amorphe, à l'équateur entièrement cristalline et un mélange des deux aux latitudes moyennes. Bien que notre modèle suppose une distribution uniforme des particules chargées, en réalité, les électrons se concentrent principalement sur l'hémisphère "trailing".

Les simulations de ces processus en compétition ont révélé des variations périodiques dans les profils de cristallinité. Notamment, les variations saisonnières atteignent des fluctuations de cristallinité jusqu'à 35 % aux latitudes moyennes. Ceci est significatif, car les missions à venir comme Europe Clipper et JUICE pourraient observer de telles variations. De plus, des variations plus petites mais notables sont attendues sur des échelles de temps de $\sim 55\,000$ ans, et des variations journalières pourraient être observables si l'amorphisation induite par les radiations dépasse l'intensité de notre modèle actuel.

Cette étude représente l'une des premières tentatives de modélisation couplée de la cristallinité d'Europe, nécessitant plusieurs simplifications pouvant introduire des écarts avec la réalité. Nous proposons d'observer des régions clés — Dyfed Regio, Balgatan Regio, Pwyll Crater, et Tara Regio — lors des missions Europe Clipper et JUICE pour valider ou affiner notre modèle. Des modèles de spectroscopie améliorés seront également essentiels pour estimer précisément la cristallinité, étant donné la nature non linéaire du processus.

Conclusion Générale

De nombreux processus affectent la surface d'Europe, et ils doivent être considérés de manière couplée. Dans cette thèse, nous avons adopté une approche de modélisation numérique pour étudier les surfaces glacées, inspirée par les modèles de manteau neigeux sur Terre (Brun et al., 1992; Vionnet et al., 2012; Lehning et al., 2002; Sauter et al., 2020). Ces modèles, utilisés pour la prévision des avalanches, intègrent généralement des équations unidimensionnelles régissant le transfert de chaleur, le transport de l'eau, la diffusion de vapeur et la déformation mécanique de

la neige. Bien que les processus à la surface des lunes glacées soient différents, le concept est similaire : la surface est soumise à des chauffages, radiations, bombardements, métamorphismes, etc. Tous ces processus sont interdépendants et doivent être modélisés ensemble (voir Figure 6.11).

Quel est donc l'état actuel de la microstructure de la glace d'Europe ?

La microstructure de la surface d'Europe semble hétérogène, influencée par l'équilibre variable des processus de surface. La cristallinité montre une variabilité en fonction de la localisation, de la profondeur et du temps, allant de la glace principalement amorphe à entièrement cristalline. La porosité est probablement élevée et ne se compacte pas par effet de gravité près de la surface. Le métamorphisme se produit probablement sur la majeure partie de la surface d'Europe, résultant en une glace multi-couche avec des grains interconnectés en surface et un gradient vertical de l'intensité du métamorphisme en profondeur.

Nous avons acquis de nombreuses connaissances grâce à ces modèles numériques, mais il reste encore beaucoup à découvrir. Il reste encore six ans avant que le premier engin spatial de l'histoire humaine n'orbite autour d'Europe, éclairant certains des mystères de la microstructure de la surface. En attendant, beaucoup de recherches peuvent être effectuées pour faire progresser le domaine. Développer et améliorer les modèles numériques nous aidera grandement à affiner les valeurs des paramètres non contraints décrivant la microstructure d'Europe. Ces modèles numériques complètent les études expérimentales et observationnelles. Une meilleure compréhension de la surface d'Europe grâce à la modélisation numérique améliorera l'interprétation des données spatiales, et sera cruciale pour les missions à venir JUICE et Europa Clipper. D'autres glaces du Système Solaire présentent des caractéristiques d'intérêt qui seraient pertinentes de modéliser, commme sur Ganymède, un autre satellite jovien, ou sur Mars. J'espère que l'avenir de LunaIcy ne sera pas le fruit d'un travail isolé, mais qu'il résultera de collaborations entre divers experts, chacun apportant sa contribution à l'étude des différents processus affectant les surfaces glacées.

List of Figures

List of Tables

Glossary

amorphous phase The amorphous phase refers to a state of matter in which atoms or molecules are arranged in a long-range disordered, non-crystalline structure. Unlike crystalline materials, which have a regular and repeating lattice, amorphous materials lack long-range order. This phase can occur in various substances, including solids like glass and ice, under certain conditions.. 2

bond albedo The bond albedo is the fraction of the total incident solar radiation that is reflected by a planetary body back into space, averaged over all wavelengths and angles of incidence. 15

density Density is the mass per unit volume of a substance. The SI unit is $\mathrm{kg\,m^{-3}}$. 34

heat capacity Heat capacity is the amount of heat energy required to raise the temperature of a given quantity of a substance by one degree. It is an extensive property that depends on the amount of material present. The SI unit is $\mathrm{J\,K^{-1}}$. The corresponding intensive property is the specific heat capacity, with the SI unit $\mathrm{J\,K^{-1}\,kg^{-1}}$. 34

ice Ih Ice Ih is the most common form of ice found on Earth, also known as hexagonal ice. It has a hexagonal lattice structure and is the form of ice typically found in snow, ice cubes, and glaciers on Earth. It has a lower density compared to liquid water.. 2

Laplace resonance The Laplace resonance is a type of orbital resonance where three or more orbiting bodies have orbital periods that are in a ratio of whole numbers, typically found in a system where the gravitational interactions between the bodies result in a stable configuration.. 15

porosity Porosity is the measure of the void spaces (pores) in a material, expressed as a percentage of the total volume. 36

porous material A porous material is a substance that contains pores (voids) throughout its structure. These pores can vary in size, shape, and distribution, affecting the material's properties such as density, permeability, and strength.. 36

thermal conductivity Thermal conductivity is the property of a material to conduct heat. The SI unit is $\mathrm{W\,m^{-1}\,K^{-1}}$. 34

thermal emissivity Thermal emissivity is the measure of a material's ability to emit thermal radiation relative to that of a perfect black body following Stefan–Boltzmann law. It is a dimensionless quantity, ranging from 0 to 1, where 1 corresponds to a perfect black body. 34

thermal inertia Thermal inertia is a measure of a material's ability to conduct and store heat. It quantifies how quickly a material can respond to changes in temperature. The thermal inertia (Γ) is given by $\Gamma = \sqrt{k\rho c_\mathrm{p}}$, where k is the thermal conductivity, ρ is the density, and c_p is the specific heat capacity. The SI unit of thermal inertia is $\mathrm{J\,m^{-2}\,K^{-1}\,s^{-1/2}}$. 35

thermal solver A thermal solver is a numerical tool used to simulate and analyze the thermal behavior of materials. It solves the heat transfer equation(s) to predict temperature distribution, heat flow, and thermal responses under various conditions. For the cases studied in this thesis, the heat equation is limited to the conduction of heat. . 35